COMPUTATIONAL AND EXPERIMENTAL ANALYSIS OF MULTI-CONE GEOMETRY UTILIZATION DURING REENTRY AT HYPERSONIC SPEEDS

A thesis submitted to the
University of Petroleum and Energy Studies

For the Award of
DOCTOR OF PHILOSOPHY
in
Aerospace Engineering

BY
Karthik Sundarraj

December 2019

SUPERVISOR (s)

Dr. Om Prakash
Dr. Ugur Guven

UPES
UNIVERSITY WITH A PURPOSE

Department of Aerospace Engineering
School of Engineering
University of Petroleum & Energy Studies
Dehradun – 248007: Uttarakhand

COMPUTATIONAL AND EXPERIMENTAL ANALYSIS OF MULTI-CONE GEOMETRY UTILIZATION DURING REENTRY AT HYPERSONIC SPEEDS

A thesis submitted to the
University of Petroleum and Energy Studies

For the Award of
DOCTOR OF PHILOSOPHY
in
Aerospace Engineering

BY
Karthik Sundarraj
(SAP ID 500024033)

December 2019

SUPERVISOR (s)

Internal Supervisor
Dr. Om Prakash
Professor
Department of Aerospace Engineering
University of Petroleum & Energy Studies

External Supervisor
Dr. Ugur Guven
Professor & Advisory Council
United Nations Affiliated Center on Space Science and Space Technology
Education in Asia-Pacific

UPES
UNIVERSITY WITH A PURPOSE

Department of Aerospace Engineering
School of Engineering
University of Petroleum & Energy Studies
Dehradun – 248007: Uttarakhand

Dedicated to my family

Inspired by my Grandfather

"Learning gives creativity

Creativity leads to thinking

Thinking provides knowledge

Knowledge makes you great"

                                        - *Avul Pakir Jainulabdeen Abdul Kalam*

October 2020

DECLARATION

I declare that the thesis entitled **COMPUTATIONAL AND EXPERIMENTAL ANALYSIS OF MULTI-CONE GEOMETRY UTILIZATION DURING REENTRY AT HYPERSONIC SPEEDS** has been prepared by me under the guidance of Dr. Om Prakash, Professor, Department of Aerospace Engineering, University of Petroleum & Energy Studies and Dr. Ugur Guven, Professor & Advisory Council, United Nations Affiliated Center on Space Science and Space Technology Education in Asia-Pacific. No part of this thesis has formed the basis for the award of any degree or fellowship previously.

Karthik Sundarraj

Department of Aerospace Engineering
School of Engineering
University of Petroleum & Energy Studies
Dehradun – 248007: Uttarakhand

Date: 11th October 2020

CERTIFICATE

I certify that Karthik Sundarraj has prepared his thesis entitled "**COMPUTATIONAL AND EXPERIMENTAL ANALYSIS OF MULTI-CONE GEOMETRY UTILIZATION DURING REENTRY AT HYPERSONIC SPEEDS**," for the award of PhD degree of the University of Petroleum & Energy Studies, under my guidance. He has carried out the work at the Department of Aerospace Engineering, University of Petroleum & Energy Studies supported by Department of Aerospace Engineering, Indian Institute of Science for CFD simulations and experimental studies under Dr. P. S. Kulkarni, Professor/Chief Scientist.

Internal Supervisor,

Dr. Om Prakash

Professor
Department of Aerospace Engineering
School of Engineering
University of Petroleum & Energy Studies
Dehradun – 248007: Uttarakhand

Date: 12th October 2020

CERTIFICATE

I certify that Karthik Sundarraj has prepared his thesis entitled "**COMPUTATIONAL AND EXPERIMENTAL ANALYSIS OF MULTI-CONE GEOMETRY UTILIZATION DURING REENTRY AT HYPERSONIC SPEEDS",** for the award of PhD degree of the University of Petroleum & Energy Studies, under my guidance. He has carried out the work at the Department of Aerospace Engineering, University of Petroleum & Energy Studies.

External Supervisor,

Dr. Ugur Guven

Professor & Advisory Council
United Nations Affiliated Center on Space Science
and Space Technology Education in Asia-Pacific

Date: 12th October 2020

ABSTRACT

The effects of attaching multiple ramps to the standard double ramp configuration along with variations in ramp angle, free-stream Mach number, surface temperature and leading-edge bluntness are discussed in this investigation. This study investigates the changes associated with shock wave boundary layer interaction (SWBLI) due to ramp induced flow breakdown and the flow field fluctuation with changes in flow characteristics and design. This type of ramp junctions typically features in re-entry vehicles, engine intakes, system and sub-system junctions, control surfaces, etc. Ramp junctions usually are associated with strong separation bubble that has significant upstream influence impacting the effectiveness of aerodynamic surfaces, engine performance, thermal behavior and stability. Computation studies are carried out using Second order accurate, finite volume RANS solver considering compressible laminar flow characteristics, with solver settings provided like experimental conditions as per literature. Comprehensive double ramp studies with suggestions on reducing the separation bubble size are invariantly considered in literature, however there has been no study in understanding the inclusion of additional ramps in such flow scenarios. Computational studies of varying ramp angle on third ramp configuration indicated decrease of bubble length at the first ramp junction when compared to double ramp configuration in the presence of a third ramp. The current research involves detailed study of flow around triple and quad ramp configurations, where the effect of ramp angle variations and freestream Mach number variations on the separation bubble behavior and the flow physics are studied in detail. Additionally, the effects of changing the leading-edge bluntness on the separation bubble behavior and the surface temperature variations on the separation and reattachment points are investigated in detail for triple ramp configuration. Studies on the effect of LE bluntness on SWBLI indicates that first critical radius or the inversion radius is noticed anywhere between 3.8^0 to 4.4^0 where the boundary layer and the entropy layer are assumed to be of same thickness. With further increase in leading-edge radius, the separation point seems to move downstream, and the reattachment point upstream decreasing the length of the separation bubble, indicating the fact the dominance of entropy layer over boundary layer. Yet again it can be noticed the reattachment point for 15^0 third ramp angle is increasing with increase in blunt radius and the separation point also indicating the same proving completely detached flow. It also confirms that the addition of third ramp does not alter the correlation between blunt radius and the separation bubble length, while there are noticeable upstream effects on the separation, reattachment and the overall shock wave boundary layer interaction. By varying freestream Mach number and ramp angle is was seen that the biggest bubble corresponds to the double ramp measuring 36.8 mm while all other bubble sizes corresponding to triple ramp are smaller indicating an upstream influence. The upstream influence could be because of the thickening of the boundary layer due to the compression corner at

second junction. The entropy layer might be engulfed inside the boundary layer leading to the increase of separation bubble size at the first junction. Completely engulfed entropy layer alters the flow properties which is assumed to affect the separation and reattachment points at the first junction. It is critical to understand this flow physics in detail which is identified to occur in situations where there could be a complex junction in a system or a subsystem of high speed vehicles and so experimentation must be considered as the next step for better understanding of such complex flow physics and also to add basis for all the computational investigations. Investigations done on triple ramp configurations with varying wall temperature showed that increase in Mach number does reduce the bubble length at both junctions while bubble length remains to be bigger for higher wall temperatures. Biggest separation bubble of size 36.47 mm and 21.6 mm at the first and second junctions respectively can be seen for Adiabatic wall condition at Mach 6 indicating the effects of surface temperature on boundary layer thickness. The bubble size continues to increase at the first junction in case of adiabatic conditions with bubble size reaching a maximum of 44.31 mm at first junction for Mach 8 while the maximum bubble size in case of isothermal surface temperature of 330 K at Mach 8 freestream condition in just 14.31 mm. This is a considerable reduction in bubble size noticed due to surface temperature changes. Hence it is evident that increase in freestream velocity with increase in wall temperature reduces the bubble size considerably while also reducing the heat flux, on the contrary considering adiabatic wall conditions with increase in freestream Mach number has adverse bubble growth at the first junction. At the end of this study it was evident that such complex junction needs detailed understanding on how they benefit or impact the overall design of the system. It also gave a very good insight on the nature of flow around such complex junctions and instills motivation for detailed experimental understanding.

Experimental investigations are performed in the 0.5m Hypersonic wind tunnel at freestream condition of Mach 6. The experiments were performed at a freestream Mach of 6, with freestream pressure (P_∞) and temperature (T_∞) being 108psig and 411K respectively, the viscosity (μ) is calculated to be 23.31×10^{-6} Pa-s and the thermal conductivity (k) is calculated as 0.0317 W/mK. Five models are chosen to perform the experimental analysis, four models are triple ramp configuration with varying third ramp angle of 7.5^0, 10^0, 12.5^0 and 15^0 and one model of quad ramp configuration with third ramp angle 7.5^0 and fourth ramp angle 12.5^0. The experimental runs were validated through CFD study to establish confidence in the tool capability to predict complex flow physics. The pressure plots obtained through simulations predicted the separation locations accurately when compared with the schlieren, the reattachment and post-reattachment points had good agreement with the experiment, proving HiFUN to be able to capture complex flow physics. Experimental studies give clear understanding about flow physics around complex multi-ramp configurations, following points are the major derivatives from this experimental study.

a. Experimental results clearly indicate presence of a highly turbulent shear region at the second and third ramp junctions having its influence at the upstream separation locations along with considerable influence on the bubble size and intensity.

b. With increase in ramp angle the reattachment points are pushed upstream and closer to the junction itself, causing complex flow at the junction with multiple shock interactions which is eventually seen as a pressure peak both in experiment and validates well with CFD predictions.

c. Through experimental study it is deduced that the upstream influence is majorly attributed to the flow deflections and the upstream flow of information in the form of turbulent shear through the boundary and entropy layer. This encourages for an entropy and boundary layer study as future research.

d. With increase in number of ramps and the ramp angles the flow physics tend to become highly complex, resulting in high pressure complex flow interactions where it becomes difficult to interpret the shock and separation physics from the schlieren, which through simulation studies gives better understanding and perspective, making simulation studies inevitable.

e. The outcome of experimental study with validation through CFD simulations give confidence on the ability of simulation software such as HiFUN to predict such highly complex flow physics, capable of deriving insights on unseen and inexperienced physics.

ACKNOWLEDGEMENT

At the very outset of this report, I would like to express the deepest appreciation to Dr. Ugur Guven, my mentor, without whose continuous motivation and follow-ups this work would have not become a reality. My association with Dr. Guven and his mentorship methods are unbelievably simplistic, mainly for the freedom he offers to his research students and above all the level of support and ownership he takes in making his students successful. "Work and money are temporary, while this research and the PhD degree is going to be permanent" are his very own words that kept me motivated all along this journey, be it extremely strenuous work-research balance or slow and problematic research phase. I am deeply indebted to him for guiding me through all the challenges. I am extremely thankful and indebted to Dr. Om Prakash, my co-mentor. He has been the knowledge base for a lot of research and technical insights. The quality of this research work and the research methodology is because of the suggestions and insights given by Dr. Om Prakash. He comes with exceptional knowledge in the field of Aerospace and working with him under his guidance has always been a fruitful experience.

It is with sense of profound gratitude that I express my sincere thanks to Prof. P S Kulkarni for his inspiring guidance, valuable counsel, stimulating discussions and constant encouragement throughout my career as a research student and working professional. I am deeply indebted to him for introducing me to the field of Computational Fluid Dynamics (CFD). My association with him has been an experience of immense value and I shall always cherish its memory. Prof. Kulkarni is more than just a mentor but a well-wisher, who has been an integral part of many important moments in my life and he shall continue to be an important driving force for my future progressions. I also thank him for allowing me to use his laboratory facility for all my computational studies. He took the step forward in helping me get all necessary permissions to enter the campus and use the necessary facilities. Apart from this he took a lot of effort in introducing me to the High-Speed wind tunnel complex for my experimental works and to SandI for the HiFUN simulation software. Without these efforts, it would have been almost impossible for me to use the High-Speed Wind Tunnel facility at IISc. It is certain that a big chunk of my professional excellence is because of the opportunities given by Dr. Kulkarni. A lot can be written about the role of Dr. P S Kulkarni in my life, but I would like to stop by thanking him unconditionally. I must thank Prof. Hiremat, the person who introduced me to both IISc and Dr. Kulkarni almost 10 years back. He is also the person because of whom I started liking Fluid Dynamics and a huge fan of his lectures.

I take this opportunity to thank the people who were key contributors for the execution of this research work. I cannot thank enough for the support given by Dr. Nikhil Shende, the Director for Simulation and Innovation Engineering solutions. He has been very generous in providing me with

TABLE OF CONTENTS

LIST OF FIGURES

LIST OF TABLES

NOTATION AND ABBREVIATIONS

The symbols used in the manuscript have the following meanings

Notation

$\bar{X}_L$	Viscous interaction parameter at junction
ρ	Density
θ	Ramp angle
θ_{is}	Incipient separation angle
μ	Dynamic viscosity
τ	Shear stress
a	Speed of sound
C	Chapman-Rubesin constant
C_f	Skin friction coefficient
H	Enthalpy
L	Reference length
L_b	Bubble length
M	Mach number
P	Pressure
P_r	Prandtl number
q	Heat flux
r	Leading edge radius
Re	Reynolds number
S	Sutherland's constant
St	Stanton number
T	Temperature
T_{ref}	Reference temperature
U	Conservative variable vector
u	Velocity component in x-direction
v	Velocity component in y-direction
X_{sep}	Separation point
X_{re}	reattachment point

Subscripts

∞	Free stream conditions
0	Total or Stagnation values
ref	Reference values
CR	Critical

Abbreviations

BHEEMA	Boltzmann Hypersonic Euler Equation for Missile Aerodynamics
CFD	Computational Fluid Dynamics
CML	Computational Mechanics Laboratory
DR	Double Ramp
FB	First Bubble
HiFUN	High Resolution Flow Solver on Unstructured Meshes
SB	Second Bubble
SWBLI	Shock Wave Boundary Layer Interactions
TR	Triple Ramp
QR	Quad Ramp

CHAPTER 1. INTRODUCTION

The current technological advancements stand at a stage where the gap between space flight and atmospheric flight are closing in through human interventions and are now a dream that can be realized. The advent of hypersonic vehicle has created hope in this closure of gap and hence a lot of research is conducted in this area. Man's desire to explore deep space led to many space missions and through these the concept of reentry and reentry vehicles were understood. Apart from hypersonic reentry vehicles there are other hypersonic vehicles such as missiles and transport aircrafts in existence or at least in their nascent stages of development. Most of the reentry vehicles enter earth's atmosphere at very high velocities leading to excessive aerodynamic heating [1]. The temperature of the object becomes very high due to the transformation of kinetic energy of the falling object into heat energy. At such situations the design of the spacecraft is of prime importance. Various researchers [2-11] have investigated shock wave boundary layer and interaction physics through design modifications such as blunting, cavitation, ramping, flaring, external attachments such as aero disc or spike etc. to evaluate and understand the importance of these design features and also to measure the dependency on these features.

1.1   COMPUTATIONAL FLUID DYNAMICS (CFD)

"Computational Fluid Dynamics (CFD) is the science of determining a numerical solution to the governing equations of fluid flow whilst advancing the solution through space or time to obtain a numerical description of the complete flow field of interest" [17]. The equations can represent different flow characteristics involving steadiness, compressibility, viscosity and reacting fluid behavior. The equation and its form depend on the application planned for simulation. The simulation is considered to be as state of the art based on factors such as complexity of the model, flow nature and the type of infrastructure [17].

The general attempt at understanding and then predicting the world around us is achieved by using three tools: experiment, theory and computation. To understand what computational fluid dynamics is not, remember that computation is used along with experiment and theory in numerous ways. Experiments can be automated. Raw experimental data can be reduced to physically meaningful quantities. For example, one may have to do some post-processing to clean up the data, like de-noising and so on. Data can be processed to convert many measurements to useful forms: like obtaining streamlines or master curves that capture behavior so as to aid design. All of this can be done with the help of computers.

Similarly, computers can be used to perform symbolic manipulation for a theoretician. They can be used for visualizing closed-form solutions or solving intermediate numerical solutions. Computational fluid dynamics is the use of computer algorithms to predict flow features based on a

set of conservation equations. However, we may have encountered computer packages that simulate flow over and through objects. One could classify the use of these packages as experimental computational fluid dynamics. After all, we are using something like a simulated wind tunnel to understand the problem at hand. It is important to have some knowledge of CFD in general and the algorithms used in that package in particular would help. Though, an understanding of the physical principles and fluid mechanics may often suffice.

We use the conservation laws that govern the universe to build computer models of reality. We want to understand the computer models and would like to predict its behavior. How faithful is it? How robust is it? How fast is it? All of these questions are asked and answered in the context of fluid dynamics, so discipline is called Computational Fluid Dynamics [reference: Elements of Compuational Fluid Dynamics by M. Ramakrishna].

Fluid flow is governed by three fundamental equations:

➢ Mass conservation equation.

➢ Momentum conservation equation.

➢ Energy conservation euqation.

The general forms of all these fundamental equations are usually PDE's [17].

Continuity Equation:

For incompressible fluid flow problems, the continuity equation states that "the mass of fluid flowing into a control volume must equal the mass of the fluid leaving the control volume". If the density is constant throughout the flow the equation is given as [17]:

$$\nabla.V = \frac{\partial u}{\partial x} + \frac{\partial v}{\partial y} + \frac{\partial w}{\partial z} = 0 \qquad\qquad 1.1$$

Momentum Equation:

These equations are used to calculate velocity and pressure at a given position in the flow. The equations in x, y and z directions respectively are as shown below [17]:

$$\rho\left(\frac{\partial}{\partial t} + \nabla.V\right)u = -\frac{\partial p}{\partial x} + \mu\nabla^2 u + \rho f_x \qquad\qquad 1.2$$

$$\rho\left(\frac{\partial}{\partial t} + \nabla.V\right)v = -\frac{\partial p}{\partial y} + \mu\nabla^2 v + \rho f_y \qquad\qquad 1.3$$

$$\rho\left(\frac{\partial}{\partial t} + \nabla.V\right)w = -\frac{\partial p}{\partial z} + \mu\nabla^2 w + \rho f_z \qquad\qquad 1.4$$

Several applications arise in the aerospace industry for the numerical solution to Navier-Stokes equations. Flow past multi-bodies of interest in high lift, large angle of attack aerodynamics, accurate prediction of drag are few important applications to cite. There are numerous applications pertaining

to simulation of laminar separated flows. These include flow past Mini-Aerial vehicles, flapping wings. Accurate computation of heat transfer coefficients in case of high-speed viscous flows in one of the challenging areas. Numerous applications arise in the turbine cascade flows; internal flows encountered in the propulsion systems.

Thom [18] was the first to simulate a substantial fluid dynamic problem, flow past circular cylinder at a Reynolds number of 10, by solving Navier – Stokes equation applying finite difference method. Later on, solution of these equations became more and more desirable and practical for aerodynamic problems. Tremendous increase in performance of workstations as wall as of parallel computers and improvements made in numerical algorithms have permitted CFD to simulate grand challenging flows.

1.2   HYPESONIC FLOW CHARATERISTICS

Hypersonic Aerodynamics can be defined as "The phenomena associated with very high-speed flight, such as the one encountered during atmospheric reentry". The Apollo Lunar capsule holds the current record for highest altitude and speed at 10973 m/s. One of the notable aspects of the Apollo Mission was its atmospheric reentry after the lunar mission. As the word hypersonic makes its presence in all the reentry flights it is now justifiable to discuss its characteristics [1].

Development of thin shock layers are the primary characteristics of hypersonic flows. The consequence of the presence of thin shock layer is the frequent interaction between inviscid and viscous boundary layer. Generally high-speed vehicles fly at high altitudes where the density is very low and hence the Re (Reynolds no.). Therefore, the boundary layer created over the object is thick, besides the thickness of boundary layer at hypersonic speeds is directly proportional to M_∞^2. In most cases the boundary layer thickness and the shock layer thickness are same in magnitude as shown in figure 1.1. In this figure the shock layer is fully viscous and hence it affects the surface pressure distribution and the shock shape, and this phenomenon is known as *viscous interaction phenomena*. Figure 1.2 (a) and (b) shows hypersonic flow over flat plate with and without viscous interaction [1].

Fig. 1.1 Thin Shock Layer [1]

2

(a) Inviscid Interaction   (b) Viscid Interaction
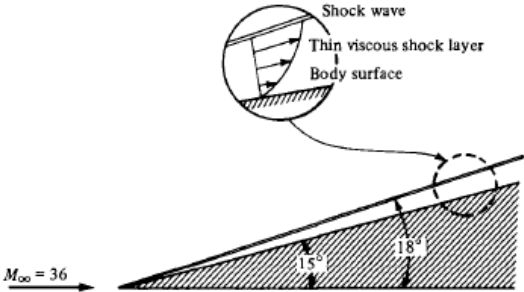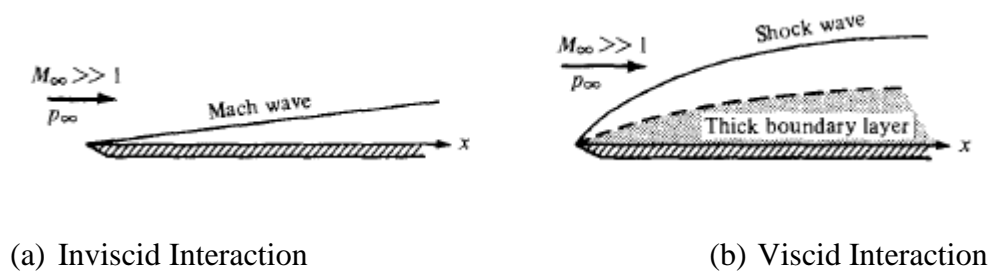
Fig. 1.2 Viscous flow over flat plate [1]

Fig. 1.2 (a) shows a case where the flow is completely inviscid and where a Mach wave is seen attached to the trailing edge trailing downstream. The freestream pressure and the pressure distribution over the flat plate is same as there is no flow deflection. Fig. 1.2 (b) shows a realistic case where thick boundary layer is present due to hypersonic flow conditions. The thick boundary layer pushes the flow outwards and leading to deflection of external flow region causing a bent strong shock. The pressure at the leading edge is considerably high when compared to the freestream pressure and it normalizes far downstream. This increase in pressure at the leading edge also increases the aerodynamic heating and hence hypersonic viscous interaction is of prime importance [1].

The second most important characteristic of hypersonic flow is aerodynamic heating due to high temperatures within the shock wave. As a reference to this phenomenon refer to fig. 1.3. The stagnation temperature obtained is very high of the order of 11,000 K. At such high temperatures the gas in this region will become highly reactive. When the temperature crosses 9000 K, oxygen and nitrogen dissociate, and ionization will begin to occur. The process of ionization emits free electrons which is one of the major reasons for communication blackouts [1].
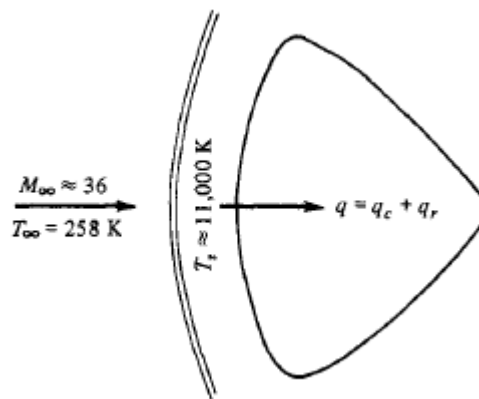
Fig. 1.3 Shock Layer ahead of Blunt Body [1]

At reentry velocities, design of space vehicle is dictated by aerodynamic heating and hence blunt body concept evolved to address the aerodynamic heating. This brings to the third important characteristic of hypersonic flow over an object i.e. Heat transfer. Aerodynamic heating usually occurs by the means of thermal conduction by means of convective heating from the shock layer to

the body surface. For velocities about 8000 m/s this type of heating is the most meaningful means of heat transfer. At higher velocities temperature at the shock layer reaches even higher values where radiation dominates the heat transfer mode over convection. For the example given in the above figure the temperature reached is as high as 11,000 K, where thermal radiation from the hot gas becomes the dominant heat transfer to the system. Hence the factors that distinguish hypersonic flow from supersonic flows are these above-mentioned characteristics [1].

1.3   SHOCK WAVE BOUNDARY LAYER INTERACTION

High speed flows mainly are dependent on shocks and shock interactions that change the course of flow field and their behavior. The aerodynamic body is affected by these forces and heat loads. The study along these lines is called shock wave and boundary layer interaction (SWBLI) which is related to interaction between inviscid and viscous regions. These interactions in the flow affect both internal and external flow aerodynamics. Generation of separation bubble, boundary layer separation, increased heating and even turbulent re-attachment could be caused through the presence of SWBLI. The shock wave and boundary layer interaction are majorly experienced by subsystems such as wing and body junction, nozzles, inlet of engines etc. As an outcome of design refinement several flow control techniques have been developed to suppress the effects of SWBLI [4]. Hypersonic flow field around blunted cone flare is a very good example that exhibits SWBLI. Such flows around a cone exhibit features bow shock detached from the cone and oblique shock at cone-flare interacting with the boundary layer. The SWBLI produces separated flow at the upstream forward-facing corner where the deflection in the form of a ramp/flare is present. The separation length impacts the control, stability etc., of a hypersonic reentry vehicle [2].

Ramp Induced Shock Wave Boundary Layer Interaction: A pictorial representation of Ramp induced Shock wave and boundary layer interaction is shown in Fig. 1.4 (a) & (b). A separation shock wave is generated due to an abrupt change in flow direction in the presence of ramp. The shock interacts with the boundary layer which experiences unfavorable pressure gradient. Flow separation caused due to such gradients majorly depends on factors associated with flow conditions, geometrical conditions and boundary layer behavior. The parameter at interest is the angle known as incipient separation angle given by Needham and Stollery [7].

$$M_\infty \theta_{is} = 80\sqrt{\overline{X_L}} \qquad\qquad 1.5$$

Where $\overline{X}_L$ – Viscous interaction parameter at junction

$$\overline{X}_L = M_\infty^3 \sqrt{C} \,/\, \sqrt{Re_L} \qquad\qquad Where, \ C = \frac{\mu_w}{\mu_\infty}\frac{T_\infty}{T_w} \qquad\qquad 1.6$$
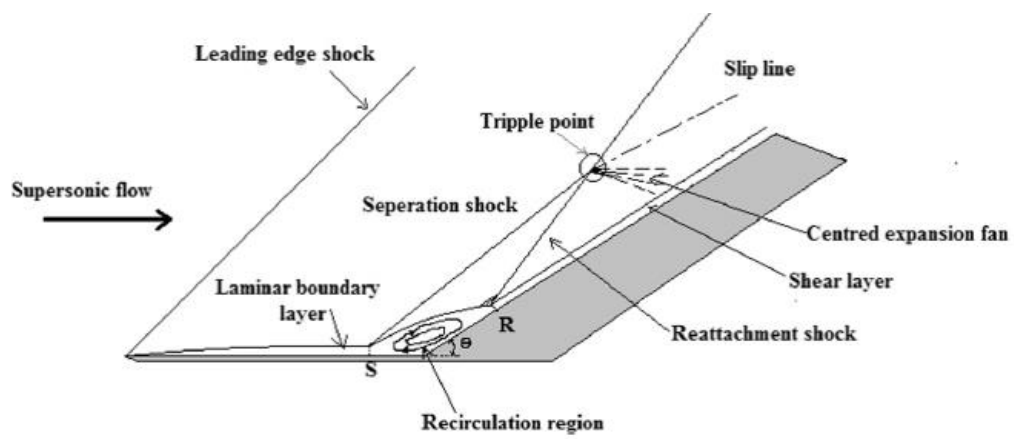
(a)[3]
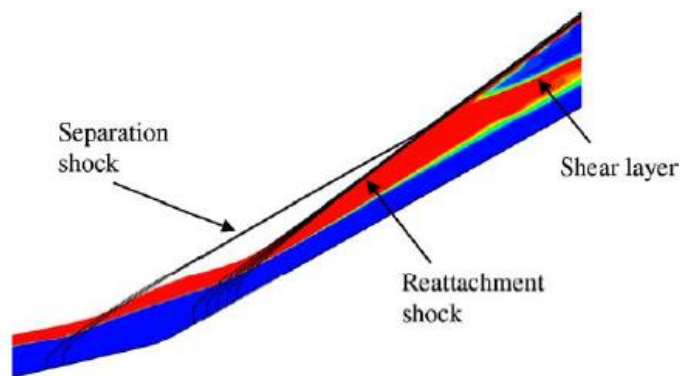
(b)[5]

Fig. 1.4 Pictorial representation of hypersonic flow over a ramp with SWBLI

Flow separation takes place when the incipient separation angle is lesser than deflection angle. From fig. 1.4 (a) separation occurs at point 'S' upstream of the ramp. The separation creates compression region creating a separation shock ahead of the separation region. Separation bubble can be identified by sudden increase in the pressure from nearly constant in the downstream region to a sudden increase in the compression region. The flow reattaches at point 'R' on the ramp surface. The recirculation zone extends between point 'S' and point 'R', which is the separation bubble length. In case the ramp angle was smaller than the incipient separation angles the flow would have not undergone much deflection as in the previous case and would have followed the profile of a laminar boundary layer without separation at ramp [4].

Leading-Edge Bluntness effects on SWBLI: To enhance the performance of Ramp based SWBLI by reducing the intensity of this interaction through delayed separation several control mechanisms are reported to have been employed. The most widely used control mechanism to control shock interaction is a forward-facing leading edge with significant bluntness. Bluntness changes the shock wave dynamics and boundary layer physics, mainly because the attached oblique shock is replaced

by an even stronger bow shock detached from the surface. This replacement leads to the formation of strong entropy layer that interacts with the boundary layer, accelerating the flow over the object due to the favorable pressure gradients. Hence a high-speed shear flow approaches the ramp which influences the location of separation bubble, bubble size, θ_{is} and the reattachment point. Based on research the addition of bluntness to the leading edge provides better suppression of shock interaction when compared to the sharp leading edge. The representation of the flow over blunted leading-edge is shown in Fig. 1.5 [5]
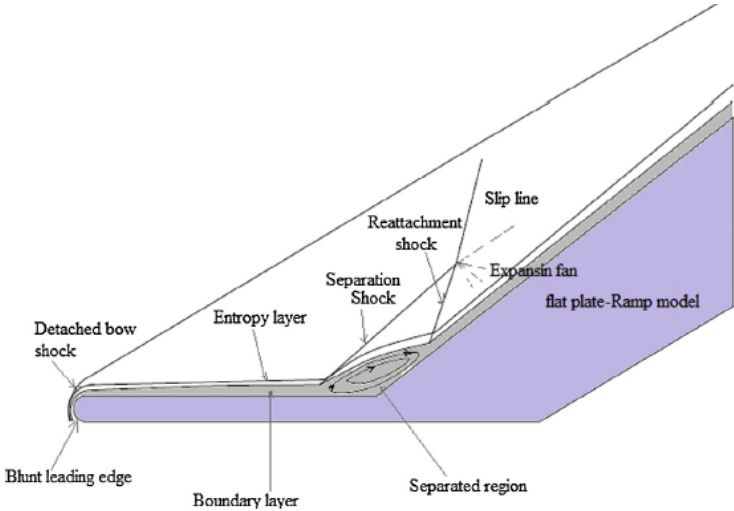
Fig. 1.5 Flow over Blunted Leading edge with SWBLI [5]

CHAPTER 2. LITERATURE

2.1 OVERVIEW

High speed aerodynamics mainly revolves around shocks and shock interactions that change the course of flow field and their behavior. The heat loads and forces are affected due to these alterations. The current technological advancements stand at a stage where the gap between space flight and atmospheric flight are closing in through human interventions and are now a dream that can be realized. The advent of hypersonic vehicle has created hope in this closure of gap and hence a lot of research is conducted in this area.

Various researchers [2-11] have investigated shock wave boundary layer and interaction physics through design modifications such as blunting, cavitation, ramping, flaring, external attachments such as aero disc or spike etc. to evaluate and understand the importance of these design features and also to measure the dependency on these features. The study of interactions between inviscid and viscous regions is called as shock wave and boundary layer interaction and the presence of these interactions in the flow affect both internal and external flow aerodynamics [4]. Generation of separation bubble, boundary layer separation, increased heating and even turbulent re-attachment could be caused through the presence of SWBLI. Careful attention must be given to the design of space vehicle systems and subsystems which experience such SWBLI [4]. As an outcome of design refinement several flow control techniques have been developed to suppress the effects of SWBLI [3]. Hypersonic flow field around blunted cone flare is a very good example that exhibits SWBLI. This example exhibits major features of flow around a space vehicle such as detached bow shock ahead of the cone and oblique shock with boundary layer interaction at the cone flare junction [2]. The SWBLI can produce separated flow at the upstream forward-facing corner where the deflection in the form of a ramp/flare is present. The separation length has implications over control, stability etc., of a hypersonic reentry vehicle [5]. A separation shock wave is generated due to an abrupt change in flow direction in the presence of ramp. The shock interacts with the boundary layer over the wall which experiences unfavorable gradients in pressure. Flow separation in the presence of such gradients majorly depends on factors associated with flow conditions, geometrical conditions and boundary layer behavior. The parameter at interest is the angle known as incipient separation angle given by Needham and Stollery [7].

$$M_\infty \theta_{is} = 80\sqrt{\overline{X_L}} \qquad\qquad 2.1$$

Where $\bar{X}_L$ is the viscous interaction parameter at ramp junctions;

$$\bar{X}_L = M_\infty^3 \sqrt{C} \ / \ \sqrt{Re_L}$$

$$where \; C = \frac{\mu_w}{\mu_\infty} \frac{T_\infty}{T_w} \qquad\qquad\qquad\qquad 2.2$$

Boundary layer separation takes place if the incipient separation angle is lesser than deflection angle. Separation occurs at a point ahead of the compression corner, separation leads to compression waves forming a separation shock ahead of the separation region. Separation bubble can be identified by sudden increase in the pressure from nearly constant in the downstream region to a sudden increase in the compression region. The flow reattaches at a point on the ramp surface, the recirculation zone extends between the separation and reattachment point and the distance between these two points is called as length of separation bubble [3]. In case the ramp angle was smaller than the incipient separation angles the flow would have not undergone much deflection as in the previous case and would have followed a laminar boundary layer profile without separation at the ramp [4]. Such flow alterations occur mainly due to the influence of the ramp on the upstream flow physics. The area of interest shall be the distance between the ramp junction and the upstream point of influence. To enhance the performance of Ramp based SWBLI by reducing the intensity of this interaction through delayed separation several control mechanisms are reported to have been employed, reference to such control mechanisms can be seen is many past investigations. The current research work also pursues the idea of enhancing the performance of any system or subsystem functioning at hypersonic flow regime by altering flow paths through design modifications or study the nature of flow behavior in an unforeseen and unexplored design conditions such as multi-ramps.

Several researchers have investigated shock wave boundary layer phenomenon through several design modifications as stated in earlier sections. R. Savino and D. Paterna [2] conducted validation studies of flow around blunted cone flare in hypersonic flows. Experimental studies were performed in H3 Mach 6 wind tunnel at Von Karman Institute under laminar flow conditions. This work gives a detailed insight on the importance of grid independent study and the influence of mesh size on wall pressure, heat flux and skin friction parameters. It has also been noted through this study that the accuracy of separation bubble size, its location, the flow separation and reattachment locations are all dependent on the resolution of mesh near the wall and at the ramp junction. Sensitivity of wall pressure and heat flux to small changes in surface temperature has also been studied. It is noticed that the length of separation bubble increases with increase in surface temperature. The authors have also considered thermal conductivity effects by considering different materials properties of the experimental model and validating the same through computational methods. Bibin John and Vinayak Kulkarni [3 − 5] have performed wide range of numerical investigations addressing the ramp induced shock wave boundary layer interactions. Extensive and in-depth details on the effect of various flow and geometric parameters and their correlation with the SWBLI in hypersonic flows performed through finite volume based computational solver are presented. Importance of Quantitative approach

over qualitative measurements to estimate the length of separation bubble and upstream influence through skin friction and wall shear has been detailed out, which gives a clear insight on the method of approach to understand separation physics [4]. It is also clear from the study, the concept of incipient separation angle can apply only for flows that are fully separated. It is found from these investigations that the separation bubble length is clearly dependent on flow and design parameters, where the bubble length increases in size with rise in wall surface temperature and with increase in freestream Mach the bubble length seems to decrease in size. The research also discusses about the strong correlation between separation bubble length and the LE bluntness. It is understood from this investigation the presence of two critical radius of leading-edge bluntness [5].

Interactions between a shock wave and a boundary layer can produce a region of separated flow. At the upstream facing corner formed by a deflected control surface on a hypersonic reentry vehicle, where the length of the separation has a implications for the control effectiveness. Flow separation takes place, when a shock wave generated internally to a hypersonic air-breathing propulsion system impinges on a boundary layer. The non-equilibrium real gas effects tend to change separation length in high enthalpy shock wave boundary layer interactions are poorly understood. Most of the experiments performed with the flow regimes where real gas effects are insignificant or may not have found expected results, and most of the numerical studies have found to be dissimilar real gas effects under different conditions [19].

The analytical procedure to compression corner flows with Mach number 12 and enthalpy lesser than 12 MJ/kg and found that chemical equilibrium resulted in reduced separation length compared to chemically frozen flow at the same conditions. For most of the equilibrium results increased separation length with increasing enthalpy [20]. Another study [21], also found smaller separation length for reacting flow, by the integration of momentum further extended to include the species conservation equation for a binary dissociating gas, and taking further fully dissociated or fully recombined boundary layer edge conditions with a fully recombined wall condition.

2.2   FUNDAMENTAL PROBLEM: SHOCK-WAVE INTERACTION

The shock-wave interaction with the streamlined body surface is one of the fundamental problems of modern aerodynamics. This problem is important for actual high-speed vehicles having wings, control surfaces, and air inlets. The presence of compressing surfaces generating oblique shock waves is a characteristic feature of a supersonic or hypersonic air inlet. The leading edges of a hypersonic inlet must be blunted to restrict the surface temperature, and the bluntness should be small in order to reduce total pressure losses. Due to the impact of these factors the heat flux at the inlet achieves extreme values. Both the leading edges and vast zones of the channel inner surface, where the shock waves interact with the boundary layer, are subjected to intense heating.

The interaction of the oblique shock with the boundary layer has been studied for more than 60 years [22-25]. It has been found that a sufficiently strong incident shock causes the boundary-layer separation. A region of free interaction is formed in front and at the beginning of the separation zone. The flow in this region does not depend on the incident-shock intensity. The pressure and heat transfer coefficients sharply increase in the region of boundary-layer reattachment. Several approximate methods for calculations of flow characteristics in the interference region have been developed. Asymptotic solutions (for the Reynolds number approaching infinity) were obtained for the laminar flow at the beginning and at the end of separation zone [26]. However, a global solution of this problem can be obtained only numerically. At moderate strengths of the impinging shock wave the numerical solutions provide satisfactory results. In the case of a strong shock the predicted values of heat flux and friction for the turbulent flow significantly differ from the experimental data.

The influence of small bluntness on flows over plates and cones attracted the attention of researchers at the very beginning of hypersonic investigations [27-29]. This was caused by the fact that, on one hand, it is impossible to make perfectly sharp wing edges and fuselage noses on an actual vehicle and, on the other hand, some bluntness of the leading edge and nose is required to reduce aerodynamic heating. A theoretical study of hypersonic flows over weakly blunted bodies was first carried out in the framework of the inviscid gas theory using the strong-blast analogy. According to this theory an extended region of high pressure is formed on the plate behind the bluntness. At a large distance from the leading-edge pressure tends to its value in the undisturbed flow. The bluntness causes an increase of flow temperature and decrease of flow density near the body surface due to the total pressure losses in the bow shock. For $M_\infty \to \infty$ the flow density tends to zero. A theory of hypersonic viscous gas flow over a blunt plate and wedge was developed in [29]. This theoretical model is based on the strong-blast theory including the boundary-layer displacement effect. The parameter ranges, where the bluntness or the displacement effect is dominant, were identified. The experimental study of heat transfer on a slightly blunted plate at $M_\infty = 12$ and relatively small Reynolds numbers was performed in [29]. The theoretical study was continued in [30] using the integral equations for the boundary layer. The experimental investigation of the bluntness effect was carried out in [31] for a plate in the free stream Mach number range from 14 to 20 and low Reynolds numbers (the parameter of viscous-inviscid interaction was varied in a wide range from weak to strong interaction, namely, $1 < \chi_L < 30$). Later the experimental investigation of laminar flows over sharp and blunt plates was extended to lower Mach numbers ($M_\infty = 6$–10) and higher Reynolds numbers (from 0.2×10^6 to 1.3×10^6) [42]. In these experiments, the boundary-layer displacement effect was negligible or weak ($\chi_L < 1.4$). A mutual influence of the leading-edge bluntness (for a plate or wedge) and the shock wave on the gas flow and heat transfer was studied in [27, 28, 32-37].

2.3 DEATILED SURVEY

"Blunted Cone-flare in hypersonic flow" by R. Savino & D. Paterna

In this study a blunted con-flare has been analyzed using CFD and compared with experimental results obtained from Von Karman Institute H3 Mach 6 Wind tunnel. The flow around blunted cone-flare almost every physics of high-speed flows around re-entry vehicles. The junction between the flare and the cone is very important as the region exhibits complex flow phenomenon and surface heat flux. The cone-flare arrangement can dramatically increase surface heat transfer through separation and subsequent reattachment. Surface pressure distribution and surface heat flux are obtained and analyzed in comparison with experiment. The influence of wall temperature on surface pressure and surface heat flux is critically assessed. The experimental and computational analysis is done using the flow field parameters where the Freestream Mach is 6 and freestream pressure is 673.67 Pa at Temperature 67.07 K. The geometry considered is as shown in Fig 2.1, where the nose radius is 3.5 mm. The angle of the cone is 7.5^0 and the flare forms an angle of 10^0 with the cone [5].
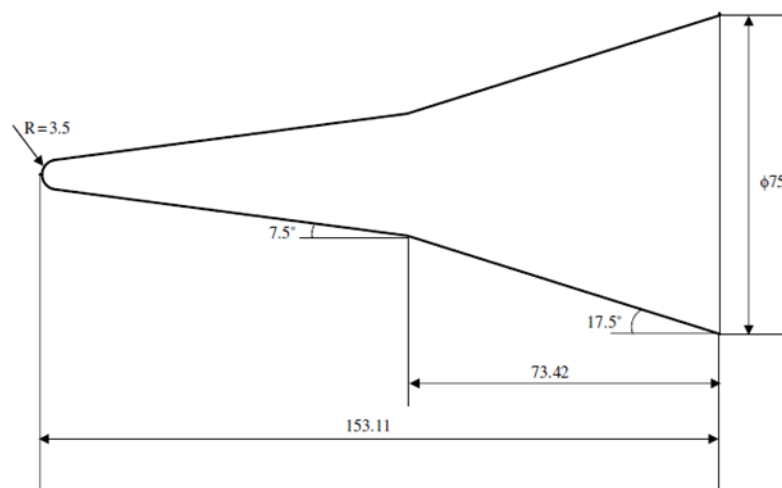
Fig. 2.1 Cone-flare model geometry [5]

Computational Results

Fig. 2.2 (a) & (b) shows the Mach number and pressure contours over the geometry and at the stagnation region respectively. The figure clearly depicts the detachment of shock ahead of the blunted nose cone and the SWBLI in the cone-flare junction. The bow shock wave is weakened as it moves downstream, and the bow shock produces an entropy region behind the shock. The entropy layer causes variations to the flow variables normal to the body which cannot be neglected. Fig. 2.3 shows the SWBLI in the cone-flare region where the separation occurs upstream of the flare. A reattachment shock is formed downstream of the flare junction. Shear layer is developed parallel to the wall surface due to the presence of a corner shock formed due to the intersection of separation and reattachment shocks [5].

(a)

(b)
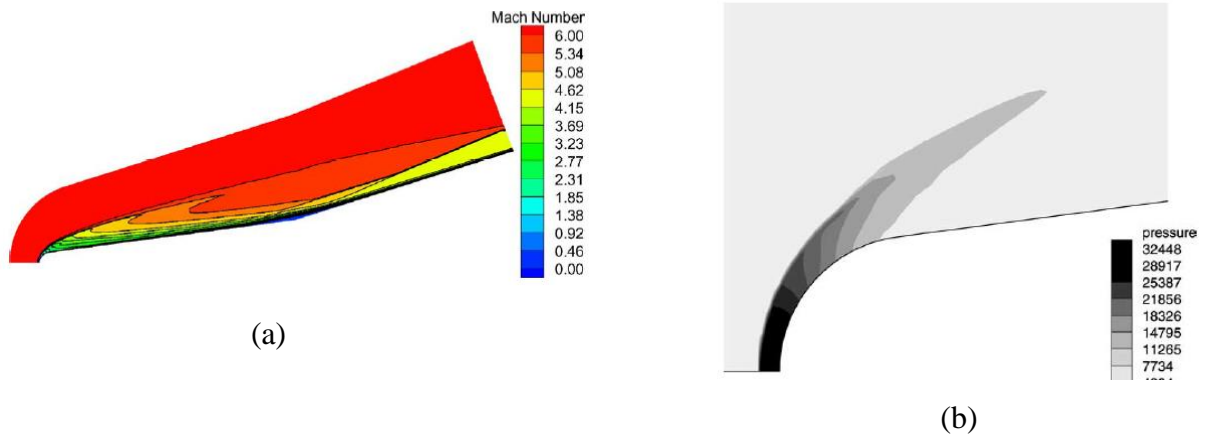
Fig. 2.2 (a) Mach Contour (b) Pressure contour at the Compression region [5]
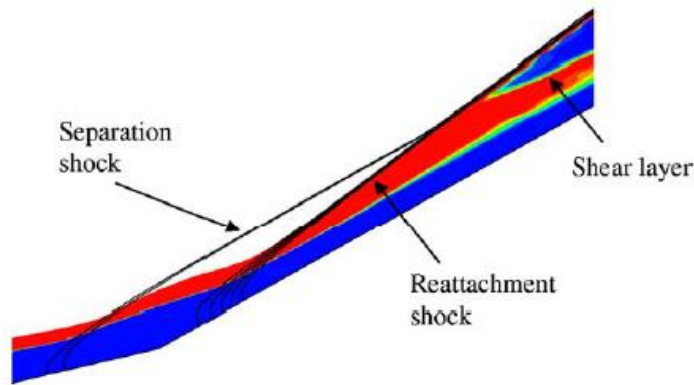
Fig. 2.3 SWBLI at the Cone-flare region [5]
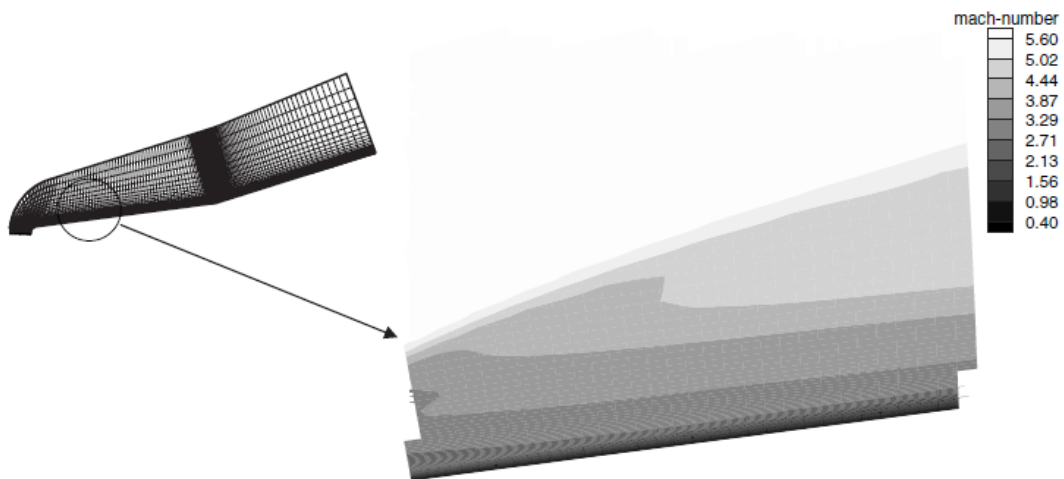
Fig. 2.4 Mach Contour at the Entropy Layer [5]

Flow over a cone-flare is characterized by the separation point where the flow separates causing a separation shock leading to a rise in temperature. The separation shock is followed by recirculation region which is represented as a plateau in the surface pressure distribution curve in Fig. 2.5. After the junction the flow reattaches creating a second shock causing an increase in surface pressure and heat flux. The length of separation bubble can be obtained with the help of skin friction coefficient plot.
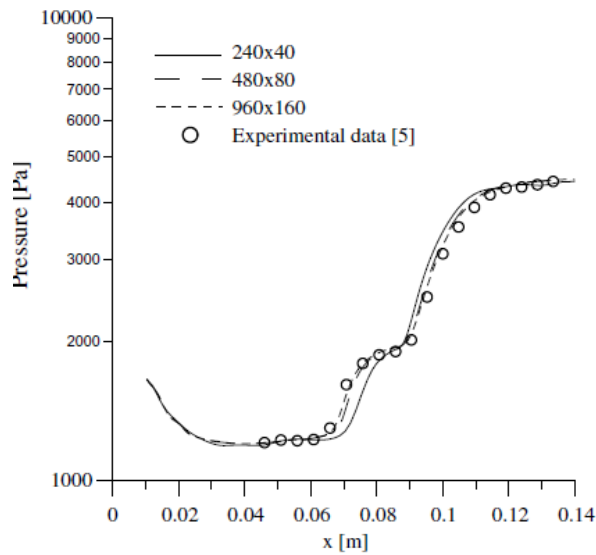
Fig. 2.5 Pressure Distribution over Blunt Cone-flare [5]

Effect of varying Wall Temperature on Surface Pressure and Heat flux

In experimental situation the measurements are captured with a certain time delay and this increases the model wall temperature as compared to initial value before the blowdown due to high heat fluxes at hypersonic conditions. To analyze the effect of wall temperature on other parameters a computational study has been done with 10% increment to the initial temperature i.e. 330 K the initial temperature being 300 K. The graphical results are shown in Fig 2.6 (a) & (b) representing surface heat flux and surface pressure respectively. It can be deduced from the graph that the surface heat flux is lower than the initial case and the peak heat flux has decreased drastically by about 15%. With change in surface temperature the wall pressure is affected. The separation bubble length has increased with increase in temperature [5].

In a hypersonic propulsion system, inlet of an engine comprises of a series of external compression ramps and a successive interior isolator or diffusor assembly.
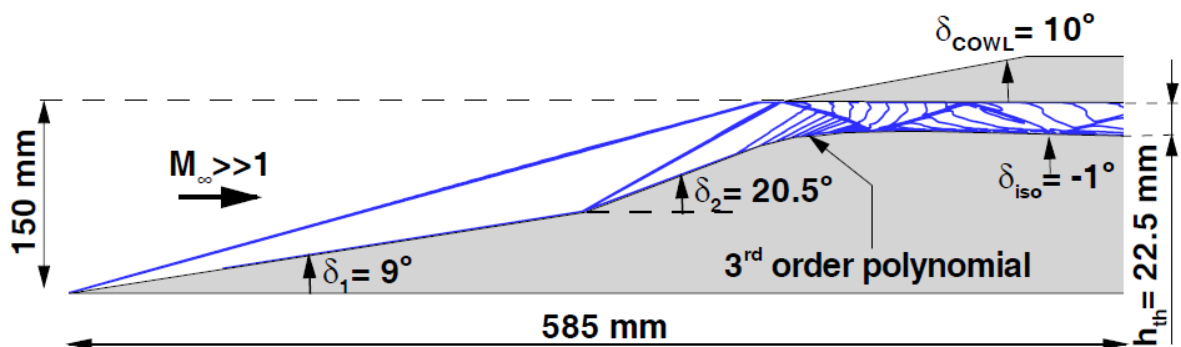
The oblique shock waves with or without a final normal shock will lead to the compression of the incoming flow. The two major aspects, that signifies the technological problems of the engine is: the interaction of the strong shock waves with dense hypersonic boundary layer which will lead large separation of the flows that minimizes the captured mass flow and thus the engine performance. The

13

other aspect is that, the very large total enthalpy of the flow leads to extensive aerothermodynamics heating, further enhanced by turbulent heat fluxes [38]. An increase in surface temperature will further increase the thickness, and thus the subsonic portion of the dense hypersonic boundary layer. Later, the separation is induced, or the upstream influence of the shock wave boundary layer interaction is enhanced, leading to an increase in spillage drag through flow blockage by pushing the flow away from the surface [39]. It is observed, an increase in wall temperature will reduce the overall wall heat flux distribution. However, peak heating occurs due to the strong compression of streamlines near the reattachment region and the secondary effect of the surface temperature by changing the flow interactions structure is not understood very well [40].

"*Shock Wave boundary layer interactions in hypersonic flows*" by Bibin Josh, Vinayak N Kulkarni, Ganesh Natarajan[2]

This work provided a detailed explanation on the effect of various geometry features and many flow characteristics on SWBLI in laminar hypersonic flow conditions. The correlation between incipient separation angle and deflection angle has been predicted accurately for well separated flows. Other paramenters that affect the SWBLI are changes in ramp angle, wall temperature, free stream total enthalpy, freestream Mach number and LE bluntness has been analysed.

Numerical investigation of SWBLI over a flat plate of length 0.05 m with a ramp angle of 15^0 has been carried out at Mach 6 and Reynolds Number of 8 x 10^5 /m and wall temperature 300 K. Concentrated grid points are considered at the leading edge and near the ramp junction while clustering is done along the wall to capture the boundary layer. A 180 x 90 mesh size was employes after conducting grid independence study over the skin friction coefficient. The domain considered in this literature is as shown in Fig 2.6.
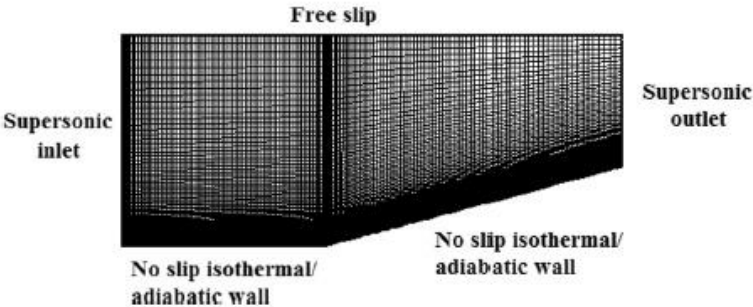
Fig. 2.6 Domain Consideration and Mesh Clustering[3]

Effect of Ramp Angle on SWBLI:

Studies are done to check the effectiveness of incipient separation angle on shock induced boundary layer interaction. The test conditions are similar to that of experiments conducted by Marini [46]. Three different ramp angles $\theta = 10, 12.5 \ and \ 15$ has been chosen to find the effect of separation in comparison with the incipient separation angle which is considered as 13.5^0 for this test condition. The computational results are compared & validated with experimental results of Marini [46] and

they find good agreement. Fig. 2.7 exhibits the pressure distribution over all three ramp angles. The pressure distribution of 15^0 ramp angle shows upstream variation on the ramp indicating the presence of a separation bubble.
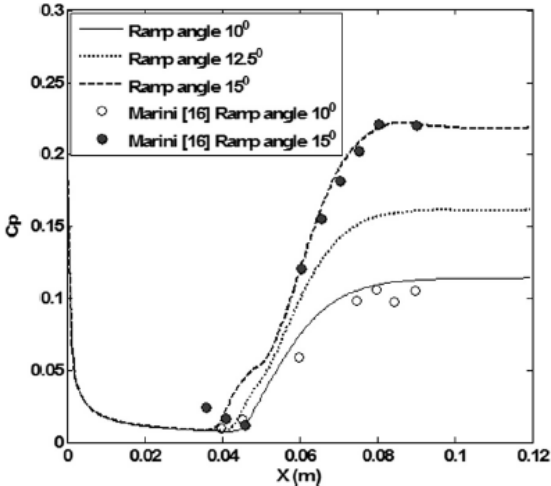
Fig. 2.7 Graph showing effect of changing ramp angle on Pressure distribution [3]

The variation of heat flux for all the three angles are also dipicted graphically following the usual V-shaped curve. The angles lesser than the incipient angle show a typical V-shaped curve while the ramp angle 15^0 follows a U-shaped or a diffused V-shaped curve. This is due to the early rise in pressure ahead of the ramp and the presence of a separation bubble along this region. Fig. 2.8 shows the graph of Heatflux over the ramped flatplate length. The bubble length can be identified through the skin friction distribution curve as shown in fig. 2.9. It can be seen from the graph that 10^0 ramp does not produce any separation bubble while the 15^0 ramp produces a separation bubble of length approximately 17.75mm. The 12.5^0 ramp does not produce a fully developed separation bubble as the ramp angle is leass than the incipient separation angle [3].
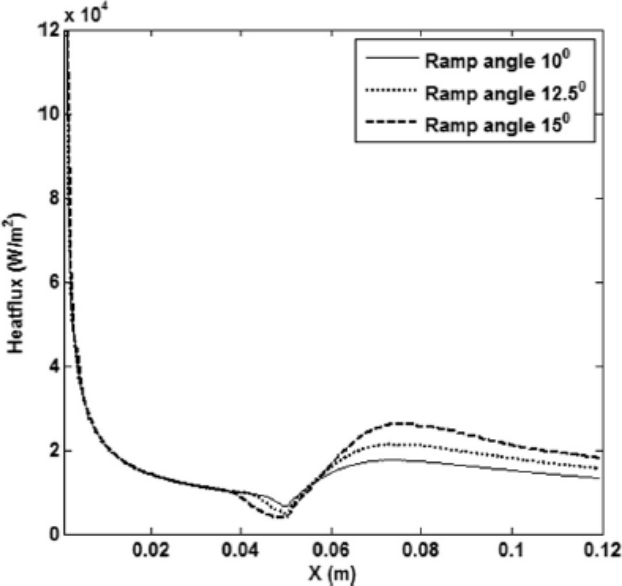
Fig. 2.8 Effect of Heatflux due to ramp angle variation [3]
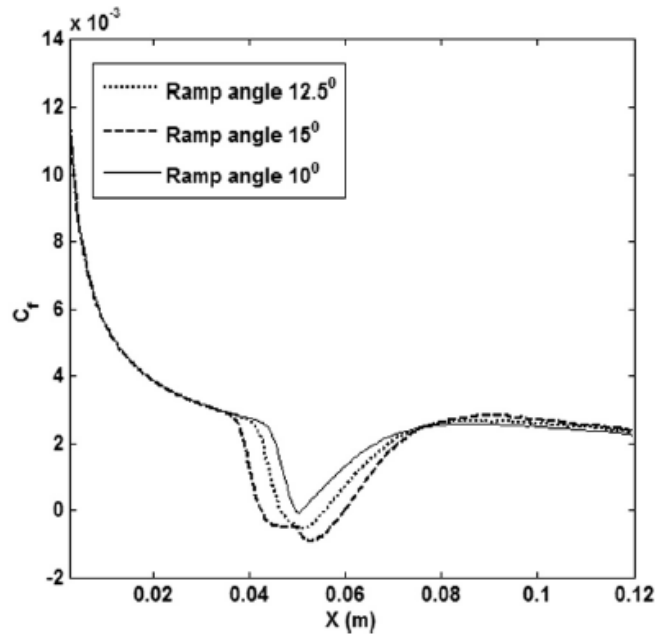
Fig. 2.9 Skin friction distribution with varying ramp angle [3]

Effect of variation of freestream Mach Number on SWBLI:

To analyse the effect of varying mach number on SWBLI, four different Mach numbers were used i.e 5, 6 , 7 & 8 at fixed value of freestream reynolds number as 8 x 10^5 /m with a constant temperature of 131.7 K at the freestream and wall temperature of 300 K. The incipient separation angle can be calculated by the formula;

$$M_\infty \theta_{is} = 80\sqrt{\overline{X_L}} \hspace{4cm} 2.3$$

It is evident from the relation that as the Mach number increases the incipient angle decreases. The ramp angle under consideration is 15^0 as it satisfies the incipient separation angle required for all the freestream velocities considered. The effect of freestream Mach number variations on pressure distribution and skin friction distribution are as shown in Fig. 2.10 (a) & (b). From both the graphs at lower Mach number the plateau effect is prominent near the separation shock and this effect reduces gradually with increase in Mach number depicting the reduction in separation bubble length. The longest separation bubble occurs for Mach 5 and the smallest occurs for Mach 8, which is not considered as well separated flow.
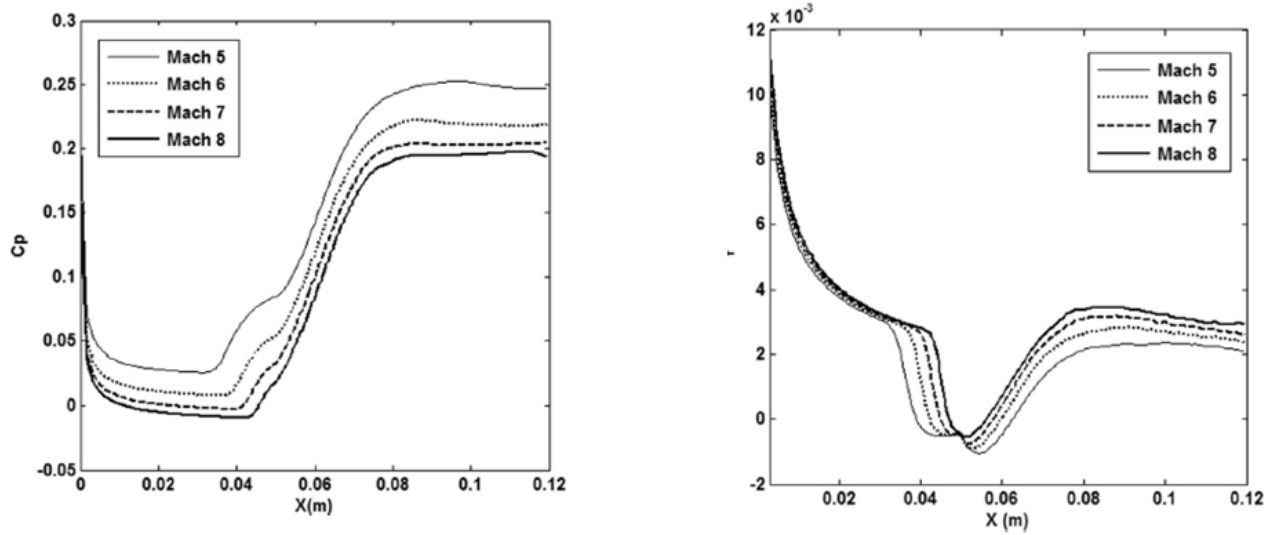
(a) Pressure Distribution   (b) Skin Friction Distribution

Fig. 2.10 Effect of freestream Mach Number on SWBLI [3]

Leading-Edge Bluntness effects on SWBLI:

LE bluntness has proven to reduce surface heating rates in hypersonic vehicles and hence this makes it important to understand the effect of bluntness on SWBLI. Experimental work has been carried out by Coet et al [52] at Mach number 10 with ramp angle as 15^0 attached to a flat plate with three different leading-edge geometries sharp, r = 2.5 mm bluntness and r = 5mm bluntness. The present study computationally validates the same study.

From the computational investigation it was found that a detached bow shock was present in case of blunt leading and an oblique shock attached to the LE in case of sharp leading edge. The presence of bow shock reduces the ramp approach Mach number which in turn increases the prominence of SWBLI. An entropy gradient gets created normal to the flow due to the presence of bow shock. This entropy gradient results in strong vertical activity behind the shock and creates stabilizing effect which counters the effect of reduced Mach number on SWBLI. Hence as the bluntness increases, the intensity of the SWBLI decreases. From the surface pressure distribution graph shown in Fig. 2.11 the peak pressure at the downstream region of the reattachment point in case of sharp leading is twice higher than that of the blunt leading edge. This shows that the separation shock produced by sharp leading edge is much stronger than that of blunt leading edge [3].
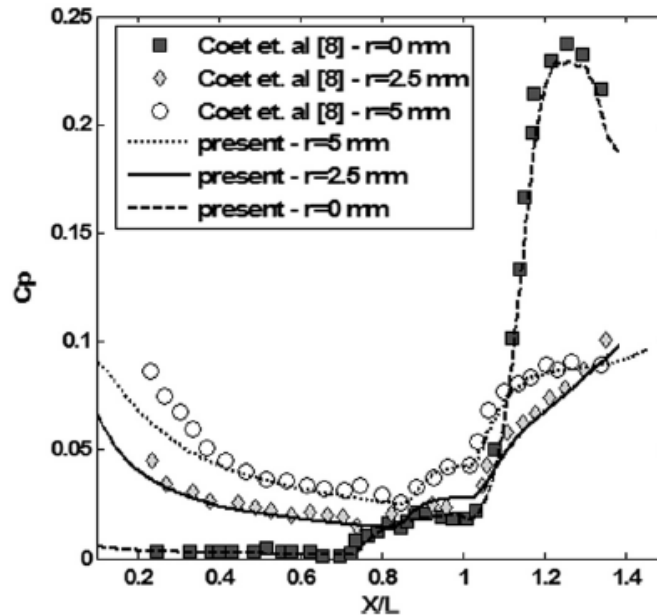
Fig. 2.11 Effect of bluntness of Pressure distribution and SWBLI [3]

CFD simulations are performed to check the effect of leading-edge bluntness of very small radius. These simulations are carried out for blunt radius of 0.1mm, 0.5mm, 1mm, 1.5mm and 2mm for a ramp angle of 15^0 at Mach 6 flow condition. The skin friction coefficients are compared to analyze the changes in the separation bubble length. From Fig. 2.12 even small leading-edge bluntness alters the separation and attachment points significantly. The separation point moves upstream, and the reattachment point moves downstream significantly for radius 0.1mm and 0.5mm whilst the shift is more prominent in the later. Further increase in bluntness shows decrease in the separation bubble size. At 1.5 and 2mm leading edge bluntness the separation point shifts downstream and reattachment point moves upstream. This shows that up to certain increase in leading edge bluntness the separation bubble size increases and there is a decrease in separation bubble size as the bluntness radii crosses a certain moderate value. The existence of critical nose radii is thus confirmed [3].
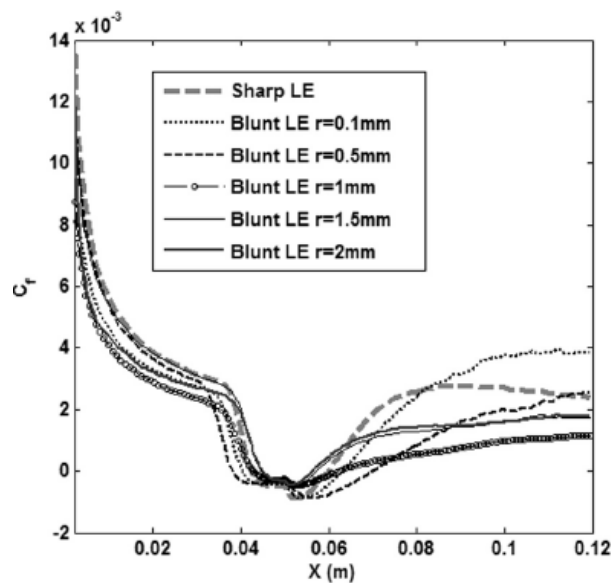
Fig. 2.12 Effect of bluntness on skin friction coefficient distribution [3]

18

In conclusion the following inferences can be made at the end of the above literature discussion.

PARAMETER	INFERENCE
Increase in Ramp Angle (θ) above incipient angle	Increases Length of Separation Bubble
Increase in free stream Mach Number	Decreases Length of Separation Bubble
If Leading edge Radius < Critical Radius	Length of Separation bubble increases
If Leading edge Radius > Critical Radius	Length of Separation bubble decreases

Table 2.1 Inference on Influence of Parameters on SWBLI

"Effect of Leading-edge bluntness on the interaction of ramp induced shock wave with laminar boundary layer at hypersonic speed" by Bibin John & Vinayak Kulkarni [4]

Leading-edge bluntness and its effects on SWBLI have been thoroughly assessed in this investigation. The effectiveness of the leading-edge bluntness on reducing the separation bubble size is examined. It is evident from this study, the presence of two critical radii of leading-edge bluntness which influence the SWBLI. The first critical radius is called as 'inversion radius'. Increase in the radius of LE bluntness upto the inversion radius increases the size of separation bubble. The maximum extent of separation is reached when the leading-edge radius reaches inversion radius. The inversion radius falls between 0.3 and 0.6mm. The separation zone increases when the entropy layer is swallowed by the boundary layer and the separation zone decreases in size when the boundary layer is swallowed by the entropy layer. When the leading-edge radius is equal to inversion radius both the boundary layer and entropy layer are seen to have same thickness. The second critical radius is called as the 'equivalent radius'. When the LE radius increases beyond the second critical radius decreases the separation zone size when compared to the size in case of sharp LE. This reduction is mainly due to the presence of a large high-pressure region. The equivalent radius is found to lie between 1 and 1.2 mm.

Figure 2.13 shows the pressure variation along the wall for different radii. From the graph it can be observed that there is a streamwise decrement in the static pressure at the leading edge of all geometries. This is mainly due to flow expansion downstream of the stagnation point, where the pressure is higher than in the case of sharp leading edge. With increase in leading edge radius both the expansion and pressure gradients increase. The over pressure region is seen to extend up to the separation region for all the blunt cases when compared to sharp leading edge. From the graph it can be noted that the increase in pressure downstream of the expansion region indicated the presence of separation region which forms a plateau region. An upstream shift in the separation point can be noted for initial increase in radius until 0.3 mm. Increase in radius beyond 0.3 mm shows a downstream shift in the separation station. It is also evident that the maximum pressure on the ramp decreases with increase in LE bluntness. This is mainly due to the presence of weak separation shock compared to that generated in case of sharp LE [4].
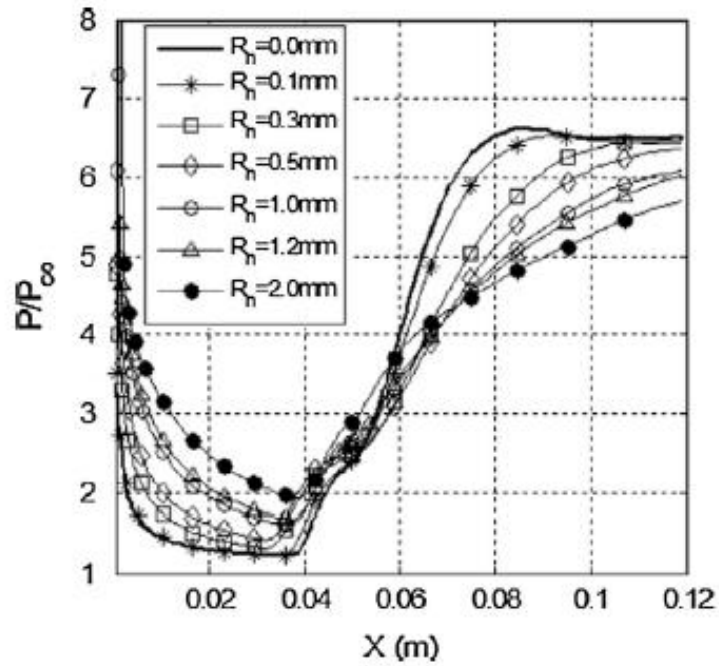
Fig. 2.13 Effect of Leading-edge radius on Pressure distribution & SWBLI [4]

The variation of skin friction coefficient and Stanton number is shown in fig 2.14 (a) & (b). Noticeable decrease in both skin friction coefficient and surface heat flux can be seen at the upstream location of the separation station. This indicated the location of separation gained due to flow deflection is confirmed. From the graph it is noticed that there is a reduction in peak heat flux on the ramp portion with increase in radii, this is a similar trend followed by pressure distribution on the ramp region. From Fig. 2.15 (a) the separation and reattachment regions can be identified as points that cross the zero-skin friction coefficient line.

(a) Skin Friction Coefficient

(b) Stanton Number
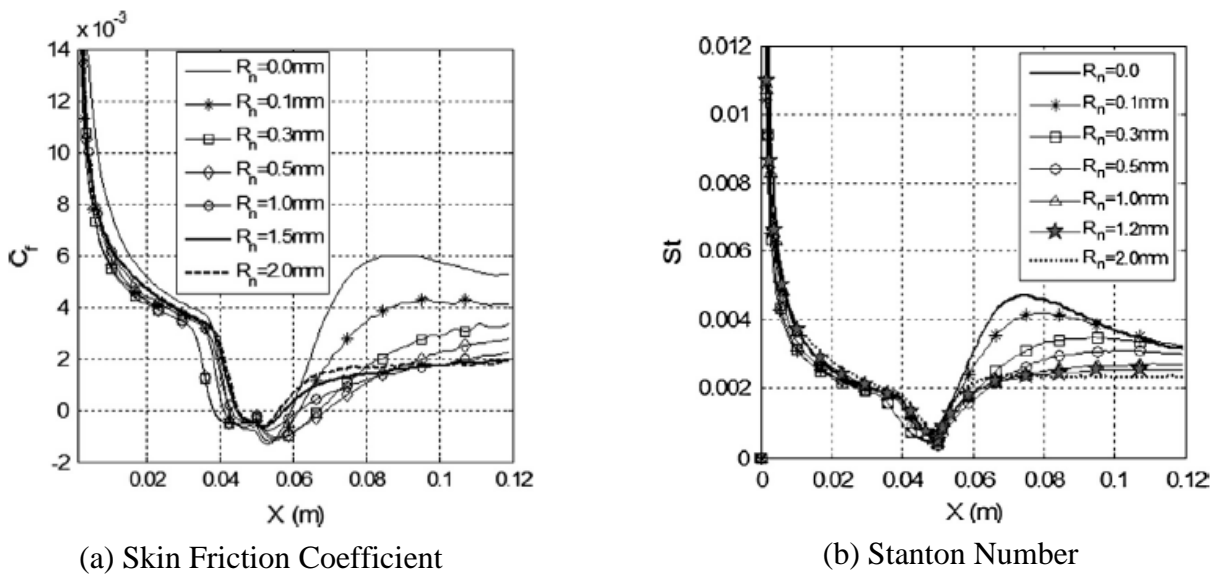
Fig. 2.14 Leading-edge bluntness effect on Skin Friction coefficient and surface heat flux [4]

The variation of separation and reattachment point is along the body for different leading-edge radii is as plotted in Fig. 2.15 (a). From this graph it is evident that the reattachment point moves downstream, and separation point moves upstream for initial increase in radii up to 0.3 mm. This indicated the increment in the size of separation bubble. This trend is followed only up to 0.6 mm radii and then it reverses. Fig 2.15 (b) indicates the size of separation bubble for different leading-edge radii. From the graph it is observed that the separation bubble size increases with increase in leading edge radii until it reaches the Inversion radius, which is the first critical radius. After this point the separation bubble size begins to decrease until it reaches the reference separation bubble size set by the sharp leading edge. As the separation bubble size reaches the reference bubble size it is said to have reached the second critical value called as the Equivalent radius for which the size of separation bubble of both sharp and blunted leading edge is the same. With further increase in radii smaller separation bubble size is observed.

(a)

(b)
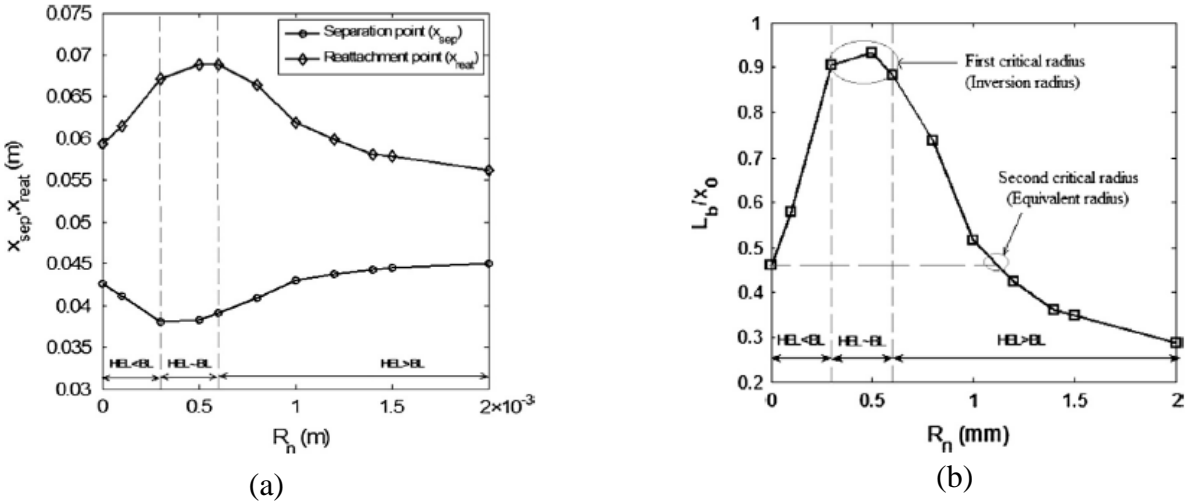
Fig. 2.15 (a) Variations in separation and reattachment locations (b) Separation bubble size [4]

(a)

21

(b)
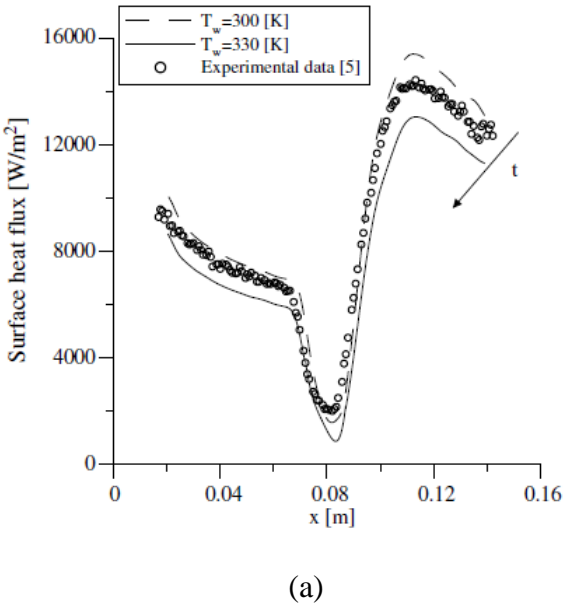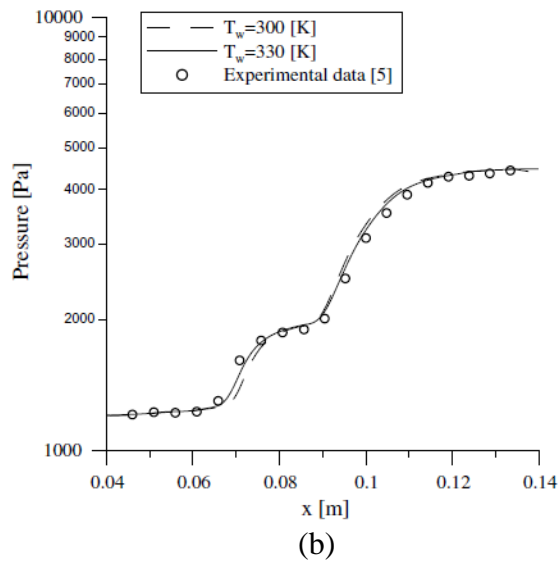
Fig. 2.16 Effect of Surface temperature on (a) Surface Heat flux (b) Surface Pressure [4]

2.4 SUMMARY

It is evident from the many literature studies that control of separation bubble is critical to minimize the effects of shock wave interactions in space vehicle systems and sub-systems. It can also be noticed that almost every literature investigated addresses only regions with single and double ramp junctions, but there are almost no investigations related to multi-ramp junctions which also gets featured in such hypersonic vehicle component and system designs.

Multi-ramp junctions also pose severe design challenges and it is necessary to take conscious efforts while designing space vehicles. While the earlier research studies provide very good insights on the SWBLI by varying ramp angles, leading edge bluntness, freestream velocity etc., which becomes the core of the current work, the present research work focuses on the study of shock wave and boundary layer interactions with triple ramp and quad ramp configurations, considering the basic understanding of flow physics around single and double ramp configurations. This way it also helps in understanding the effects of having a multiple ramp on the upstream separation bubble already present at the second ramp junction along with the understanding of how the presence of additional downstream ramps overall changes the shock structure and flow.

Computational investigations are carried out to study and understand the behavior of ramp induced shock wave and boundary layer interactions for three and four ramp configurations, wherein the first two ramps are considered as specified by R. Savino and D. Paterna [2], while the third and fourth ramp angles are varied in combination along with variations in freestream and surface temperature, to study the effects on the separation bubble length at all three ramp junctions. Since the studies presented by Bibin John and Vinayak Kulkarni [4] address in detail the relation between flow conditions and design variations on separation bubble size, it becomes a key consideration to test these correlations on multi-ramp configurations and to assess if these variations still continues to be an effective technique to understand and predict separation and hence the current research work

considers triple ramp angles of 7.5^0, 10^0, 12.5^0 and 15^0, with same angles considered for fourth ramp along with a blunt radius of 3.5mm. All combinations of ramp angle variations between third and fourth ramps are considered for this simulation study. The freestream Mach number is varied between 6 to 8 and the surface temperatures as 270K, 300K and 330K.

Simulation tool validation is performed using the base geometry and boundary conditions as provided by R. Savino [2] in their computational and experimental validation studies. Post successful validation, efforts are taken to initially study the effect of adding multiple ramp junctions to the base geometry on the shock wave boundary layer interaction, followed by considering variations in freestream Mach number and surface temperatures in the presence of third and fourth ramp. Details on the solution methodology, model and discretization details are presented in the next section. Discussions on the findings of adding multiple ramp junctions in association with freestream variations, thermal variation and its implications on the separation bubble are discussed in Chapter 5 for Triple Ramp configuration and Chapter 6 for Quad-ramp configurations, followed by experimental validations in Chapter 8 and Chapter 9 and then conclusions are discussed in Chapter 10 along with future works.

Even with the intense numerical and experimental investigation conducted to understand SWBLI, there is always a limited number of findings [30, 31] that have identified adverse effect of reduction in the freestream Mach number and stagnation enthalpy on this viscous – inviscid interaction. Furthermore, the challenges involved in measurements of wall shear stress in high speed facilities necessitate the use of pressure and heat transfer measurements to understand the phenomenon of shock induced separation. Results on separation length from pressure or heat transfer measurements must be interpreted qualitatively and quantifying these predictions is possible only through high-resolution computations.

CHAPTER 3. COMPUTATION METHODOLOGY

The numerical investigations are carried out using High Resolution Flow Solver on Unstructured meshes (HiFUN). This work involves solving using density-based solver, which solves the simultaneous equation. Mass conservation solves the mass conservation and is satisfied by rigorously tracking the density change. Since density, pressure, temperature, and velocity are mutually dependent, the system of equations is generally closed by adding an equation of state to each conservation equation. In a mass conservation, density change always dominates over other conditions so that this type of solver is called density-based solver. Flow with less energy influence can be solved without using energy equation, however, all three conservation equations (mass, momentum and energy) are solved simultaneously on the general way [42].

The density-based solver is not appropriate for the analysis with slow flow and rapid density change which is smoothly solved in pressure-based solver. The density-based solver is suitable for a compressible fluid analysis with fast flow and the significant influence of energy change. Further the accuracy of mass conservation tends to be the higher than that of pressure-based solver. Thus, such as non-linear waves such as a shock wave in a high-speed air current can be stably solved with Riemann solver.

The basic equations and concept of finite volume methodology are discussed in below sections.

3.1 BASIC GOVERNING EQUATIONS

The time-dependent, non-dimensional, compressible Reynolds-Averaged Navier Stokes equations in conservation form can be written as,

$$\frac{\partial W}{\partial t} + \frac{\partial (f+F)}{\partial x} + \frac{\partial (g+G)}{\partial y} = 0 \qquad 3.1$$

In the above equation,

$$W = [\rho \ \rho u \ \rho v \ e]^T$$

Is the vector of conserved variables. The terms f and g are inviscid flux vectors given by,

$$f = \begin{bmatrix} \rho u \\ \rho u^2 + p \\ \rho uv \\ u(e+p) \end{bmatrix} \quad g = \begin{bmatrix} \rho v \\ \rho uv \\ \rho v^2 + p \\ v(e+p) \end{bmatrix} \qquad 3.2$$

The terms F and G represent the viscous flux vectors given by,

$$F = \begin{bmatrix} 0 \\ -\tau_{xx} \\ -\tau_{xy} \\ -(u\tau_{xx} + v\tau_{xy} - q_x) \end{bmatrix} \quad G = \begin{bmatrix} 0 \\ -\tau_{xy} \\ -\tau_{yy} \\ -(u\tau_{xy} + v\tau_{yy} - q_y) \end{bmatrix} \qquad 3.3$$

Viscous flux consists of shear stress and heat conduction terms given as,

$$\tau_{xx} = \frac{(\mu+\mu_t)}{Re_\infty}\left(2\frac{\partial u}{\partial x} - \frac{2}{3}\left(\frac{\partial u}{\partial x} + \frac{\partial v}{\partial y}\right)\right) \qquad 3.4$$

$$\tau_{xy} = \frac{(\mu+\mu_t)}{Re_\infty}\left(\frac{\partial u}{\partial y} + \frac{\partial v}{\partial x}\right), \qquad 3.5$$

$$\tau_{yy} = \frac{(\mu+\mu_t)}{Re_\infty}\left(2\frac{\partial v}{\partial y} - \frac{2}{3}\left(\frac{\partial u}{\partial x} + \frac{\partial v}{\partial y}\right)\right), \qquad 3.6$$

$$q_x = -\frac{(k+k_t)}{M_\infty^2 Pr_\infty Re_\infty(\gamma-1)}\frac{\partial T}{\partial x} \qquad 3.7$$

$$q_y = \frac{(k+k_t)}{M_\infty^2 Pr_\infty Re_\infty(\gamma-1)}\frac{\partial T}{\partial y} \qquad 3.8$$

The quantity ρ is the density of the fluid, u and v are the Cartesian components of the velocity, p is the pressure. The variable e represents the total energy per unit volume and is given by,

$$e = \frac{p}{\gamma-1} + \frac{\rho(u^2+v^2)}{2} \qquad 3.9$$

The definition of the local Mach number is,

$$M = \frac{\sqrt{u^2+v^2}}{a} \qquad 3.10$$

Where the speed of sound a is given by the relation:

$$a = \sqrt{\gamma\frac{p}{\rho}} \qquad 3.11$$

The total enthalpy per unit volume is defined as,

$$H = \frac{a^2}{\gamma-1} + \frac{u^2+v^2}{2} \qquad 3.12$$

25

The equation is closed by the equation of state given by,

$$p = \frac{\rho T}{\gamma M_\infty^2}$$

3.13

Where, M_∞ is the freestream Mach number.

The flow variables are non-dimensionalised by the free stream density ρ_∞, free stream velocity U_∞, free stream temperature T_∞. Pressure is non-dimensionalised with the dynamic head $\rho_\infty U_\infty^2$. The fluid viscosity is non-dimensionalised with the free stream value μ_∞ and the thermal conductivity with k_∞. A reference length L is used for non-dimensionalizing the coordinates. A laminar viscosity and thermal conductivity are determined using Sutherland formula

$$\frac{\mu}{\mu_{ref}} = \left(\frac{T}{T_\infty}\right)^{\frac{3}{2}} \left(\frac{T+S_1}{T+T_\infty}\right)$$

3.14

$$\frac{k}{k_{ref}} = \left(\frac{T}{T_\infty}\right)^{\frac{3}{2}} \left(\frac{T+S_2}{T+T_\infty}\right)$$

3.15

In the above formulae, S_1= 111.0 and S_2 = 194.0.

The freestream Reynolds number is based on the reference conditions chosen for non-dimensionalising the equations,

$$Re_\infty = \frac{\rho_\infty U_\infty L}{\mu_\infty}$$

3.16

The term Pr_∞ represents the freestream Prandtl number and is equal to 0.72 for air.

The turbulent viscosity μ_t and turbulent thermal conductivity k_t are computed using Baldwin – Lomax turbulence model.

3.2   FINITE VOLUME METHOD

The finite volume is a part of flow/thermal field, thus fluid flow in and out between neighbouring elements. Such flow between elements is called as 'Numerical flux'. Numerical flux is computed based on the governing equations with discretized data on each element. If the numerical flux is determined for each face of all elements, time and spatial variation of data at each element can be found, then data can be updated along the time and spatial variation. This calculation method is called finite volume method. Finite volume method is based on numerical flux, and numerical flux is a quantity balance between elements. Thus, summation of numerical flux for all elements is equal to the total numerical flux of the computational domain. This is quite suitable for representing the conservation laws in the governing equations.

In a finite volume, the total balance between inflow and outflow is considered within each control volume to represent a conservation equation.

Inflow

Accumulation = Inflow – Outflow

Outflow
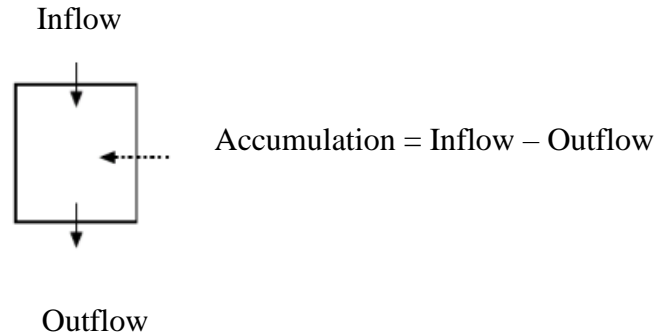
Here, to have sketchy image, we can use example of water container as shown below.

Inflow of water
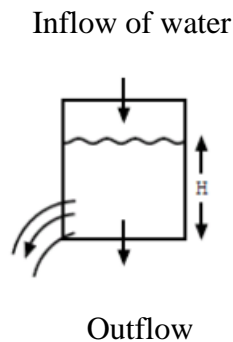
Outflow

Let the water level be H. Then, the height variation in one second, ΔH, can be expressed by the following equation on the balance of water.

Change of water level ΔH = Inflow per second – Outflow per second

Although this example is just trivial, a finite volume method equates all the causes and effects that result in the change of physical quantities in each of control volume [41].

3.3   INVISCID FLUX

Density based solver is often used for analyzing a high-speed flow because of the characteristics of the solver. In a high-speed flow, the time scale of density change or pressure change (propagation characteristics through the fluid) approaches that of the flow change, as a result, the effect of compressibility produces some improvements. As one of the effects of compressibility, a wave motion such as a shock wave or an expansion wave appears.

The problem in the wave motion is its non-linearity. Both shock wave and expansion wave are nonlinear waves which cause a long computation time. To solve Riemann problem numerically and accurately, an iterative algorithm should be used to capture status ahead and behind the waves. There are many kinds of Riemann solver, but most of them solves Riemann problem with some approximation technique such as linearity assumption to avoid the iterative calculation. In density-based solver using finite volume method, numerical flux between adjacent discretization points is

calculated by the approximate Riemann solver. In density-based solver there are different methods adopted as approximate Riemann solver, for the current study HLLC flux is adopted due to its wave stabilization because of its strong dissipation effect [42].

3.4 VISCOUS FLUX

Basically, the viscous term can smooth the numerical solution, the discretization of the viscous term seems to be easier when comparing with that of inviscid term. However, the viscous flux may cause numerical oscillation to depend on the quality of mesh. Further, the discretization method is determined by the accuracy of a friction force and a heat flux on the wall. Viscous flux is calculated between the adjoined discretization points in the same manner when calculating inviscid terms. The viscous flux also contains the gradient of the variables so that the gradients must be evaluated numerically [43].

3.5 RECONSTRUCTION

The accuracy of the inviscid flux discretization depends on the degree of the polynomial used to reconstruct the solution variation in a given finite volume. Inviscid fluxes computed at the volume interface using the cell averaged state are first order accurate. For achieving higher order accuracy, a k-exact reconstruction procedure can be made use of. A reconstruction is said to be k-exact if it can reconstruct exactly any polynomial of degree k or less.

The procedure developed based on the method of least squares and Green-Gauss theorem are commonly used for the solution reconstruction within the cell centre finite volume framework [44].

3.6 SUMMARY

At this point it is worth to summarize the approach of finite volume formulation for compressible fluid flows. They are,

- Finite volume formulation being an integral formulation, can admit solution discontinuities. Therefore, this methodology is ideally suited for solving the compressible fluid flow problems admitting discontinuous solutions such as shocks and contacts.

Finite volume formulation is a conservative formulation. Here, for a given finite volume interface, the flux leaving one volume is equal to the flux entering the other volume sharing the interface. Hence, $\int W_t \, d\Omega$ taken over the entire computational domain would involve only the fluxes leaving the boundaries of the computational domain. Therefore, finite volume formulation does not allow for the appearance of numerical sources and sinks in the computational domain. This aspect is particularly a great advantage for shock capturing schemes.

CHAPTER 4. NUMERICAL INVESTIGATION

4.1   MODEL AND MESH

Inter-code comparison, grid dependency study and theoretical validation of stagnation pressure and post shock temperature are performed on the model and boundary conditions as considered by R. Savino [2]. The base model considered for initial validation studies is henceforth referred as double ramp, which is 159.11 mm in total length, with first ramp angle 7.5^0, second ramp angle 10^0 and a leading-edge bluntness of radii 3.5 mm.

4.1.1   TRIPLE RAMP

A third ramp of length 63 mm is attached to the base double ramp model along with the consideration of various leading-edge bluntness, for the current investigation on ramp induced shock wave boundary layer interactions. Model details along with the computation domain and boundary conditions are shown in Fig. 4.1. The freestream conditions and the details about ramp angles and leading-edge bluntness are mentioned in Table 4.1. Multi-block structured meshing has been performed to discretize the computation domain. Four different mesh combinations with variations in mesh spacing both in normal and along the body are considered, the details of the same are shown in Table 4.2, a sample grid used throughout this investigation is shown in Fig. 4.2.

(a) Double Ramp [1]

(b) Triple Ramp

(c) Computational Domain
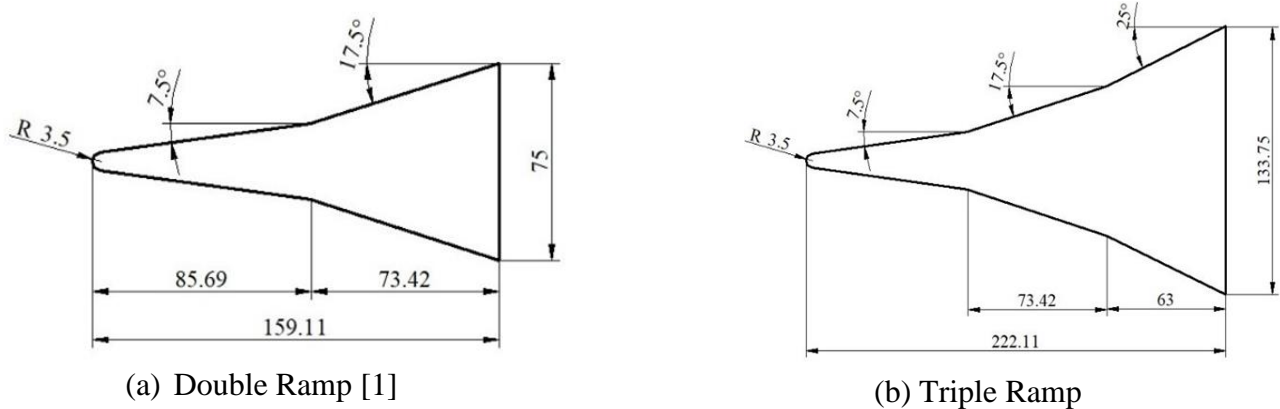
Fig. 4.1. Models and computation domain (model dimensions are in mm)

M_∞	P_∞ (Pa)	T_∞ (K)	μ (Pa-s)	k (N/s-K)	Ramp Angle (α)	Nose Radius (mm)
6	673.67	67.07	$4.47e^{-6}$	0.00607	7.5, 10, 12.5, 15	0, 0.5, 1, 1.5, 2.5, 3.5, 5

Table 4.1. Freestream and Geometry Conditions

Grid	Δn_0	Δn_h	Δs_0	Δs_h
240 x 40 [1]	0.003	0.05	0.0675	0.018
480 x 80 [1]	0.0015	0.005	0.0337	0.009
960 x 160 [1]	0.00075	0.0025	0.0168	0.0045
240 x 40	0.0015	0.0015	0.0675	0.018
480 x 80	0.0015	0.0015	0.0337	0.009
240 x 40			0.0675	0.018
480 x 80	0.015	0.015	0.0337	0.009
660 x 120			0.0337	0.009
960 x 160			0.0168	0.0045
240 x 40			0.0675	0.018
480 x 80	0.03	0.03	0.0337	0.009
660 x 120			0.0337	0.009
960 x 160			0.0168	0.0045
240 x 40			0.0675	0.018
480 x 80	0.045	0.045	0.0337	0.009
660 x 120			0.0337	0.009
960 x 160			0.0168	0.0045
240 x 40			0.0675	0.018
480 x 80	0.06	0.06	0.0337	0.009
960 x 160			0.0168	0.0045

Δn_0, Δn_h = normal spacing at stagnation and ramp; Δs_0, Δs_h = tangential spacing at stagnation and ramp

Table 4.2. Details of grids used for grid independence study
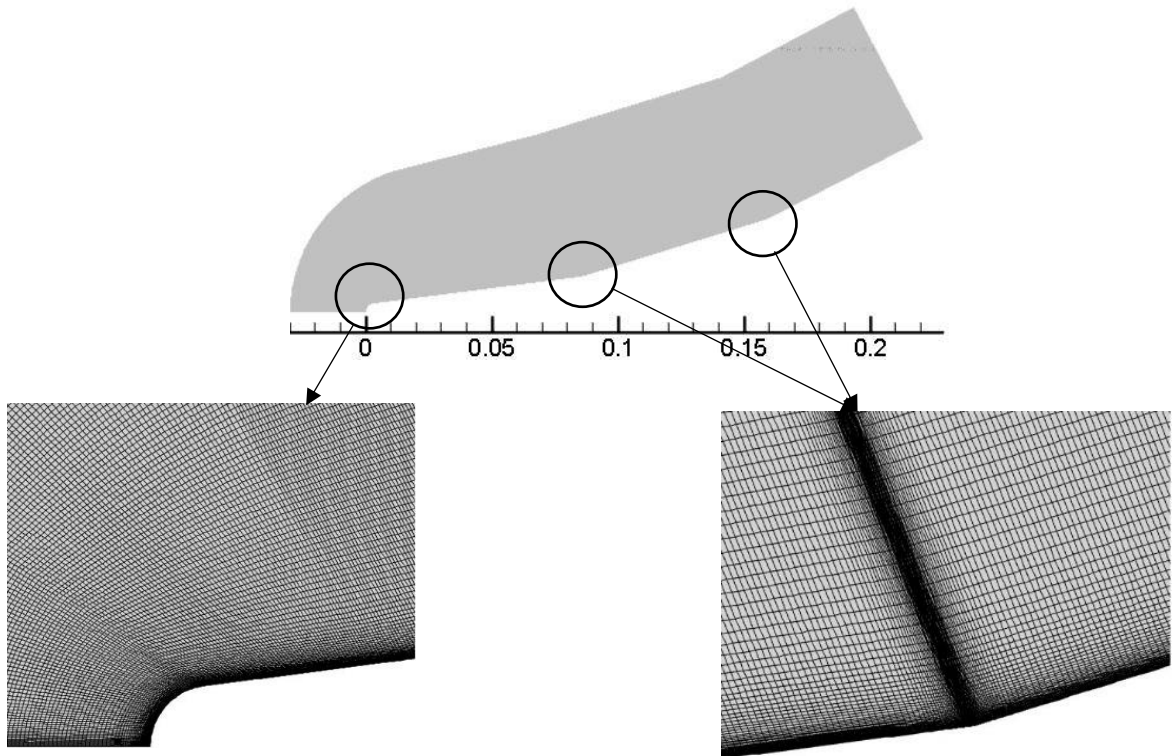
Fig. 4.2. Sample Grid used for triple ramp

4.1.2 QUAD RAMP

Third and fourth ramps of lengths 62.5 mm and 53.5 mm respectively are attached to the base double ramp model, for the current investigation on ramp induced shock wave boundary layer interactions. Model details along with the computation domain and boundary conditions are shown in Fig. 4.3 & 4.4. The freestream conditions and the details about both the ramp angles are mentioned in Table 4.3. Multi-block structured meshing has been performed to discretize the computation domain. Different mesh combinations with variations in mesh spacing both in normal and along the body are considered, the details of the same are shown in Table 4.4, a sample grid used throughout this investigation is shown in Fig. 4.5.

| Ramp 1 | Ramp 2 | Ramp 3 | Ramp 4 |
| (Constant angle) | (Constant angle) | (Variable angle) | (Variable angle) |
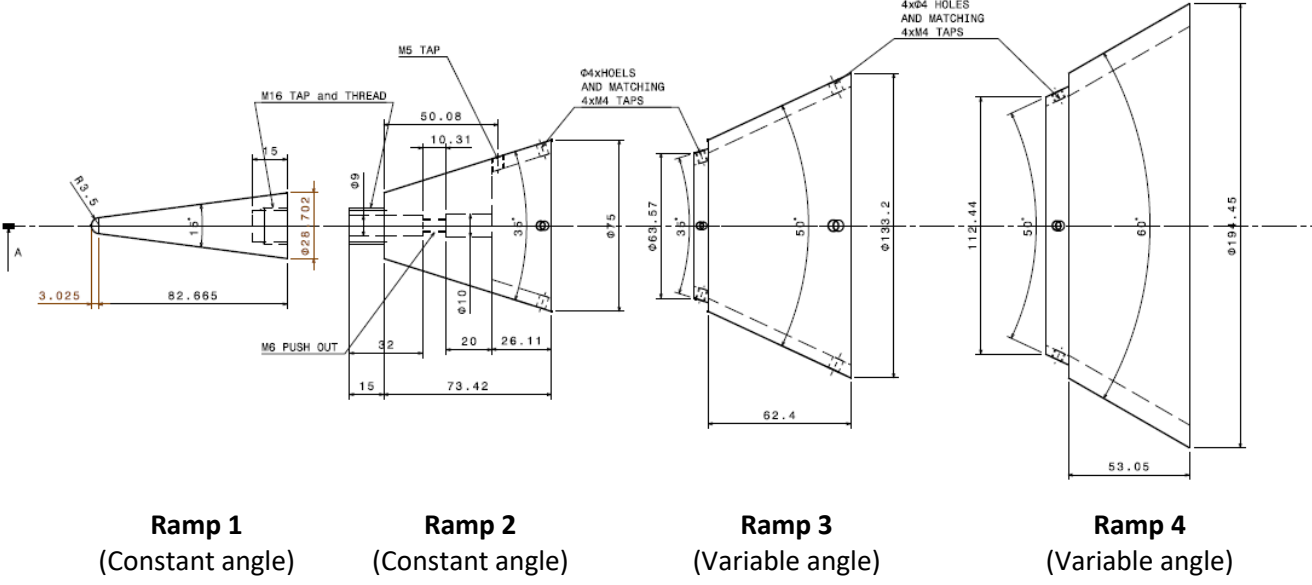
Fig. 4.3 Multi-ramp model details
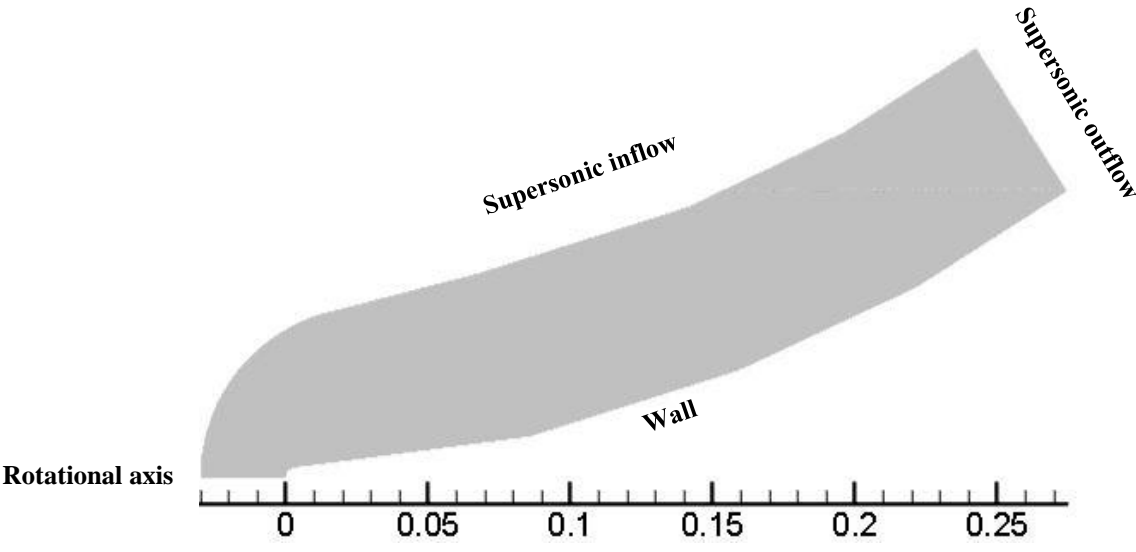
Fig. 4.4. Computational Domain

31

M_∞	P_∞ (Pa)	T_∞ (K)	μ (Pa-s)	k (N/s-K)	Ramp 1 (α)	Ramp 2 (α)	Ramp 3 (α)	Ramp 4 (α)
6	673.67	67.07	$4.47e^{-6}$	0.00607	7.5	10	7.5, 10, 12.5, 15	5, 7.5, 10, 12.5

Table 4.3: Freestream and Geometry Conditions

Model	Grid	Δn_0	Δn_h	Δs_0	Δs_h
Double Ramp	240 x 40	0.0015, 0.015, 0.03, 0.045, 0.06	0.0015, 0.015, 0.03, 0.045, 0.06	0.0675	0.018
	480 x 80			0.0337	0.009
	960 x 160			0.0168	0.0045
Triple Ramp	680 x 80	0.03	0.03	0.0168	0.0045
	1320 x 160				
Quad Ramp	1720 x 160	0.03	0.03	0.0168	0.0045

Δn_0, Δn_h = normal spacing at stagnation and ramp; Δs_0, Δs_h= tangential spacing at stagnation and ramp

Table 4.4: Details of grids used for grid independence study
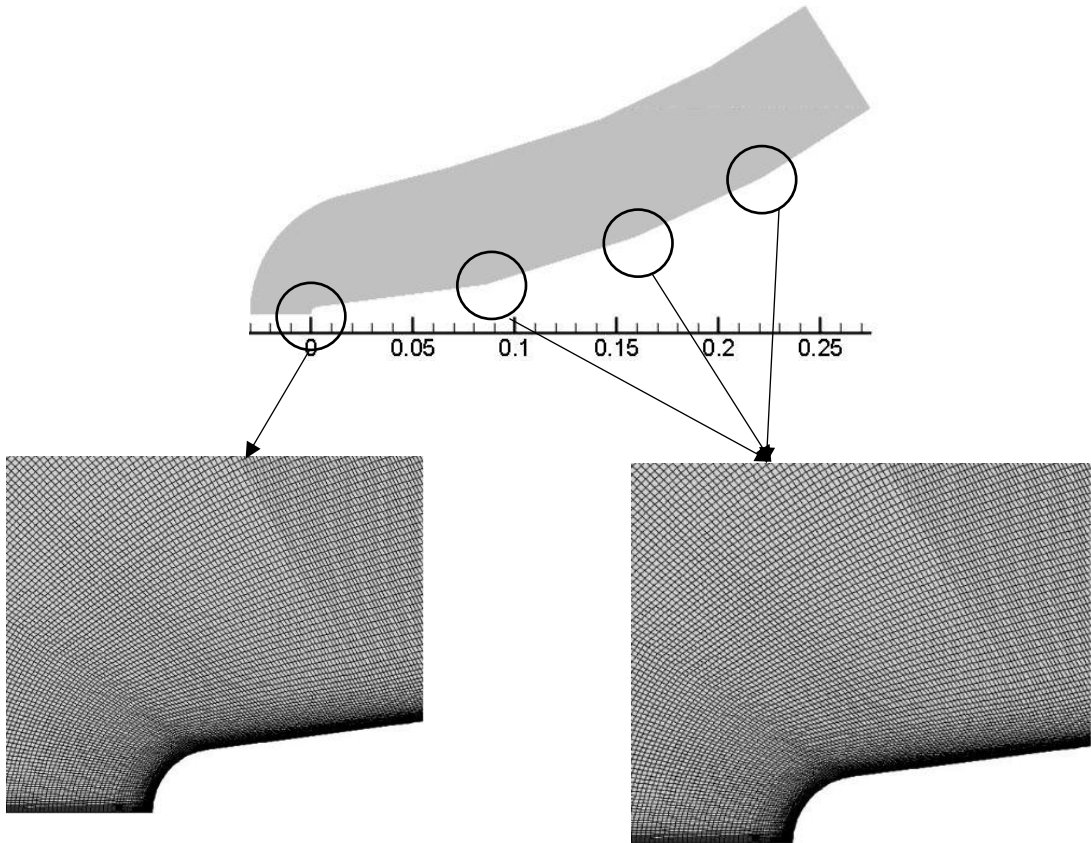
Fig. 4.5. Sample grid used for quad ramp configuration

4.2   VALIDATION STUDY

Inter-code comparison was necessary due to availability of multiple computation tools, to ensure the chosen tool is the best to capture the flow physics that involves, laminar high-speed flows with high gradient flow separations along with the formation of shocks. The pressure distribution along the double ramp model [2] was taken as a standard to perform the inter-code comparison. Both the simulation tools were run with the same mesh count and boundary conditions, while different solver settings were tried to ensure the best solver setting specific to the tool has been explored. It is evident from Fig. 4.6, there is excellent agreement with the experimental pressure plot, the separation and reattachment points for simulations done with HiFUN, for this reason it has been used for all simulations in this investigation.

Through grid independence study it was found that the mesh parameters used by R. Savino [2] was not suitable for HiFUN to match the experimental data. Grid spacing normal to the model was found as the major criterion to reach solver accuracy, while maintaining the overall mesh count same as in literature. It was found from grid independence study that the mesh size of 960 x 160 and 480 x 80 with 30micron normal mesh spacing had excellent agreement with experimental surface pressure values as shown in Fig. 4.7. The separation and reattachment points have very good match while there is slight but acceptable computational underprediction in the post attachment zone. It can be noticed that 480 x 80 captures the bubble region better, but the post reattachment region is extremely critical for multi-ramp studies which is captured better by 960 x 160 grid.

The importance of qualitative approach to determine the separation bubble length as emphasized by Bibin John [4], the skin friction co-efficient parameters were also validated, shown in Fig. 4.8. There is underprediction of the separation bubble length as compared to the CFD simulations results in the literature, this could be attributed to the difference in mesh count and the solver setting differences but it is evident that the HiFUN code is predicting the separation bubble length accurately as indicated in the inter-code comparison. In addition, a theoretical comparison of stagnation pressure and post-shock temperature with simulation outcome using the HiFUN solver also proves the solution to be independent of the grid and the code. Fig. 4.9 & 4.10 shows the closer view of stagnation region, where the stagnation pressure is about 31,683 Pa and the temperature post-shock is 549 K, which matches with values calculated using normal shock theory, where the stagnation pressure is calculated to be 31,538 Pa and temperature 533 K.

Quantitative parameters such as surface heat flux was also validated, represented in Fig. 4.11. As can be seen, there is underprediction of the separation point and a higher heat flux prediction post reattachment when compared to the experimental data. As indicated in the findings by R. Savino et. al [2], there are noticeable changes in bubble length and heat flux with time during an experimental study. The surface temperature increases with time while conducting a high-speed flow experimentation study. There is delay associated with data acquisition during which time the surface

temperature increases by almost 10%. Increase in surface temperature over time has proven to increase the size of the separation bubble and reduce the heat flux prediction. This phenomenon can exactly be noticed in Fig. 4.11, where the simulation cases are run for steady state conditions at t = 0, which underpredicts the separation point and the surface heat flux is higher than the experimental value. The experimental values show the exact trend of predicting a bigger separation bubble and a reduced surface heat flux, indicating a possible delay in data acquisition. There are also chances of non-uniform flows in the test section resulting in boundary layer excitation causing early separation and lower heat flux due to turbulent convection.
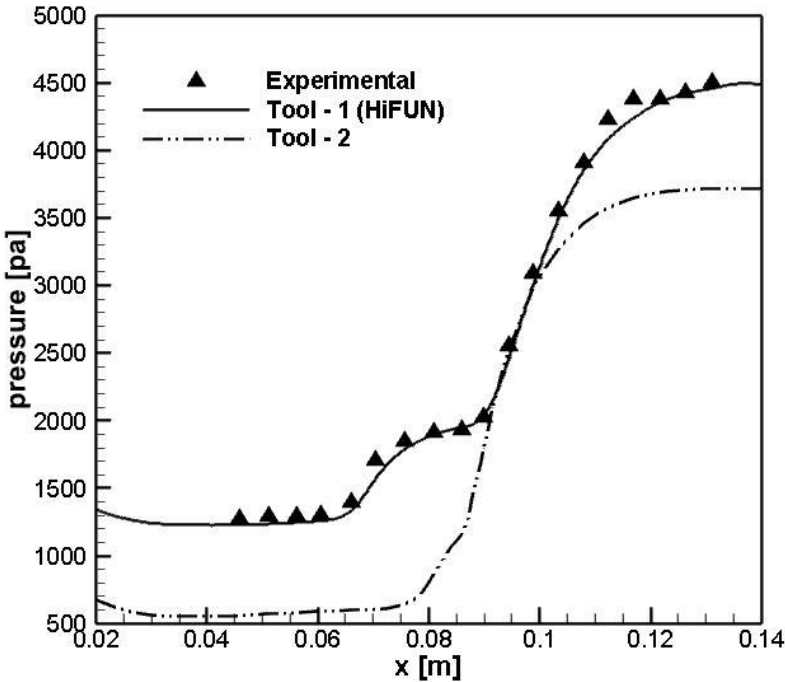
Fig. 4.6 Inter-code comparison of surface pressure
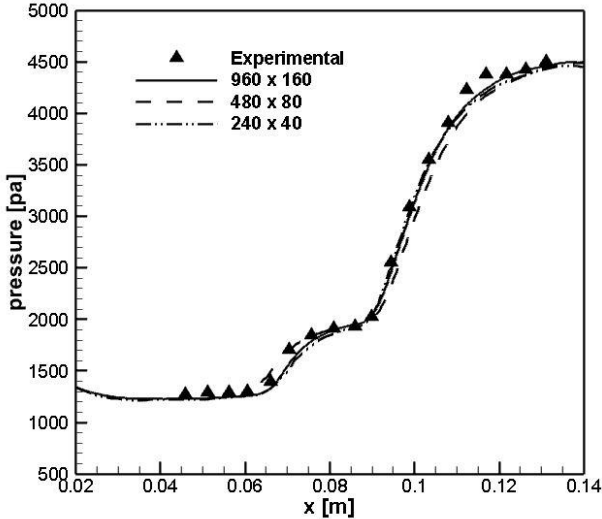
Fig. 4.7. Grid independence study of surface pressure profile over double ramp
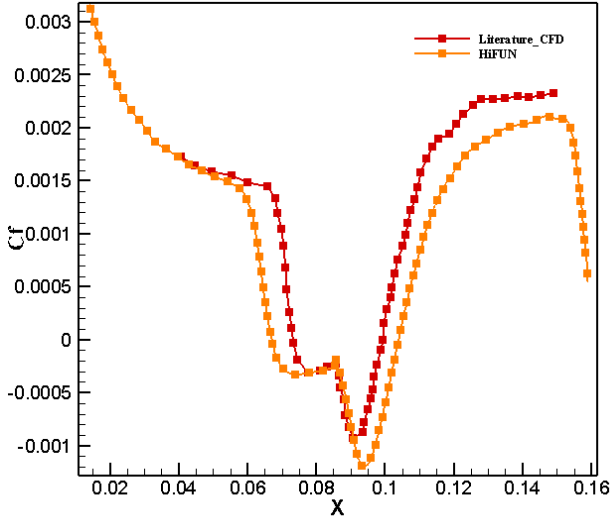
Fig. 4.8 Grid independence study of skin friction coefficient

34

Similar methodology was followed to perform grid independence study for triple ramp configuration. From the double ramp validation, it was found that 960 x 160 was the most reliable mesh for all design variations and hence the same mesh sizing was continued for the multi-ramp configurations having third and fourth ramps by adding equal mesh divisions of 400 elements on each ramp making it 1320 x 160 on triple ramp configuration and 1720 x 160 on quad ramp configuration, any lesser mesh count was unable to capture separation and reattachment points accurately on downstream ramp junctions, a sample grid independence plot for triple ramp configuration is shown in Fig. 4.12. It is evident that lesser grid size is unable to capture the separation bubble accurately.
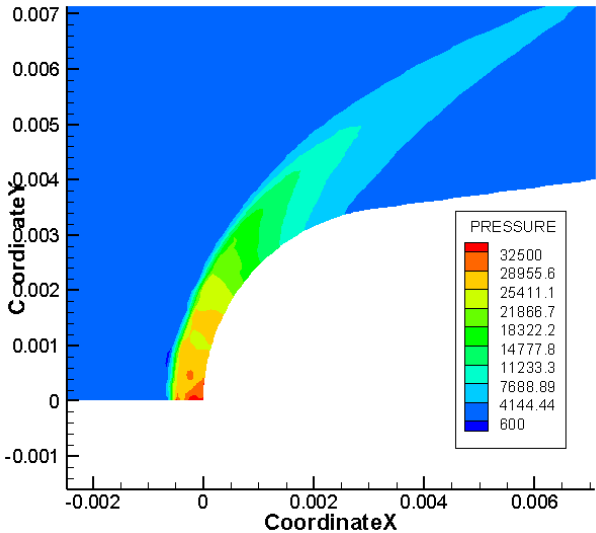
Fig. 4.9 Stagnation pressure
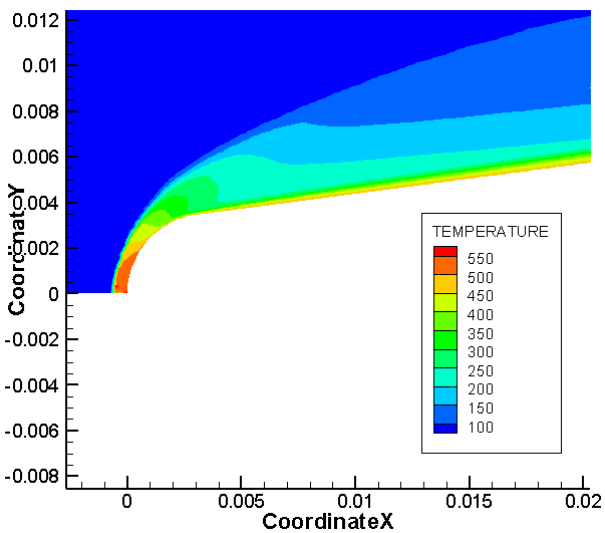
Fig. 4.10 Stagnation Temperature
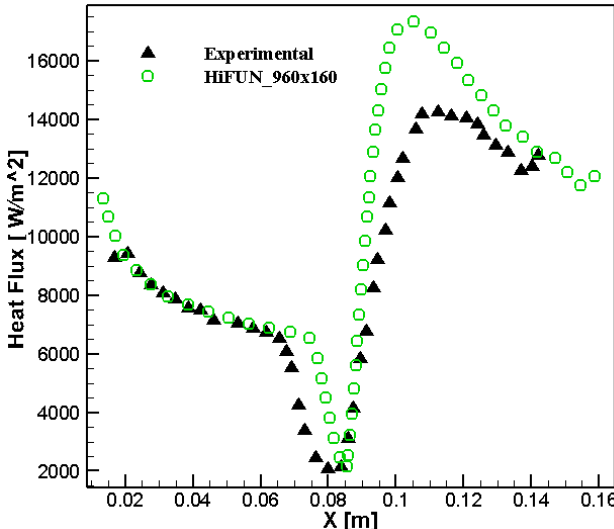
Fig. 4.11. Grid independence study of surface heat flux profile over double ramp
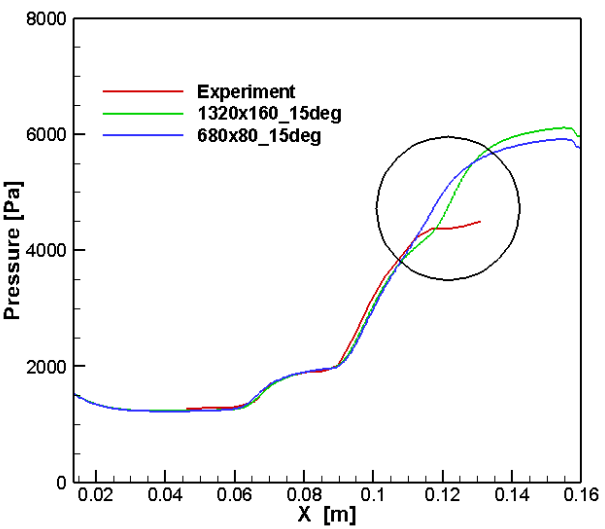
Fig. 4.12. Grid Independence study of surface pressure over triple ramp

4.3 SUMMARY

In summary, a detailed Inter-code comparison, grid dependency study and theoretical validation of stagnation pressure and temperature were performed on the standard double ramp or the base model, triple and quad ramp models. Multiple grid configurations with variations in normal and tangential grid spacing was considered to perform grid independence study. The boundary conditions used throughout the validation is same as considered by R. Savino [2] with 6 Mach freestream flow velocity.

Pressure distribution along the surface of base double ramp model was considered as standard parameter for inter-code comparison. Two simulation tools were used to perform this study, and from the outcome it was evident that HiFUN had excellent agreement with the experimental pressure plots and in predicting the separation and reattachment points. During the grid independence study, it was found that the grid spacing normal to the model was critical and key to prove the accuracy of the solver. From the study, 30 micron normal spacing has excellent agreement with experimental values of surface pressure on all grid configurations, while the separation and reattachment points were captured fairly by both 480 x 80 and 960 x 160 mesh combinations, the later was chosen since it captured the post attachment zone better which was crucial for this study.

In addition, a theoretical comparison of stagnation pressure and post-shock temperature with simulation outcome using the HiFUN solver also proves the solution to be independent of the grid. Qualitative and Quantitative parameters such as skin friction and surface heat flux were considered to reinstate the accuracy of the solver in predicting the bubble size and the points of separation and attachment. Similar methodology was followed to perform grid independence study for triple and quad ramp configurations, and it was conclusive that adding 400 elements on each additional ramp was capable of capturing separation and attachment points accurately.

CHAPTER 5. TRIPLE RAMP CONFIGURATION

The study on effect of adding a third ramp to the standard double ramp model used by R. Savino [2] and consequently varying the third ramp angle are carried out and the changes observed in shock wave boundary layer interactions, separation bubble lengths and surface pressure due to this addition are discussed in this section. This study also enumerates the observations done by Bibin John [4, 5] from the computational studies the importance of reducing the separation bubble length for better design performance and to verify the incipient separation condition through boundary layer separation.

5.1   EFFECT OF VARYING RAMP ANGLE

The triple ramp configuration (Fig. 4.1-b) with different third ramp angle $\theta = 7.5^0$, 10^0, 12.5^0 and 15^0 are considered to study the effects of such unique junction configurations. The freestream conditions are as mentioned in Table 4.1, which are same as per the experiments conducted by R. Savino et al [2]. As mentioned in earlier section the simulation tool has been validated and the grid fixed based on grid independence study done using the experimental data obtained by R. Savino et al [2], the same grid parameters are considered for this study.

The variation of surface pressure distribution for different third ramp angles and its implications on the bubble is shown in Fig. 5.1. The pressure distribution on double ramp is also integrated in the plot to give a perspective on separation bubble of double ramp and the formation of secondary bubble region in case of third ramp. From the graph it can be deduced that the presence of third ramp does not majorly affect the flow over second ramp and follows almost the same pressure trends. As per the findings by Bibin John et al. [4] and Marini [45, 46], the size of separation bubble increases with increase in ramp angle, which continues to be true even with a third ramp as can be seen in the figure. As can be seen in Fig. 5.3, this configuration has highly complex flow structure, with a detached bow shock at the leading edge, the separation shock at the first ramp along with the reattachment shock forming the first corner shock, which can also be seen in Fig. 5.1 as a spike in pressure, followed by second corner shock formed due to the second separation bubble, leading to a highly turbulent reattachment shock.

From the pressure distribution plot there is no conclusive evidence on the effects of having a third ramp on the bubble size and based on studies done by Bibin John et al. [5], a quantitative approach is considered by measuring the separation bubble size through skin friction distribution as shown in Fig. 5.2. The separation and reattachment points are determined where the curves cross the zero line. Summary on the separation bubble details are given in Table 5.1, where it can be noticed the length of the bubble at the first ramp is decreasing in the presence of a third ramp when compared with the

double ramp. These reductions may be small in magnitude but cannot be neglected as the overall objective is to reduce the bubble size and can provide considerable insights for design consideration.

Referring to Fig. 5.2 and 5.3, a clear separation bubble is indicated for ramp angles 7.5^0 and 10^0, while a complex bubble activity can be noticed for 12.5^0 and 15^0 ramp angles. This could be indicative of the presence of a strong shock and a weak circulation zone caused due to turbulent reattachment or even transitional in the presence of a strong shock which can be noticed in the form a high fluctuation, both in pressure and skin friction plots. It is evident from this simulation study that design considerations while encountering scenarios of ramp type junctions with more than the typical two ramps must be carefully assessed and fine-tuned to ensure reduced flow separations and shock interactions.
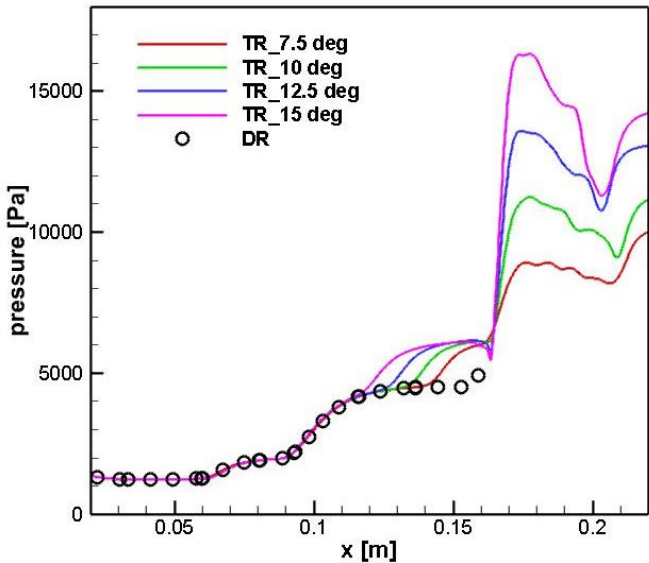
Fig. 5.1. Effect of third ramp angle variations on pressure distribution

Fig. 5.2. Effect of third ramp angle on skin friction distribution and bubble length

38

	Double Ramp	Triple Ramp 7.5^0		Triple Ramp 10^0		Triple Ramp 12.5^0		Triple Ramp 15^0	
	FB	FB	SB	FB	SB	FB	SB	FB	SB
L_b	0.0368	0.0366	0.0216	0.035	0.0299	0.0346	0.0378	0.0345	0.0469

L_b = bubble length (in meter), FB = Bubble at 1st ramp junction, SB = bubble at 2nd ramp junction

Table 5.1: Summary on changes in separation bubble parameters
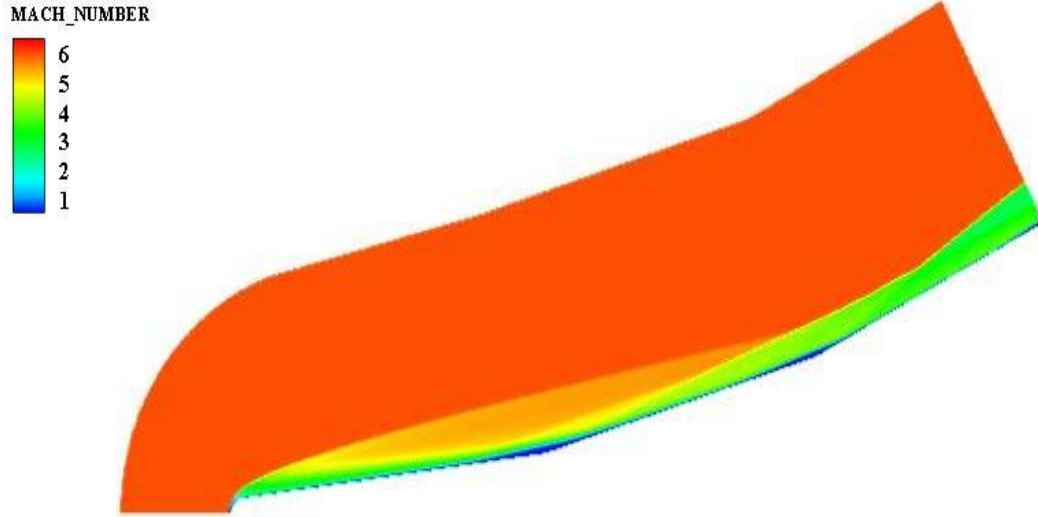
Fig. 5.3. Shock wave boundary layer interaction over triple ramp configuration (Mach contour)

5.2   EFFECT OF BLUNTED LEADING EDGE

This study presents a detailed understanding on the effect of blunted leading edge over shock wave boundary layer interactions with triple ramp configuration. The boundary conditions are the same as mentioned in Table 4.1, with variations in the leading-edge bluntness and ramp angle. The first two ramps are retained as per the experimental model considered by R. Savino et al.[2], while the third ramp with varying angle is attached to this base model. Considering leading edge bluntness is primarily logical as it is nearly impossible to manufacture with a sharp leading edge. Apart from this very point, leading-edge bluntness has significant effect on shock wave and boundary layer, primarily because the bluntness causes a detached bow shock when compared to sharp leading edge with attached oblique shock [4]. Presence of a bow shock reduces the flow velocity approaching the ramp even while the freestream Mach number in both cases are same.

Investigations by Bibin John et al. [4] also indicates with reduction in freestream Mach, the shock wave and boundary layer interaction become prominent. Presence of leading-edge bluntness also helps in significantly reducing the surface heating rate and stabilizes the flow through strong circulations at the boundary layer. The computed surface pressure distributions over triple ramp models with varying ramp angles and leading-edge bluntness are shown in Fig. 5.4 – 5.7. Commonly noticeable trends in all these surface pressure distribution plots are the behavior of the separation bubble, the reattachment shock and the shear layer region. Interestingly, the length of separation

bubble at the double ramp junction is more prominent at lower triple ramp angles (Fig. 5.4), while the separation bubble at triple ramp junction becomes more prominent at higher triple ramp angles (Fig. 5.6, 5.7). This is primarily because the reattachment shock at the double ramp junction tends to grow weaker with combined increment of nose bluntness and the third ramp angle, leading to an early upstream separation at the third ramp junction. What can also be noticed from the pressure distribution plots is that, the reattachment shocks after the double ramp junction is strong but not turbulent over the second ramp, causing a laminar shear region, whereas the reattachment shocks post the triple ramp junction is increasingly strong with increase in third ramp angle and highly turbulent causing a highly unstable shear region over the third ramp. It can be noticed in Fig. 5.7, there is almost no reattachment at the double ramp junction for both 3.5 and 5 mm blunt radius, there is a considerable downstream shift in the reattachment point at the double ramp junction and upstream shift in the separation point at the triple ramp junction leading to singularization of both the bubbles causing detached flow between both the junctions. The flow reattaches only after the third ramp junction characterized by highly turbulent strong post shock shear region.

The present study also considered the qualitative approach to measure the length of separation bubble though skin friction coefficient. As observed by Bibin John et al. [5] a strong correlation exists between the leading-edge bluntness and the separation bubble length. It is noticed from this study that even bluntness has significant effect on the flow field. Bibin John et al. [4] identified the presence of two critical nose radius, inversion and equivalent radius. The separation bubble size increases with increase in blunt radius (BR) until it reaches the inversion radius. This increase in separation bubble size is attributed to the dominance of boundary layer over the entropy layer. Post the inversion radius the bubble tends to decrease in size with increase in LE bluntness due to the shift in dominance of entropy layer over boundary layer.

Computational results of skin friction coefficient over triple ramp configuration with varying blunt radius is shown in Fig. 5.8 – 5.11. Like the pressure distribution plots it is noticed that the separation bubble size at the double ramp decreases in size with increase in third ramp angle and the reverse is noticed with respect to the bubble size at the third ramp junction. In case of 15^0 third ramp angle the separation behavior is reconfirmed through Fig. 5.11, where it can be noticed that the reattachment does not occur post the double ramp junction leading to detached flow between both the junctions. From the skin friction coefficient, the separation and reattachment points can be located as the ones where the distribution curve crosses the x-axis line. The changes in the locations of these two points for different third ramp angles along with different leading-edge radii are plotted in Fig. 5.12. Separation and reattachment points of both the separation bubbles, one over double ramp junction called as first bubble (FB) and the other over triple ramp junction called as second bubble (SB) are both considered for analogy in this plot. From this figure it is evident, with initial increase in leading

edge blunt radius the separation point shifts upstream and the reattachment point shifts downstream, increasing the separation bubble length for initial radii indicating the dominance of boundary layer over entropy layer. The first critical radius or the inversion radius is noticed anywhere between 3.8^0 to 4.4^0 where the boundary layer and the entropy layer are assumed to be of same thickness. With further increase in leading-edge radius, the separation point seems to move downstream, and the reattachment point upstream decreasing the length of the separation bubble, indicating the fact the dominance of entropy layer over boundary layer. Yet again it can be noticed the reattachment point for 15^0 third ramp angle is increasing with increase in blunt radius and the separation point also indicating the same proving completely detached flow. It also confirms that the addition of third ramp does not alter the correlation between blunt radius and the separation bubble length as reported by Bibin John et al. [4, 5], while there are noticeable upstream effects on the separation, reattachment and the overall shock wave boundary layer interaction.
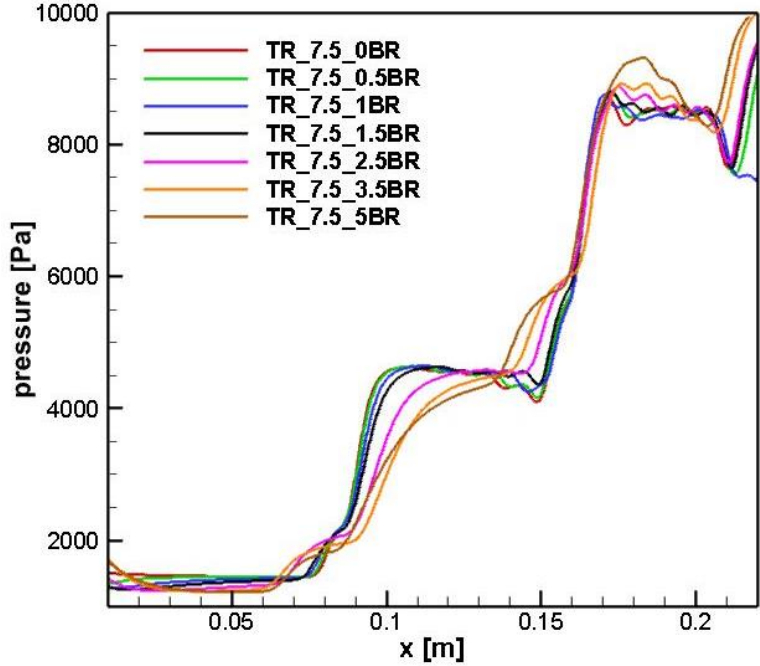
Fig. 5.4. Pressure distribution over 7.5^0 third ramp angle
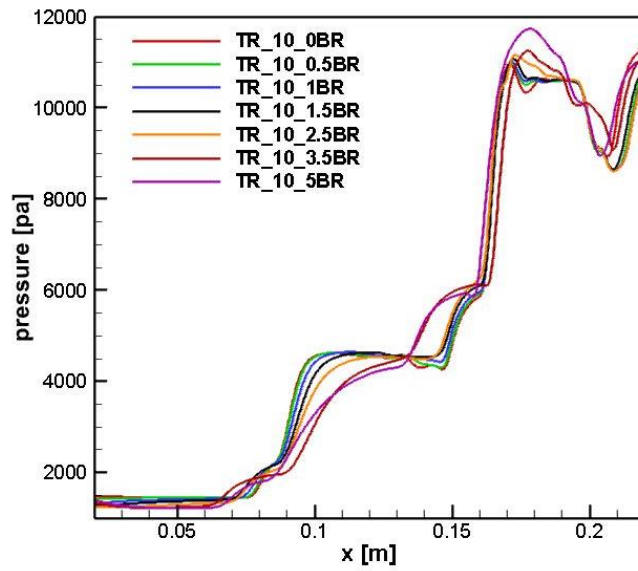
Fig. 5.5. Pressure distribution over 10^0 third ramp angle
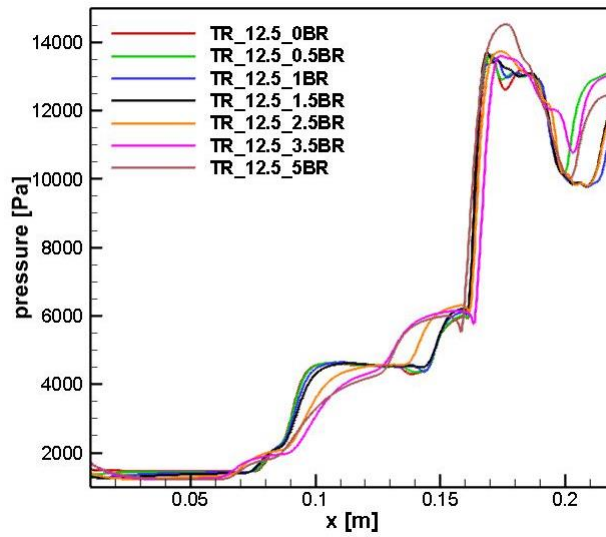
Fig. 5.6. Pressure distribution over 12.5^0 third ramp angle
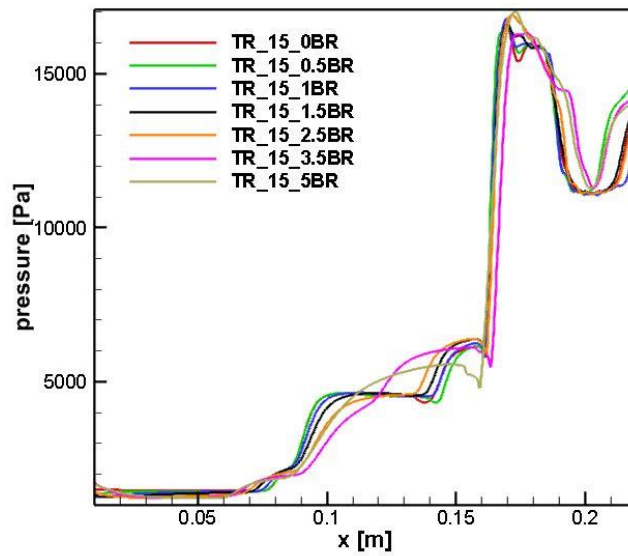
Fig. 5.7. Pressure distribution over 15^0 third ramp angle
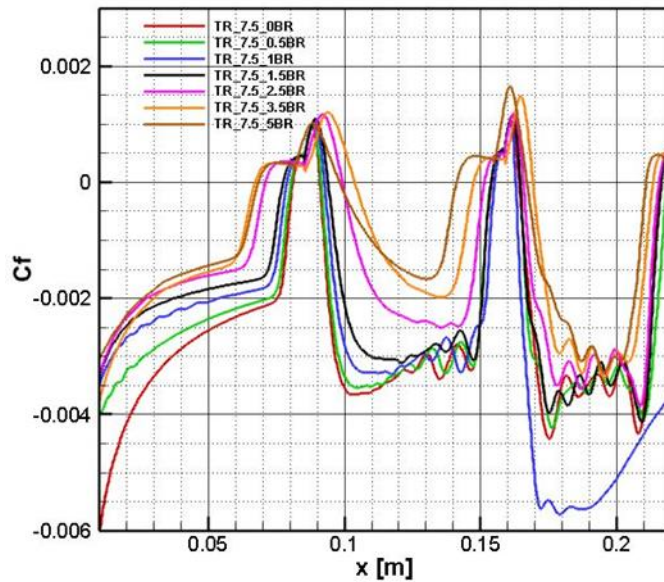
Fig. 5.8. Skin friction coefficient over 7.5^0 third ramp angle for different leading-edge radius
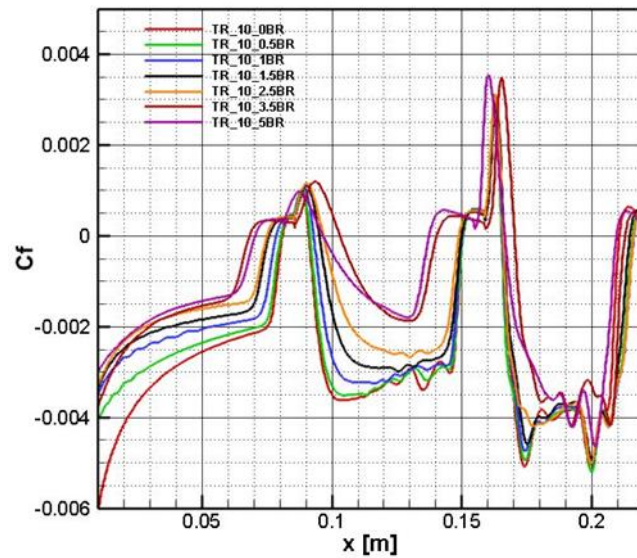
Fig. 5.9. Skin friction coefficient over 10^0 third ramp angle for different leading-edge radius
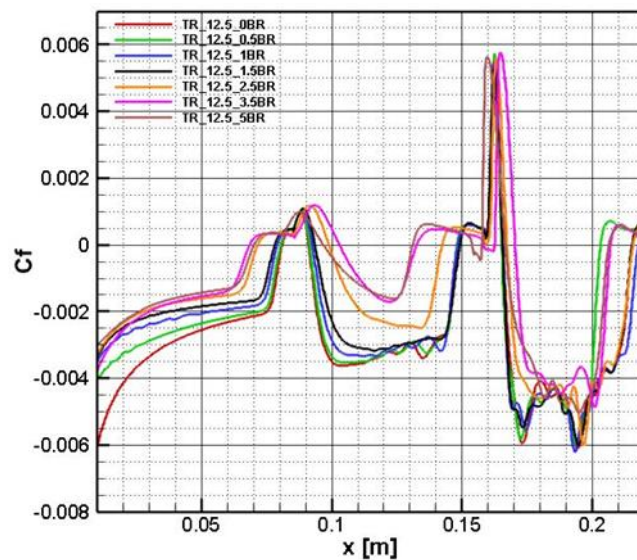
Fig. 5.10. Skin friction coefficient over 12.5^0 third ramp angle for different leading-edge radius

43
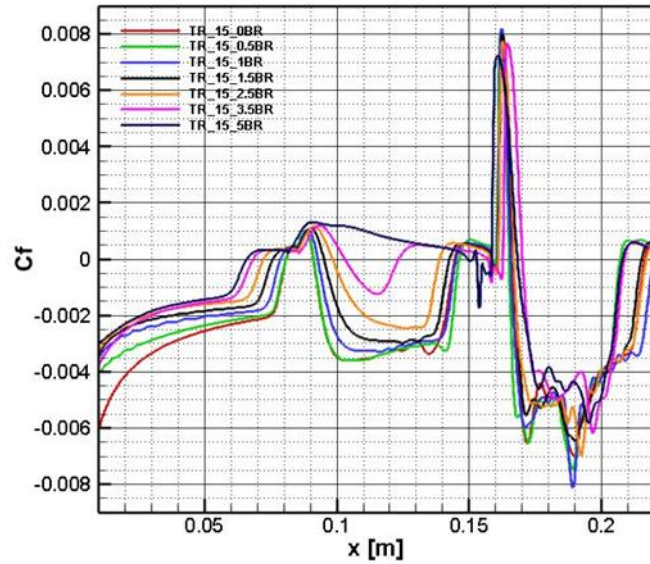
Fig. 5.11. Skin friction coefficient over 15^0 third ramp angle for different leading-edge radius
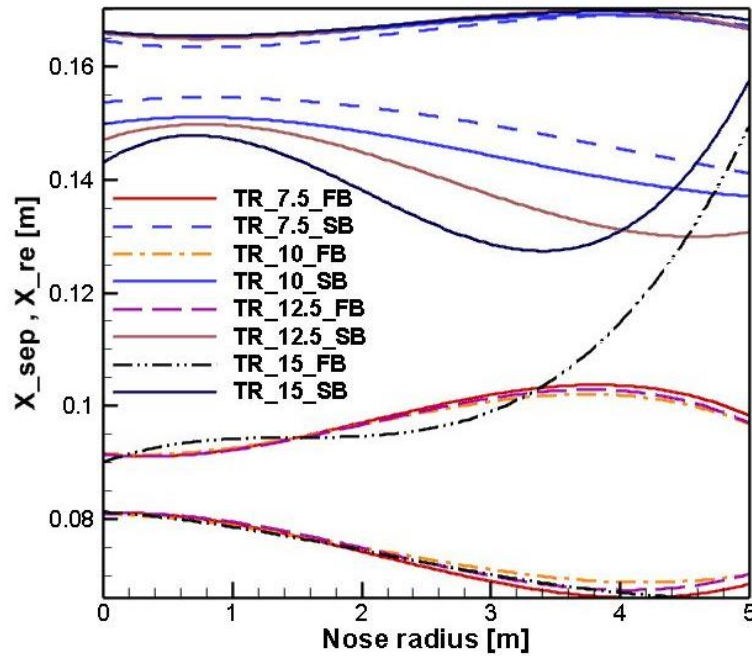
Fig. 5.12. Separation and reattachment points variation for different blunt radii and third ramp angle

5.3 COMBINED EFFECTS OF VARYING FREE-STREAM MACH NUMBER AND RAMP ANGLE

From the investigations done by Bibin John et. al. [4], it is evident that variation in ramp angle has a direct connect with freestream Mach number, the incipient separation angle decreases with an increase in freestream flow velocity (Mach). The study also reveals the fact that increasing ramp angle increases the bubble length and increasing the freestream Mach number reduced the length of bubble. The current study details out the combined effects of varying the free-stream Mach number and ramp angles to understand the changes in flow field and the shock wave boundary layer interactions.

The base model or a double ramp configuration with first ramp angle of 7.5^0 and second ramp angle of 10^0 [2] is considered. To this base model a third ramp with varying angles as mentioned in Table 4.1 is attached. Freestream Mach number is varied over all third ramp conditions to understand the changes in surface pressure distribution, skin friction coefficient and the separation bubble length. The surface pressure distributions are presented from Fig. 5.13 (a-d) and the skin friction coefficients are presented from Fig. 5.14 (a-d). From the plots it is evident that the flows are fully separated at both the ramp junctions and hence the deflection angles are above the incipient separation angle as described in the literature. Interestingly it is noticed that the correlation between Mach number and bubble size seems to not follow the trend as mentioned in earlier studies. Ideally the separation bubble length must be smaller for higher Mach numbers as per earlier findings, but from the pressure distribution plots, Fig. 5.13a to 5.13d, it is evident that this correlation no more is valid for configurations above double ramps. The correlation has been reversed in the case of triple ramp configurations wherein the separation point and reattachment points have been pushed upstream and downstream respectively in case of higher Mach number, while the separation point has moved downstream, and reattachment point upstream in case of lower Mach number. This trend remains same for all third ramp angles with increase in freestream Mach conditions, this could be attributed to the upstream influence of the presence of a third ramp junction.

Quantitative understanding through skin friction coefficient gives even better insights on separation and reattachment behavior in the presence of a third ramp. From Fig. 5.14 (a-d) it is interesting to notice that the size of the separation bubble is bigger for higher Mach numbers at the first junction while the separation bubble size is smaller for higher Mach numbers at the second junction. This is unique as two different correlations between Mach number and bubble size can be noticed at the same time, wherein the correlation is following inverse trends at the first junction while it follows the typical trend at the second junction as compared to the study by Bibin John et. al [4]. This is indicative of a significant downstream effect of having a third ramp on the flow physics. The separation point at the first junction moves downstream with increase in third ramp angles. The downstream effects are primarily due to changes in boundary layer caused by the compression corner at the second junction. What can also be noticed is that the reattachment shocks are becoming weaker at the first junction with increase in third ramp angle which are resulting in upstream shift in separation points at the second junction leading to increase in bubble size for lower Mach and reduction in bubble size for higher Mach. This is attributed to the reduction in inertia of the flow, where the lower Mach flows tends to become slower at the second junction resulting in early separation, while the higher Mach flows are still faster at the second junction resulting in later separation and so reduced bubble length.

The skin friction peaks that can be noticed in the plots are indicative of a turbulent reattachment shock that also leads to a highly turbulent post shock shear region which are indicated as fluctuations

post the reattachment point at the second junction. Table 5.2 reassures that the presence of third ramp has effects on the length of the separation bubble located at the first junction. The table compares size of separation bubble between double ramp and triple ramp configurations. As can be seen the biggest bubble corresponds to the double ramp measuring 36.8 mm while all other bubble sizes corresponding to triple ramp are smaller indicating an upstream influence. The upstream influence could be because of the thickening of the boundary layer due to the compression corner at second junction. The entropy layer might be engulfed inside the boundary layer leading to the increase of separation bubble size at the first junction. Completely engulfed entropy layer alters the flow properties which is assumed to affect the separation and reattachment points at the first junction. It is critical to understand this flow physics in detail which is identified to occur in situations where there could be a complex junction in a system or a subsystem of high speed vehicles and so experimentation must be considered as the next step for better understanding of such complex flow physics and also to add basis for all the computational investigations.

(a) 7.5^0 third ramp angle

(b) 10^0 third ramp angle

(c) 12.5^0 third ramp angle

(d) 15^0 third ramp angle

Fig. 5.13. Surface pressure distributions of triple ramp configurations at different Mach numbers
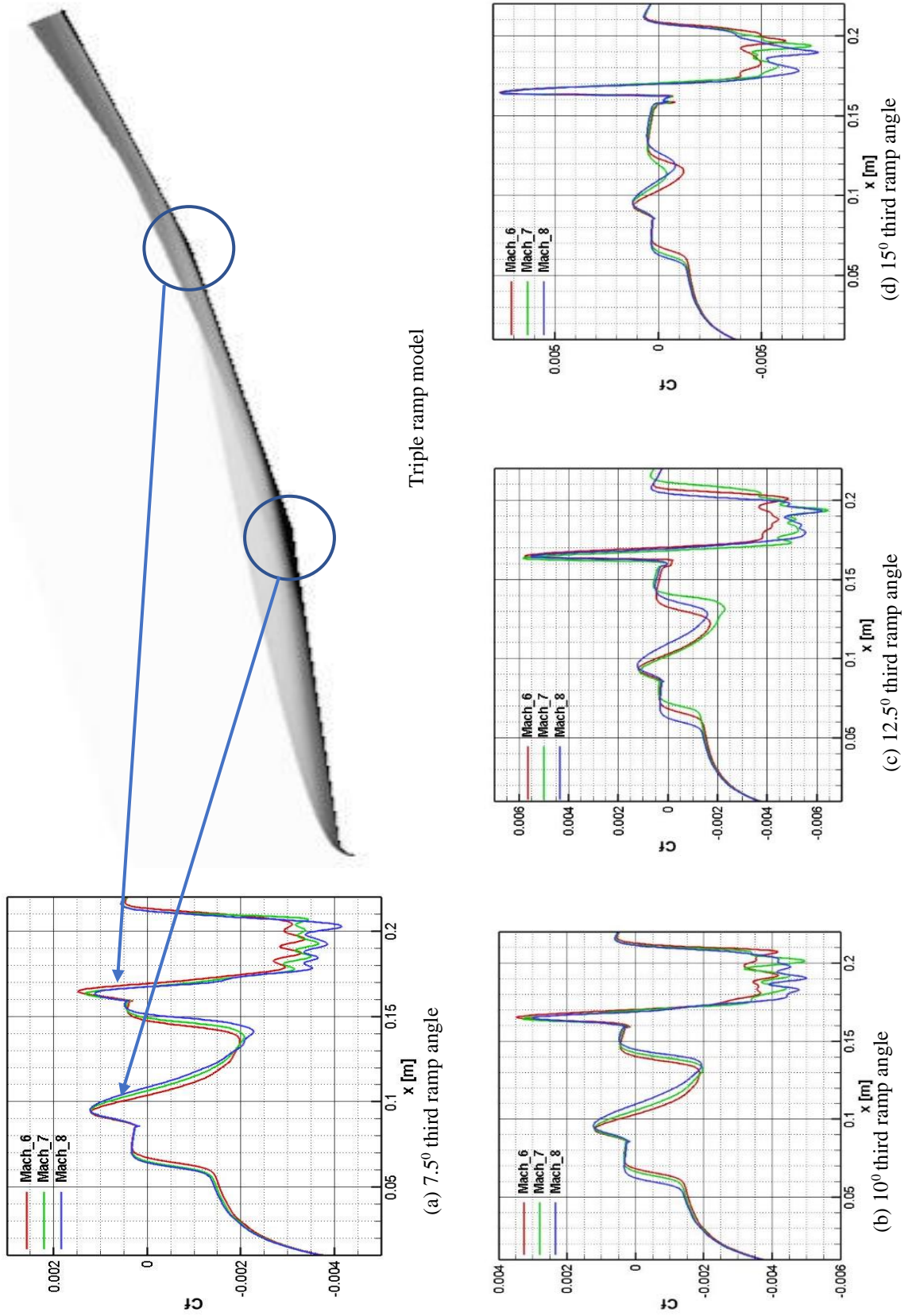
Fig. 5.14. Skin friction coefficients of triple ramp configurations at different Mach numbers

M_∞	Configuration	α	Bubble	L_b
6	DR		FB	36.8
	TR	7.5	FB	36.47
			SB	21.6
	TR	10	FB	34.87
			SB	29.94
	TR	12.5	FB	34.47
			SB	7.88
	TR	15	FB	34.6
			SB	12.95
8	DR		FB	31.72
	TR	7.5	FB	44.31
			SB	15.92
	TR	10	FB	47.2
			SB	24.06
	TR	12.5	FB	46.8
			SB	31.95
	TR	15	FB	46.3
			SB	11.83

DR = double ramp, TR = triple ramp, α = third ramp angle, FB = first bubble, SB = second bubble, L_b = bubble length

Table 5.2: Summary of separation bubble sizes for varying freestream Mach numbers and ramp angles

5.4 WALL TEMPERATURE EFFECTS AT DIFFERENT MACH NUMBERS

It is evident from the investigations done by R. Savino [2] and Bibin John [4] that variations in surface temperature has significant effect on the shock wave boundary layer interaction, hence it is important to study this parametric change on triple ramp configuration as well, to understand whether the correlation still follows the same trend for multi-ramp junctions. For this study triple ramp configuration with 7.5^0 third ramp angle is considered as it exhibits fully separated flow at both ramps with lowest pressure peaks at second junction. Freestream Mach number chosen are between 6 to 8 and surface temperatures considered are 270 K, 300 K and 330 K. Surface heat flux for different Freestream Mach numbers are shown in Fig. 5.15-5.17 and the surface pressure distribution for Mach 6 is shown in Fig. 5.18. Simulation with adiabatic wall condition is also considered and plotted along with the isothermal wall boundary, to understand the upstream influence on the flow physics with these different wall thermal treatments.

Table 5.3 gives a detailed perspective on the effects of bubble sizes due to the variations in freestream Mach number in combination with varying surface temperature. It can be understood from this study that there is a definite upstream influence with increase in wall temperature. This influence is seen throughout the configuration at all locations and the presence of third ramp does not alter the correlation between surface heat flux and SWBLI. It is interesting to observe from the heat flux plots

that the combined study of freestream Mach number, surface temperature and the third ramp has major upstream influences and has noticeable increase in peak pressure values post reattachment at both the junctions. The increase in peak pressure values are mainly attributed to smaller but stronger separation bubbles at higher freestream Mach which causes stronger compression corner shocks and a much stronger reattachment shock followed by highly turbulent shear zone. Increase in surface temperature causes rise in viscosity properties of the flow which causes an increase in the boundary layer thickness. Thicker boundary layer reduces heat flux while also causes early separation as can be seen in Table 5.3. It is also noticed that the separation point is moved downstream with increase in freestream Mach number at both ramp junction while still early separation is noticed with increased wall temperature.

It can be deduced that increase in Mach number does reduce the bubble length at both junctions while bubble length remains to be bigger for higher wall temperatures. Biggest separation bubble of size 36.47 mm and 21.6 mm at the first and second junctions respectively can be seen for Adiabatic wall condition at Mach 6 indicating the effects of surface temperature on boundary layer thickness. The bubble size continues to increase at the first junction in case of adiabatic conditions with bubble size reaching a maximum of 44.31 mm at first junction for Mach 8 while the maximum bubble size in case of isothermal surface temperature of 330 K at Mach 8 freestream condition in just 14.31 mm. This is a considerable reduction in bubble size noticed due to surface temperature changes. Hence it is evident that increase in freestream velocity with increase in wall temperature reduces the bubble size considerably while also reducing the heat flux, on the contrary considering adiabatic wall conditions with increase in freestream Mach number has adverse bubble growth at the first junction.

Fig. 5.15. Wall temperature effects on surface heat flux distribution at Mach 6
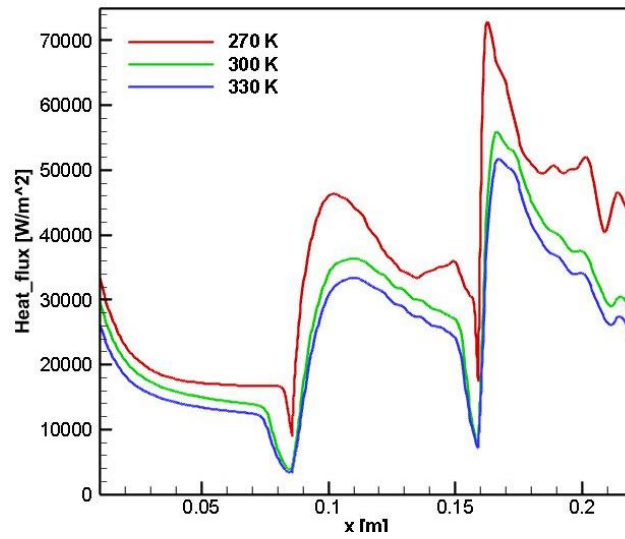
Fig. 5.16. Wall temperature effects on surface heat flux distribution at Mach 7
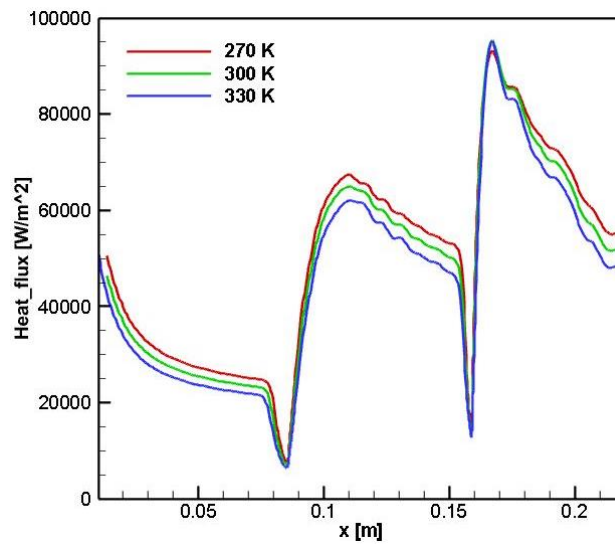
Fig. 5.17. Wall temperature effects on surface heat flux distribution at Mach 8
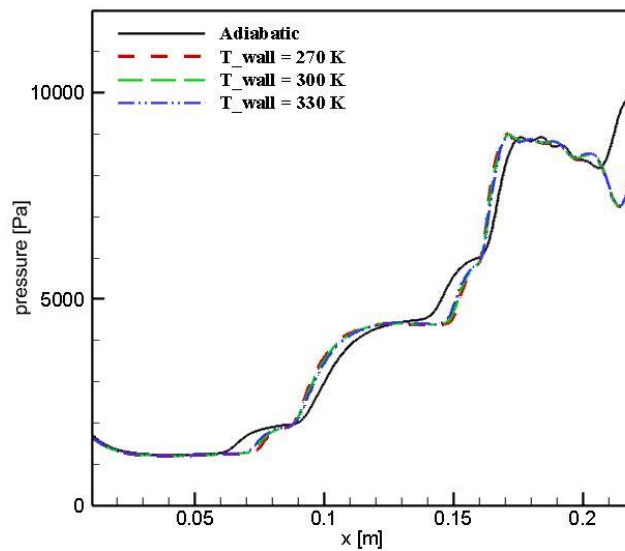
Fig. 5.18. Wall temperature effects on pressure distribution at Mach 6

M_∞	T_W (K)	FB			SB		
		X_{sep} (mm)	X_{re} (mm)	L_b(mm)	X_{sep} (mm)	X_{re} (mm)	L_b(mm)
6	Adiabatic	67.31	103.78	36.47	147.6	169.2	21.6
7	Adiabatic	65.01	106.58	41.57	149.2	167.5	18.3
8	Adiabatic	64.27	108.59	44.31	151.38	167.3	15.92
6	270	77.15	94.7	17.54	153.4	163.98	10.58
7	270	84.07	88.01	3.93	158.4	159.9	1.5
6	300	75.94	95.79	19.84	152.8	164.5	11.7
7	300	78.31	94.3	15.99	154.92	162.5	7.58
6	330	74.76	96.96	22.20	152.1	165.28	13.18
7	330	77.27	95.4	18.12	154.55	162.8	8.25
8	330	79.45	93.76	14.31	156.4	162.3	5.9

M_∞= freestream Mach, X_{sep}= separation point, X_{re}= reattachment point, L_b= bubble length, T_W= wall temperature

Table 5.3: Summary on effects of bubble sizes due to the variations in freestream Mach number and surface temperature

5.5 SUMMARY

In this chapter, the behavior of shock wave boundary layer and the associated bubble sizes for triple ramp configuration are studied for various geometric, flow and thermal conditions. This chapter studies in detail the effects of varying ramp angles, considering leading edge bluntness, varying freestream velocity and wall temperature on the shock wave boundary layer interaction and in-turn the size of the separation bubble.

Variations of surface pressure distribution for different third ramp angles and its implications on the bubble size is studied. Initial investigations through pressure plot indicated no major implications of adding a third ramp on the flow and bubble characteristics at the first compression corner, but with quantitative approach of measuring the separation bubble size through skin friction distribution, it was noticed that the bubble length at the first ramp was decreasing with increase in third ramp angle. These reductions may be small in magnitude but cannot be neglected as the overall objective is to reduce the bubble size and can provide considerable insights for design consideration.

Computational investigations were performed to study the effect of leading-edge bluntness on shock wave boundary layer interactions in triple ramp model configuration. The simulation has led to following conclusions,

- Separation bubble length was prominent at first compression corner at lower third ramp angle, while it was inverse at higher third ramp angle.
- It was identified that the reattachment shock at first compression corner was growing weaker with increase of both nose bluntness and the third ramp angle, leading to early upstream separation at the second ramp junction.

- The investigation also indicated that the reattachment shocks after the first junction was stronger but not turbulent, causing a laminar shear region over the second ramp, whereas the reattachment shocks post second junction was increasingly strong and highly turbulent causing highly unstable shear region over the third ramp.

- For higher blunt radius, there was considerable downstream shift in the reattachment point causing singularization of both the bubbles causing detached flow over both junctions.

- From quantitative approach of measuring bubble length through skin friction coefficient, it was evident, with initial increase in leading edge blunt radius the separation point shifts upstream and the reattachment point shifts downstream, increasing the separation bubble length for initial radii indicating the dominance of boundary layer over entropy layer.

- The first critical radius or the inversion radius is noticed anywhere between 3.8^0 to 4.4^0 where the boundary layer and the entropy layer are assumed to be of same thickness.

- Further increase in leading-edge radius, the separation point seems to move downstream, and the reattachment point upstream decreasing the length of the separation bubble, indicating the fact the dominance of entropy layer over boundary layer.

Simulations were performed to study the combined effects of varying free-stream Mach and ramp angles. Interesting correlations were noticed during this study as the bubble behavior was not following the trends of earlier literature studies.

- It was noticed that the size of the separation bubble is bigger for higher Mach numbers at the first junction while the separation bubble size is smaller for higher Mach numbers at the second junction. This is indicative of a significant downstream effect of having a third ramp on the flow physics.

- The downstream effects are primarily due to changes in boundary layer caused by the compression corner at the second junction.

- Reattachment shocks were becoming weaker at the first junction with increase in third ramp angle, leading to increased bubble size for lower Mach, attributed to reduction in inertia of the flow.

- An upstream influence of third ramp was distinctly evident with the bubble sizes of all triple ramp configurations proving to be smaller when compared to that of double ramp.

From the simulations to study the effect of wall temperature on SWBLI, it was evident that increase in freestream velocity with increase in wall temperature reduces the bubble size considerably while also reducing the heat flux, on the contrary considering adiabatic wall conditions with increase in freestream Mach number has adverse bubble growth at the first junction.
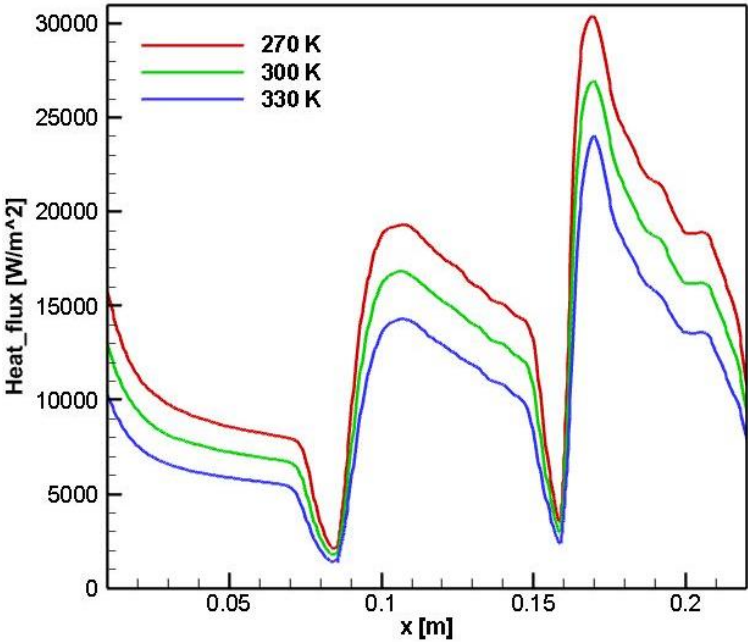
CHAPTER 6. QUAD RAMP CONFIGURATION

From earlier investigations, it is evident that multi-ramp design configurations have significant effects in the flow physics leading to changes in correlations between freestream and design modifications. It is also certain that the flow around such complex multi-junction configurations have some of the most complex flow structure and shock interactions and must be studied in detail. These multi-ramp junctions also change the understandings derived from earlier research findings of Bibin John et. al [4] where the correlation between freestream Mach number and bubble length vary with increase in ramp junction as noticed in the earlier section.

6.1 EFFECTS OF VARYING FREESTREAM MACH NUMBER AND RAMP ANGLE

Numerical simulations are carried out to study the effects of adding a fourth ramp to the earlier considered three ramp configurations on the flow physics associated with shock wave boundary layer interaction. The first and second ramp are the same as base model, the third ramp is fixed at 7.5^0 ramp angle. To this triple ramp configuration, a fourth ramp is attached making it a Quad-ramp configuration. Fourth ramp angles are varied between 5^0 to 12.5^0 with a varying freestream Mach number between 6 to 8 and the associated effects on skin friction coefficient and surface pressure distributions are shown in Fig. 6.1 (a-d) and Fig. 6.2. (a-d) respectively. A minimum ramp angle of 5^0 is considered for the fourth ramp as it is critical to test the validity of incipient separation angle. It is evident from the pressure distribution plots that the incipient separation theory by Bibin John et. al [4] still holds, where the separation bubble for 5^0 ramp angles is almost negligible in size indicating that it is not a fully separated flow whereas, the bubble sizes increase with higher ramp angles beyond 7.5^0 as per earlier studies.

From the skin friction coefficient plots, the trends upto the second junction is exactly as depicted in triple ramp configuration, where the bubble size is larger for higher freestream Mach at first junction and the bubble size is least for lower freestream Mach. At the third junction the separation and reattachment points do not show noticeable variations with increase in freestream Mach number, indicating that the separation bubble size at the third junction is no more dependent on the freestream velocity conditions. This could attribute to low inertia by the time the flow reaches the third junction across all Mach conditions. It is also noticed across all ramp variations that the region after the reattachment at the second junction is highly turbulent due to a turbulent reattachment causing a highly turbulent shear region, the effects of the turbulent shear and the shock follows downstream towards the third junction increasing the intensity of reattachment shock at the third junction. This could be attributed to turbulence dissipation downstream through shear layers causing a stronger corner shock at the third junction. These studies indicate that such complex junctions have very unpredictable flow natures and may not follow every correlation that proves well for a simple double

ramp configuration, encouraging the need for detailed and in-depth experimental studies to clearly understand flow physics when design scenarios lead to such complex multi-ramp junctions.

Fig. 6.1. Skin friction coefficients of quad-ramp configurations at different Mach numbers

(a) 5^0 quad-ramp angle

(b) 7.5^0 quad-ramp angle

(c) 10^0 quad-ramp angle

(d) 12.5^0 quad-ramp angle
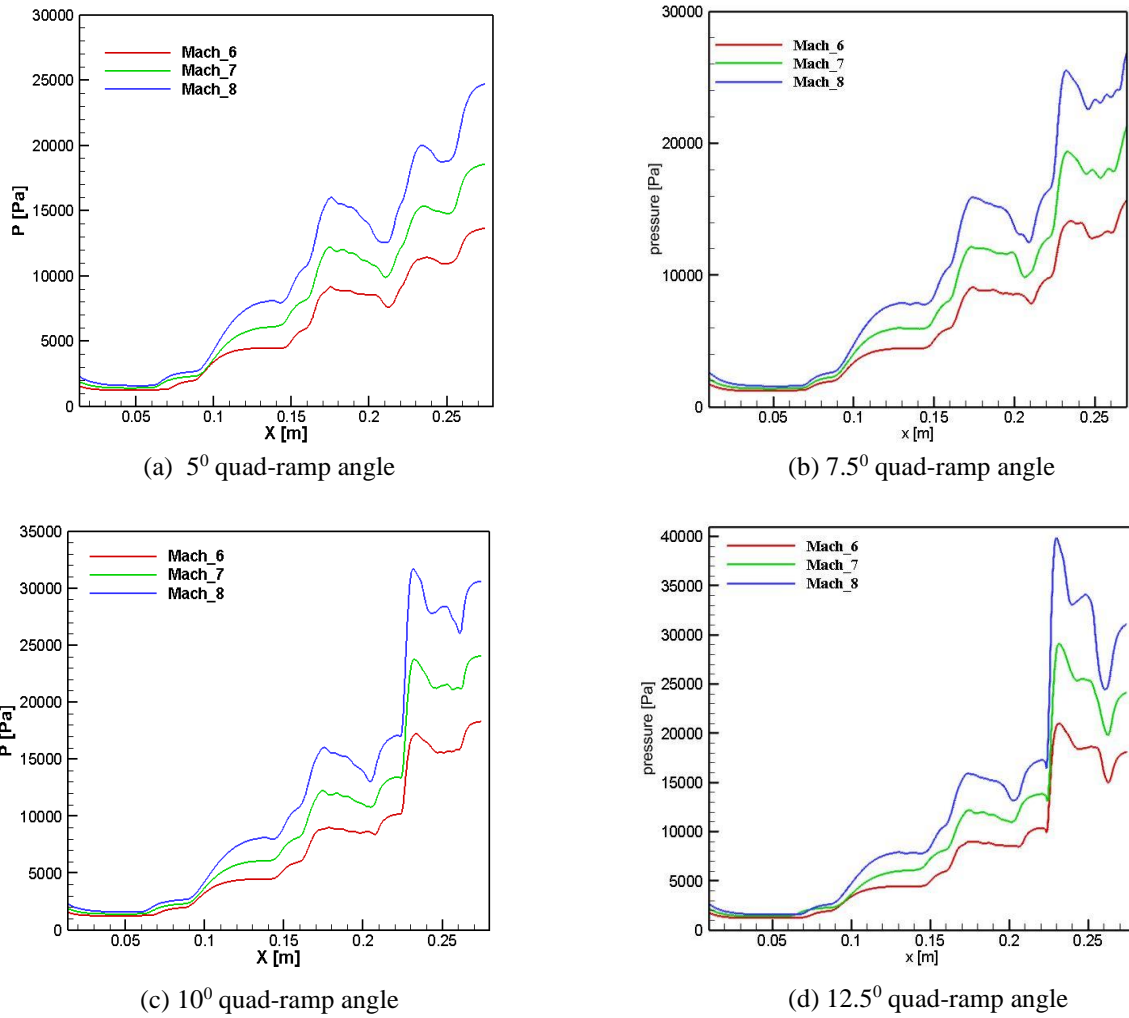
Fig. 6.2. Surface pressure distributions of quad-ramp configurations at different Mach numbers

Simulations are carried out with variations in third and fourth ramp angles as mentioned in Table 4.3 in Chapter 4. The following section discusses the various combination of ramp angles and the changes noticed in the bubble size, separation and reattachment points and the shear layer behavior. From the surface pressure distribution plots it can be deduced, for all cases where the third ramp angle is greater than the fourth ramp angle, the reattachment shock is strong at the second junction with a highly turbulent post shock region when compared to the separation and reattachment shock at the third junction. This is mainly because the flow turn angle is higher at the second junction which causes stronger corner shock when compared to the third junction. When the third and fourth ramp angles are equal, an almost similar separation and reattachment behavior can be seen at both the junctions and when the fourth ramp angle is higher than the third ramp angle the reattachment shock at the second junction is relatively weaker when compared to the reattachment at the third junction, at the same time the separation and reattachment shocks seem to become weaker at the first junction indicating significant downstream effects of a larger fourth ramp.

56
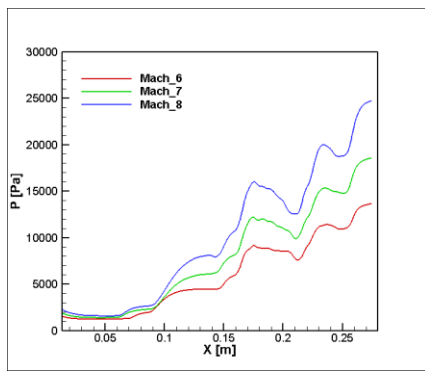
(a) 7.5^0 third-ramp angle
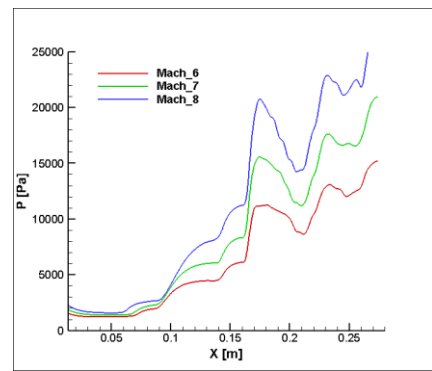
(b) 10^0 third-ramp angle
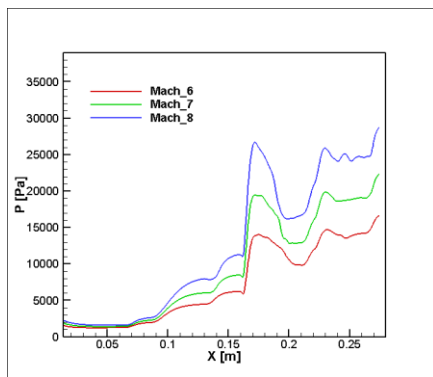
(c) 12.5^0 third-ramp angle
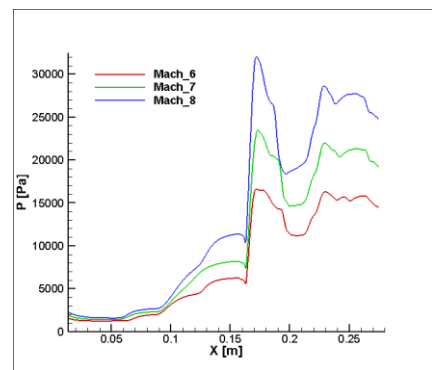
(d) 15^0 third-ramp angle

Fig. 6.3. Surface pressure distributions: 5^0 Quad Ramp Angle & Varying Third Ramp angle
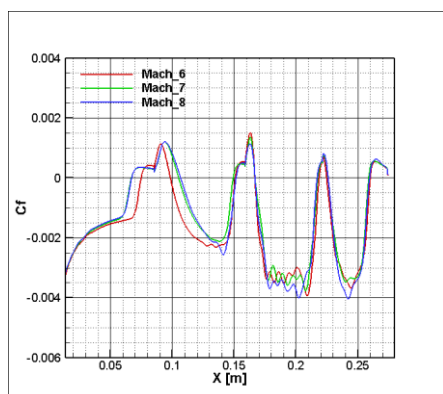
(a) 7.5^0 third-ramp angle
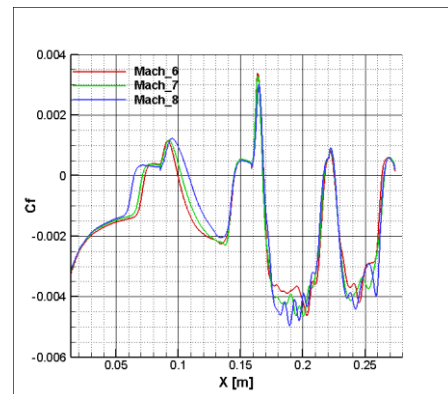
(b) 10^0 third-ramp angle
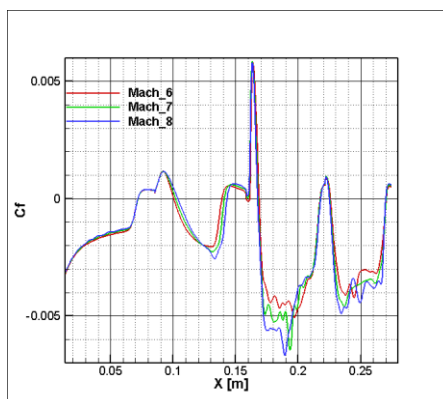
(c) 12.5^0 third-ramp angle
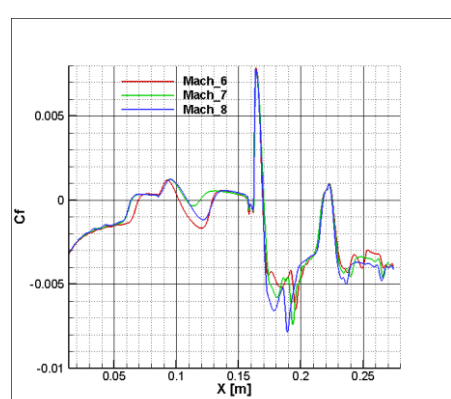
(d) 15^0 third-ramp angle

Fig. 6.4. Skin friction co-efficient: 5^0 Quad Ramp Angle & Varying Third Ramp angle
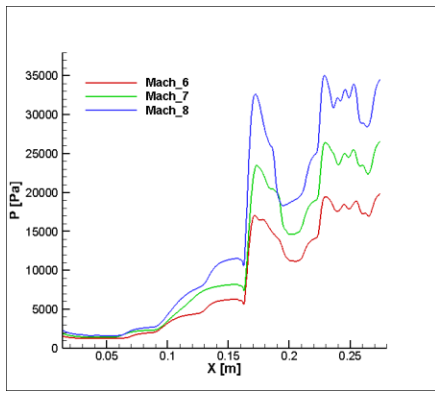
(a) 7.5^0 third-ramp angle
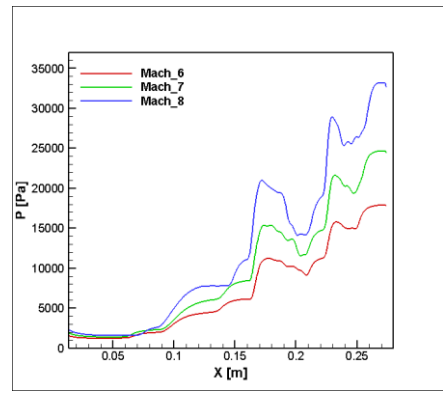
(b) 10^0 third-ramp angle
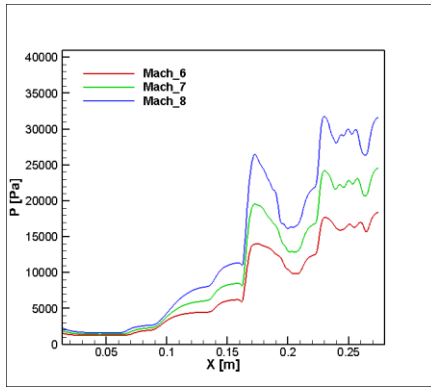
(c) 12.5^0 third-ramp angle
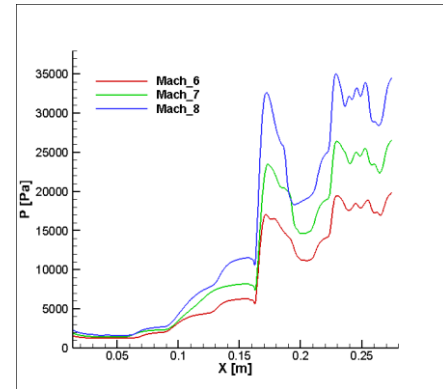
(d) 15^0 third-ramp angle

Fig. 6.5. Surface pressure distributions: 7.5^0 Quad Ramp Angle & Varying Third Ramp angle
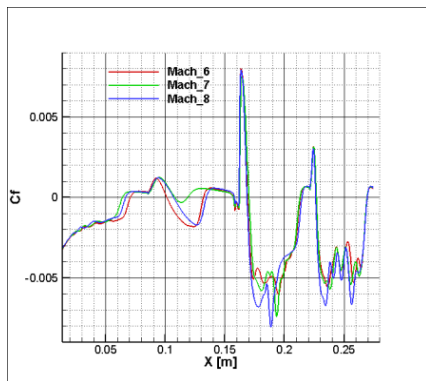
(a) 7.5^0 third-ramp angle
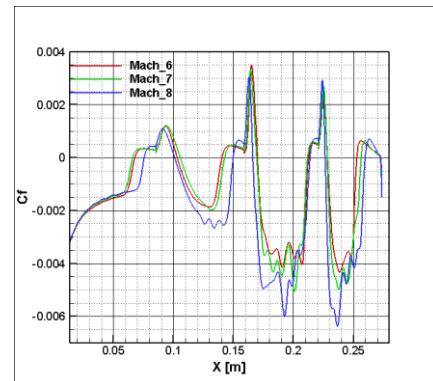
(b) 10^0 third-ramp angle
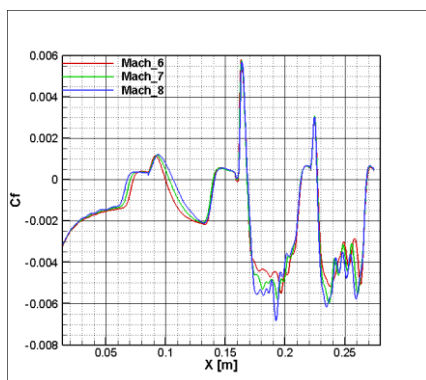
(c) 12.5^0 third-ramp angle
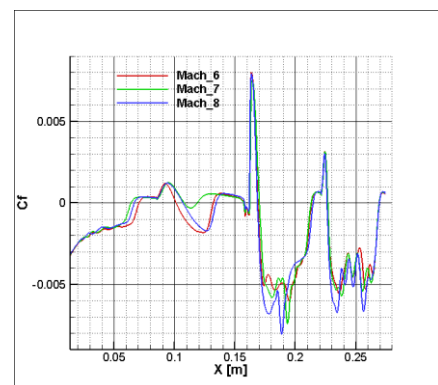
(d) 15^0 third-ramp angle

Fig. 6.6. Skin friction co-efficient: 7.5^0 Quad Ramp Angle & Varying Third Ramp angle
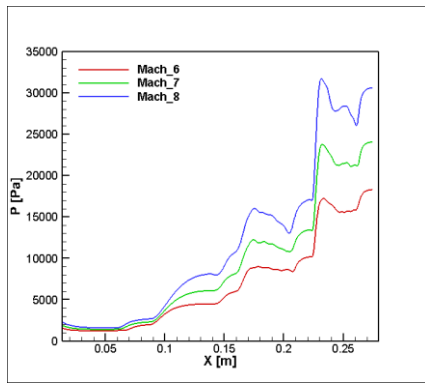
(a) 7.5⁰ third-ramp angle
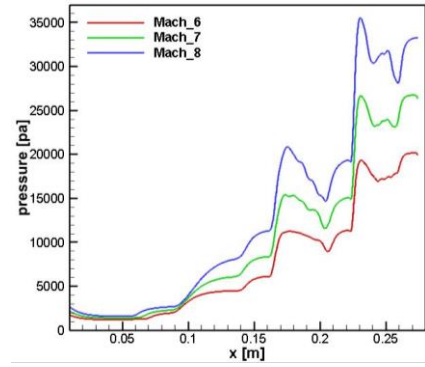
(b) 10⁰ third-ramp angle
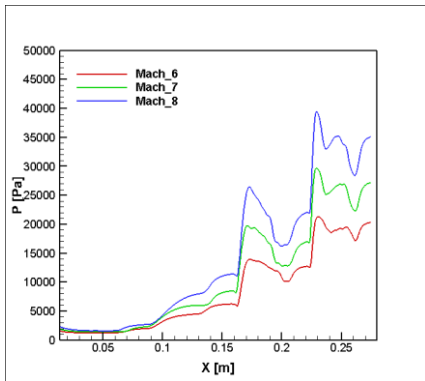
(c) 12.5⁰ third-ramp angle
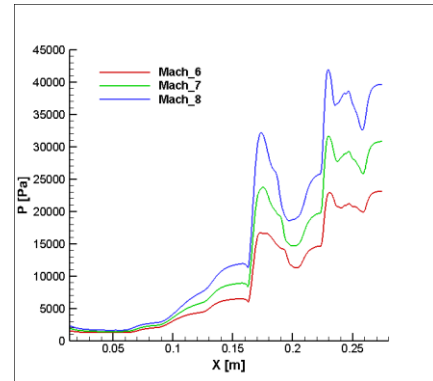
(d) 15⁰ third-ramp angle

Fig. 6.7. Surface pressure distributions: 10^0 Quad Ramp Angle & Varying Third Ramp angle
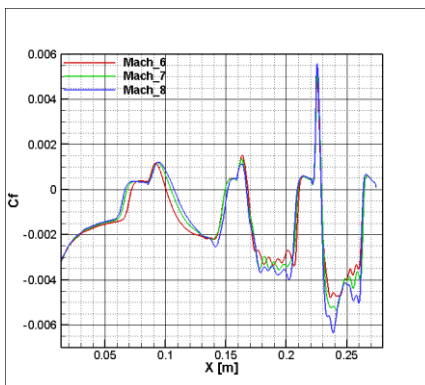
(a) 7.5⁰ third-ramp angle
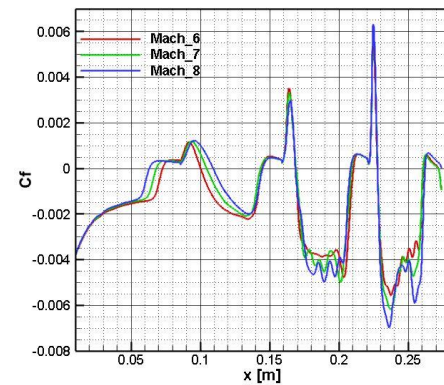
(b) 10⁰ third-ramp angle
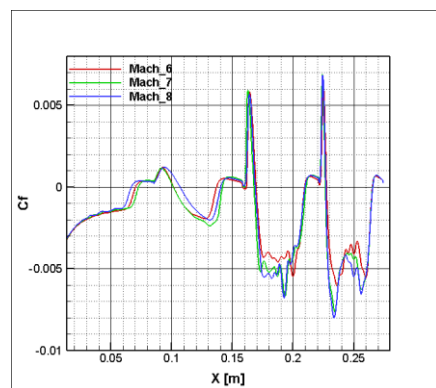
(c) 12.5⁰ third-ramp angle
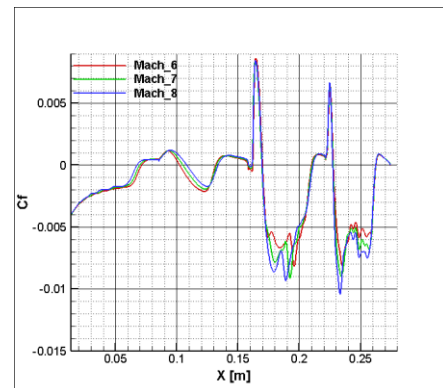
(d) 15⁰ third-ramp angle

Fig. 6.8. Skin friction co-efficient: 10^0 Quad Ramp Angle & Varying Third Ramp angle
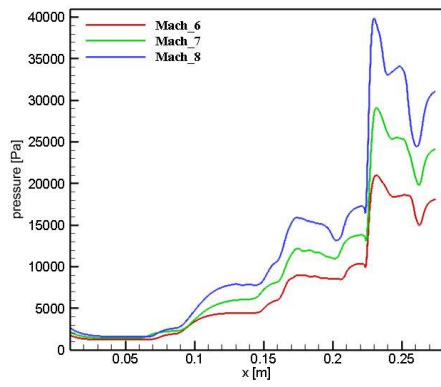
(a) 7.5⁰ third-ramp angle
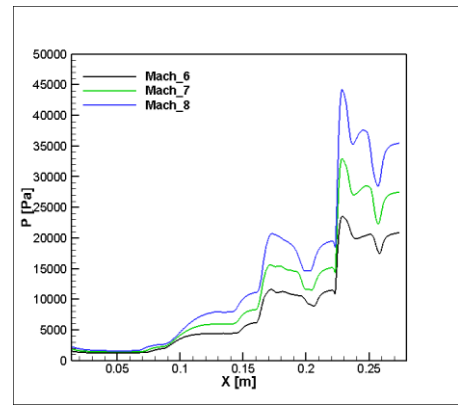
(b) 10⁰ third-ramp angle
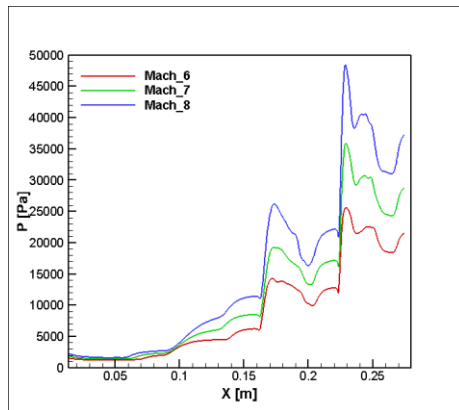
(c) 12.5⁰ third-ramp angle
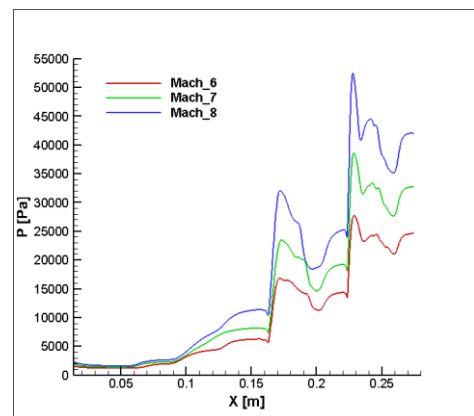
(d) 15⁰ third-ramp angle

Fig. 6.9. Surface pressure distributions: 12.5^0 Quad Ramp Angle & Varying Third Ramp angle
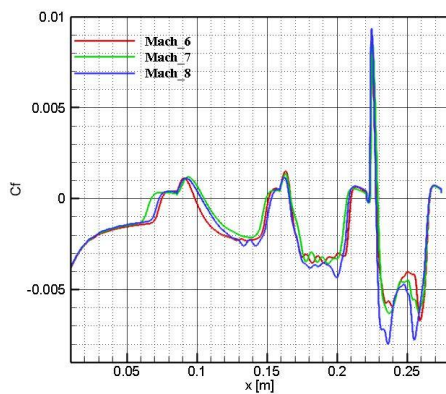
(a) 7.5^0 third-ramp angle
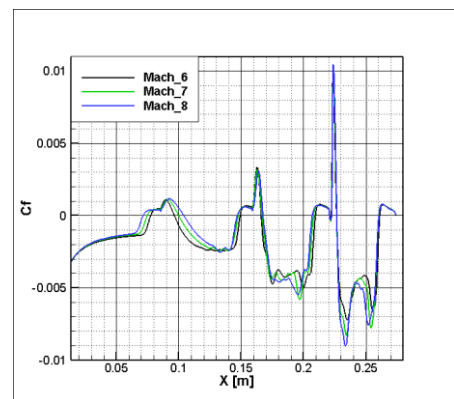
(b) 10^0 third-ramp angle
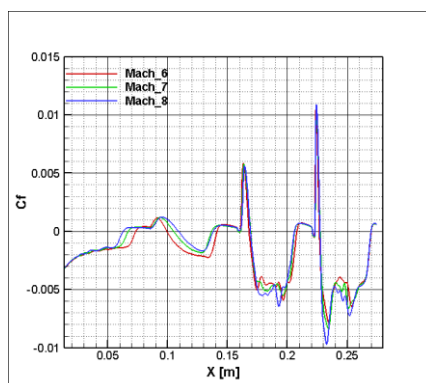
(c) 12.5^0 third-ramp angle
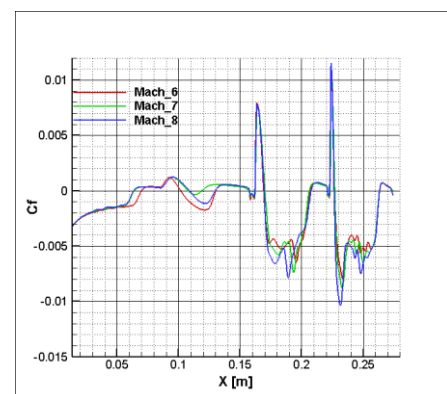
(d) 15^0 third-ramp angle

Fig. 6.10. Skin friction co-efficient: 12.5^0 Quad Ramp Angle & Varying Third Ramp angle

Fig. 6.3 and 6.4 are plots respective to surface pressure and skin friction coefficient of quad ramp configuration with fourth ramp angle fixed at 5^0 and the third ramp is varied. All the third and fourth ramp angle variations are as mentioned in Table 4.3 in Chapter 4. It is evident from the figures that the flow separation at the third junction is very weak mainly because of the low fourth ramp angle which is below the incipient separation angle, due to which there is almost very negligent bubble present at the third junction. The presence of a small bubble is attributed to the flow velocity at that junction whose inertia has reached lower values after passing through multiple shocks downstream. The presence of fourth ramp in this configuration has very minimal effect downstream which can be noticed through a strong separation and reattachment shock at the second junction indirectly explaining the fact that the bubble activity is less affected even with the presence of a weak bubble upstream at the third junction.

Fig. 6. 5 and 6.6 are plots for quad ramp with fourth ramp angle fixed at 7.5^0 which is also the angle above the incipient separation angle. There is noticeable change with respect to both surface pressure and skin friction plots when compared to the previous plots of fourth ramp angle fixed at 5^0. The bubble at the third junction has become more prominent which can be seen in Fig. 6.6 indicating the presence of strong separation and reattachment shocks. Significant upstream influence can be noticed for the case with third ramp angle of 7.5^0, whereas for third ramp angles greater than 7.5^0, which in this case is also greater than the fourth ramp angle the downstream effects are lesser, which is indicative of a stronger bubble and shock activity at the second junction overpowering the third junction. From the skin friction plots it is quite evident that the separation bubble at the third junction is lesser in intensity in all cases but is significant in terms of its intensity of reattachment shock and turbulent shear.

Fig. 6.7 and 6.8 are plots respective to surface pressure and skin friction coefficient of quad ramp configuration with fourth ramp angle fixed at 10^0 and the third ramp is varied. From these plots it is evident that the presence of a fourth ramp has taken over the flow physics and the nature of flow showing significant downstream impact on all separation physics and bubble behaviour at the first and second junctions. Fig. 6.7 shows a diffused bubble at the first junction mainly attributed to the downstream effects and the presence of a strong bubble at the third junction. The effects of the turbulent shear and shocks downstream are causing early separation for higher Mach flows and a weaker bubble as is almost tending to skip this junction with a late reattachment. This can also be seen in all the skin friction plots of Fig. 6.8, where the bubble at the third junction is compact and strong while the bubble is weaker and less intense at the first junction.

Fig. 6.9 and 6.10 are plots with higher quad ramp angle of 12.5^0, where it is more than certain that the downstream effects of this configuration has significant effects on the flow behaviour at various junctions of the model, especially for higher third ramp angles, where the intensity of bubble at both second and third junctions are stronger with highly turbulent shear boundary layer effects moving

downstream resulting in a highly diffused bubble at the first junction and the diffusion is even more prominent for higher freestream Mach.

6.2 SUMMARY

In this chapter, numerical simulations are carried out to study the effects of adding a fourth ramp to the earlier considered three ramp configurations. From the simulation studies, the separation bubble for 5^0 ramp angles is almost negligible in size indicating that it is not a fully separated flow whereas, the bubble sizes increase with higher ramp angles beyond 7.5^0 as per earlier studies, proving the incipient separation theory.

From the surface pressure distribution is understood that, when the fourth ramp angle is higher than the third ramp angle the reattachment shock at the second junction is relatively weaker when compared to the reattachment at the third junction, at the same time the separation and reattachment shocks seem to become weaker at the first junction indicating significant downstream effects of a larger fourth ramp.

The investigations done in this chapter indicate that complex junctions have very unpredictable flow natures and may not follow every correlation that proves well for a simple double ramp configuration, encouraging the need for detailed and in-depth experimental studies to clearly understand flow physics when design scenarios lead to such complex multi-ramp junctions.

CHAPTER 7. EXPERIMENTAL INVESTIGATION

7.1 ABOUT THE INSTITUTE

The Indian Institute of Science was started in 1909 through the pioneering vision of Sri J N Tata. Since then, it has grown into a premier institute for research and advanced instruction. IISc is one of the oldest and finest centres of its kind in India. The institution has a uniqueness in its characteristics, this is because it is neither a national laboratory nor a conventional university. The institution is concerned with both research education [47]. The department of Aerospace Engineering was started in 1942. It is the second oldest department in the institute. With the onset of World War II, the factory setup at HAL was used for assembly and repair of airplanes. This necessitated the establishment of Aerospace Department in the country [48]. Dr.APJ Abdul Kalam started the CFD centre at IISc, after two scientists Prof S M Deshpande and Dr. P S Kulkarni started CFD project with Defence Research and Development Laboratories (DRDL) on supersonic flow computation for a missile configuration. Later the DRDL and the CFD department developed a code BHEEMA (Boltzmann Hypersonic Euler Equation for Missile Aerodynamics). This project was carried out at the CFD Centre in IISc, Bangalore. The Computational Mechanics Lab (CML) at the Aerospace Engineering Department was used for the Numerical Analysis of this research. A Supermicro Server 8046-6RF and Dell Optiplex workstation was used for all the CFD simulations using legal software version of HiFUN. All the experimental blowdowns were performed in the High-Speed Wind Tunnel Complex under the guidance of Prof. B Vasudevan and Dr. Duvvuri Subrahmanyam.

7.1.1 HIGH SPEED WIND TUNNEL COMPLEX

The complex has evolved over seven decades starting in the year 1942, when the department of aeronautical engineering was established. During the 50's, a high-speed aerodynamics laboratory, first of its kind in India was set up in the department. Several open-circuit and closed-circuit wind tunnels working in the Mach number range of 1.15 to 4 were set up. The major open-circuit supersonic tunnels had test section sizes of 2"X1", 3"X1" and 5"X7" while the closed-circuit tunnel had a test section size of 4"X1". All these facilities were using a common high-pressure air storage vessel (35m^3) pressurized to 300psi using a multi-stage, water-cooled reciprocating air compressor. These facilities were effectively used by over two generations of doctoral and master's students at the department. Only the 5"X7" facility is still functional and presently used with colour Schlieren, ESP scanners and miniature strain gauge balances. The facility is currently working on the 'Induction' mode with a run time of about 60 seconds [49].

In the mid-seventies, work on a pilot hypersonic wind tunnel of size 200mm was started with funding from AR&DB. The facility became functional in 1985 and has been continuously generating hypersonic aerodynamic design data for several national programs. So far, a total of about 80

aerodynamic testing projects have been completed with over 27000 blow downs being conducted in the facility. In the early 90's, the tunnel was upgraded to 300mm, enclosed free-jet facility. The major equipment in the facility included a pair of Norwalk (USA), 5 stage, water-cooled, 140bar reciprocating air compressor, a set of two multi-layered air storage vessels with a total volume of 20m^3 and the technology for the same was provided by M/S Nooker, USA. There was also a high pressure (70bar), high temperature (850K) pebble bed heat exchanger and large vacuum tanks with associated vacuum pumps [49].

Fig. 7.1. High Speed Wind Tunnel Complex (Courtesy: https://connect.iisc.ac.in/)
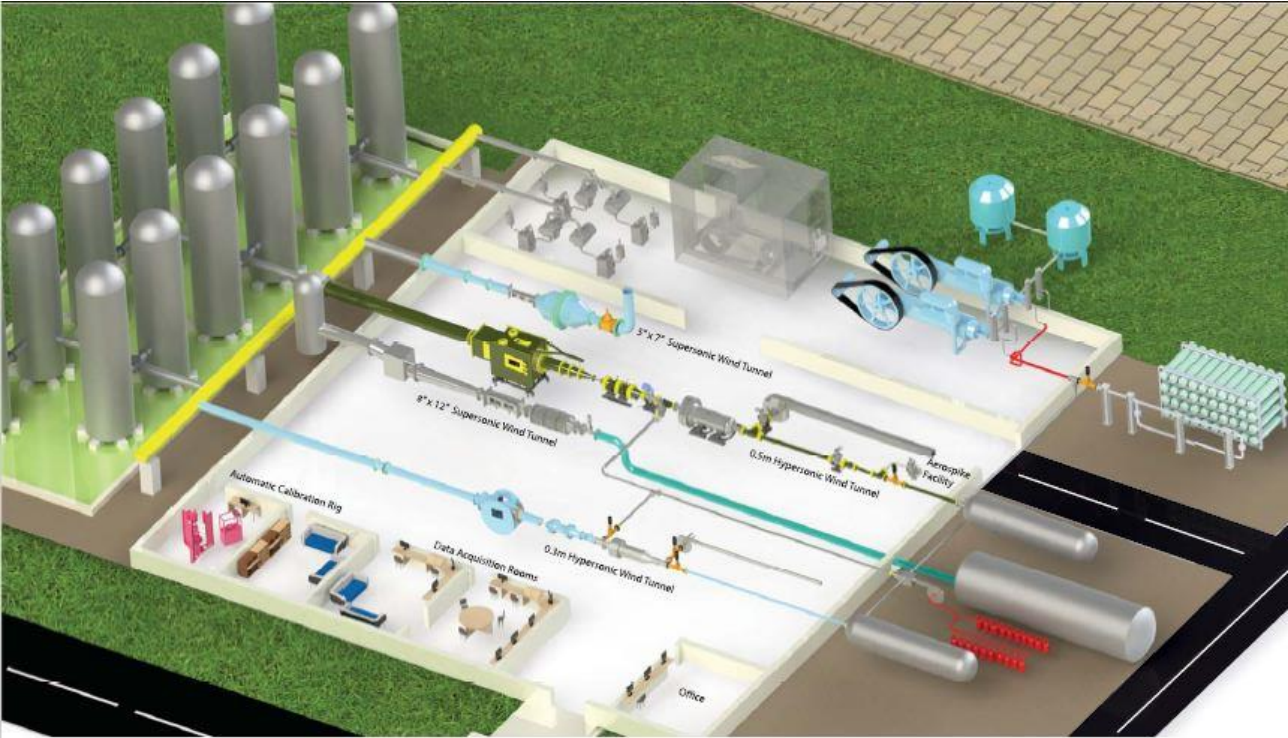
Fig. 7.2. High Speed Wind Tunnel Complex Overview (Courtesy: HSWTC Brochure)

Automatic Balance Calibration Rig:

The calibration rig was indigenously designed, developed and built internally. It has the capability of Max force 2000 N and a Max. moment of 300N. The maximum balance length is 450mm and diameter of less than 50mm. Hydraulic actuators are used for loan application with compact load cells designed in IISc. Balance repositioning system is used for model loading with the help of 5 Panasonic servomotors and Sensotec LVDT's to give position feedback. Typical calibration type is 3 hrs for 27 x 6 matrix [49].

Fig. 7.3. Automatic Balance Calibration Rig (Courtesy: HSWTC Brochure)

Compressors:

The compressor is a 5-stage water-cooled system with suction capacity of 250 cfm, powered by 125 HP, 3 phase electric motor working at 750 rpm with 140 bar discharge pressure. The compressors are provided with a pair of silica gel driers with dew point of 228K and safety relief valves at each stage. The second compressor is of 245 cfm again a 5 stage, air-cooled system powered by 132KW electric motor and a discharge pressure of 180K [49].

Fig. 7.4. Compressor (Courtesy: HSWTC Brochure)

Pressure Vessels:

The pressure vessels used are multi-layered M/S Burckhardt Compression which is first such vessel in India with a diameter of 1m, length 12m and storage volume of 10.8m^3 with a maximum working pressure of 140bar. It is a compact cascade assembly from M/S Nooker of USA. There are 40 cylinders with 250 litres capacity each with individual isolation valves for each cylinder and common 100mm outlet outlet manifold [49].

Fig. 7.5. Pressure Vessels (Courtesy: HSWTC Brochure)

Vacuum Tanks & Vacuum Pumps:

The facility has 12 cylindrical tanks of diameter 2m and height of about 7.5m vertically mounted, of which two are conventional tanks of 20mm wall thickness and 10 are thin-walled 6mm skin tanks, with a total vacuum volume of close to 300m^3 operating at vacuum pressure of 1 Torr. Four pairs of Vacuum pumps are present in the facility with two roots + rotary piston pumps powered by 10 HP AC Motors and two roots + rotary vane pumps powered by 7.5 HP AC motors. The pumps take about 90 minutes to evacuate 300m^3 to a few torr of vacuum [49].

Fig. 7.6. Vacuum Tanks and Vacuum Pumps (Courtesy: HSWTC Brochure)

Heating Systems:

The tunnels use pebble bed heaters mounted horizontally. The heater for 0.3m tunnel is designed for 70bar, 800K and the one used for 0.5m tunnel works upto 75bar, 850K. The auxiliary heating system has a capacity of 1MW which is LPG based with two high velocity burners of 500KW each. The flame control is through Honeywell electronics operating through exhaust blowers, completely insulated with ceramic blankets with SS outer body [49].
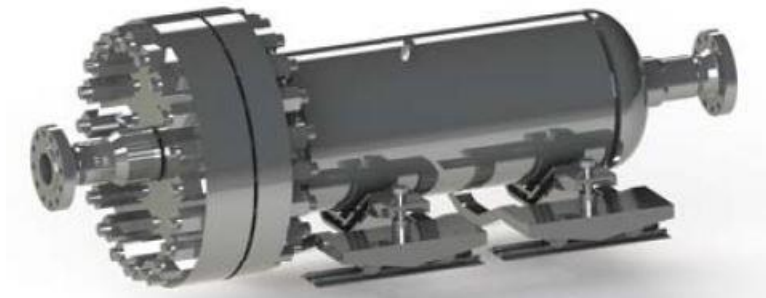
Fig. 7.7. Heat Exchanger (Courtesy: HSWTC Brochure)

Fig. 7.8. Auxilliary Heating system (Courtesy: HSWTC Brochure)

Model Incidence System:

Hydraulic servo systems are used for model incidence control and the injection time is about 1 sec using hydraulic actuators. The incidence can be varied between -6^0 to $+24^0$ with an angular accuracy of 0.1^0. The power pack uses 7.5/10HP vane pumps providing 12 litres/min oil flow at 70 bar [49].
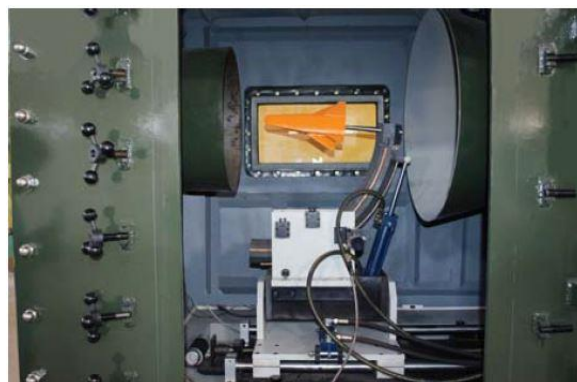
Fig. 7.9. Model Incidence System (Courtesy: HSWTC Brochure)

Plenum Chamber:

The tunnels in the facility use 12" cylindrical pressure vessels with 140 bar capacity. The 0.3m tunnel is provided with wide angle conical diffuser with thermal mixers and the 0.5m tunnel is twice as long with 3 additional screen meshes. Both the chambers have instrument ports to measure P_0 and T_o [49].

Fig. 7.10. Plenum Chamber (Courtesy: HSWTC Brochure)

Nozzle:

The tunnels in the facility use axi-symmetric contoured nozzles. The nozzle is 3.4m long for 0.5m tunnel and contours are corrected for boundary layers and are un-cooled. Throat section is made of 17-4-Ph material machined using CNC. The 0.3m tunnel have five nozzles to give Mach numbers of 5.4, 6.5, 7.0, 8.35 and 10 and the 0.5m tunnel has nozzles for Mach 6.0, 8.0 and 9.5 [49].

Fig. 7.11. Nozzle (Courtesy: HSWTC Brochure)

Instrumentation:

The instrumentation systems consist of several high speed digital data acquisition cards/ books with over 1mhz sampling rate with about 64 channels of A to D, 16 channels of D to A, 96 channels of DI/DO, counter-timers etc working with GUI software's like DASY LAB and LABVIEW modules. The facility also has signal conditioners from Vishay Instruments, USA and HBM, Germany. There are several conventional 6-component strain gauge balances and an automatic multi-component balance calibration rig which was designed, developed and built at IISc. The complex has several electronic pressure scanners in the range +/- 10" Hg to +/- 100psi, besides several individual pressure transducers in the range of 1.0psi to several 100 psi. Highly accurate conventional piezo-resistive transducers are available for precision measurement of pressures [49].

The facility complex is equipped with calibration equipment such as $6^{1/2}$-digit fluke multimeters, current/voltage calibrators, dead weight testers and vacuum leak detector units. There are several special equipment's such as colour-video Schlieren imaging systems, Infra-red thermography systems from FLIR and powerful La VIsion high speed, time-resolved PIV system for high speed flows in the complex [49].
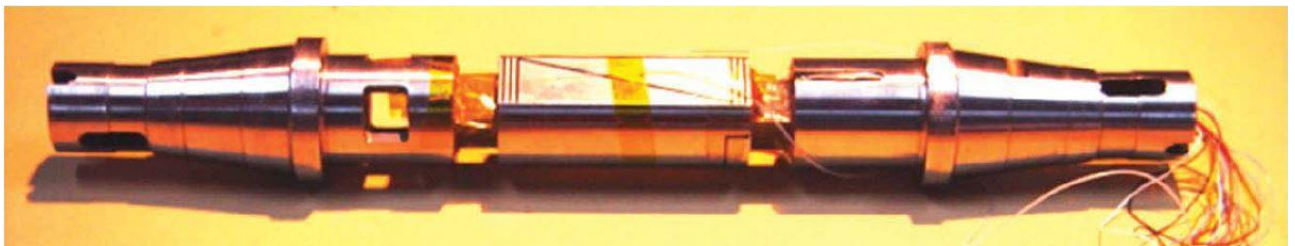
Fig. 7.12. First Fiber Optic Wind Tunnel Balance developed at IISc (Courtesy: HSWTC Brochure)

DAC	Pressure Transducers & ESP scanners	IR Camera with Germanium Window
High Speed time resolved PIV System	Different Balances designed & developed in IISc	Blowdown Control Board developed in IISc
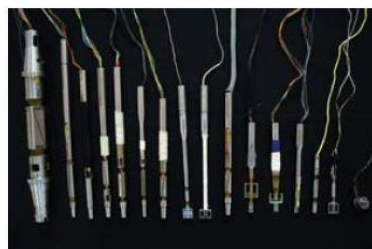
Fig. 7.13. Instrumentations (Courtesy: HSWTC Brochure)

7.1.2   0.5m HYPERSONIC WIND TUNNEL

All the experiments for this research are performed in the 0.5m Hypersonic Wind Tunnel facility at the High-speed wind tunnel complex. It is a pressure-vacuum intermittent blowdown type wind tunnel with an enclosed free-jet size of 0.5m diameter. The wind tunnel is fitted with contoured axi-symmetric nozzle and the test duration is 10 seconds. The Reynolds number range is between 1.15×10^6 to 4.15×10^7 based on jet diameter. The maximum stagnation pressure that the tunnel can attain is 100 bar and the maximum temperature is 850K, through a 1MW LPG based heating system. Air cooled reciprocating compressor with acoustic canopy of capacity 411Nm^3/hr is used and high-pressure air driers with dew point of 180 K. Colour schlieren flow visualisation system with 300mm light beam is used to capture the flow and shock structure. Data acquisition is done through 16-bit DAQ at 1M Sample/sec [49].

Fig. 7.14. 0.5m Hypersonic Wind Tunnel (Courtesy: HSWTC Brochure)

7.2   VALIDATION AND CALIBERATION
7.2.1   EXPERIMENT AND SOLVER VALIDATION

Validation studies are performed prior to the actual experimentation to ensure that the CFD software in this case HiFUN can predict the experimental physics accurately. The validation simulations are performed on two models as seen in Fig. 7.15 and Fig. 7.16, the experimental runs of the same were performed in the 0.5m Hypersonic Wind tunnel. The experiments were performed at a freestream Mach of 6, with freestream pressure (P_∞) and temperature (T_∞) being 108psig and 411K respectively, the viscosity (μ) is calculated to be 23.31×10^{-6} Pa-s and the thermal conductivity (k) is calculated as 0.0317 W/mK. The solver validation is to decide upon the best-fit methodology that can predict the experimental results well. To fix the methodology it is very important to decide the right mesh so that the results are independent of the grid and to find the right solver setting. From the

experience of all the previous simulations performed for this research work, the overall boundary and solver conditions were set, but it was required to find the right amount boundary layer resolution to capture the separation and reattachment points accurately for this specific experimental case and also
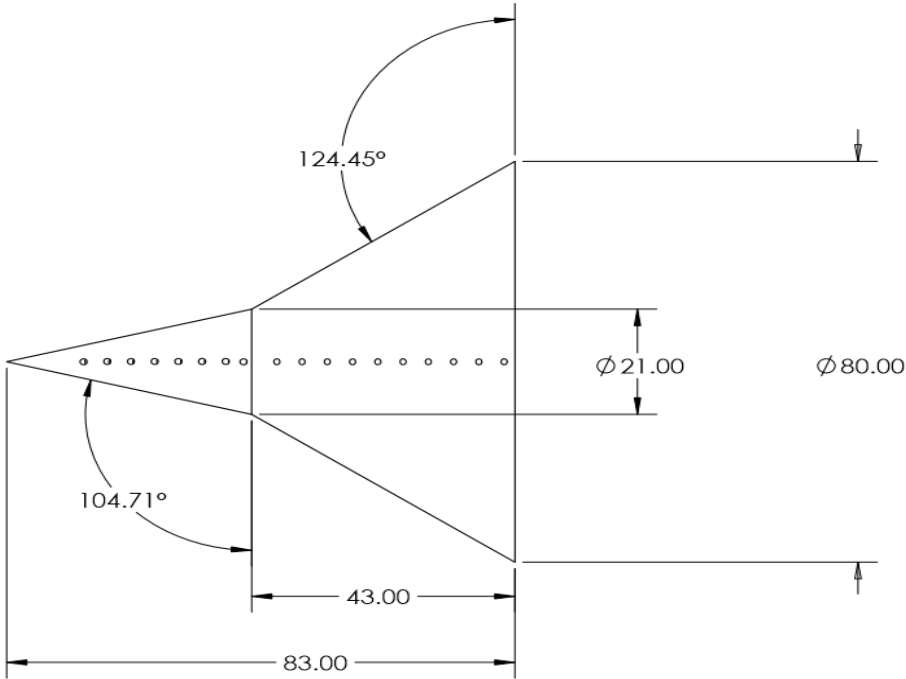
consideration of laminar and turbulent solver conditions.

Fig. 7.15. Model A: Double Ramp Cone
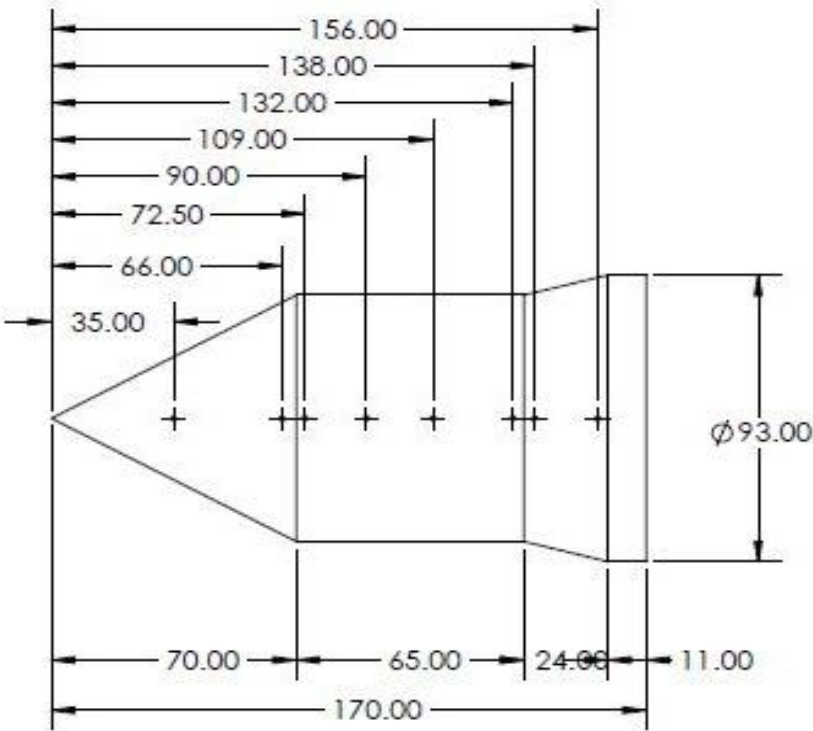
Fig. 7.16. Model B: Staggered Ramp Configuration

The validation outcomes are as shown in Fig. 7.17 for Model A and Fig. 7.18 for Model B. From Fig. 7.17 it is evident that all CFD simulations are overpredicting the peak pressures at the ramp junction where the bubble is located. This overprediction in pressure is purely attributed to the complexity of the separation bubble present at the compression corner, wherein the experimental physics shows a more diffusive nature of the bubble which can be noticed by the flattening at the peak, while the CFD simulations show a peak with immediate drop in pressure post attachment. The diffusivity in experiment can be attributed to multiple reasons, one for certain is because of the surface roughness identified on the experimental model causing boundary layer turbulence, diffusing the shock strength at the compression corner due to downstream effects of the shear. The surface roughness might also increase the entropy layer thickness, immersing the boundary layer within it reducing the separation bubble intensity.

From all the earlier studies the CFD tool is well validated and hence these overpredictions are considered as close to real physics while the experimental behaviour is attributed to surface finish of the model. The pressure predictions post reattachment is again high for CFD simulation mainly because of the peak pressure at the separation region, while the peak pressure in case of experiment is low, this difference in peak pressure is reflecting downstream. The separation and reattachment points are predicted very well in case of laminar flow conditions, while the turbulent solver condition is predicting the separation much earlier when compared to the experiment, this could be because the software is amplifying the downstream effects of the turbulent shear that is traveling from the post reattachment region. The nature of prediction does not seem to change with change in boundary layer treatment in case of turbulent flow, but a significant change can be seen in case of laminar flow setup.

The mesh with 30-micron first node distance is predicting lesser peak pressure at the separation and the pressure post reattachment in this case is much closer to the experiment. Though the peak pressures predicted by 30-micron mesh is closer to experiment, the reattachment point location is underpredicted, which is very critical for the current research work as it involves multi-ramp configurations. The 30-micron mesh also underpredicts the pressure at the first cone surface confirming that the boundary layer physics is not well captured. Between the 10 micron and 3-micron first mesh spacing there is no noticeable difference in the CFD results, and hence 10-micron mesh is chosen for all further investigations and experimental validations. For the validation of Model-B, the mesh with 10-micron spacing and laminar flow condition setup is considered based on earlier validation studies. As can be seen from Fig. 7.18, the peak pressures are predicted very well by CFD solver at the leading edge. There is very good match in the prediction of the pressure drop point which is at the flat region after the front cone, following by the prediction of the point where the pressure again increases which is the presence of the small ramp post the flat region. It can be noticed that the experiment result does not predict the pressure rise at the second deflection point, which is due to the erratic functioning of the pressure port at that location. With these two validation studies it is evident

that HiFUN solver is fully capable to capture complex high-speed flows with shock wave boundary layer interaction. From these validations, the mesh and the solver setting methodology has also been derived for all future considerations concerning this research investigation.
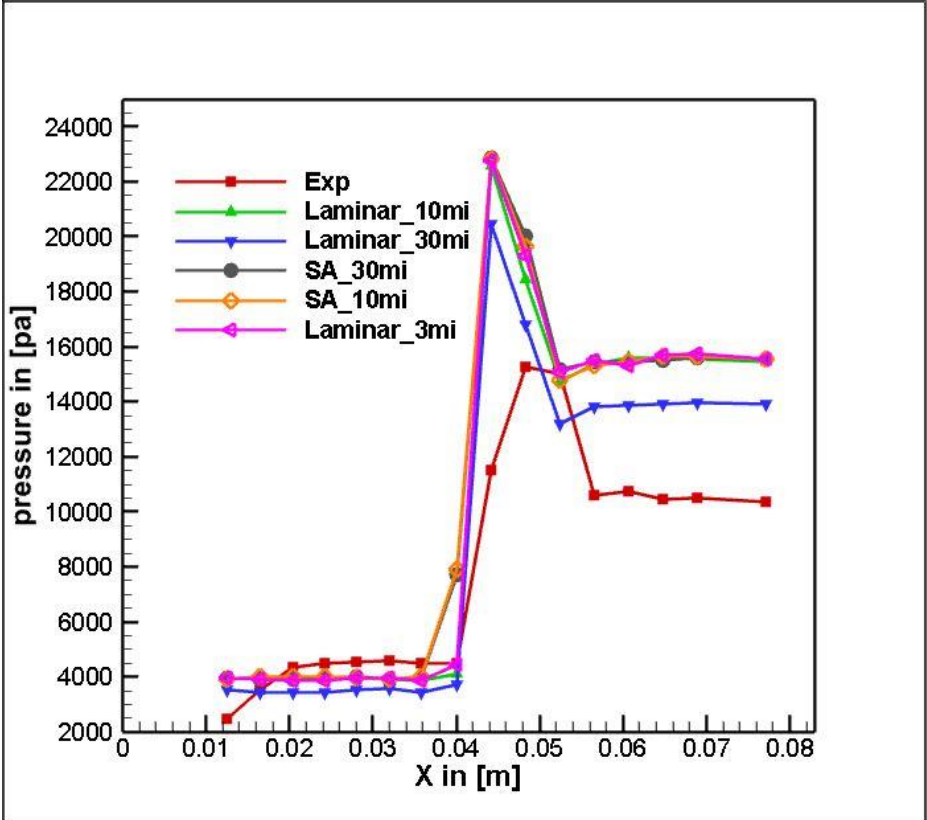
Fig. 7.17. Model A: Surface Pressure Validation
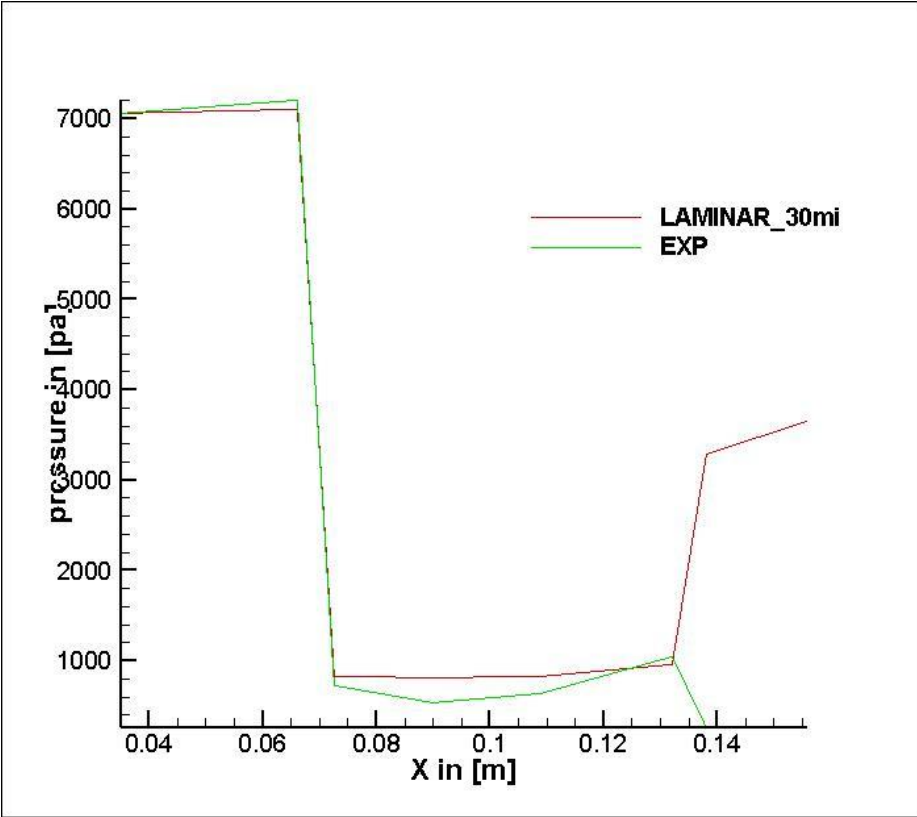
Fig. 7.18. Model B: Surface Pressure Validation

7.2.2 INSTRUMENT CALIBERATION

The 16-port data acquisition system must undergo a sequence of calibration to ensure the voltage reading are converted accurately to pressure readings. Initially the U-tube manometers are calibrated through manual procedure using simple hand-held bellow. The Max and min reading from the manometer for a given input pressure is recorded and the difference in the limb readings are calculated and converted to actual pressure felt in PSI. The difference in pressure is because constant and accurate pressure cannot be maintained using the hand-bellow. This initial manometer calibration details are given in Table. 7.1. Once the manometer is calibrated and the actual pressures are identified, all the 16-ports are then tested with these calibrated pressure readings to find the voltage readings at the ESP scanner corresponding to these pressure values at every port. The ESP port generates multiple sets of data based on time for the duration of the run at every port. The values of the data sets are averaged, and corresponding voltage value is noted for evert port pressure condition. Once the average voltage values for corresponding pressure at each port is identified, the values are plotted against an ideal curve to check deviation in data set and to verify the functioning of the ports. From this calibration it was identified that Port 2 and Port 8 are erratic and shall not be used for the experimental blowdowns. The U-tube manometer again undergoes another round of calibration check after the run. The post run manometer readings are given in Table 7.2. All the port calibration plots are given in Fig. 7.1.

Pressure (psi)	Manometer Readings		Difference	Difference	Actual Pressure
	cm of Hg		cm of Hg	mm of Hg	(psi)
0	40	40	0	0	0
0.2	39.4	40.5	1.1	11	0.2127048
0.4	38.7	40.9	2.2	22	0.4254096
0.6	38.2	41.5	3.3	33	0.6381144
0.8	37.6	42.2	4.6	46	0.8894928
1	37	42.7	5.7	57	1.1021976
1.2	36.6	43.2	6.6	66	1.2762288
1.4	36	43.7	7.7	77	1.4889336
1.6	34.9	44.3	9.4	94	1.8176592
1.8	34.8	44.7	9.9	99	1.9143432
2	34.3	45.4	11.1	111	2.1463848
2.2	33.7	45.8	12.1	121	2.3397528
2.4	33.2	46.8	13.6	136	2.6298048
2.6	32.6	47	14.4	144	2.7844992
2.8	32.1	47.5	15.4	154	2.9778672
3	31.6	48.1	16.5	165	3.190572
4	28.8	50.7	21.9	219	4.2347592
5	26.1	53.5	27.4	274	5.2982832
6	23.5	55.9	32.4	324	6.2651232
7	20.7	58.7	38	380	7.347984
8	18.2	61.2	43	430	8.314824
9	15.5	63.8	48.3	483	9.3396744
10	12.7	66.4	53.7	537	10.3838616

Table 7.1. Pre-run Manometer Calibration
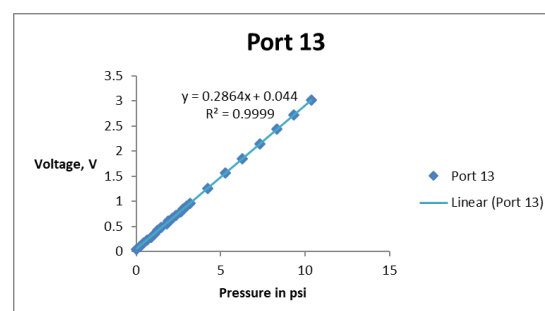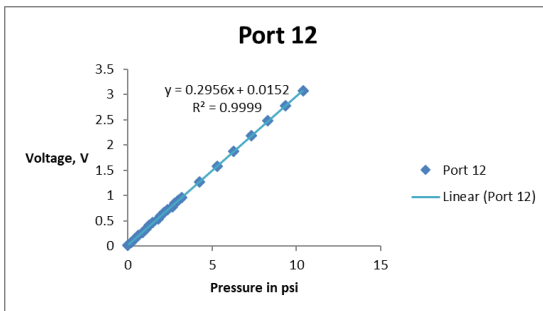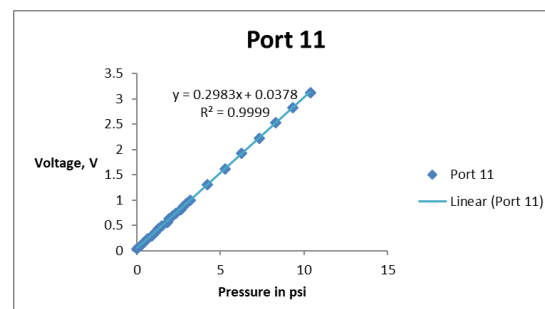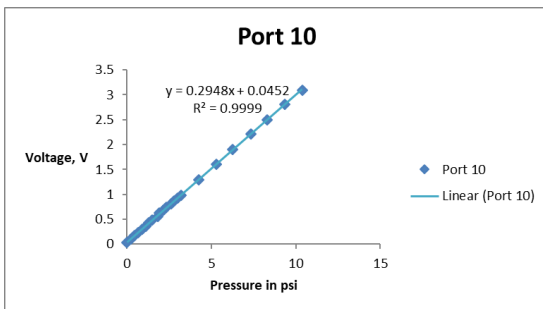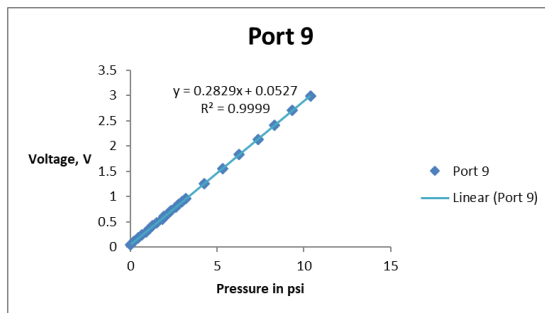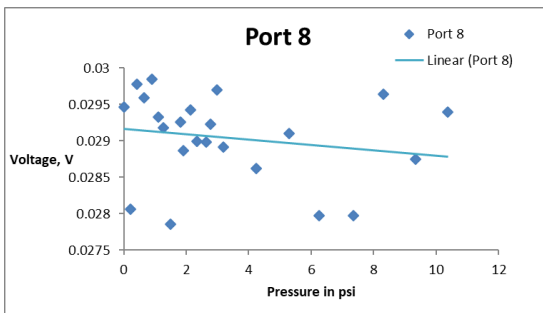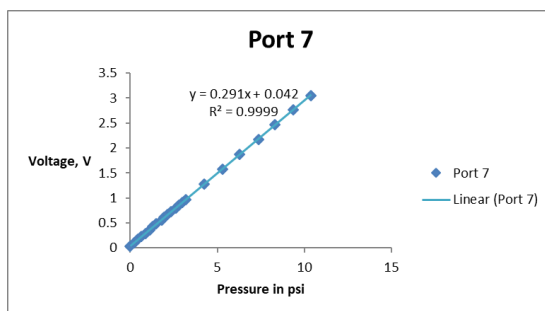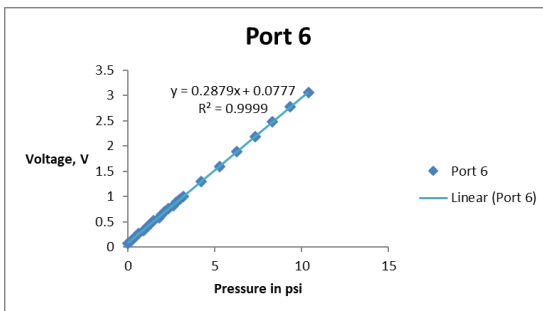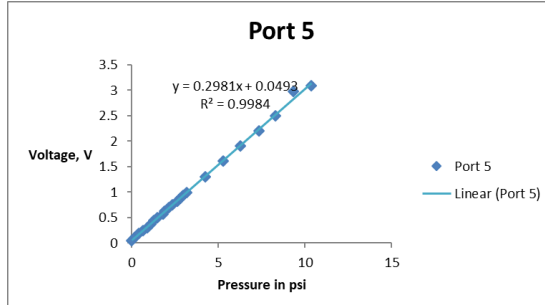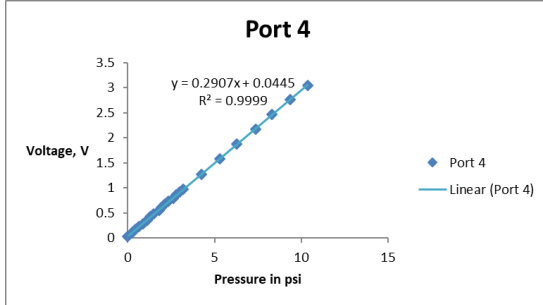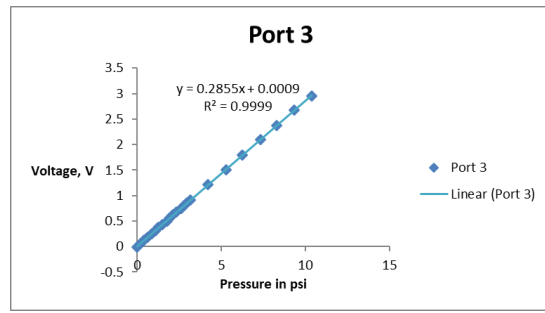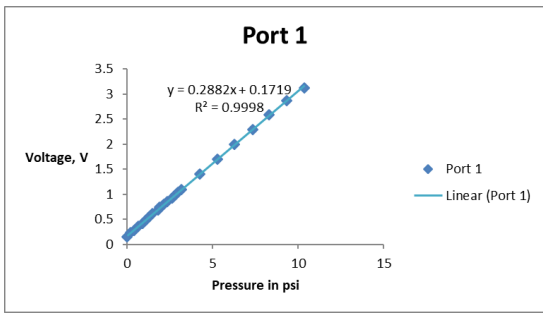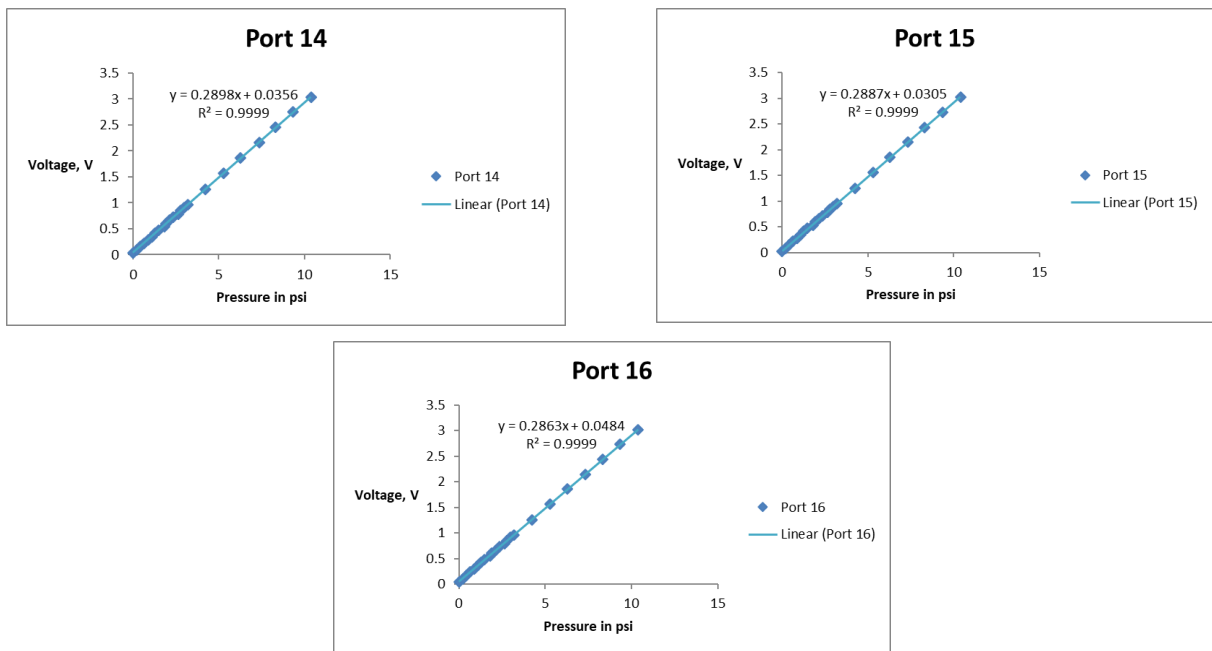
Fig. 7.19. Pressure Port Calibration Plots

Pressure (psi)	Manometer Readings		Difference	Difference	Actual Pressure
	cm of Hg		cm of Hg	mm of Hg	(psi)
0	40	40	0	0	0
0.2	39.8	40.3	0.5	5	0.096684
0.4	38.8	40.8	2	20	0.386736
0.6	38.3	41.5	3.2	32	0.6187776
0.8	37.6	42.2	4.6	46	0.8894928
1	37.1	42.7	5.6	56	1.0828608
1.2	36.6	43.2	6.6	66	1.2762288
1.4	36.1	43.7	7.6	76	1.4695968
1.6	35.4	44.3	8.9	89	1.7209752
1.8	34.8	44.7	9.9	99	1.9143432
2	34.4	45.3	10.9	109	2.1077112
2.2	33.8	45.8	12	120	2.320416
2.4	33.3	46.5	13.2	132	2.5524576
2.6	32.7	46.8	14.1	141	2.7264888
2.8	32.2	47.4	15.2	152	2.9391936
3	31.6	48	16.4	164	3.1712352
4	28.7	50.7	22	220	4.254096
5	26.2	53.3	27.1	271	5.2402728
6	23.5	55.8	32.3	323	6.2457864
7	20.8	58.6	37.8	378	7.3093104
8	18.2	61.2	43	430	8.314824
9	15.5	63.7	48.2	482	9.3203376
10	12.8	66.3	53.5	535	10.345188

Table 7.2. Manometer Calibration readings after blowdown

7.3 EXPERIMENTAL ANALYSIS

The experimental runs are performed in the 0.5m Hypersonic wind tunnel at freestream condition of Mach 6. All the experiments are performed after the experimental data validation as discussed in section 7.2.1 and the calibrations shown in section 7.2.2. Five models are chosen to perform the experimental analysis, four models are triple ramp configuration with varying third ramp angle of 7.5^0, 10^0, 12.5^0 and 15^0 and one model of quad ramp configuration with third ramp angle 7.5^0 and fourth ramp angle 12.5^0. The angles of the quad ramp configuration are chosen ensuring all angles are above incipient separation angles to capture the separation bubble and to capture downstream effects of higher fourth ramp angle. The model details of the triple ramp configurations are shown in Fig. 7.20, the first and second ramp angles and dimensions are maintained same as described by Savino et. al [2], and the third ramp angles are varied as shown. The pressure port locations and the corresponding ESP numbers are indicated in Table. 7.3. Quad ramp model details along with port locations are given in Fig. 7.21 and 7.22 respectively.
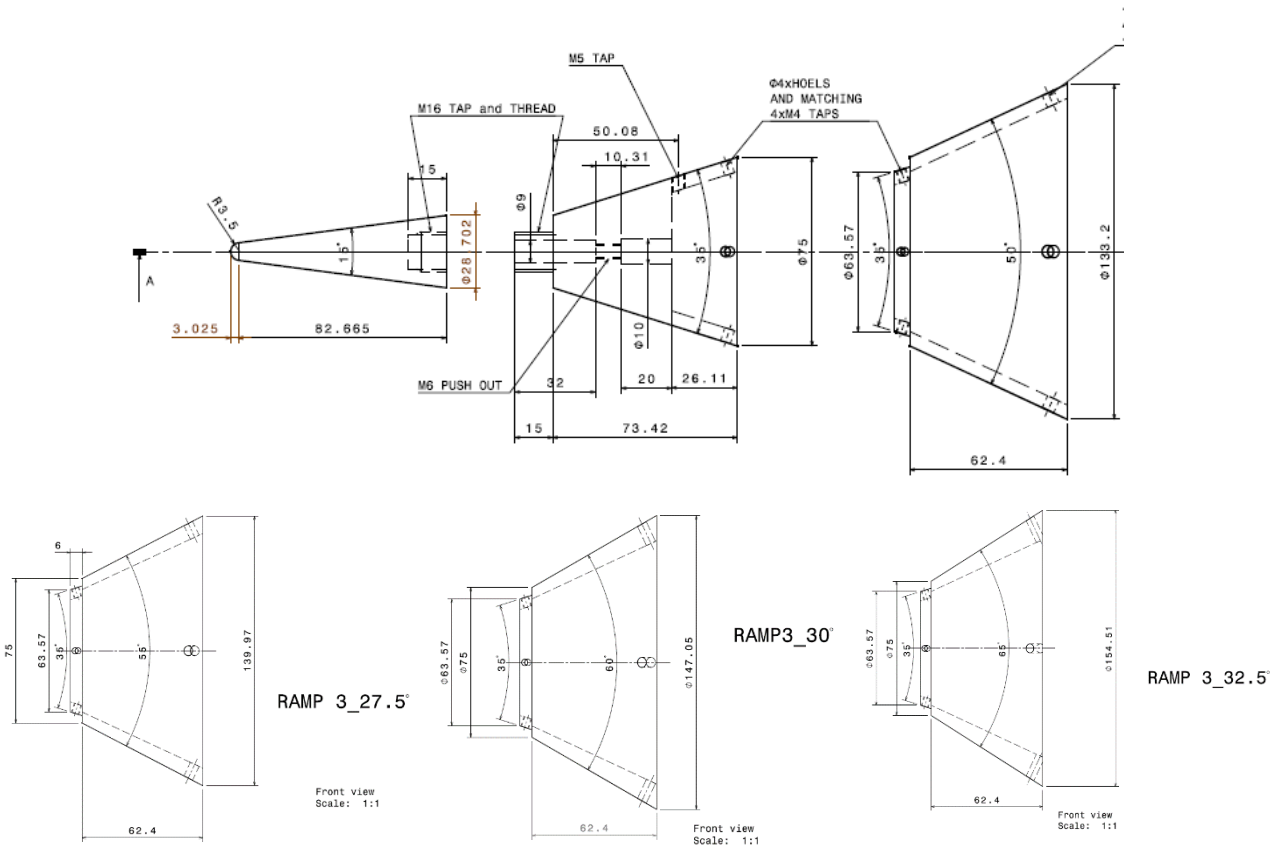
Fig. 7.20. Triple Ramp Model Details

Model Port	1	2	3	4	5	6	7
ESP Port	1	3	4	5	6	7	9
Location from the Leading Edge (in mm)	151	163	170	180	190	197	204

Table 7.3. Pressure Port Locations on Triple Ramp
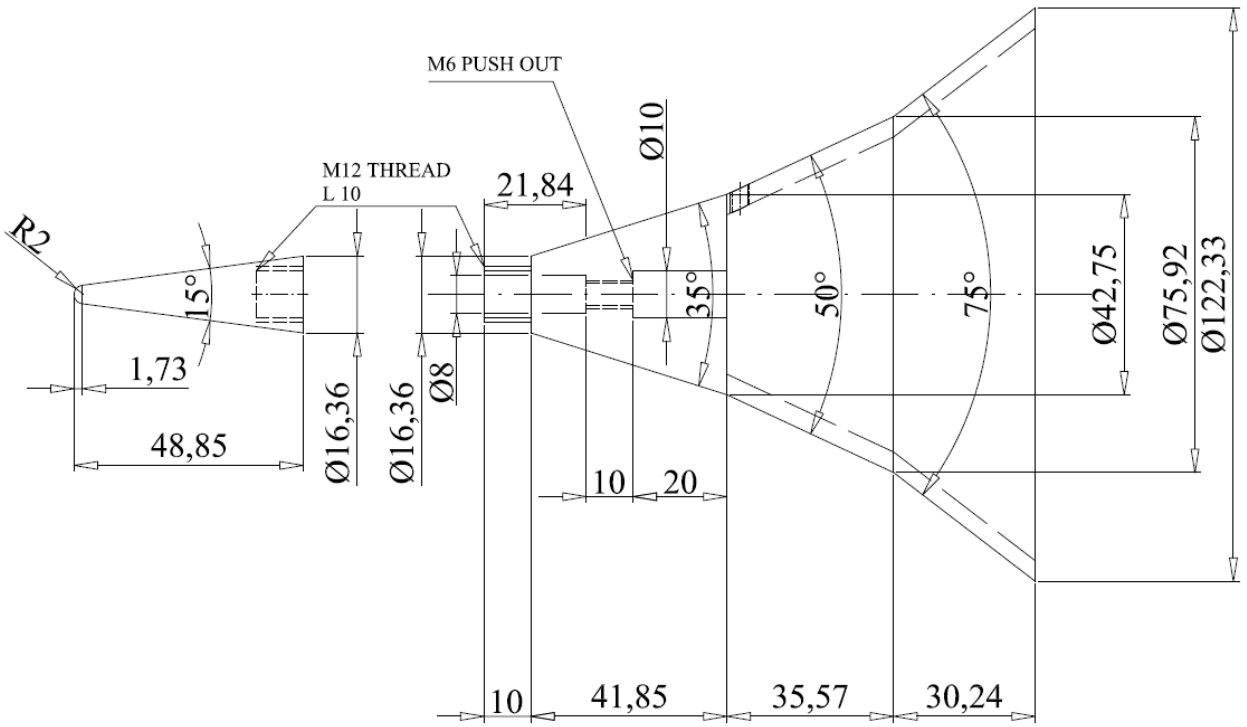
Fig. 7.21. Quad Ramp Model Details
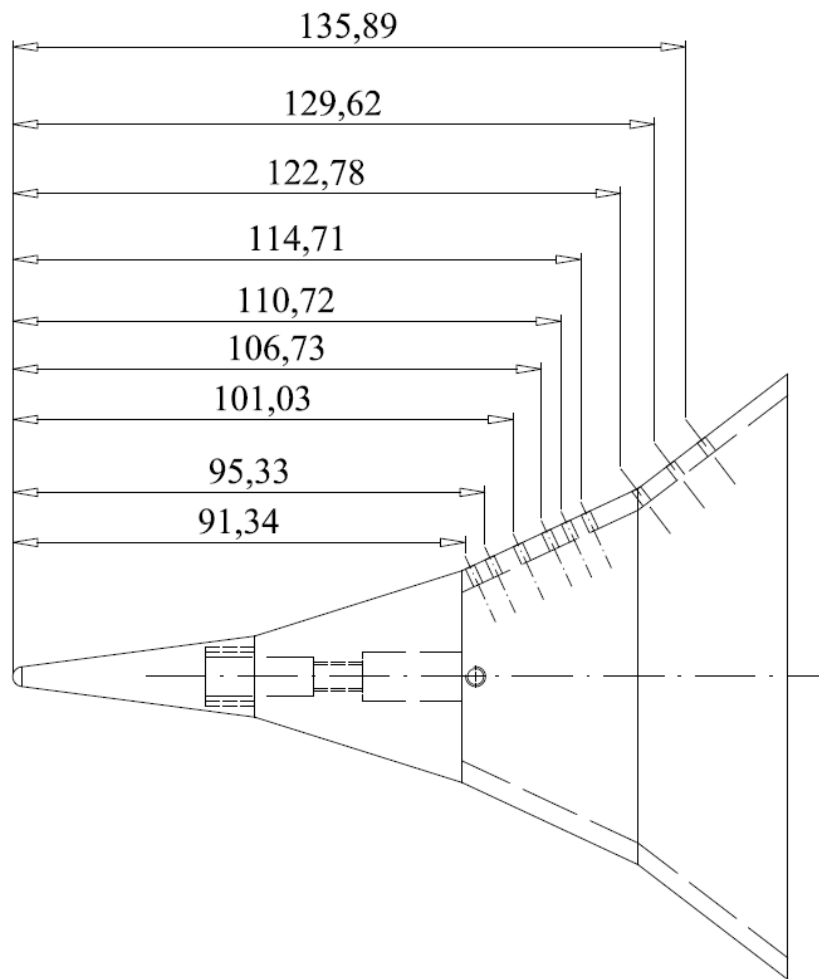
Fig. 7.22. Pressure Port locations of Quad Ramp

Fig. 7.23 to Fig. 7.26 shows both triple and quad ramp test models mounted in the test section with the pressure ports connected between the models and the ESP ports of the DAQ.
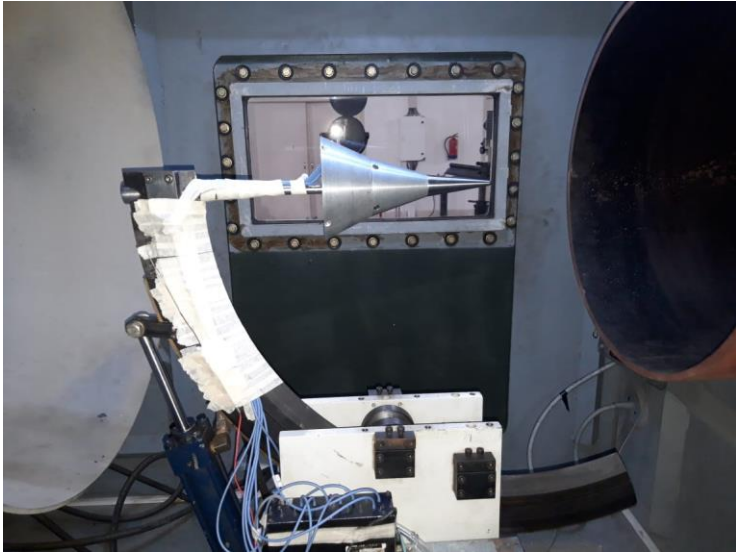
Fig. 7.23. Triple Ramp Model mounted in the test section
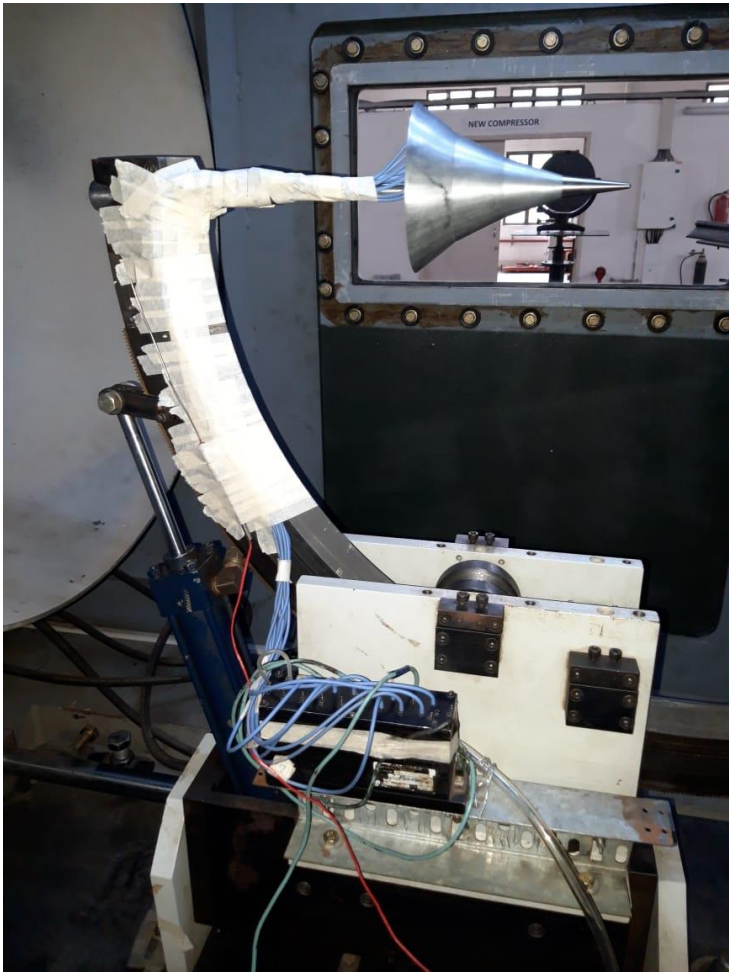
Fig. 7.24. Quad Ramp Model mounted in the test section
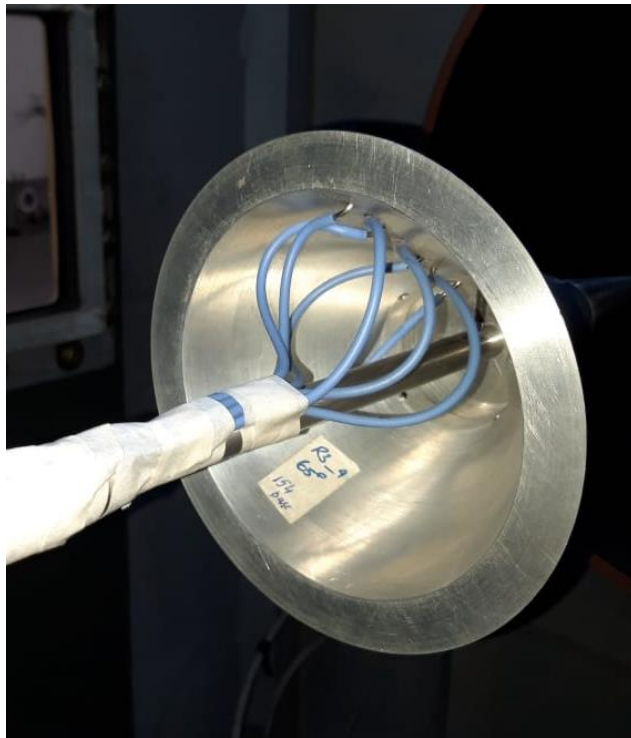
Fig. 7.25. Pressure Ports connected to the Model
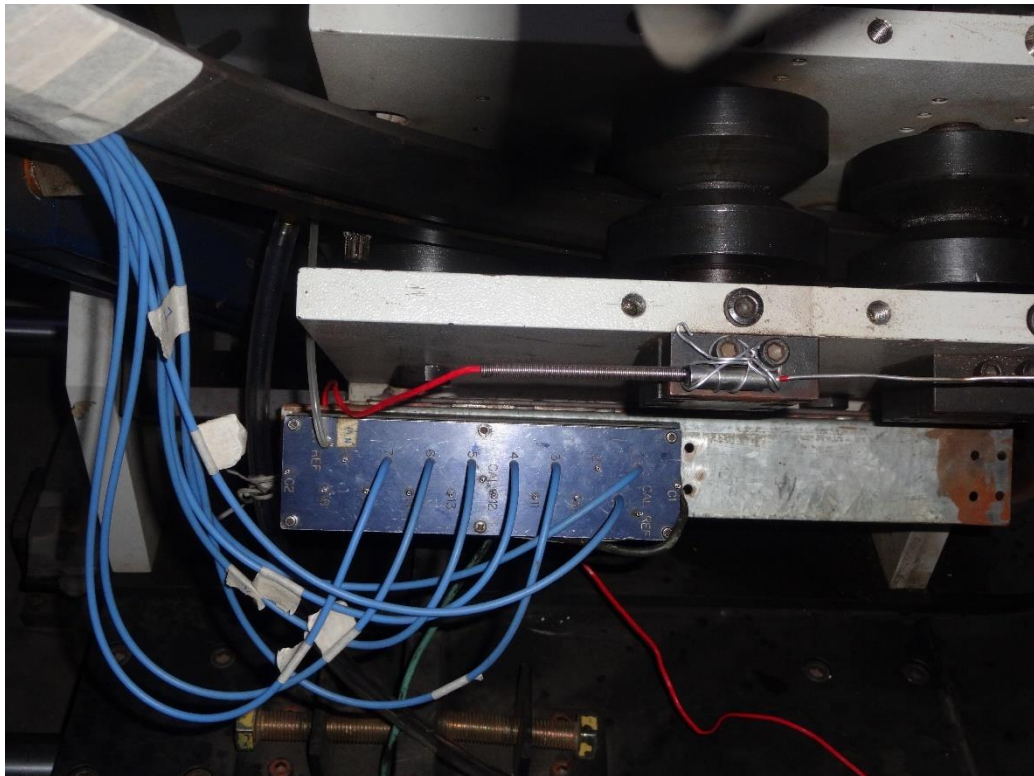
Fig. 7.26. Pressure ports connected to the ESP Ports

7.3.1 EXPERIMENTAL RESULTS

The operating conditions of each experimental blowdowns for different model configurations are given in Table 7.4. Same operating conditions are maintained for the CFD simulations as well. Fig. 7.27 is the surface pressure plot of triple ramp configuration with 7.5^0 third ramp angle. The pressure ports on the model is placed only after the second ramp and hence the experimental pressures are monitored only from the third ramp junction. From the figure it is seen that both the separation and reattachment points are predicted accurately through simulations, while there is a small difference in the pressure values between the experiment and CFD across all regions. This is mainly because of the complexity of flow, the experimental runs are highly transient in nature with fluctuations in the data acquisition occurring every second, it is possible that the averaged data from the pressure ports are predicting lesser pressure over time as the flow is past and the freestream pressure is reducing over time. Meanwhile, the CFD solver is set perfectly and has proven in multiple earlier occasions to be predicting these complex flows quite accurately. Hence these small variation in pressure can be majorly attributed to the continuous change in freestream characteristics which is getting reflected in the ESP. It is also noticed that the post shock region in the experiment is showing higher pressure values, this is due to the level of turbulence that is present in the flow and proves that the flow is highly turbulent and unstable. The CFD runs are performed in laminar conditions while the experimental outcomes indicate highly turbulent flow which can also be the reason for predicting higher pressure at the reattachment and the post shock region.
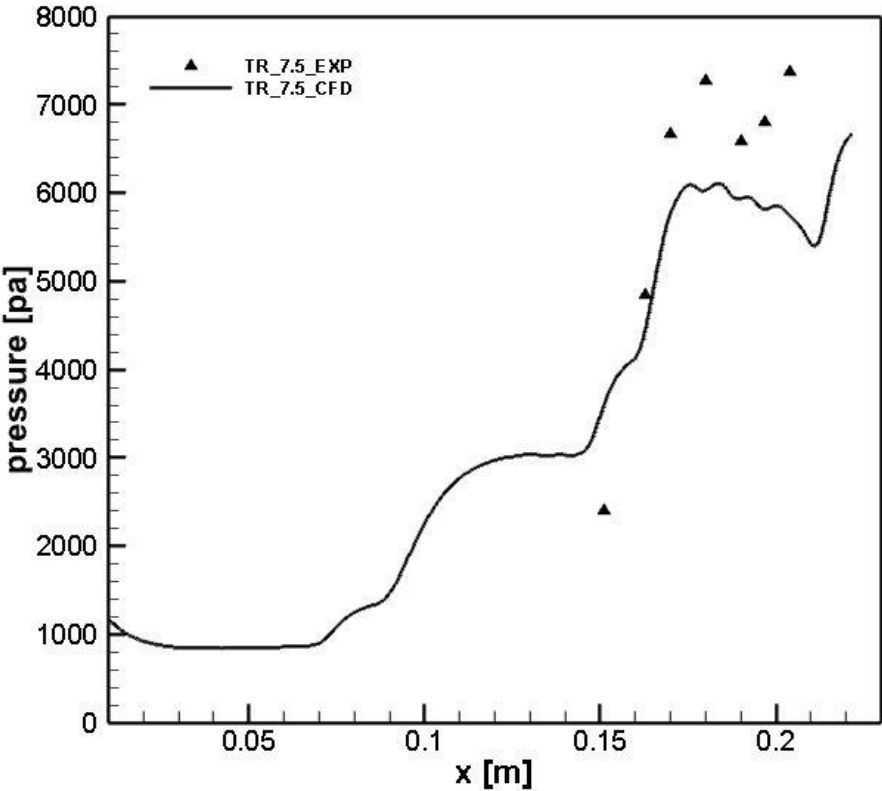
Fig. 7.27. Surface Pressure over triple ramp with 7.5^0 third ramp angle

Particulars	P_0 in psia	P_0 in pa	P_{stat} in pa	T_0 in K	T_{stat} in K	μ in pa-s	K in W/mK
QR	112.91	778487.046	493.0635599	438.33	53.45487805	3.47744E-06	0.004793222
TR_7.5	105.21	725397.415	459.4386427	445.44	54.32195122	3.54364E-06	0.00488447
TR_10	102.7	708091.57	448.4777904	399.61	48.73292683	3.11682E-06	0.004296152
TR_12.5	103.34	712504.219	451.2725915	420.3	51.25609756	3.30951E-06	0.004561757
TR_15	104.4	719812.66	455.9014751	411.69	50.20609756	3.22931E-06	0.004451215

Table 7.4. Experimental and CFD Operating Conditions

Fig. 7.28. Schlieren Image of Flow over triple ramp with 7.5^0 third ramp angle

Fig. 7.29.Schlieren with Surface pressure plot over triple ramp with 7.5^0 third ramp angle

The Schlieren image of the flow over triple ramp with 7.5^0 third ramp angle can be seen in Fig. 7.28 and Fig. 7.29 shows the surface pressure plot obtained through simulation study integrated with the schlieren image. This figure helps in understanding the separation locations predicted through CFD simulation as against the experimental separation points. Point A indicates the separation location at the first ramp junction which is in very good agreement with the separation location as seen in the schlieren, the separation shock is very faintly visible but it is certainly present very close to the location as predicted through simulation study. Point B indicates the separation point at the second junction, it is seen that the computationally predicted location is slightly underpredicted when compared to the experimental schlieren, this is certainly due to the turbulent reattachment experience post the re-attachment shock at the first ramp junction. Point C is the region from where a highly turbulent reattachment zone is identified post second junction and this is well validated through the schlieren, where multiple shock interactions are noticed which can be seen as dark patches, the dark patches are regions of high pressure zones which the surface pressure plots obtained through simulation also predicts accurately. The uneven peaks in the pressure plot might be indicating the multiple shock interactions and high levels of turbulence post the reattachment. The reattachment points at each junction are not directly validated as it is very difficult to accurately pinpoint this location due to multiple overlapping regions associated with flow, boundary and entropy layers.

The experimental and simulation results of flow over triple ramp with 10^0 third ramp angle is shown in Fig. 7.30. Very good validation can be noticed in terms of predicting the separation and reattachment points and in this case even the pressure predictions at both these locations are in good agreement with the experiment data. There is good agreement seen even in the post shock pressure rise region with slightly higher pressures predicted in the experimental runs, this again is due to the turbulent nature of the post reattachment region and the presence of a turbulent shear layer. The trends in the post reattachment region show good match with uneven pressure distribution attributed to turbulent shear and a dip in pressure due to expansion. This is good indicative that the CFD solver conditions are set precisely and can capture the complex flow physics over multi-ramp configurations. Fig. 7.31 is the schlieren image and Fig. 7.32 is the overlap between the schlieren and the surface pressure plot obtained through simulation run. Similar to earlier case, Points A and B indicate the separation shock locations at first and second junction respectively, whereas Point C indicates the turbulent reattachment and the shear region post the second junction. CFD simulations are in very good agreement in predicting the separation points at first and second junctions as seen in Fig. 7.32. It is also noticed that the turbulent shear region is moved upstream with increase in third ramp angle which can be seen located very close to the reattachment point at the second junction and to the junction itself. This makes the flow physics highly complex with evident upstream influence of the third ramp. The drop in surface pressure is due to the expansion fan which can be seen downstream to the second junction in the schlieren.

Fig. 7.30. Surface Pressure over triple ramp with 10^0 third ramp angle

Fig. 7.31. Schlieren Image of Flow over triple ramp with 10^0 third ramp angle
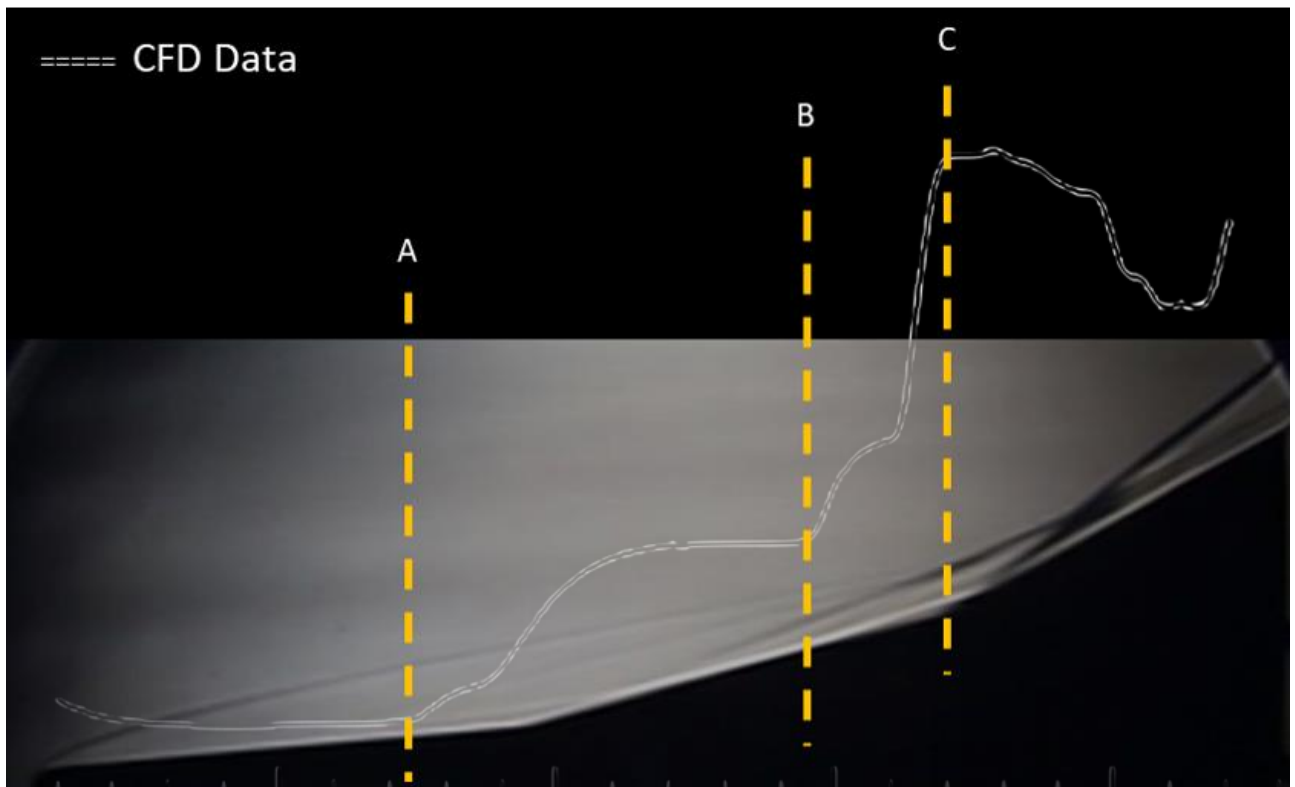
Fig. 7.32. Schlieren with Surface pressure plot over triple ramp with 10^0 third ramp angle

Surface pressures plots of triple ramp configurations with third ramp angle 12.5^0 and 15^0 are shown in Fig. 7.33 and Fig. 7.36 respectively. In both cases it is seen that the post shock reattachment regions are in good agreement with experimental data. In case of 12.5^0 the post shock region is showing typical pressure difference trends, attributed to the turbulent reattachment and shear region present in experimental conditions making the pressure values higher than that predicted in simulations, while in the case of 15^0 the post shock pressure trends are showing good match between experiment and CFD. The separation point predicted in CFD shows that the bubble size is large, and the separation point has moved upstream when compared to the earlier third ramp angles. This is due to the increase in third ramp angle which is having a considerable effect upstream on the flow forcing an early separation. From Fig. 7.27, 7.30, 7.33 and 7.36 it can be noticed that there is consistent upstream shift in the separation point indicating the influence of increase in ramp angles at the downstream location. It is also evident that the location of the pressure port is not exactly positioned at the separation point, which is very difficult to identify for each configuration. Machining difficulty is a major reason for not being able to position more pressure ports in the upstream locations of the junction. The port is positioned best for third ramp angle 10^0, whereas in all other cases either the port is located ahead of the separation point or is immersed into the bubble. Since the CFD solver has been proving to be accurate in all earlier sections, the separation locations can be considered to be predicted in accordance to the flow physics. The post reattachment region is consistently predicted in all ramp angle cases and is in good agreement with the trends because the CFD simulations are done with laminar conditions while it is evident that the flow is highly turbulent.
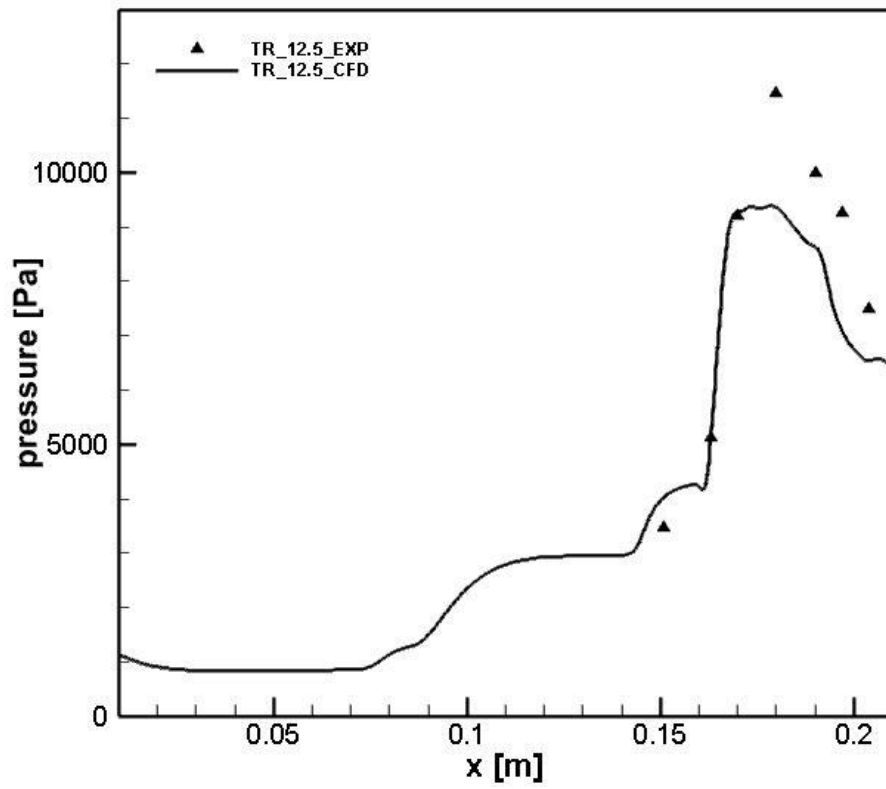
Fig. 7.33. Surface Pressure over triple ramp with 12.5^0 third ramp angle
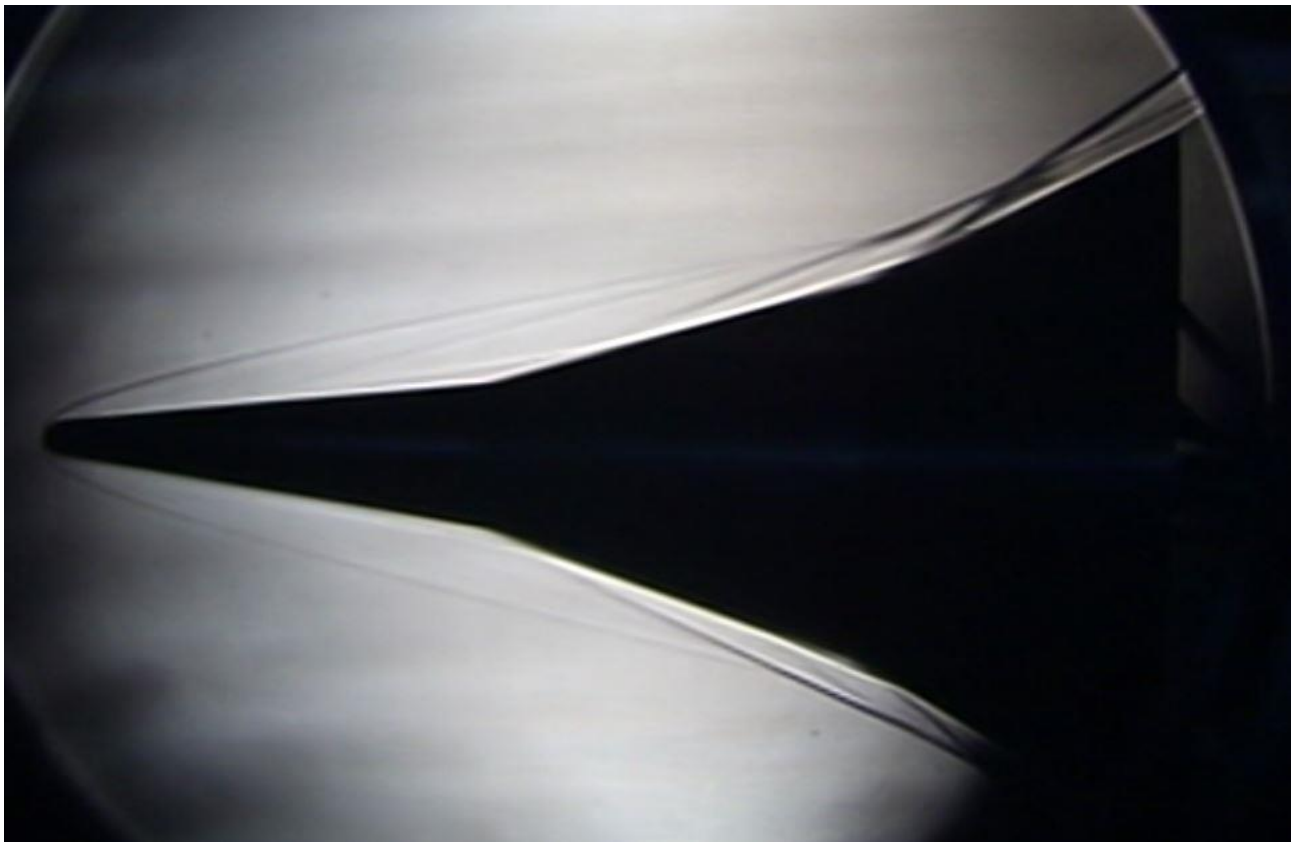
Fig. 7.34. Schlieren Image of Flow over triple ramp with 12.5^0 third ramp angle
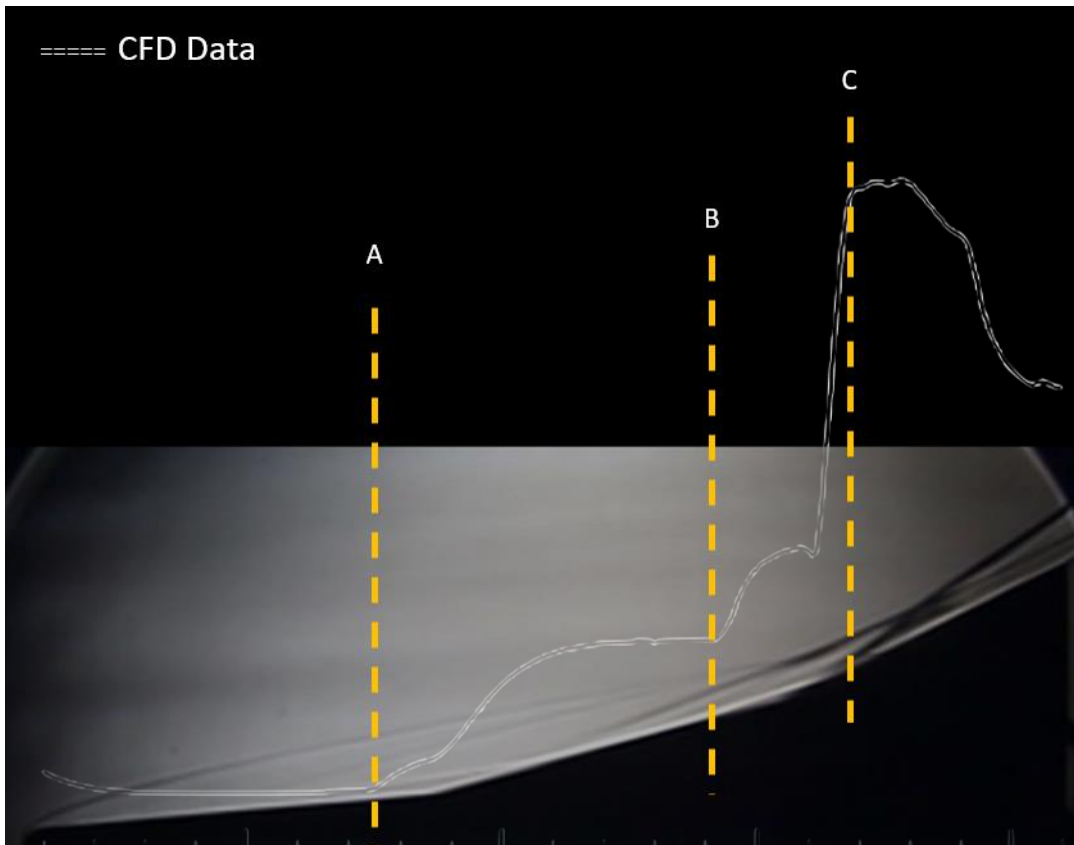
Fig. 7.35. Schlieren with Surface pressure plot over triple ramp with 12.5^0 third ramp angle
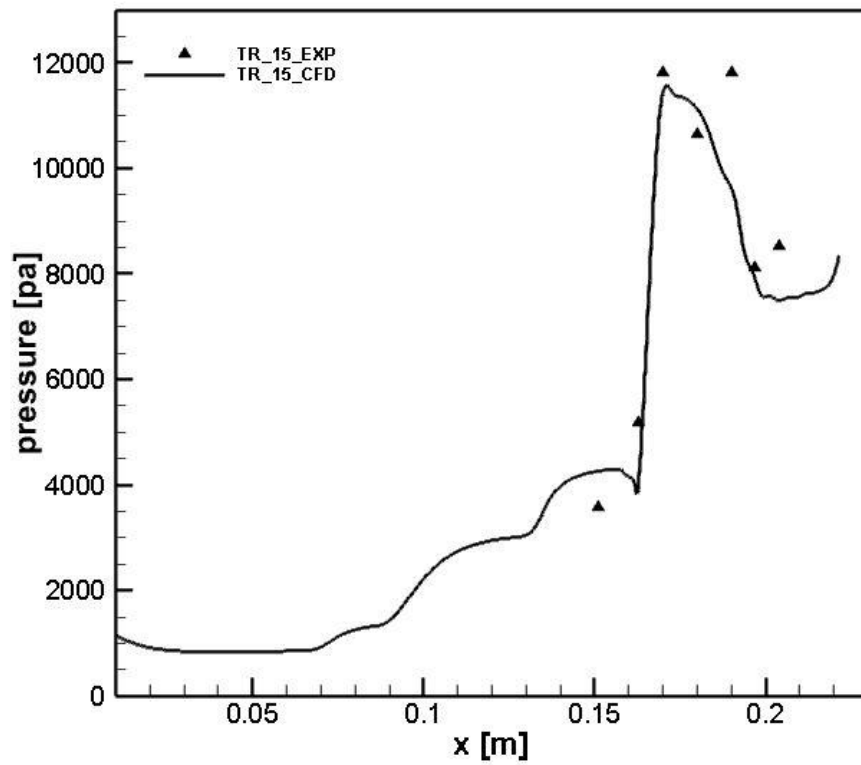
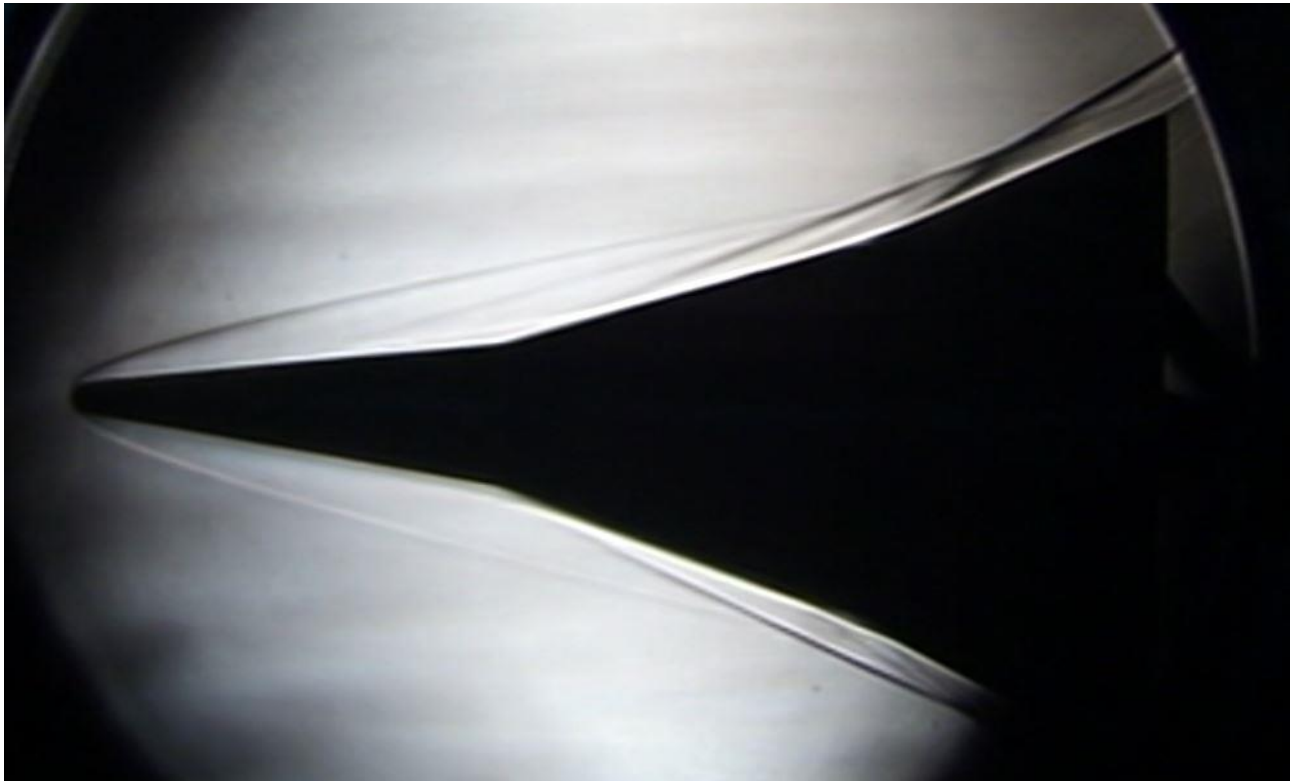Fig. 7.36. Surface Pressure over triple ramp with 15^0 third ramp angle

Fig. 7.37. Schlieren Image of Flow over triple ramp with 15^0 third ramp angle
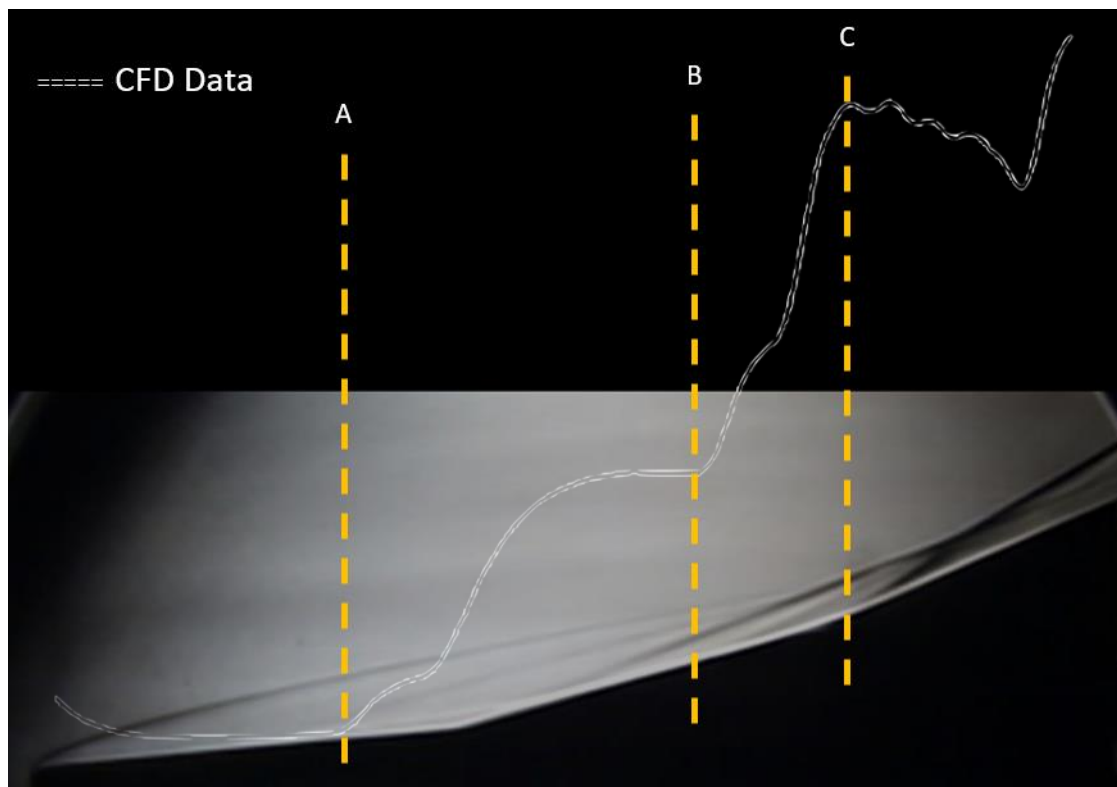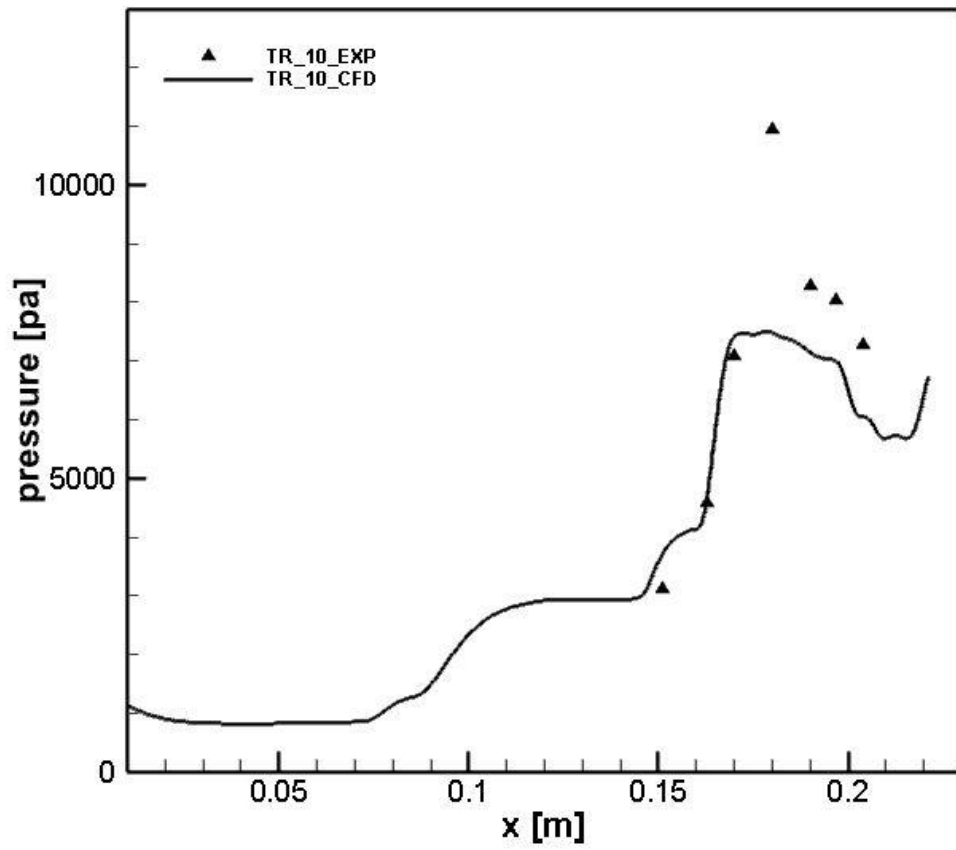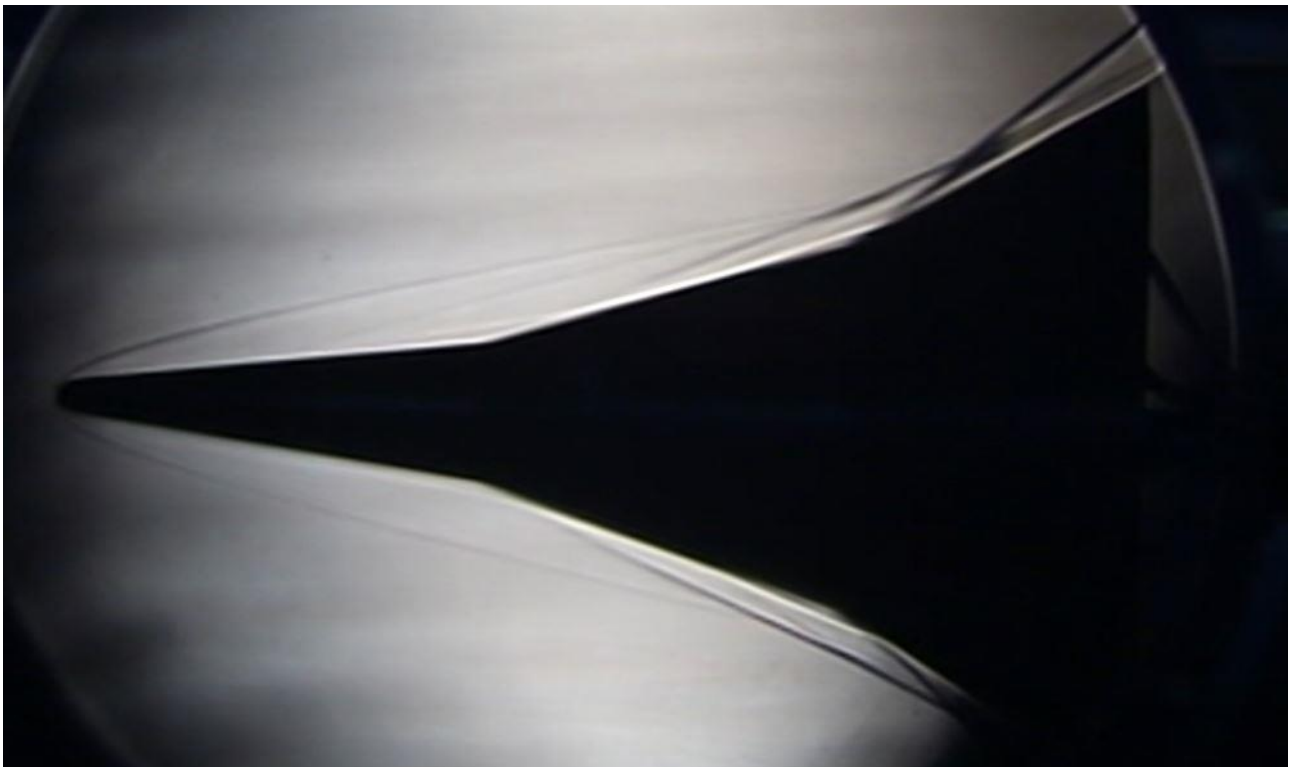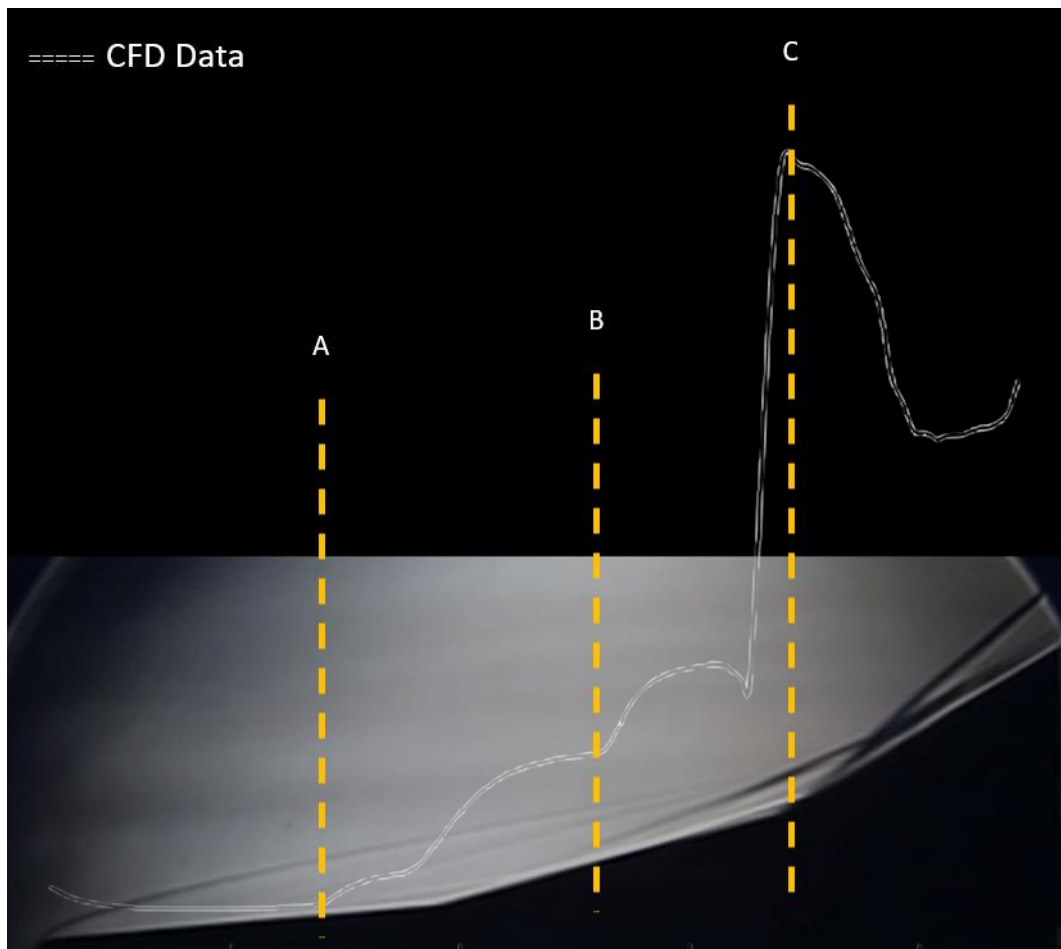

Fig. 7.38. Schlieren with Surface pressure plot over triple ramp with 15^0 third ramp angle

Schlieren image of flow over triple ramp with 12.5^0 third ramp angle and the combined view of schlieren and computational surface pressure plot are seen in Fig. 7.34 and 7.35 respectively. From Fig. 7.35 it is noticed that the size of the separation bubble at the second junction is increasing with increase in ramp angle as noticed in the computational studies, whereas the reattachment point and the turbulent shear region is moving upstream closer to the ramp junction which is represented by Point C. The separation bubble also seems to be diffused at the second junction, while the simulation results seem to predict the separation point downstream as compared to the schlieren, where it seems to separate slightly earlier. This mainly indicates a highly turbulent shear region present downstream which is influencing the flow nature at the ramp junction pushing the separation much ahead. This is a very important insight, where the presence of turbulence can further alter the separation points mainly due to the upstream flow of boundary layer shear. Fig. 7.37 and 7.38 are images corresponding to 15^0 third ramp angle, where the primary shows the schlieren image of the flow nature around triple ramp configuration with high third ramp angle, while the later gives a combined perspective of schlieren along with the surface pressure computed through simulation. From Fig. 7.38 it can be noticed that the location of Point C has moved upstream and very close to the ramp junction creating a very high pressure high turbulent reattachment, this can also be noticed as a pressure peak in the surface pressure plot. The separation point B has also moved upstream considerably, indicating very high influence of the presence of a higher angle third ramp. The upstream influence is felt even at the first junction with an upstream movement of the separation bubble.

Experimental run is performed over quad ramp configuration with 7.5^0 third ramp angle and 12.5^0 fourth ramp angle. All angles are considered above the incipient angle and the combination of third and fourth ramp angles are considered to study the upstream effects of higher turn angle at the fourth ramp. The pressure ports are places from the second junction downstream covering the separation and reattachment region of second junction, the post shock shear region, followed by the separation and reattachment at the third junction and then the post shock region. From Fig. 7.39 it is evident that there is very good agreement in the separation and reattachment point predictions at the third junction, the post reattachment region at the fourth ramp also shows good trend in capturing the pressure rise. Due to design constraints the pressure port could not be placed upstream of the second junction, but the port placed close to the second junction seems to be within the bubble region but can be seen predicting the separation point well. Due to complexity of the bubble region it is very difficult to capture the right pressure at this point with time. The pressure prediction post reattachment on the third ramp is seen to predict the trend well with increase in pressure again indicating a shear region post reattachment at the second junction. It is evident from the experimental predicts that the flow over such complex junctions can be highly turbulent with lot of boundary layer shear effects and upstream effects changing the flow nature over the surface.
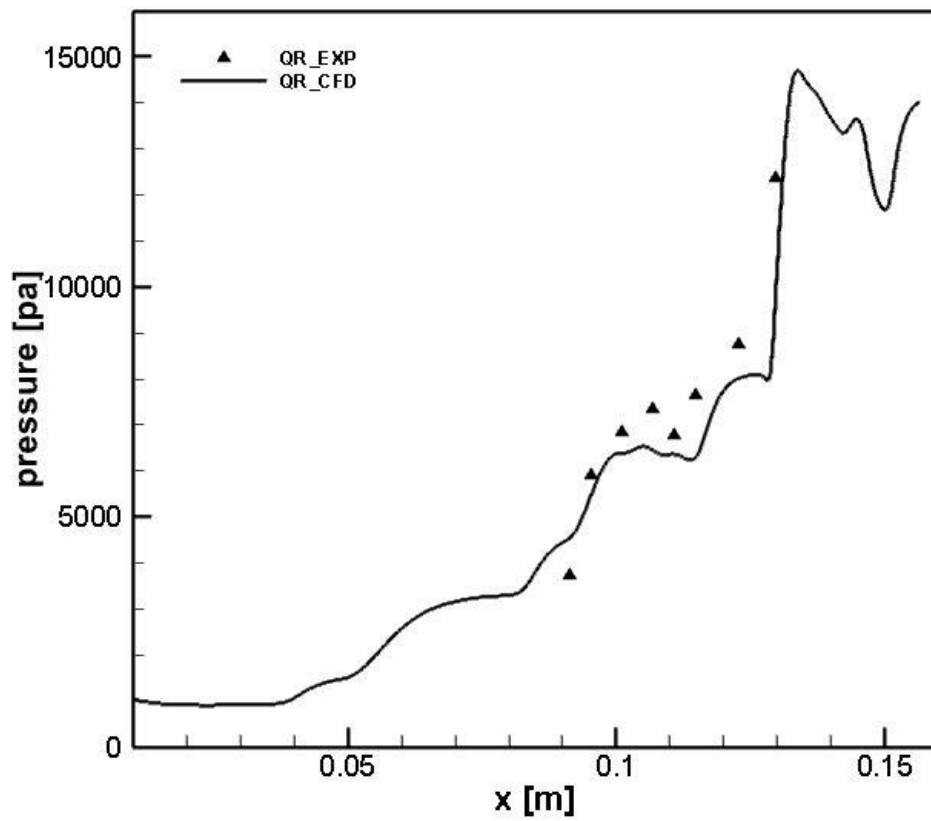
Fig. 7.39. Surface Pressure plot over Quad Ramp configuration
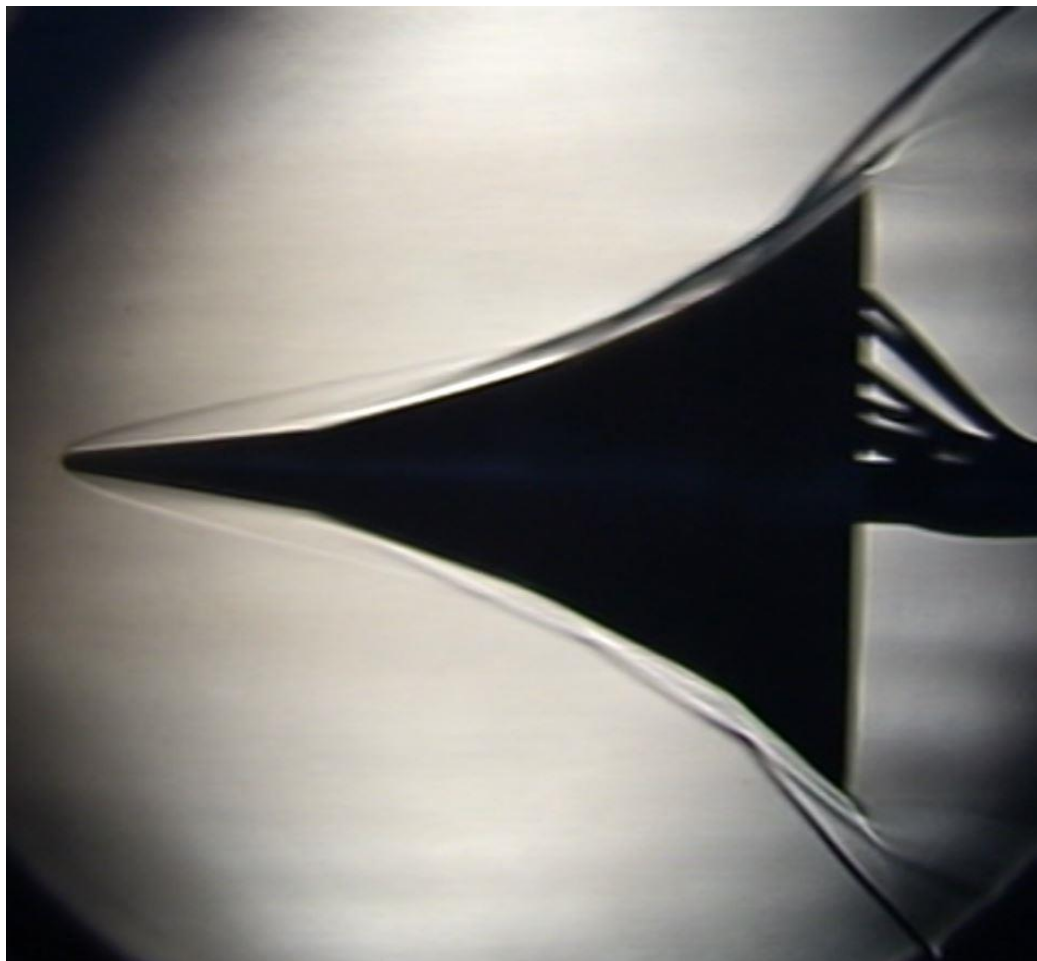
Fig. 7.40. Schlieren Image of Flow over quad ramp configuration
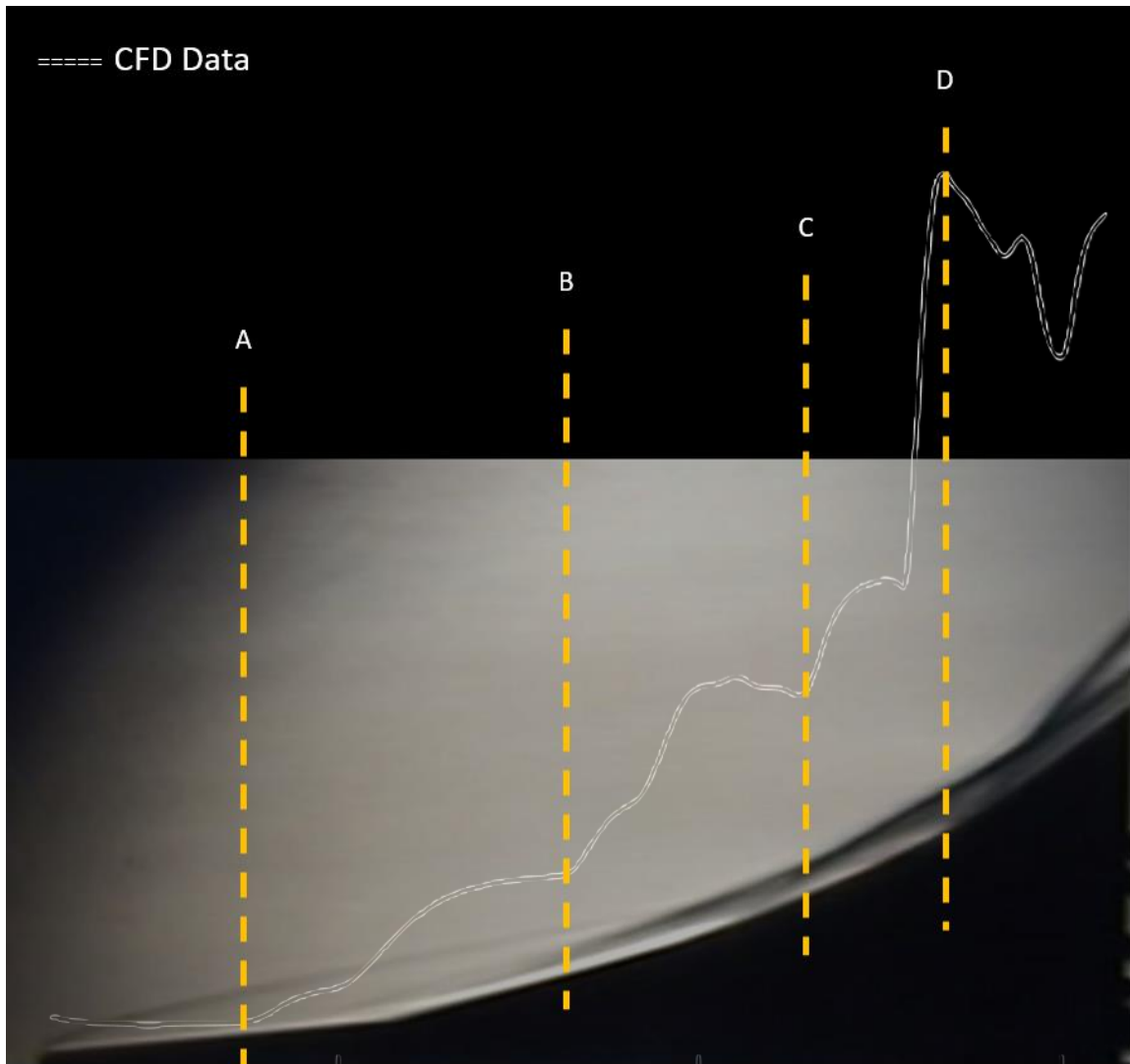
Fig. 7.41. Schlieren with Surface pressure plot over Quad ramp configuration

The schlieren image of the flow over quad ramp configuration can be seen in Fig. 7.40. Fig. 7.41 gives a combined understanding of the schlieren image and the surface pressure plot, providing detailed analogy between shock positions and separation behaviour in the presence of a fourth ramp. The figure consists of four points mainly indicating the separation points at different ramp junctions and helps in locating the post attachment turbulent shear region at the third junction. From Point C, downstream the schlieren tends to become darker, indicating high pressure regions due to multiple shock interactions and highly turbulent flow regions. Firstly the separation bubble size is seen to be highly diffused at the first junction both in the schlieren and the surface pressure plot, while the size of the separation bubble becomes smaller with upstream movement in its location, all these clearly indicating high influence on the flow due to complex ramp structure affecting the flow physics. The upstream influence is majorly attributed to the flow deflections and the upstream flow of information in the form of turbulent shear through the boundary and entropy layer. Progressively it becomes very difficult to interpret the shock and separation physics from the schlieren due to complex flow interactions and pressure gradients, proving the need for simulation-based flow understanding.

CHAPTER 8. CONCLUSIONS

Complex multi-ramp junctions were investigated to study the effects of these design modifications on flow physics followed by a detailed study on how changes in flow conditions and surface properties in combination with design, changes the different characteristics of shock wave and boundary layer interactions which includes understanding of separation and reattachment behaviours, shock interactions, shear regions and boundary layer physics.

Extensive validation activity was performed to ensure accuracy of flow solver through inter-code comparison and grid independence based on which a common solver and grid was chosen as the outcome of this validation. Two different ramp configurations with complex multi-ramp junctions are considered for flow computation studies, one the triple ramp configuration with two ramp junctions and three ramps and the other a quad-ramp with three ramp junctions and four ramps. These complex design configurations do not feature much in any of the past literatures but poses equal or even higher design challenges due to the complexity in flow patterns. Both qualitative and quantitative methods are employed to understand the overall effects of these design configurations on the shock wave boundary layer interaction.

From computational studies it is noted that the triple ramp configuration has highly complex flow structure, with a detached bow shock at the leading edge, the separation shock at the first ramp along with the reattachment shock forming the first corner shock, followed by second corner shock formed due to the second separation bubble, leading to a highly turbulent reattachment shock. This proves that computation methods can no more assume laminarity and must consider turbulent flow modelling for upcoming research studies.

Quantitative study by measuring the separation bubble size through skin friction distribution indicates the length of separation bubble at the first ramp decreases in the presence of a third ramp when compared with the double ramp. These decrements though small in magnitude cannot be neglected as the overall objective is to reduce the bubble size and can provide considerable insights for design consideration. The skin friction distribution also shows a clear separation bubble for smaller third ramp angles, while a complex bubble activity can be noticed for higher ramp angles. This could be indicative of the presence of a strong and a weak circulation zone caused due to turbulent reattachment or even transitional in the presence of a strong shock.

Study on effect of varying the leading-edge bluntness offered some interesting outcomes wherein, the length of separation bubble at the double ramp junction is more prominent at lower triple ramp

angles, while the separation bubble at triple ramp junction becomes more prominent at higher triple ramp angles. It has been identified that the reattachment shock at the double ramp junction tends to grow weaker with combined increment of nose bluntness and the third ramp angle, leading to an early upstream separation at the third ramp junction.

What was also noticed from the pressure distribution plots is that, the reattachment shocks after the double ramp junction is strong but not turbulent over the second ramp, causing a laminar shear region, whereas the reattachment shocks post the triple ramp junction is increasingly strong with increase in third ramp angle and highly turbulent causing a highly unstable shear region over the third ramp. The first critical radius or the inversion radius is noticed anywhere between 3.80 to 4.40, with further increase in radii leading to a reduction in separation bubble size.

The combined effects of varying the free-stream Mach number and ramp angles to understand the changes in flow field for both the configurations. The most crucial finding is that such complex junctions have very unpredictable flow natures and may not follow every correlation that proves well for a simple ramp junction. One such correlation that seems to fail is the behaviour of bubble length with increasing freestream Mach number.

It has been found that with increase in ramp junctions, the bubble at the first junction increases with increase in freestream Mach number which is an inverse correlation when compared to literature studies, while the bubble length decreases in size with higher freestream Mach numbers at the second junction. The bubble length at third junction seems to no more change its characteristics with increase in freestream Mach number with almost same separation and reattachment points.

The effect on the first junction is mainly attributed to the upstream influence of the presence of multiple ramps, causing the boundary layer to thicken. The entropy layer might be engulfed inside the boundary layer leading to the increase of separation bubble size at the first junction. Loss of inertia causes the bubble size to increase at higher ramp junctions for lower Mach numbers eventually becoming almost constant size for all Mach numbers at third junction. The bubble behaviour on a double ramp junction follows the correlation of smaller bubble length at higher Mach number whereas the reverse is seen when there are additional ramps, this is evident and seen in the Fig. 8.1. The bubble lengths can also be referred to in Table 5.2, where same trends are noticed.
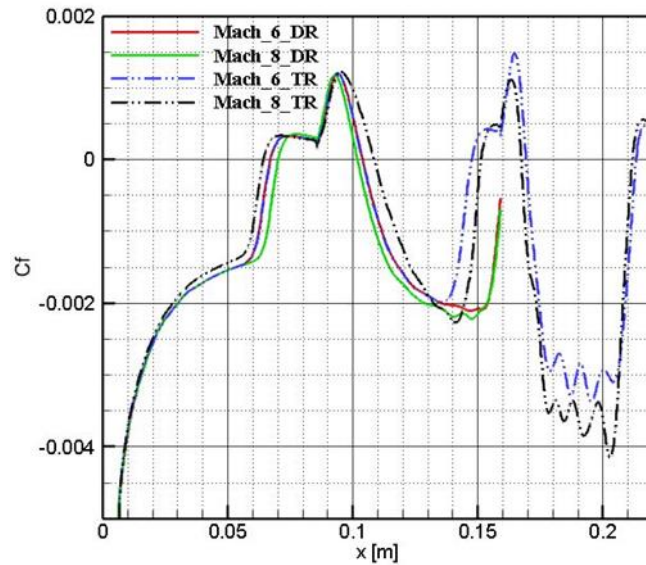
Fig. 8.1. Separation bubble comparison between double and triple ramp configurations

Wall temperature variation and its effects on shock wave boundary layer interactions are also studied in this investigation. Simulation with adiabatic wall condition is also considered and plotted along with the isothermal wall boundary, to understand the upstream influence on the flow physics with these different wall thermal treatments. It can be understood from this study that there is a definite upstream influence with increase in wall temperature.

From the investigation in can be deduced that increase in Mach number does reduce the bubble length at both junctions while bubble length remains to be bigger for higher wall temperatures. Adiabatic wall condition is found to have the biggest bubble size, this mainly is found to happen because increase in temperature increases the boundary layer thickness and hence early separation.

These studies indicate that such complex junctions have very unpredictable flow natures and may not follow every correlation that proves well for a simple double ramp configuration, encouraging the need for detailed and in-depth experimental studies to clearly understand flow physics when design scenarios lead to such complex multi-ramp junctions.

These multi-ramp configurations also exhibit highly turbulent reattachment shocks and turbulent shear regions making it evident that laminar considerations will not be the right method, while reliable understanding on physics can be achieved and yet will require turbulent computational studies to derive at more accurate inference.

Experimental investigations are performed over selected triple ramp and quad ramp configurations to better understand the flow physics and to validate the numerical findings. The experimental setup was thoroughly validated with an existing test case and the CFD methodology was set based on these validation studies. All the instrumentations used were calibrated to ensure accuracy, as the entire experimental work involves surface pressure readings the pressure ports are validated with ESP port readings so that the voltage variations are captures accurately.

The experimental investigation gave clear understanding on the flow nature over complex multi-ramp models and the upstream effects of these multiple junctions on shock wave and boundary layer interactions. Through experimental data it is understood that the flow over such complex configurations are highly turbulent in nature leading to an active turbulent shear layer. The turbulence in the shear travels upstream causing changes in the separation and reattachment shock positions which in-turn change the nature of the separation bubble.

There was very good agreement between the experimental and CFD simulations, specially the reattachment and the post reattachment regions. Experimental pressure values post the reattachment regions were higher than the simulation outcomes indicating turbulent reattachment and a disturbed shear region. From these extensive investigations both simulation and experimental indicates that multi-ramp junctions are regions with highly complex flow and shock structure and such junctions if present in an aerospace vehicle can lead to multiple aerodynamic and acoustic effects.

CHAPTER 9. REFERENCES

[1]   J. D. Anderson Jr, Hypersonic and High Temperature Gas Dynamics, New Delhi: McGraw Hill, 2011.

[2]   R. Savino and D. Peterna, "Blunted cone-flare in hypersonic flow," *Computers & Fluids,* pp. 859-875, 2005.

[3]   B. John and V. Kulkarni, "Numerical assessment of correlations for shock wave boundary layer interaction," *Computers & Fluids,* vol. 90, pp. 42-50, 2014.

[4]   B. John, V. Kulkarni and G. Natarajan, "Shock wave boundary layer interactions in hypersonic flows," *International Journal of Heat and Mass Transfer,* vol. 70, pp. 81-90, 2014.

[5]   B. John and V. Kulkarni, "Effect of leading edge bluntness on the interaction of ramp induced shock wave with laminar boundary layer at hypersonic speed," *Computers & Fluids,* vol. 96, pp. 177-190, 2014.

[6]   S. Reichel and R. Groll, "Numerical simulation and experimental validation of a hypersonic flow for numerical modulation of re-entry phenomena prediction using adaptive mesh refinement," *International Journal of Computational Methods and Experimental Measurements,* vol. 1, no. 4, pp. 381-394, 2013.

[7]   D. A. Needham and J. L. Stollery, "Boundary layer separation in hypersonic flow," *University of London,* 1966.

[8]   C. L. Runninga, T. J. Julianoa, J. S. Jewell, M. P. Borgb and R. L. Kimmel, "Hypersonic Shock-Wave/Boundary-Layer Interactions on a Cone/Flare," *Experimental Thermal and Fluid Science,* 2019.

[9]   D. V. Gaitonde, "Progress in shock wave/boundary layer interactions," *Progress in Aerospace Sciences,* vol. 72, pp. 80-99, 2015.

[10] I. G. Brykina, B. V. Rogov, G. A. Tirskiy, V. A. Titarev and S. V. Utyuzhnikov, "A comparative analysis of approaches for investigating hypersonic flow over blunt bodies in a transitional regime," *Journal of Applied Mathematics and Mechanics,* vol. 77, pp. 9-16, 2013.

[11] H. S. Massimi, H. Shen, C. Y. Wen, Y. S. Chen and S. M. Lian, "Numerical analysis of hypersonic flows around blunt-nosed models and a space vehicle," *Aerospace Science and Technology,* vol. 43, pp. 360-371, 2015.

[12] Z. Shena, W. Yan and G. Yuan, "A robust HLLC-type Riemann solver for strong shock," *Journal of Computational Physics,* vol. 309, pp. 185-206, 2016.

[13] S. Simon and J. C. Mandal, "A simple cure for numerical shock instability in the HLLC Riemann solver," *Journal of Computational Physics,* vol. 378, pp. 477-496, 2019.

[14] H. Nishikawa, "From hyperbolic diffusion scheme to gradient method: Implicit Green–Gauss gradients for unstructured grids," *Journal of Computational Physics,* vol. 372, pp. 126-160, 2018.

[15] D. Sun, F. Qu and C. Yan, "An effective flux scheme for hypersonic heating prediction of re-entry vehicles," *Computers and Fluids,* vol. 176, pp. 109-116, 2018.

[16] F. Qu, J. Chen, D. Sun, J. Bai and G. Zuo, "A grid strategy for predicting the space plane's hypersonic aerodynamic heating loads," *Aerospace Science and Technology,* vol. 86, pp. 659-670, 2019.

[17] J. H. Ferziger and M. Peric, Computational Methods for Fluid Dynamics, Delhi: Springer.

[18] A. Thom, "An Investigation of fluif flows in two-dimension," Aeronautical Research Committee. R&M 1194, Great Britain, 1928.

[19] J.-P. Davis and B. Sturtevant, "Separation length in high-enthalpy shock/boundary-layer interaction," *Physics of Fluids,* vol. 12, no. 10, 2000.

[20] J. Anders and C. Edwards, "A real-gas study of low-density wedge-induced laminar separation on a highly cooled blunt flat plate at M infinity equals 12," NASA, VA, 1968.

[21] H. Ikawa, "Real gas laminar boundary layer separation methodology as applied to Orbiter control surface effectiveness prediction," *Aerospace Research Central,* 2012.

[22] J. Delery, "Shock Phenomena in High Speed Aerodynamics: Still a Source of Major Concern," *The Aeronautical Journal,* vol. 103, no. 1019, pp. 19-34, 1999.

[23] D. Dolling, "Fifty Years of Shock-Wave/Boundary-Layer Interaction Research: What Next?," *AIAA Journal,* vol. 39, no. 8, pp. 1517-1531, 2001.

[24] D. Knight, H. P. Yan and A. Zheltovodov, "Advanced in CFD Prediction of Shock Wave Turbulent Boundary Layer Interactions," *Progress in Aerospace Sciences,* vol. 39, no. 2-3, pp. 121-184, 2003.

[25] A. Zheltovodov, "Advances and Problems in Modeling of Shock Wave Turbulent Boundary Layer Interactions," in *XII International Conference on the Methods of Aerophysical Research (ICMAR-2004)*, Novosibirsk, Russia, 2004.

[26] V. Neiland, V. Bogolepov, I. Lipitov and G. Dudin, Asymptotoc Theory of Supersonic Viscous Gas Flows, Oxford: Butterworth-Heinemann, 2008.

[27] A. Hammit and S. Bogdonoff, "Hypersonic Studies of the Leading Edge Effect on the Flow over a Flat Plate," *Jet Propulsion,* vol. 26, no. 4, pp. 259-269, 1956.

[28] G. Chernyi, "Gas Flows at High Supersonic Velocity," Fizmatlit, Moscow, 1959.

[29] H. Cheng, J. Hall, T. Golian and A. Hertzberg, "Boundary-Layer Displacement and Leading-Edge Bluntness Effects in High-Temperature Hypersonic FLow," *Journal of the Aerspace Sciences,* vol. 28, no. 5, pp. 353-381, 1961.

[30] S. M. Holden, "Boundary-layer displacement and leading-edge bluntness effects on attached and separated laminar boundary layers in a compression corner. Part I: Theoretical Study," *AIAA Journal,* vol. 9, no. 1, pp. 2179-2188, 1970.

[31] M. Holden, "Boundary-layer displacement and leading-edge bluntness effects on attached and separated laminar boundary layers in a compression corner. Part II: Experimental Study," *AIAA Journal,* vol. 9, no. 1, pp. 84-93, 1971.

[32] V. Borovoy, I. Egorov, A. Skuratov and I. Struminskava, "Laminar Heat Transfer on Sharp and Blunt Plates in a Hypersonic Air Flow," *Fluid Dynamics,* vol. 40, no. 1, pp. 148-158, 2005.

[33] G. J. Don and R. Rhudy, "Effects of Blunting and Cooling on Ramp-Induced Separation of Laminar Flows at Supersonic Speeds," in *AIAA 5th Fluid and Plasma Dynamics*, Boston, 1972.

[34] V. Borovoy, I. Egorov, A. Skuratov and I. Struminskava, "Effect of a High-Entropy Layer on Heat Transfer in the Region of the Incidence of an Oblique Shock Wave on a Blunted-Plate Surface," *Doklady Physics,* vol. 50, no. 1, pp. 3-6, 2005.

[35] V. Borovoy, I. Egorov, A. Skuratov and I. Struminskava, "Interaction between an Inclined Shock, Boundary and High-Entropy Layers on a Flat Plate," *Fluid Dynamics,* vol. 40, no. 6, pp. 911-928, 2005.

[36] V. Borovoy, A. Skuratov and I. Struminskava, "On the Existence of a threshold value of the Plate bluntness in the Interference of an Oblique shock with boundary and Entropy layers," *Fluid Dynamics,* vol. 43, no. 3, pp. 369-379, 2008.

[37] T. Neuenhahn, Investigation of the Shock Wave/Boundary layer interaction of Scramjet Intake flows, Germany: RWTH Aachen University, 2010.

[38] U. R. Birgit, "Numerical investigation of wall temperature and entropy layer effects on double wedge shock.boundary layer interaction," in *14th AIAA/AHI Space Planes and Hypersonic Systems and Technologies Conference*, 2006.

[39] B. Reinartz, J. Van Keuk, T. Coratekin and J. Ballmann, "Computation of wall heat fluxes in hypersonic inlet flows," *AIAA Journal,* pp. 1-10, 2002.

[40] M. Bleilebens and H. Olivier, "On the Influence of Elevated surface temperature on Hypersonic Shock wave/Boundary layer interaction at a Heated ramp model," *ShockWaves,* vol. 15, no. 5, pp. 301-312, 2006.

[41] S. CRADLE, "ScSTREAM User's Guide Basics of CFD Analysis," September 2020. [Online]. Available: file:///C:/Program%20Files/Cradle/Stwin2020/Manuals/HTML/Basic_eng/index.html. [Accessed August 2020].

[42] N. Munikrishna, "On Viscous Flux Discretization Procedures for Finite Volume and Meshless Solvers," Dept. of Aerospace Engineering, IISc, Bangalore, 2007.

[43] A. Jalali, M. Sharbatdar and C. Ollivier-Gooch, "Accuracy analysis of Unstructured Finite Volume Discretization Schemes for Diffusive Fluxes," *Computers and Fluids,* vol. 101, pp. 220-232, 2014.

[44] N. V. Shende, "Development of a general purpose flow solver for Euler equations," Dept. of Aerospace Engineering, IISc, Bangalore, 2005.

[45] F. Grasso and M. Marini, "Analysis of hypersonic shock-wave laminar boundary-layer interaction phenomena," *Computers & Fluids,* vol. 25, no. 6, pp. 561-581, 1996.

[46] M. Marini, "Analysis of hypersonic compression ramp laminar flows under sharp leading edge conditions," *Aerospace Science and Technology,* vol. 5, no. 4, pp. 257-271, 2001.

[47] "From the Director," IISc, [Online]. Available: https://www.iisc.ac.in/about/foreword-from-the-director/. [Accessed November 2019].

[48] "Aerospace Engineering," IISc, [Online]. Available: http://aero.iisc.ac.in/. [Accessed November 2019].

[49] HSWTC, "The high speed wind tunnel complex," Indian Institute of Science, Bangalore, 2018.

[50] W. Sutherland, "The viscosity of gases and molecular force," *Philosophical Magazine Series 5,* vol. 36, pp. 507-531, 1893.

[51] H. Mahgerefteh, Y. Rykov and G. Denton, "Courant, Friedrichs and Lewy (CFL) impact on numerical convergence of highly transient flows," *Chemical Engineering Science,* vol. 64, no. 23, pp. 4969-4975, 2009.

[52] M. Coet and B. Chanetz, "Experiments on shock wave/boundary layer interaction in hypersonic flow," *Hypersonic Flows for Reentry Problems,* 1993.

APPENDIX

A. CURRICULUM VITAE

Work Experience:

- ➢ *Technical Manager – CFD Solutions (Indo-Pacific)*
  MSC Software Corporation India, Bangalore
  Currently Employed since Feb 2019

- ➢ *National Technical Manager – Strategic Accounts*
  ARK Infosolutions Pvt. Ltd, Bangalore
  June 2015 – Feb 2019

- ➢ *Assistant Professor*
  Dept. of Aerospace Engineering
  UPES, Dehradun
  June 2012 – May 2015

- ➢ *Research Associate*
  CML, Dept. of Aerospace Engineering
  Indian Institute of Science, Bangalore
  December 2011 – June 2012

Academic Background:

- ➢ *Master of Science in Aerospace Engineering*
  Brunel University, London

- ➢ *Bachelor of Engineering in Industrial Engineering*
  JSS Academy of Technical Education, Bangalore

Publications (Relevant to current research):

- ➢ *Effect of varying ramp angle and leading-edge bluntness on the behavior of ramp induced shock wave over triple ramped cone flare configuration at hypersonic speed*
  International Journal of Recent Technology and Engineering
  Sept. 2019

- ➢ *Hypersonic flows over multi-ramp configurations*
  International Journal of Recent Technology and Engineering
  Sept. 2019

- ➢ *Flow over blunted cone flare having triple ramp*
  SAROD 2018

- ➢ *Effect of varying Mach number & wall temperature on surface heat flux of multi ramp body*
  SAROD 2018

B. CONTOUR MACH PLOTS

B.1 TRIPLE RAMP MODELS
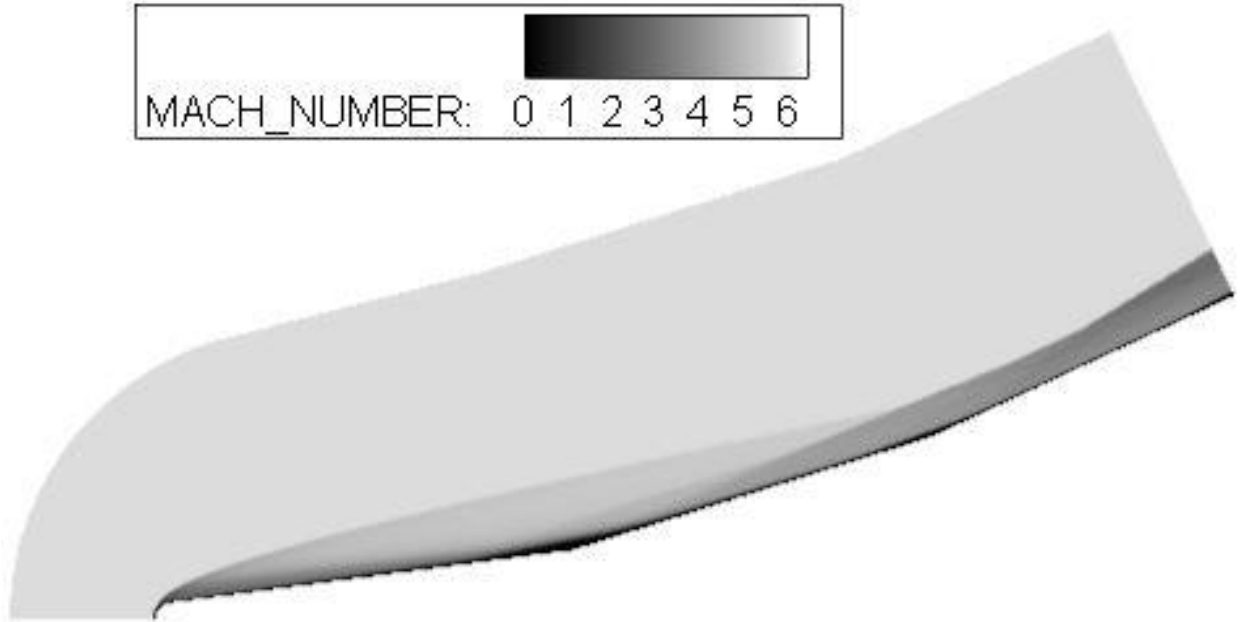
B-1. Triple Ramp 7.5 at Mach 6
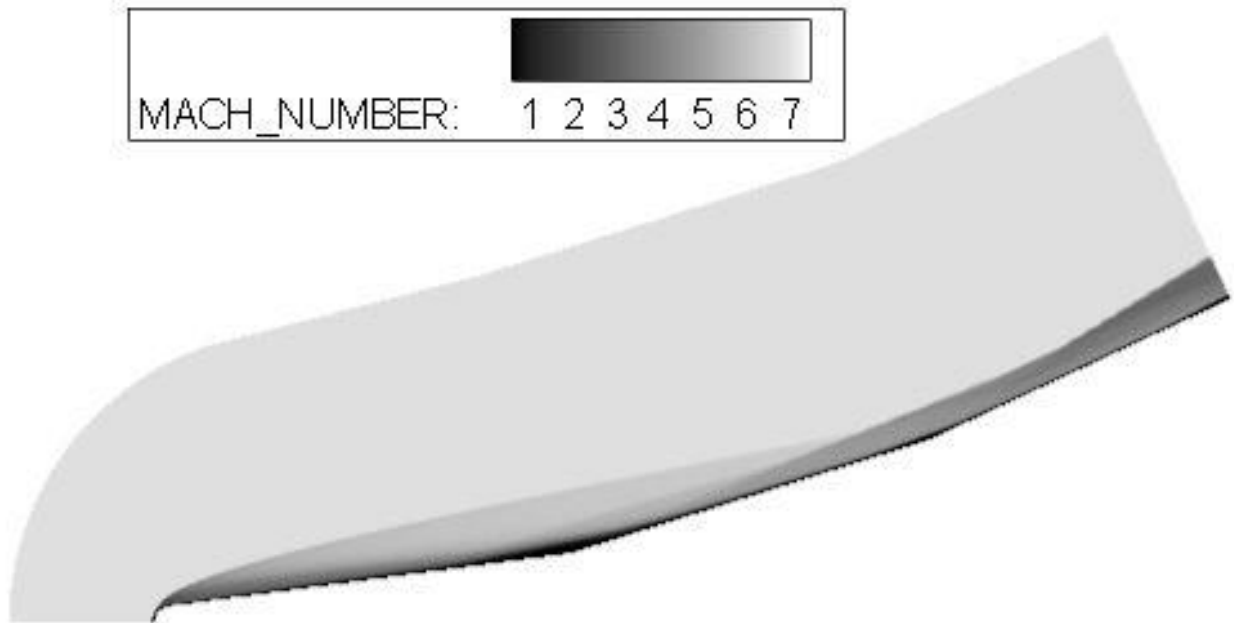
B-2. Triple Ramp 7.5 at Mach 7
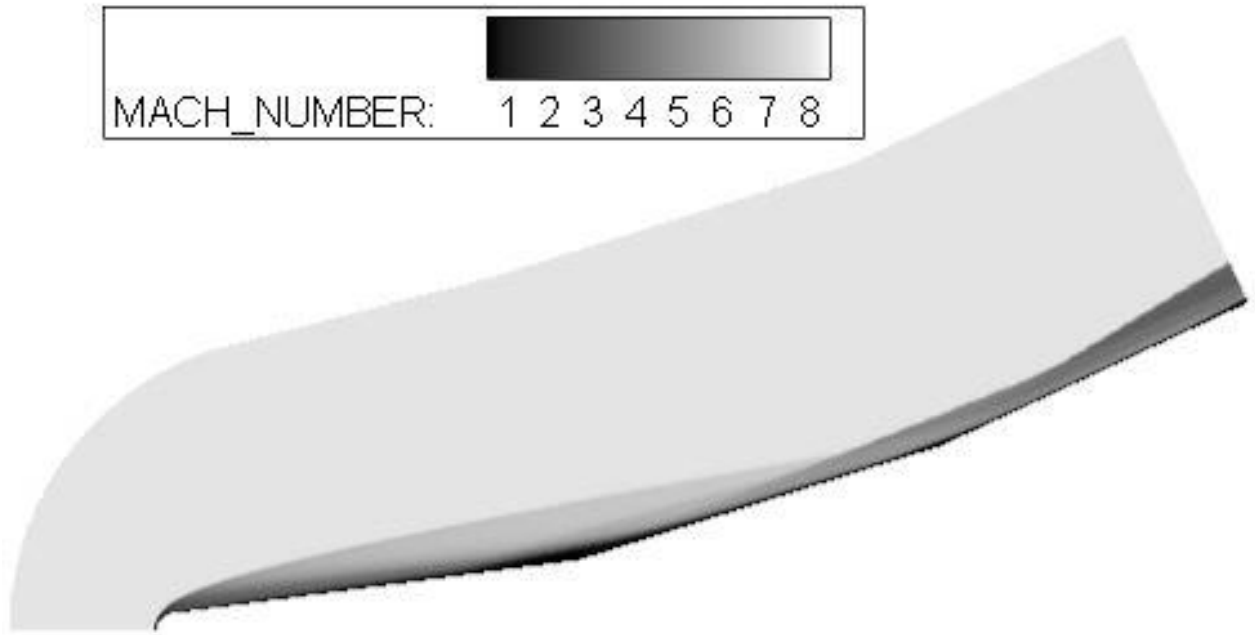
B-3. Triple Ramp 7.5 at Mach 8
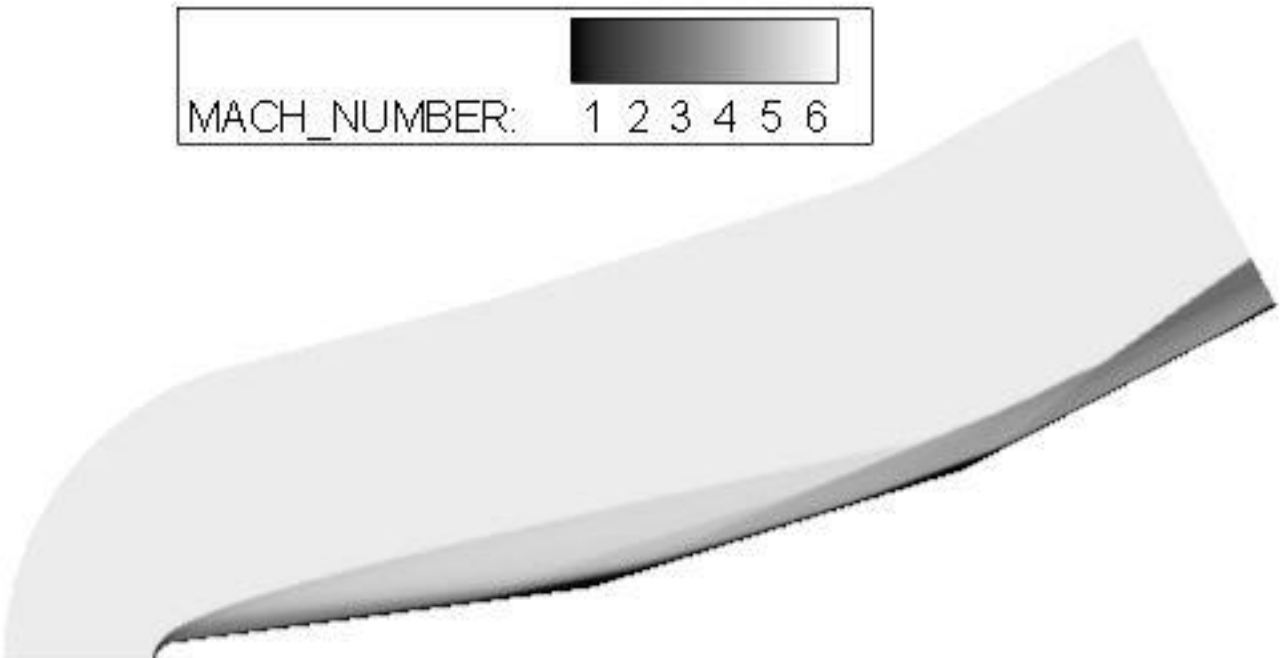
B-4.Triple Ramp 10 at Mach 6
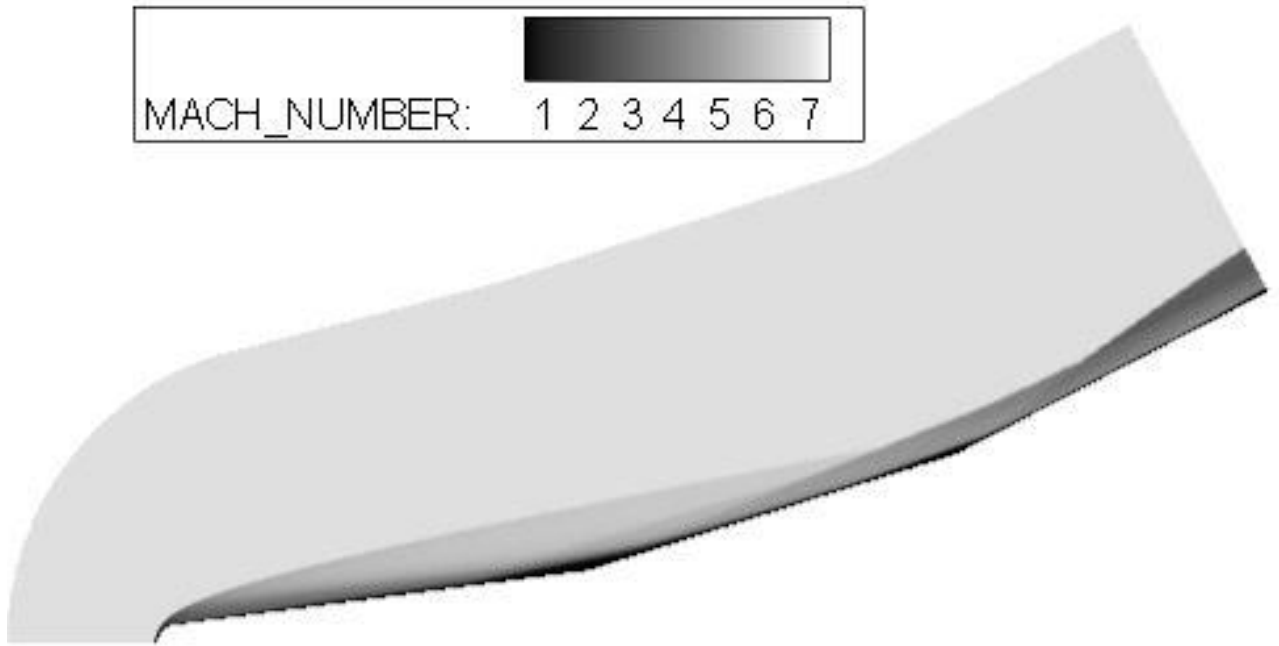
B-5.Triple Ramp 10 at Mach 7
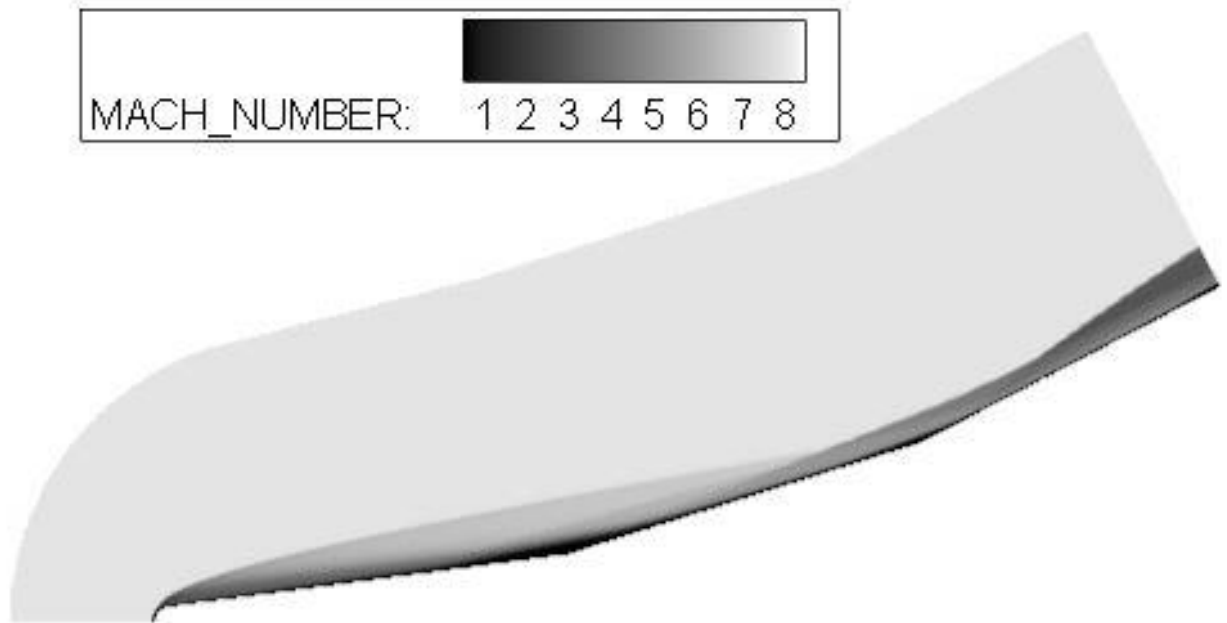
B-6. Triple Ramp 10 at Mach 8
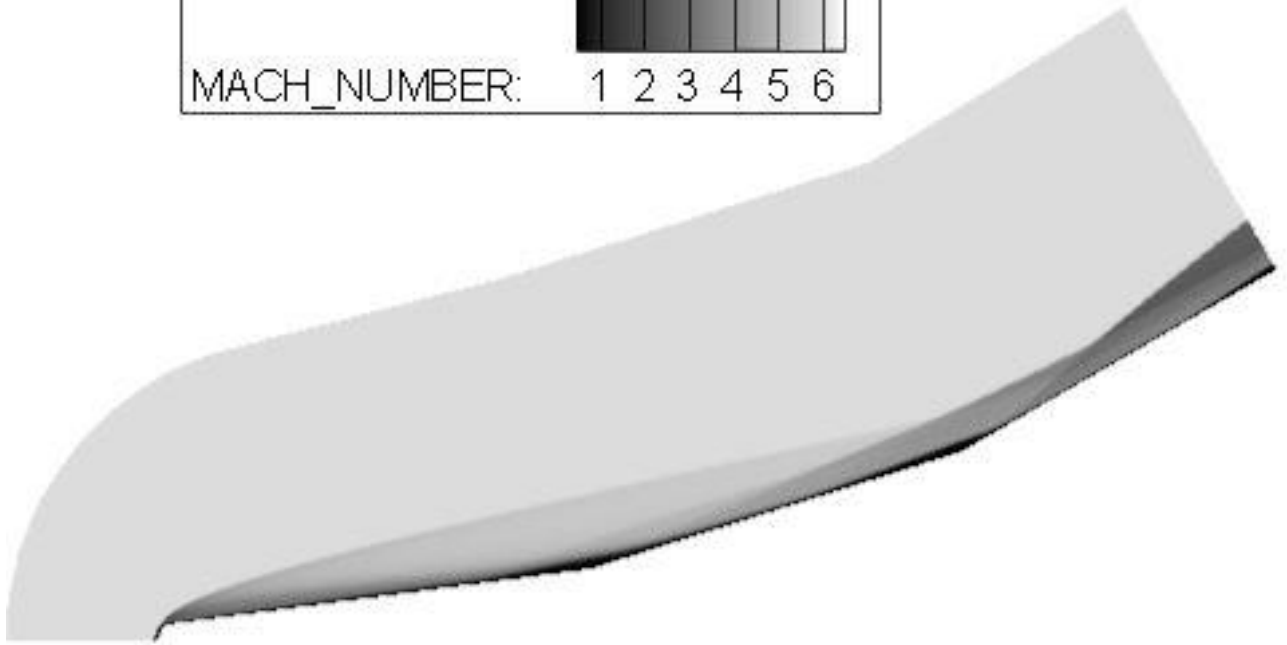
B-7.Triple Ramp 12.5 at Mach 6
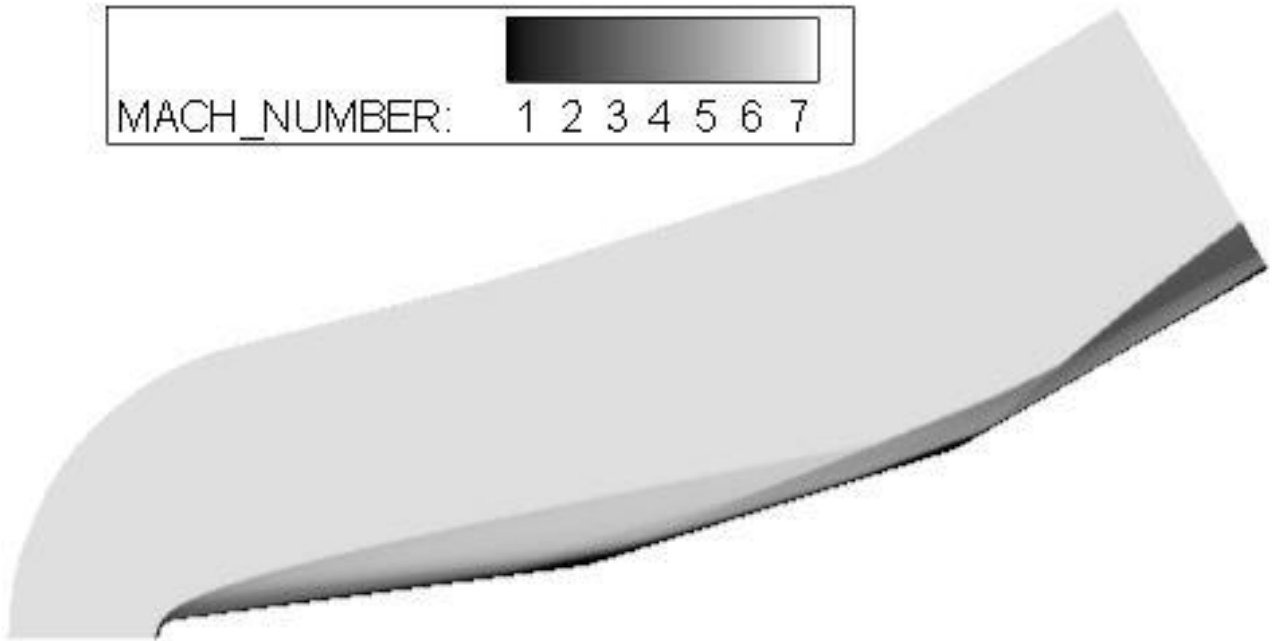
B-8.Triple Ramp 12.5 at Mach 7
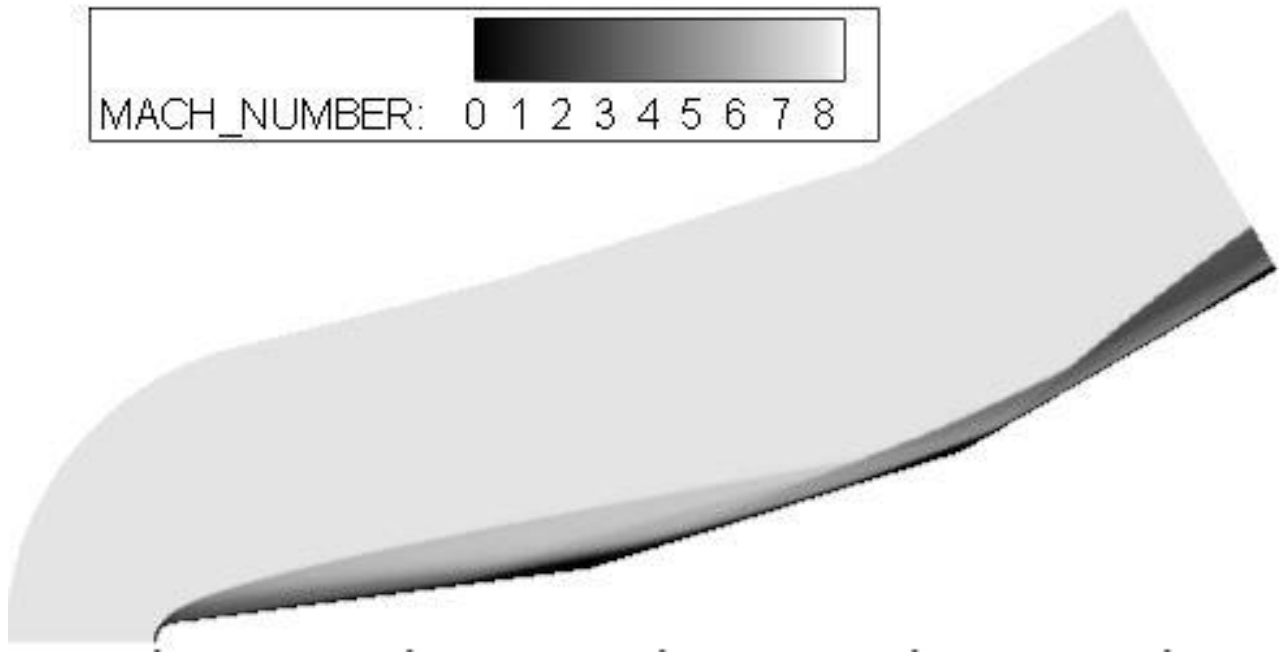
B-9.Triple Ramp 12.5 at Mach 8
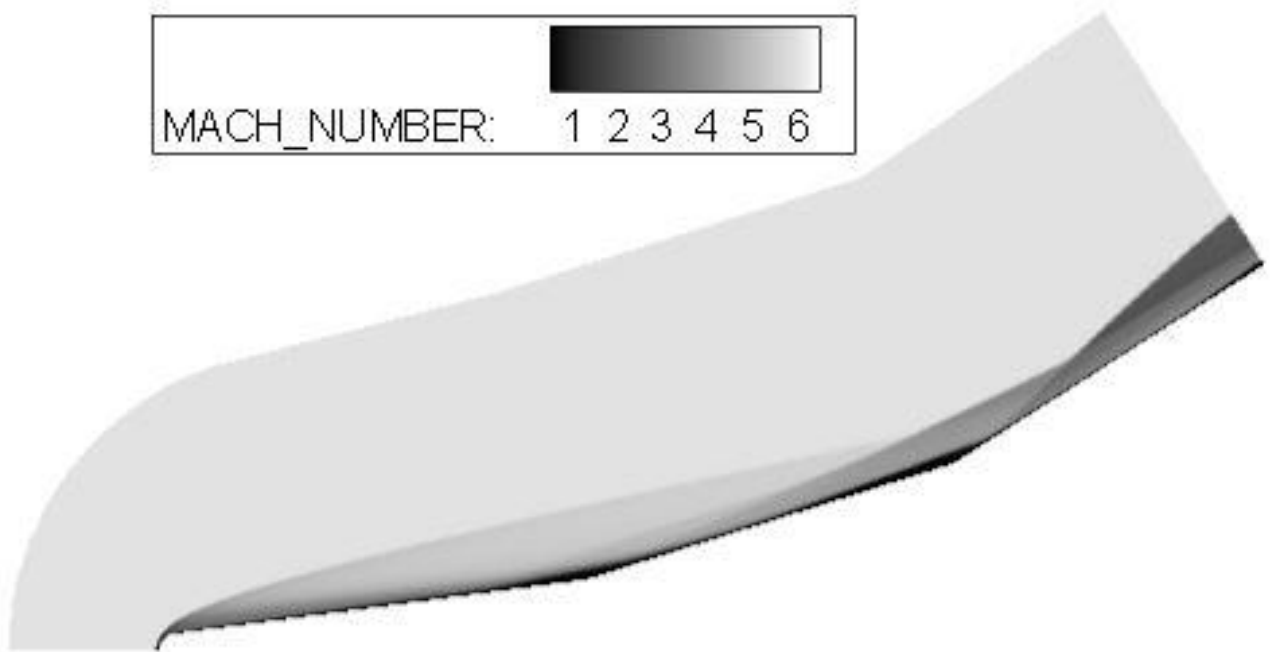
B-10.Triple Ramp 15 at Mach 6
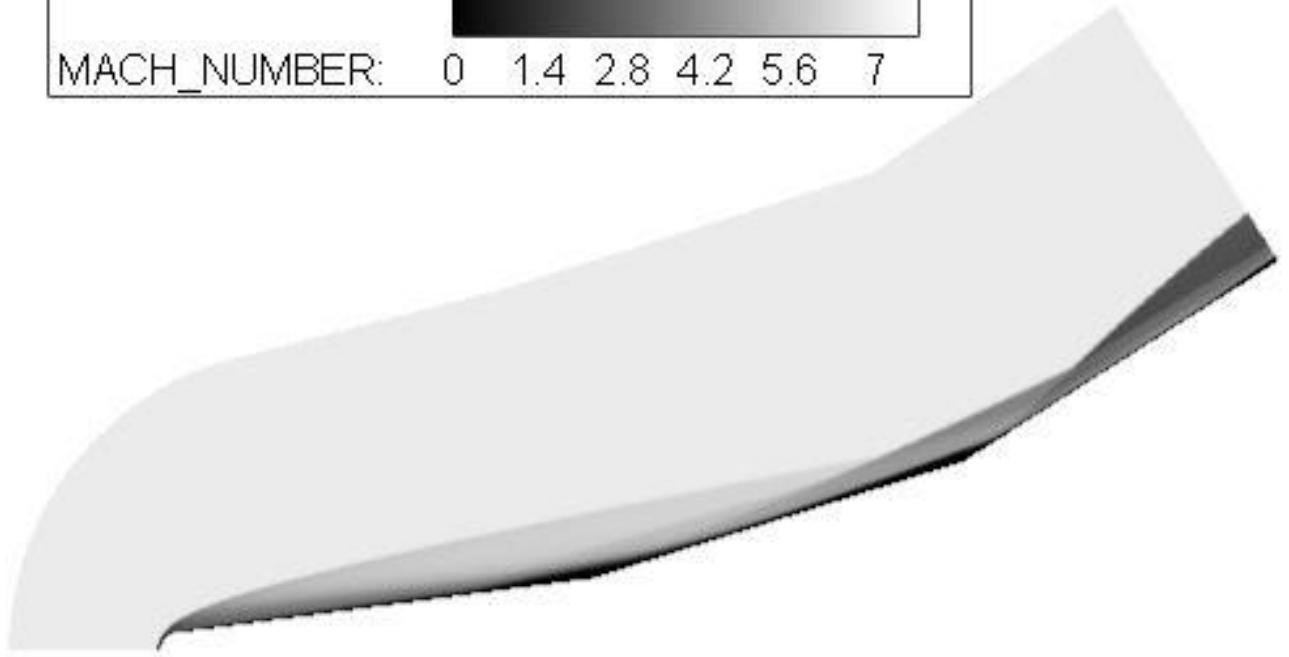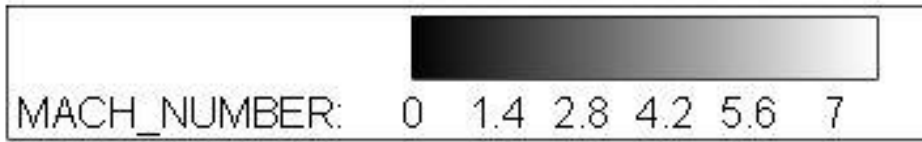
B-11.Triple Ramp 15 at Mach 7
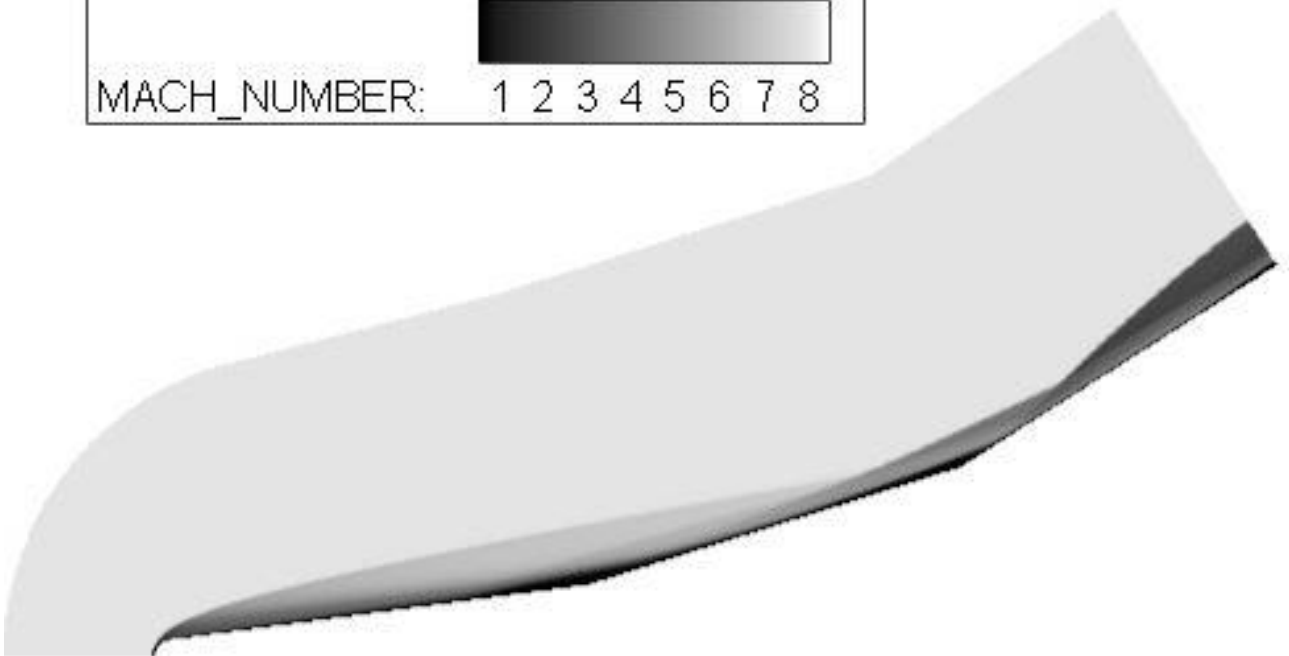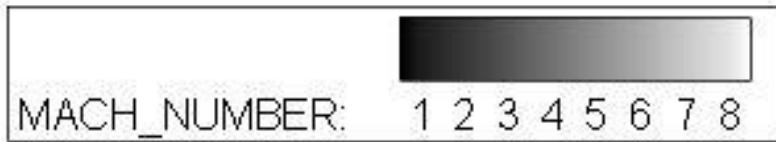
B-12.Triple Ramp 15 at Mach 8

B.2 QUAD RAMP MODELS
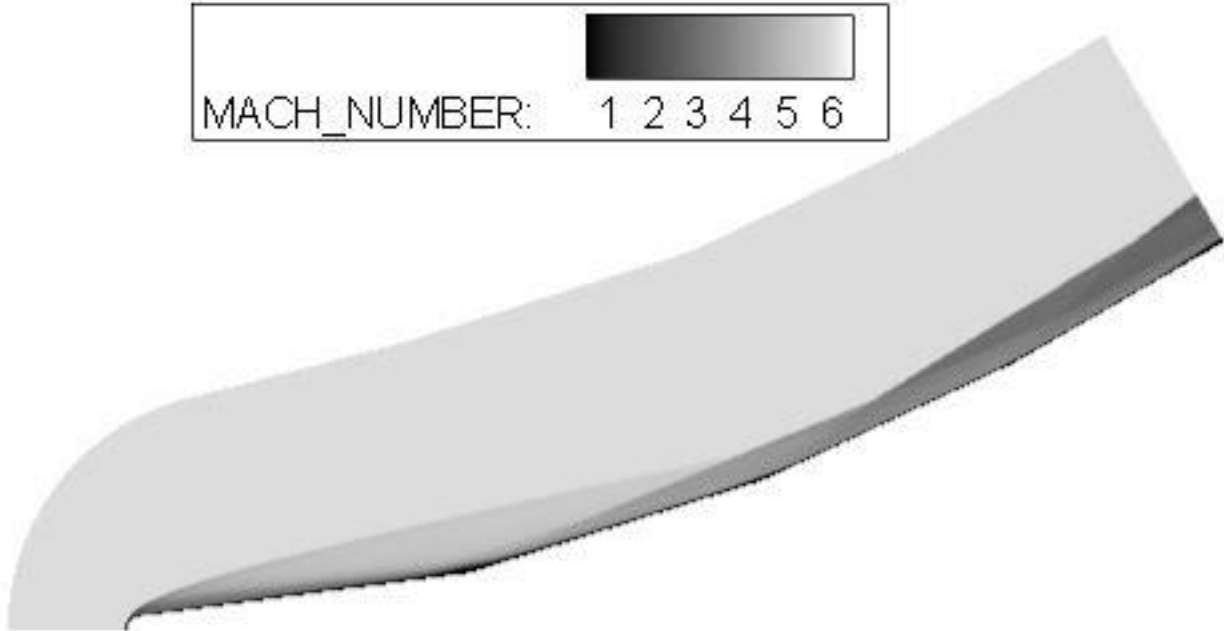
B-13.Triple Ramp 7.5, Quad Ramp 5 at Mach 6
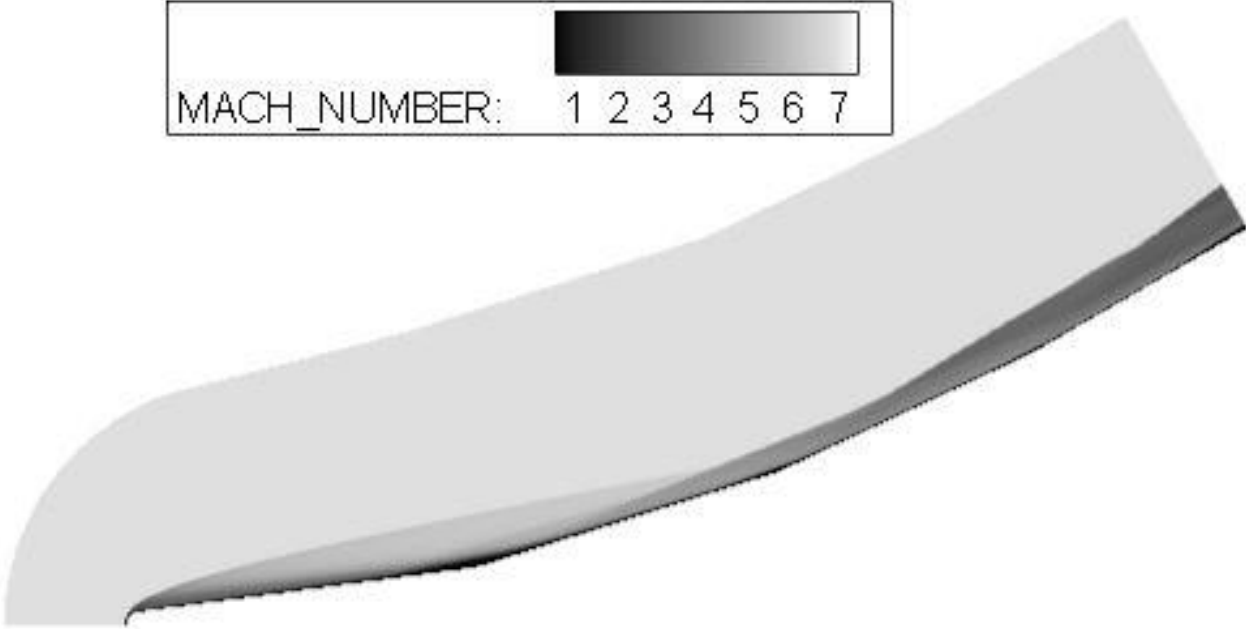
B-14.Triple Ramp 7.5, Quad Ramp 5 at Mach 7
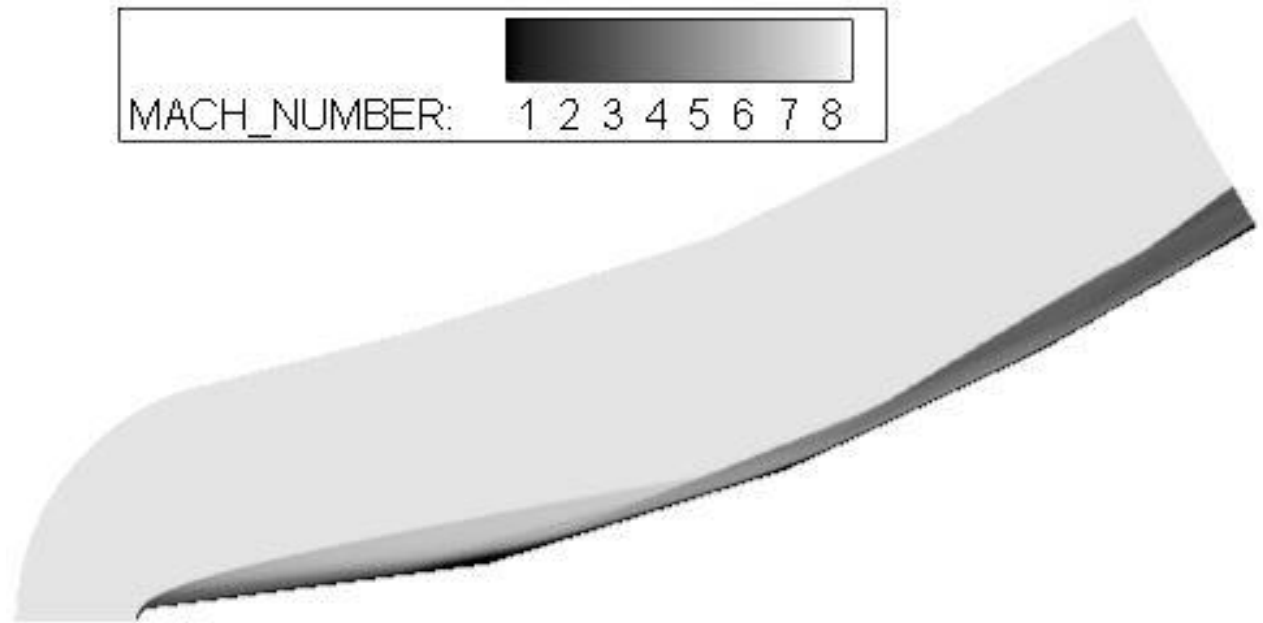
B-15.Triple Ramp 7.5. Quad Ramp 5 at Mach 8
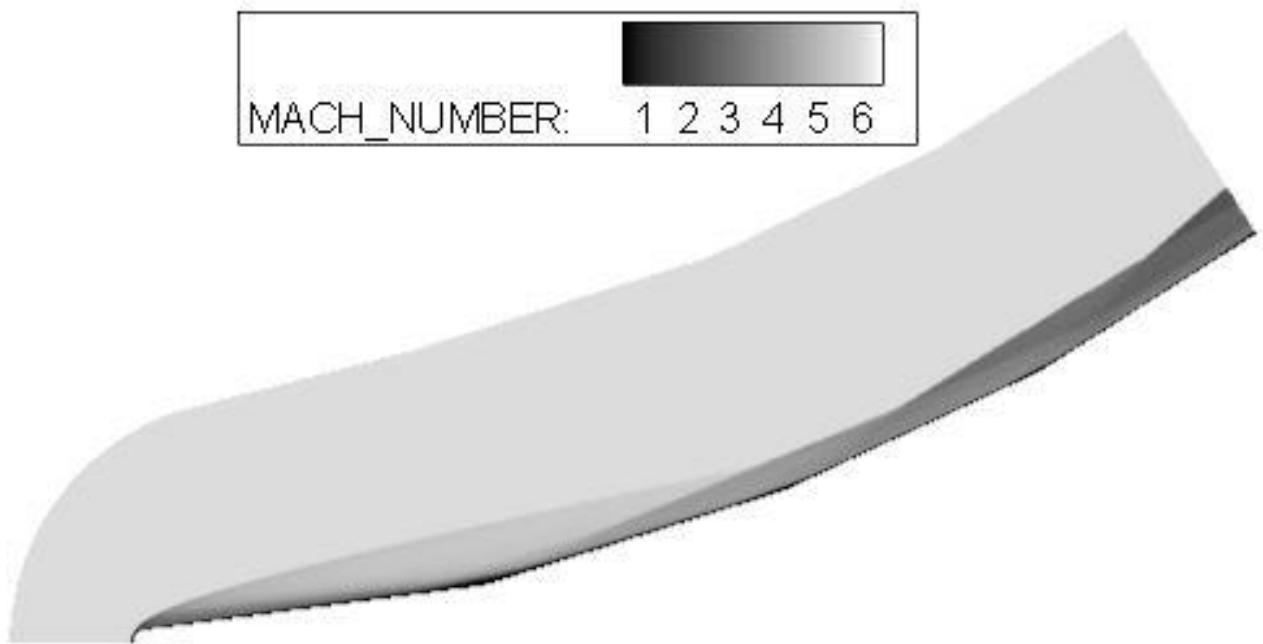
B-16.Triple Ramp 7.5, Quad Ramp 7.5 at Mach 6

MACH_NUMBER: 1 2 3 4 5 6 7
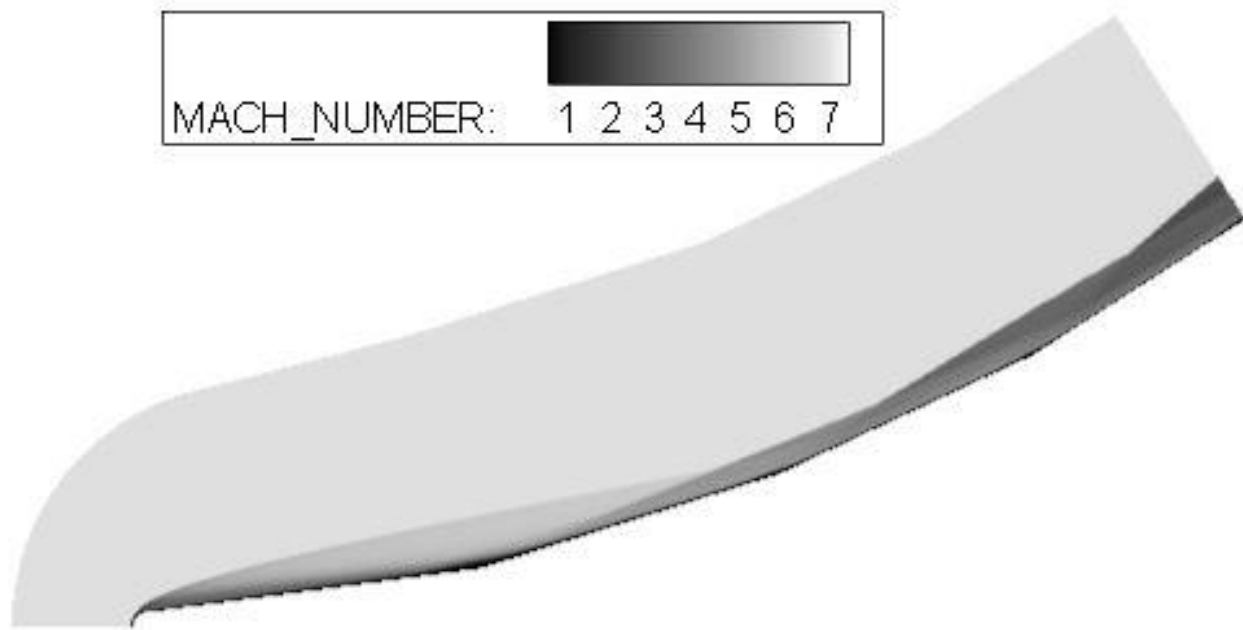
B-17.Triple Ramp 7.5, Quad Ramp 7.5 at Mach 7

MACH_NUMBER: 1 2 3 4 5 6 7 8
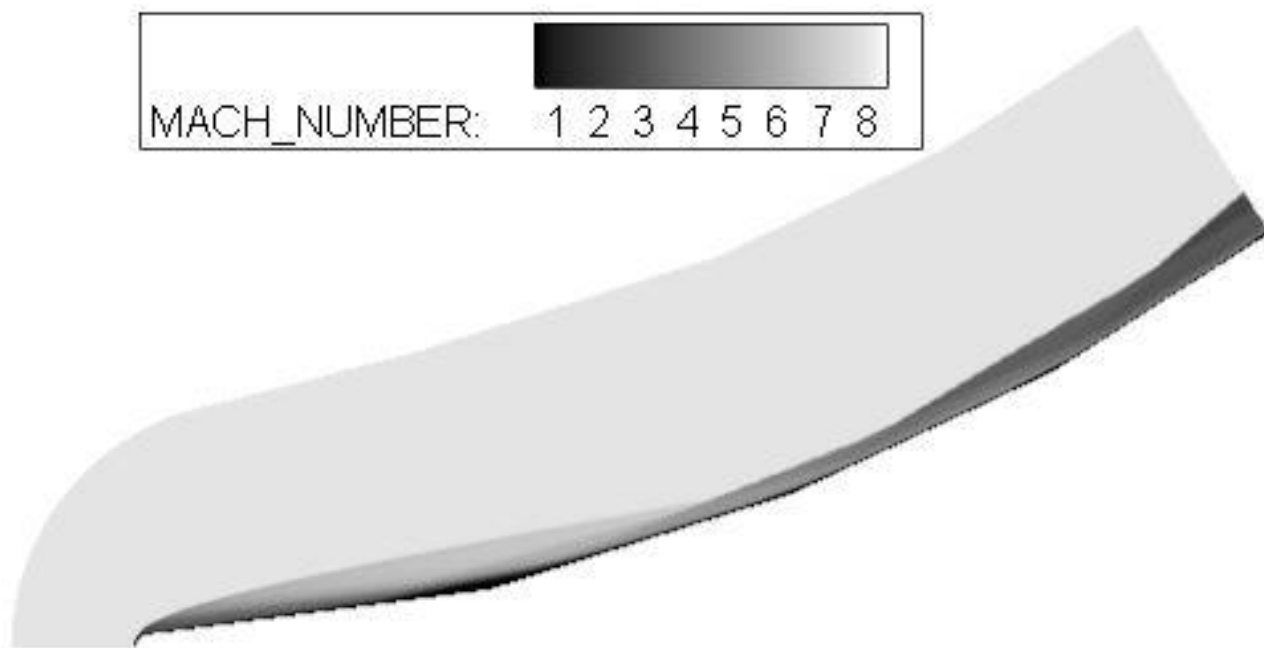
B-18.Triple Ramp 7.5, Quad Ramp 7.5 at Mach 8
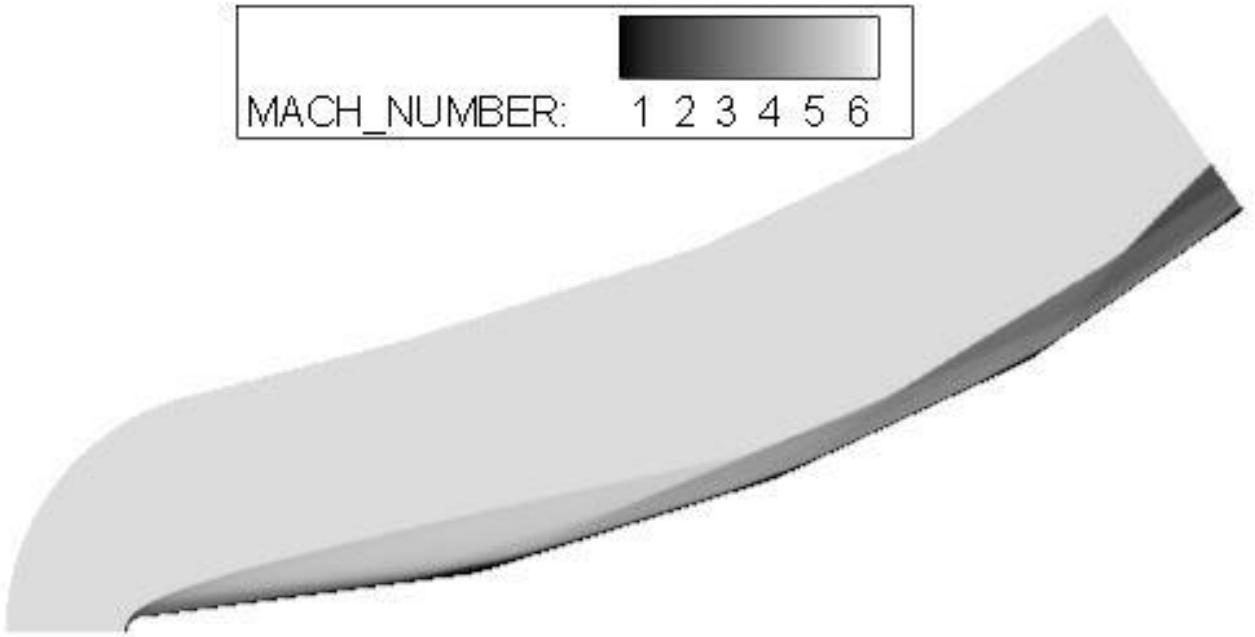
B-19.Triple Ramp 7.5, Quad Ramp 10 at Mach 6
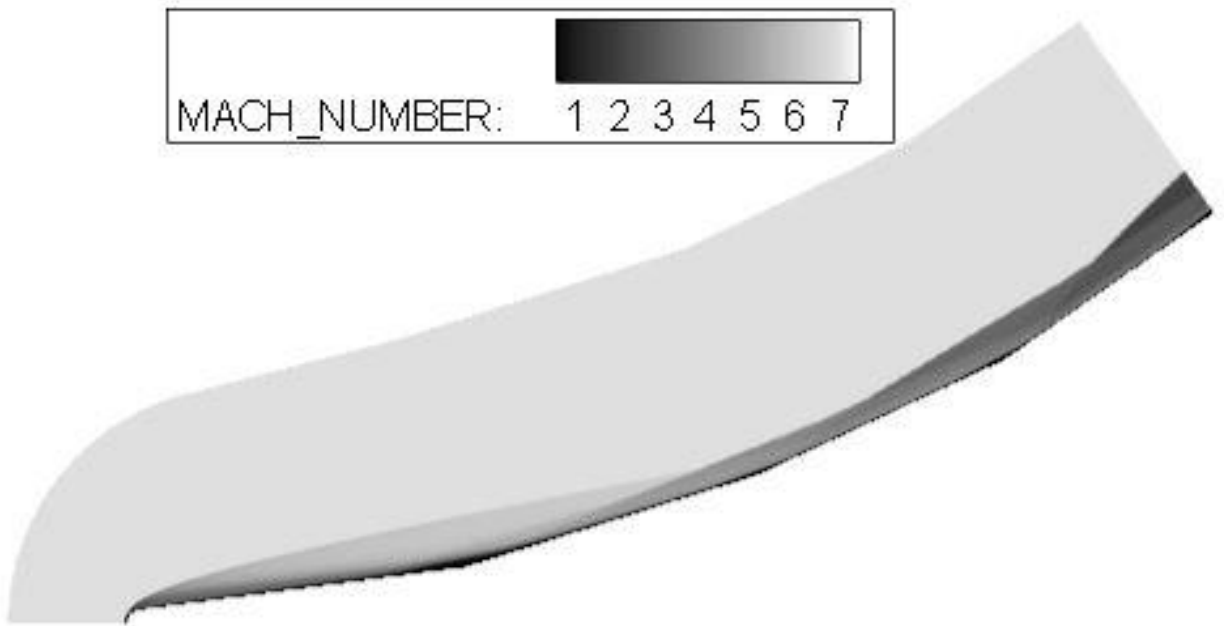
B-20.Triple Ramp 7.5, Quad Ramp 10 at Mach 7
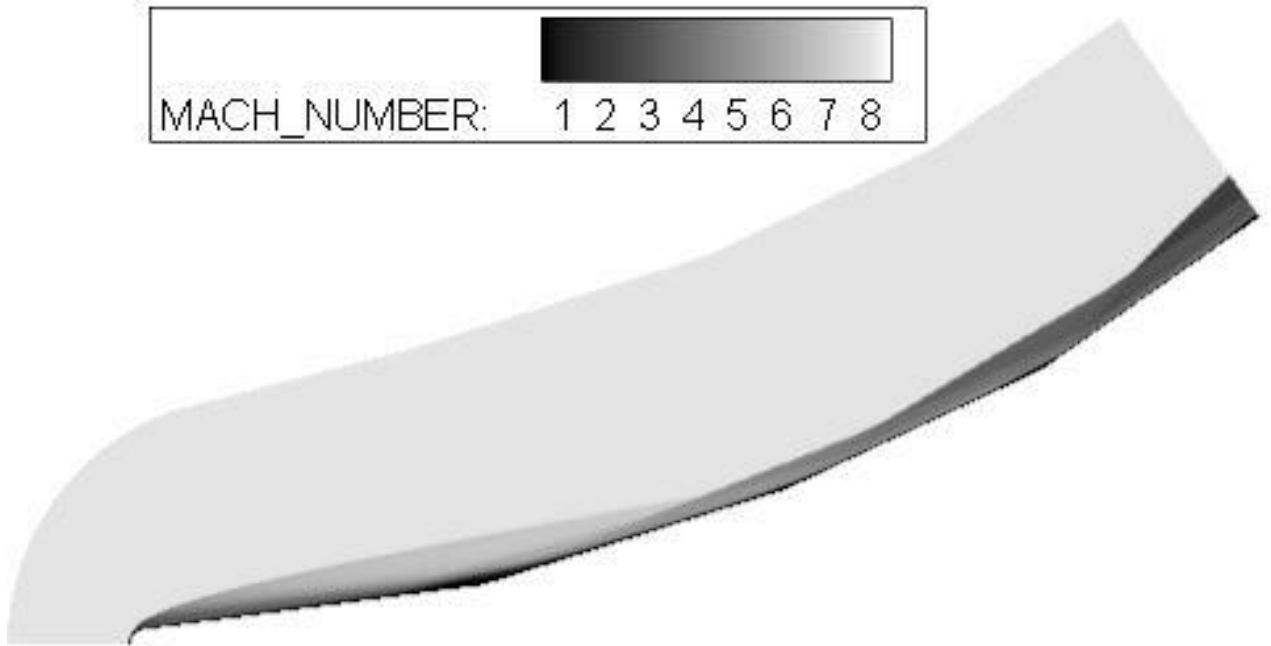
B-21.Triple Ramp 7.5, Quad Ramp 10 at Mach 8
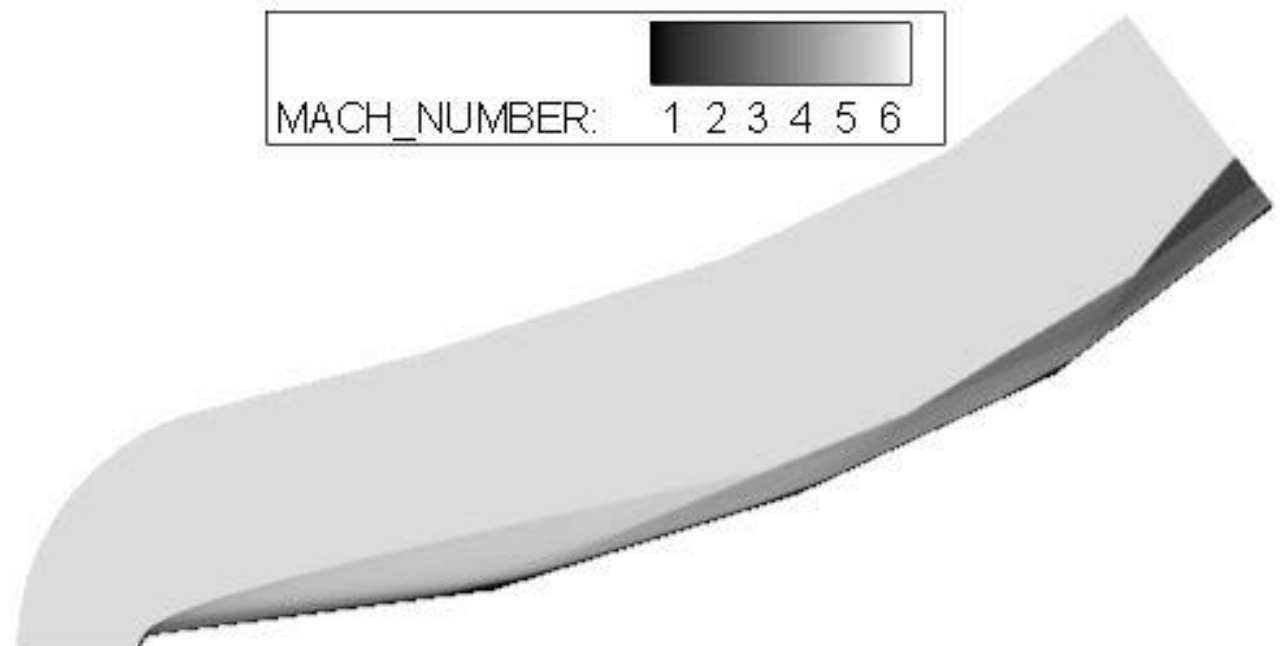
B-22.Triple Ramp 7.5, Quad Ramp 12.5 at Mach 6
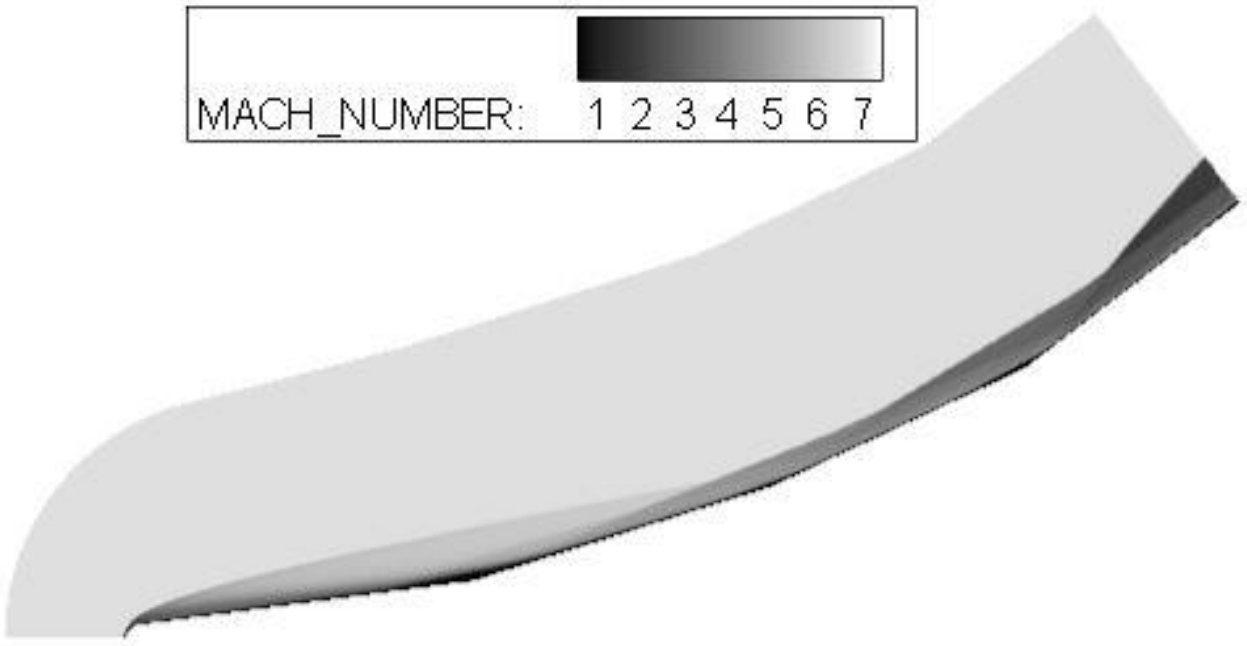
B-23.Triple Ramp 7.5, Quad Ramp 12.5 at Mach 7
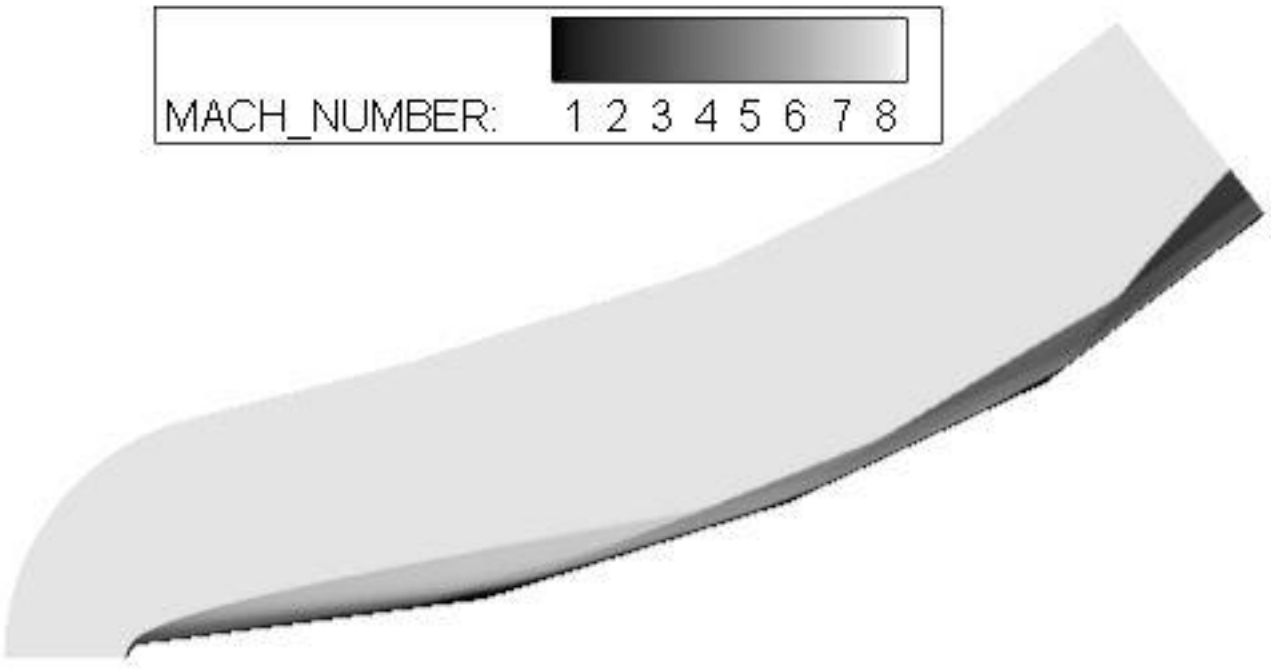
B-24.Triple Ramp 7.5, Quad Ramp 12.5 at Mach 8
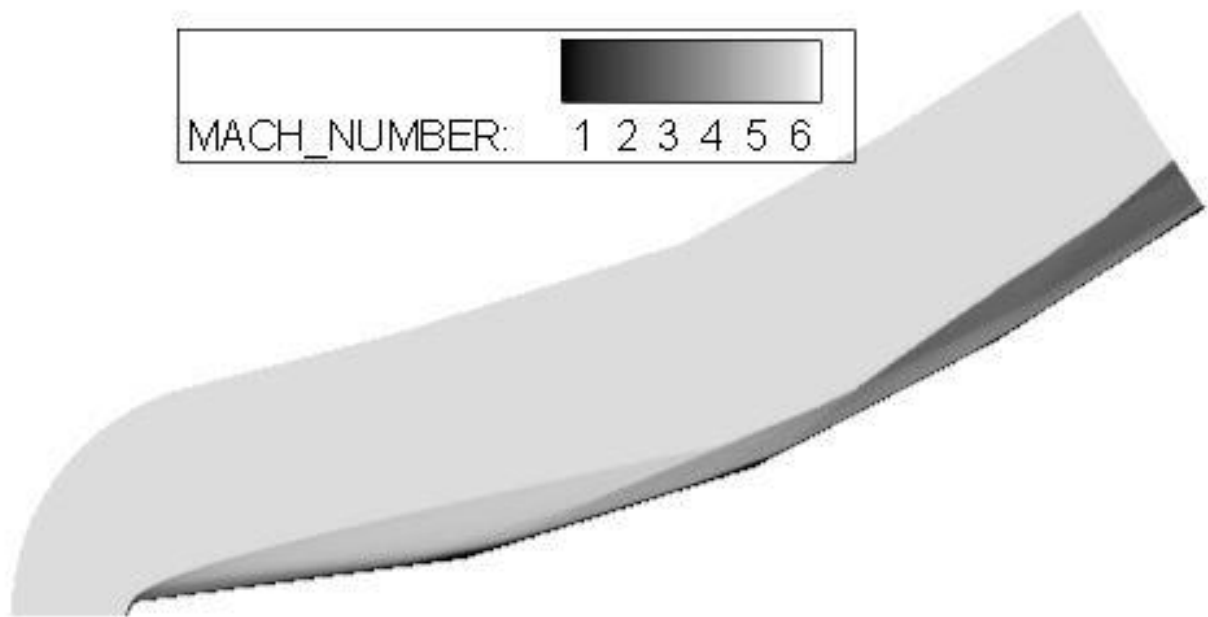
B-25.Triple Ramp 10, Quad Ramp 5 at Mach 6
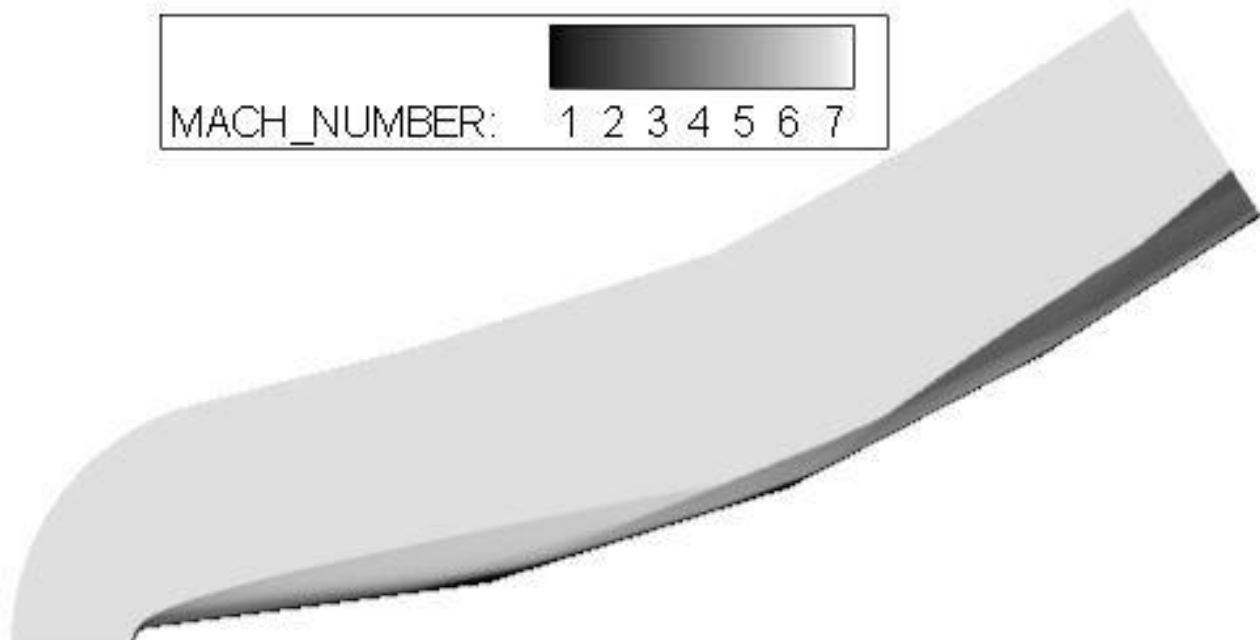
B-26.Triple Ramp 10, Quad Ramp 5 at Mach 7
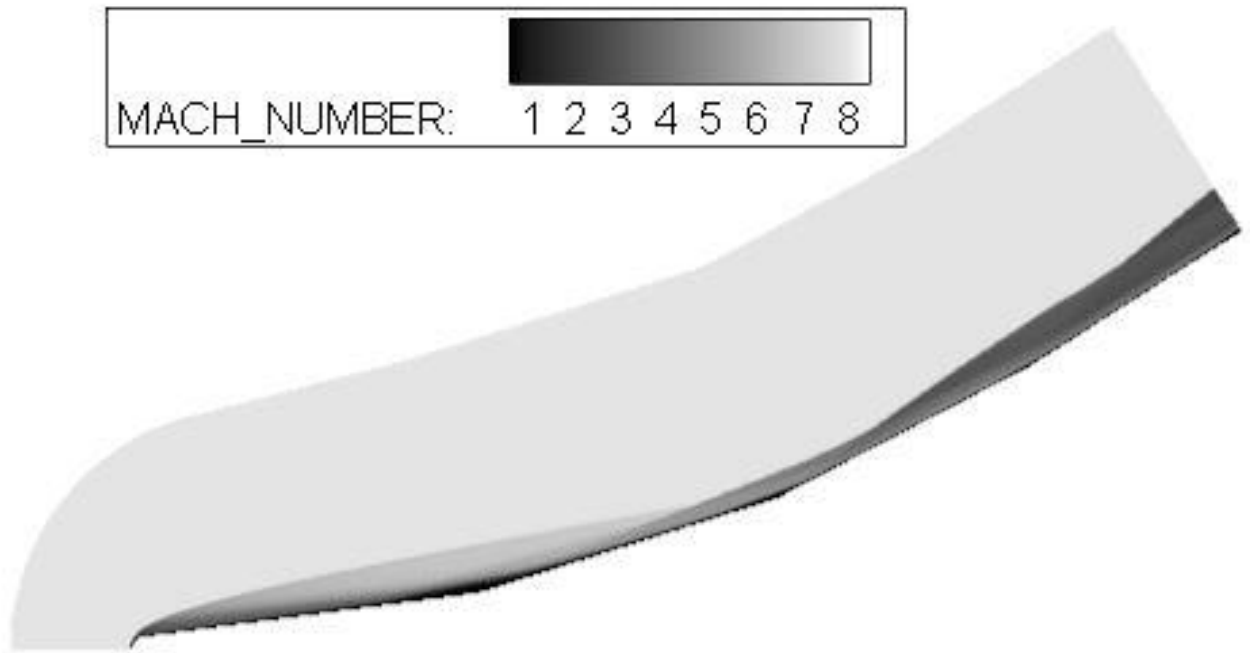
B-27.Triple Ramp 10, Quad Ramp 5 at Mach 8
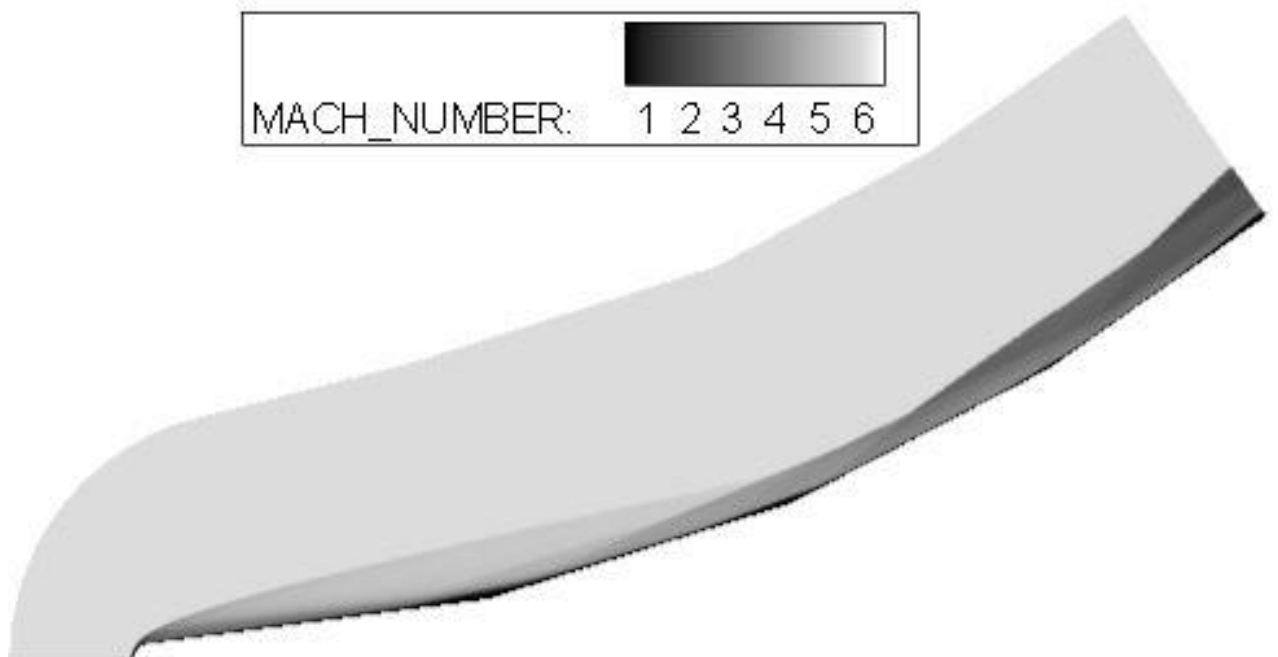
B-28.Triple Ramp 10, Quad Ramp 7.5 at Mach 6
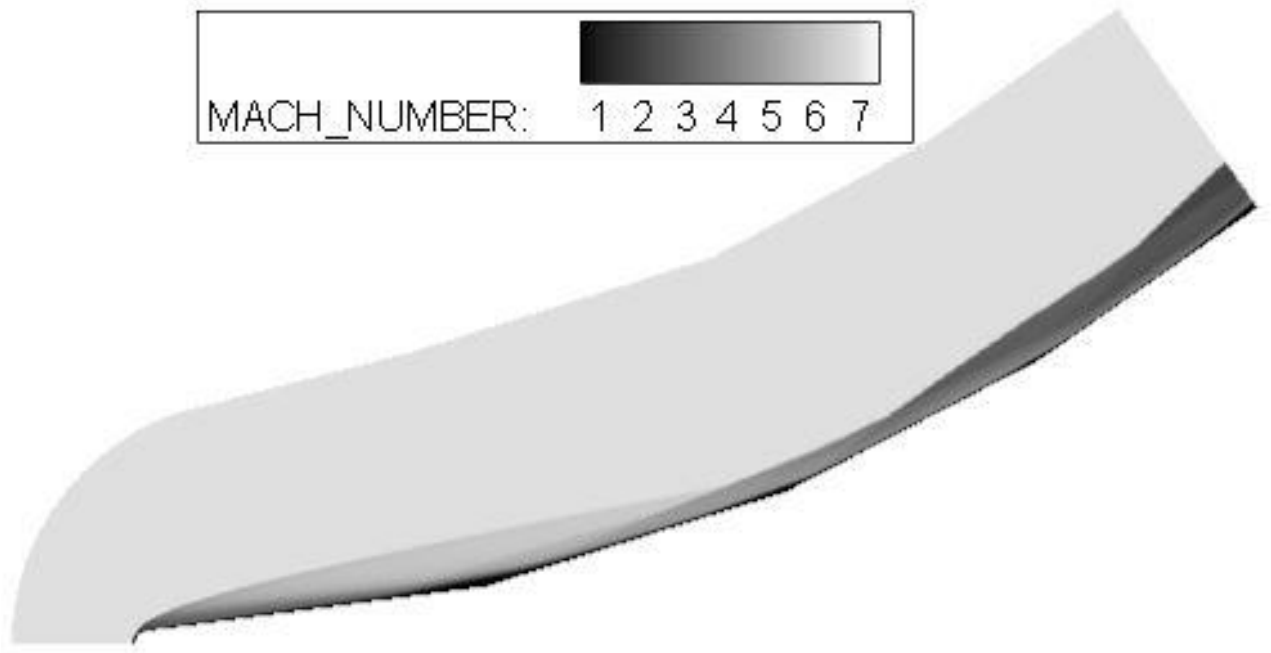
B-29.Triple Ramp 10, Quad Ramp 7.5 at Mach 7
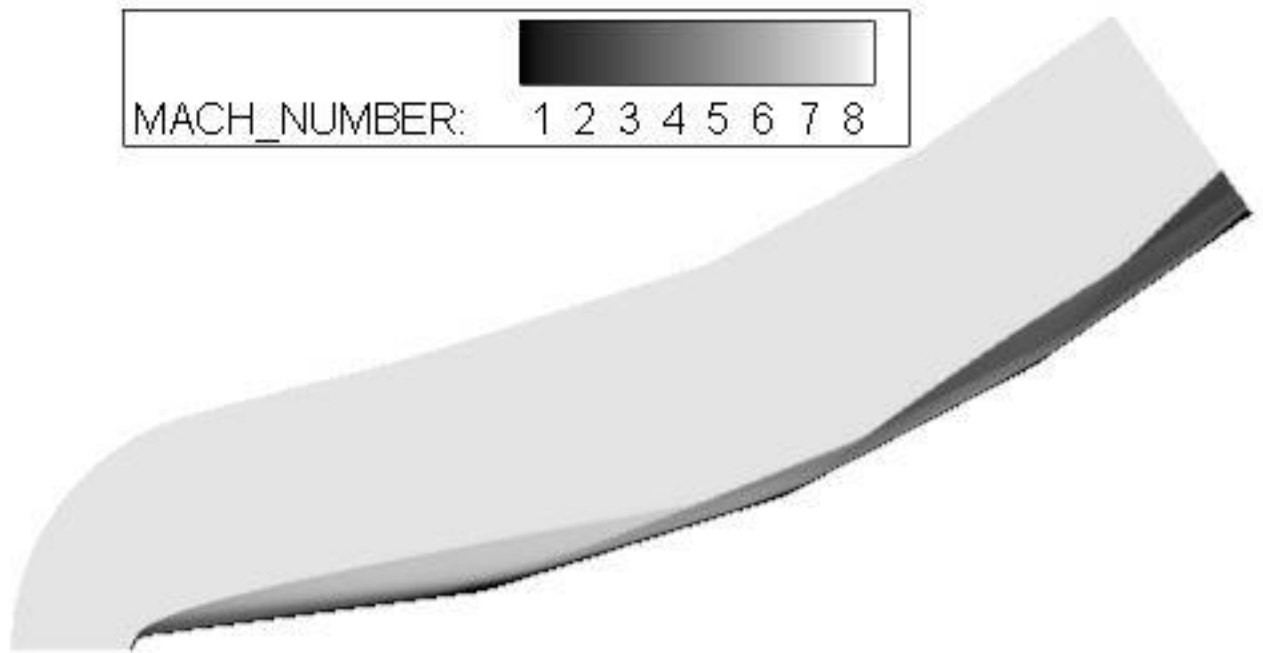
B-30.Triple Ramp 10, Quad Ramp 7.5 at Mach 8
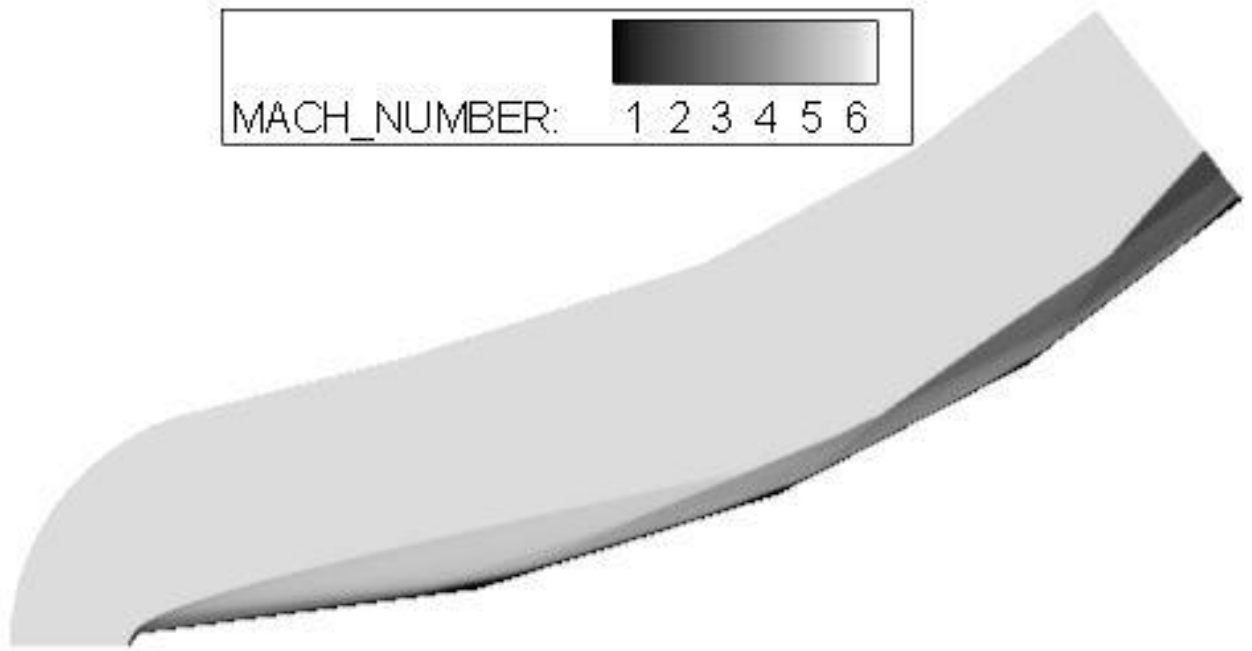
B-31.Triple Ramp 10, Quad Ramp 10 at Mach 6
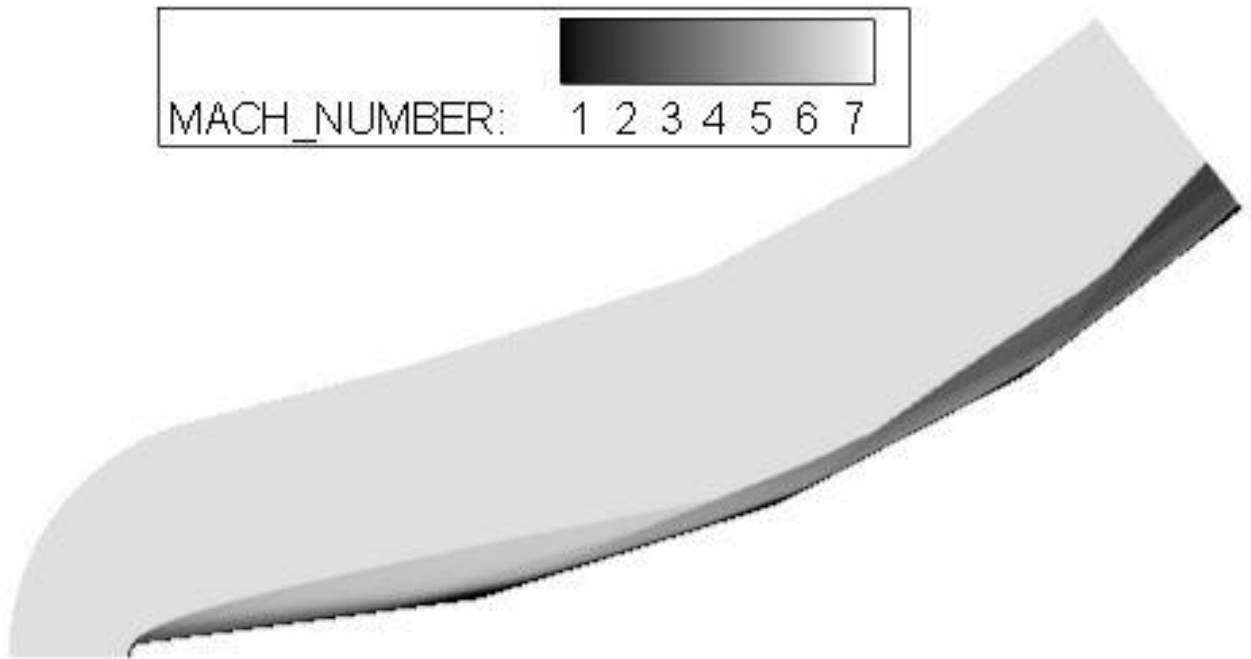
B-32.Triple Ramp 10, Quad Ramp 10 at Mach 7
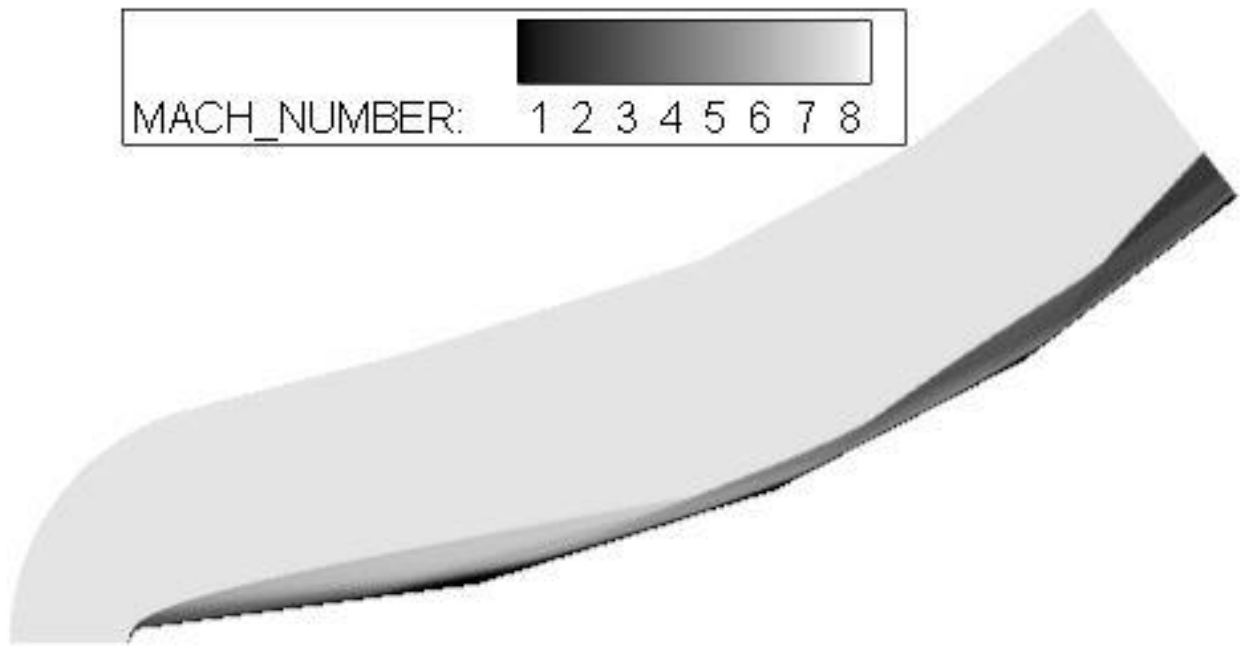
B-33.Triple Ramp 10, Quad Ramp 10 at Mach 8
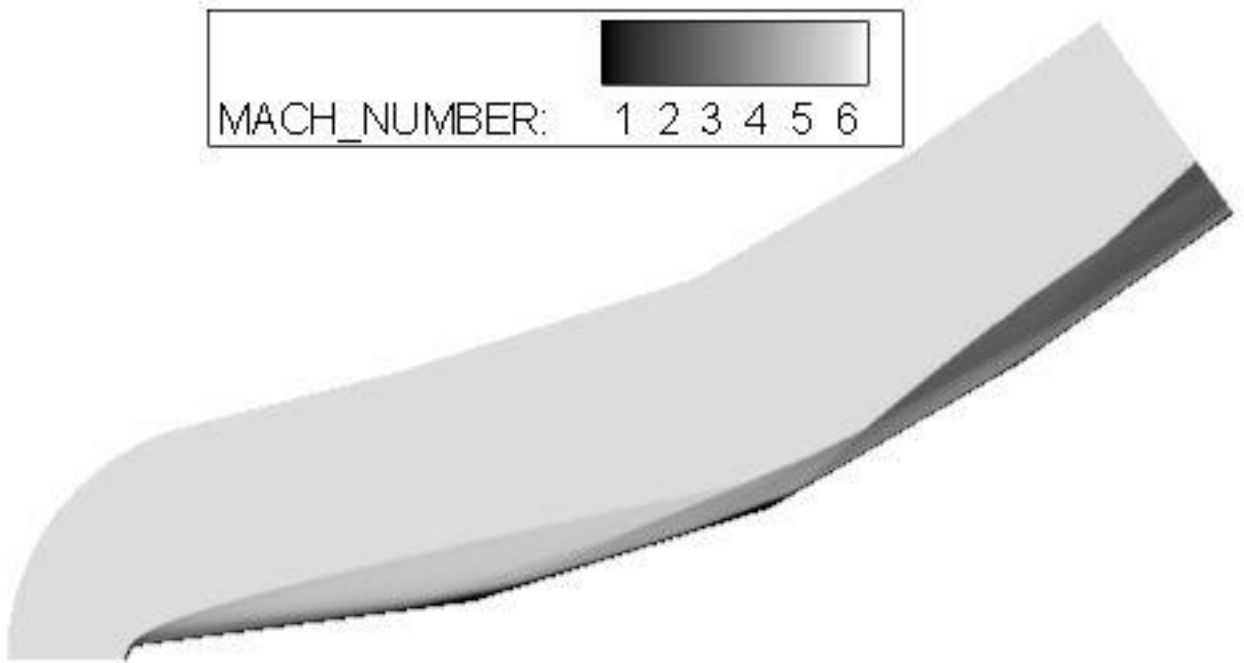
B-34.Triple Ramp 12.5, Quad Ramp 5 at Mach 6
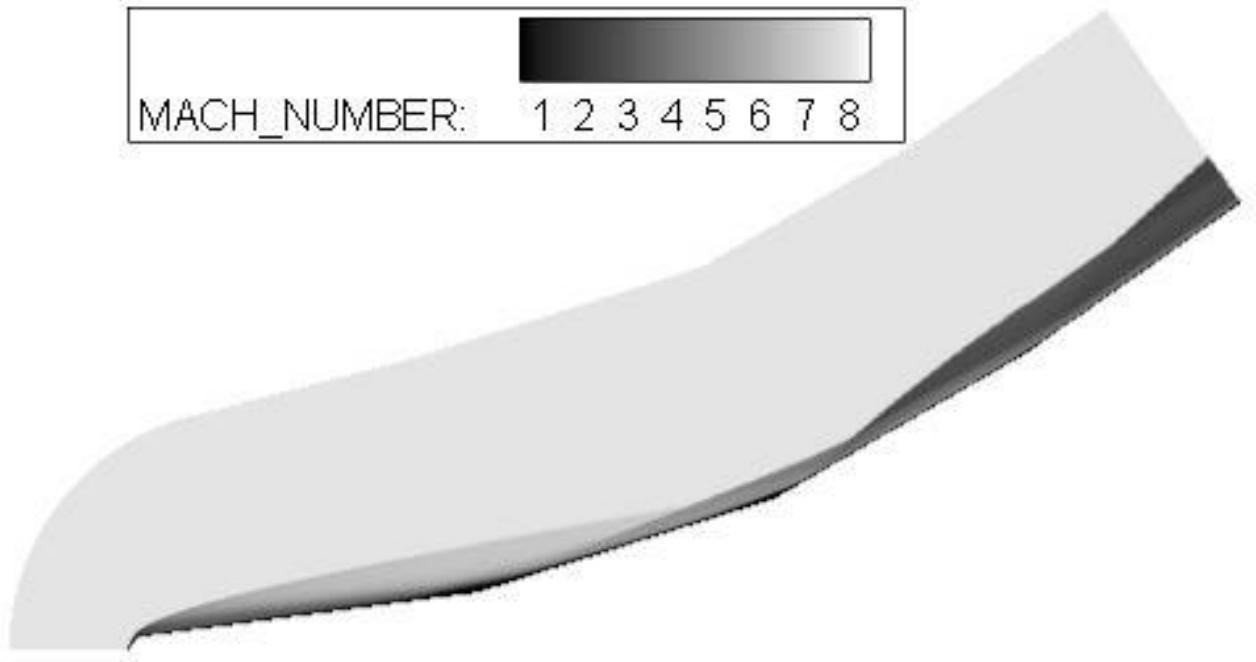
B-35.Triple Ramp 12.5, Quad Ramp 5 at Mach 7
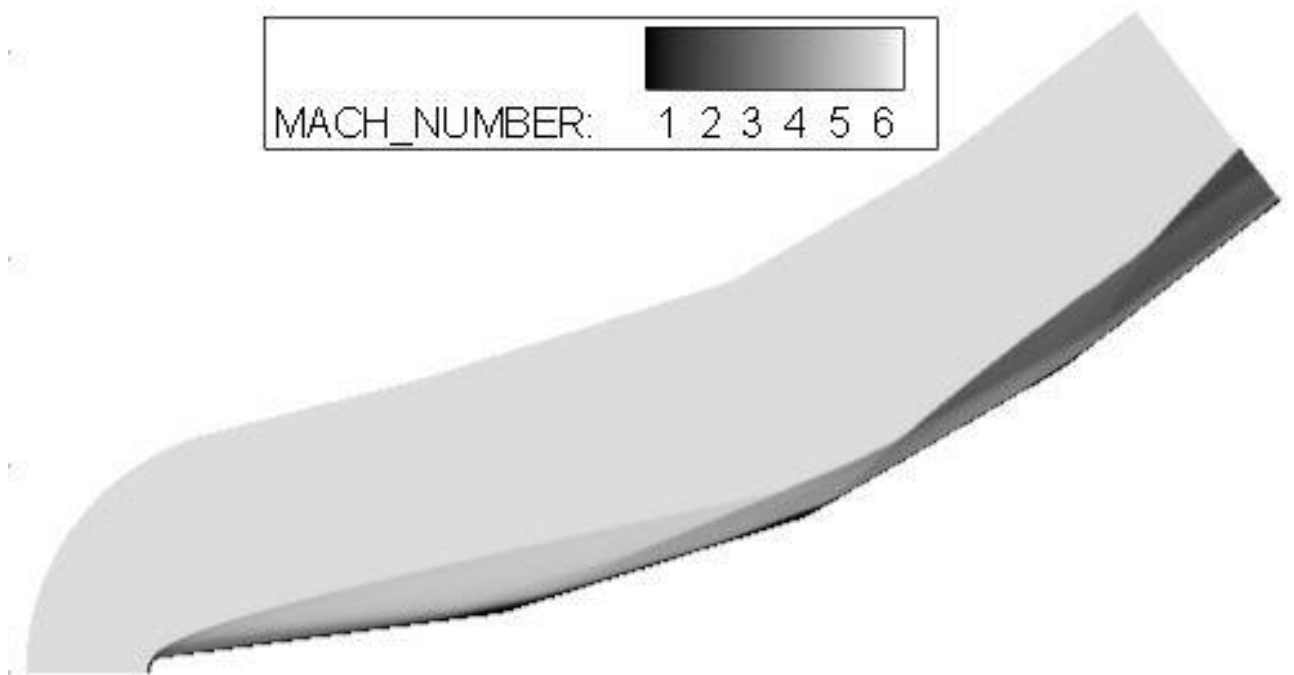
B-36.Triple Ramp 12.5, Quad Ramp 7.5 at Mach 6

MACH_NUMBER: 1 2 3 4 5 6 7
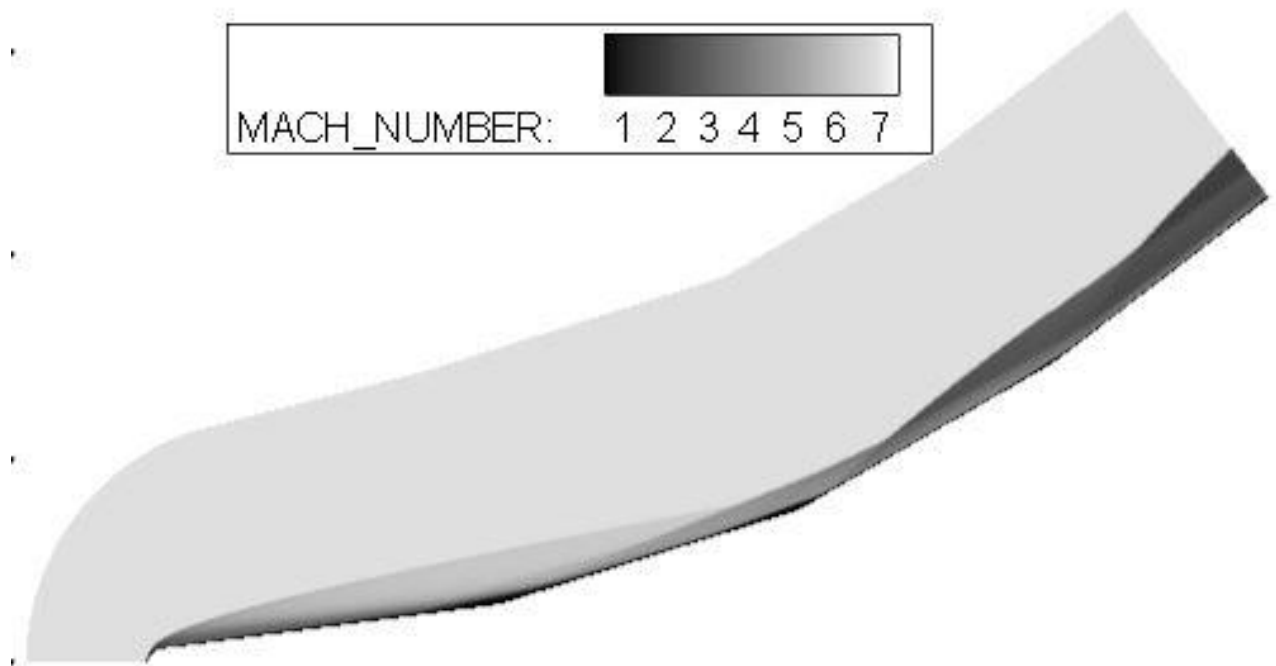
B-37.Triple Ramp 12.5, Quad Ramp 7.5 at Mach 7

MACH_NUMBER: 1 2 3 4 5 6 7 8
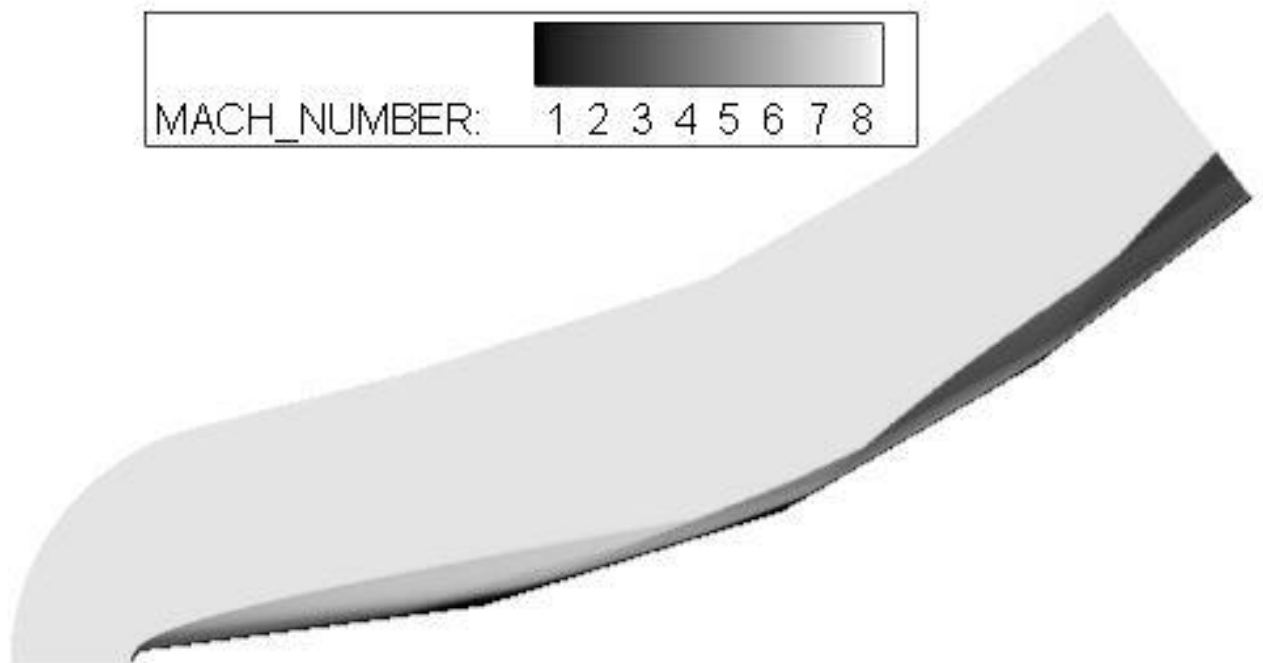
B-38.Triple Ramp 12.5, Quad Ramp 7.5 at Mach 8
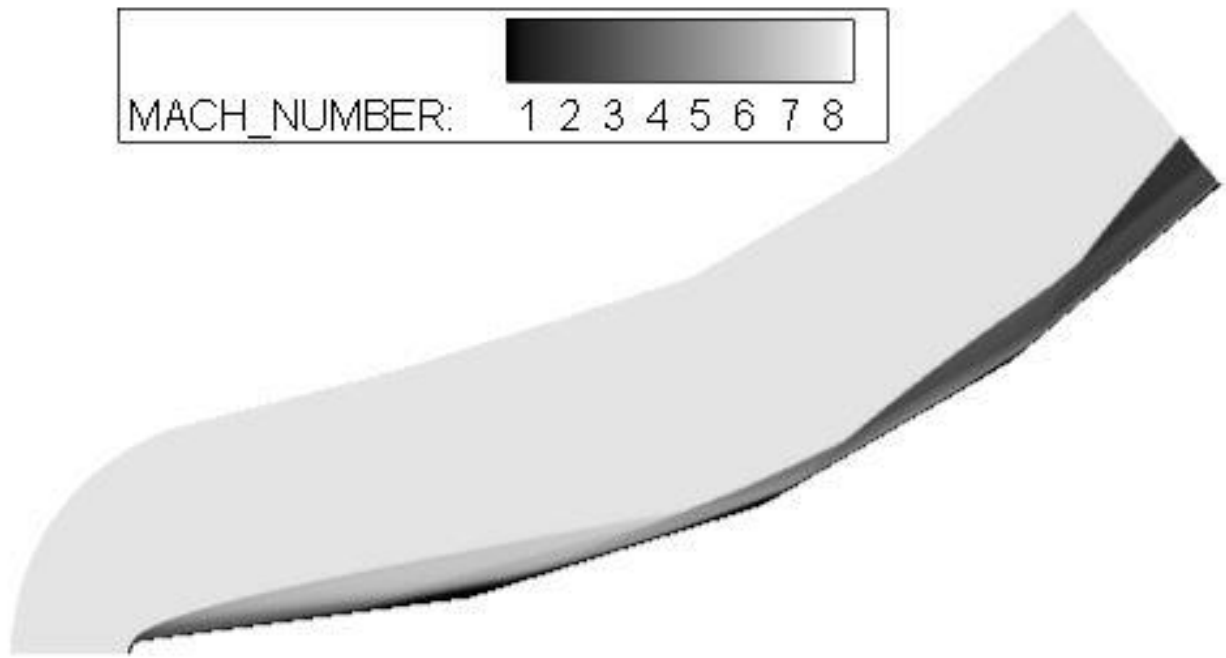
B-39.Triple Ramp 12.5, Quad Ramp 10 at Mach 8
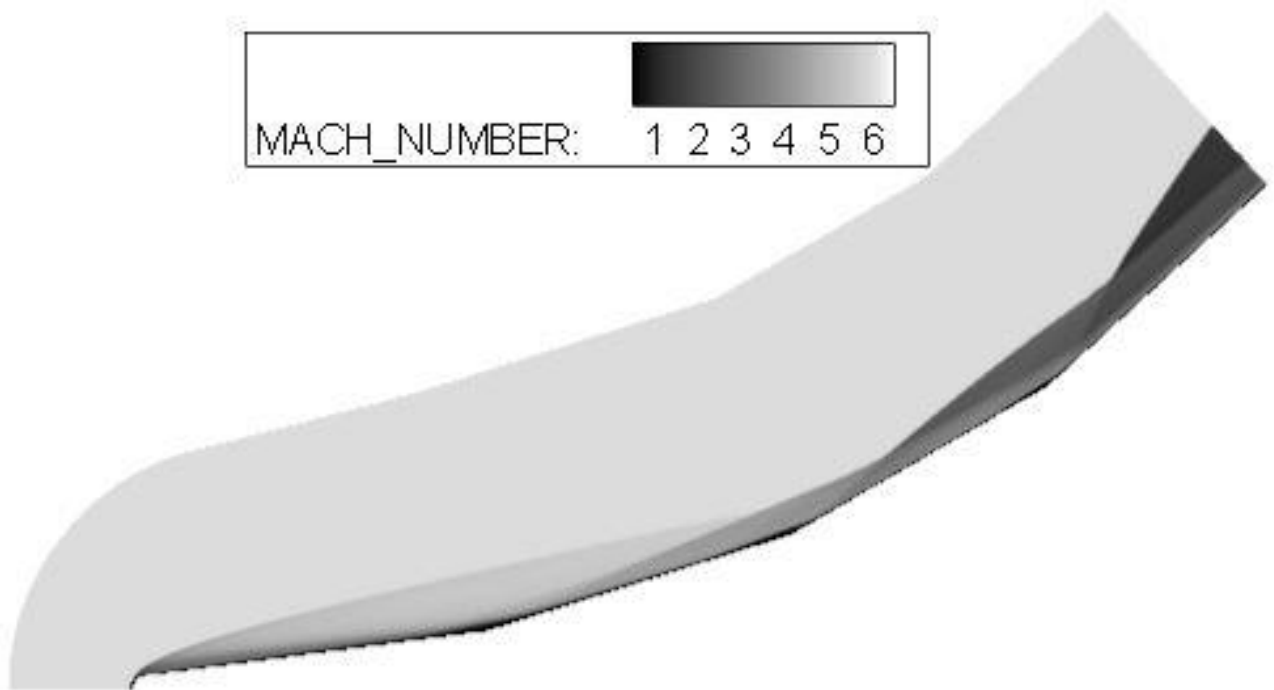
B-40.Triple Ramp 12.5, Quad Ramp 12.5 at Mach 6
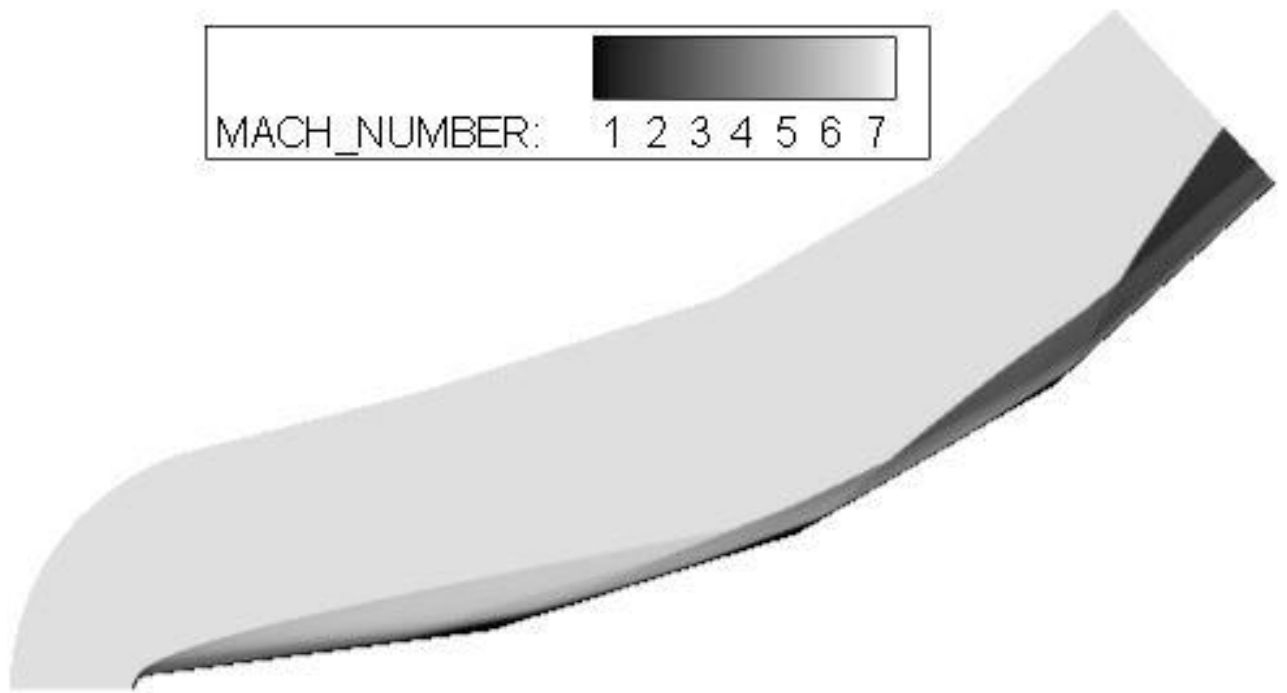
B-41.Triple Ramp 12.5, Quad Ramp 12.5 at Mach 7
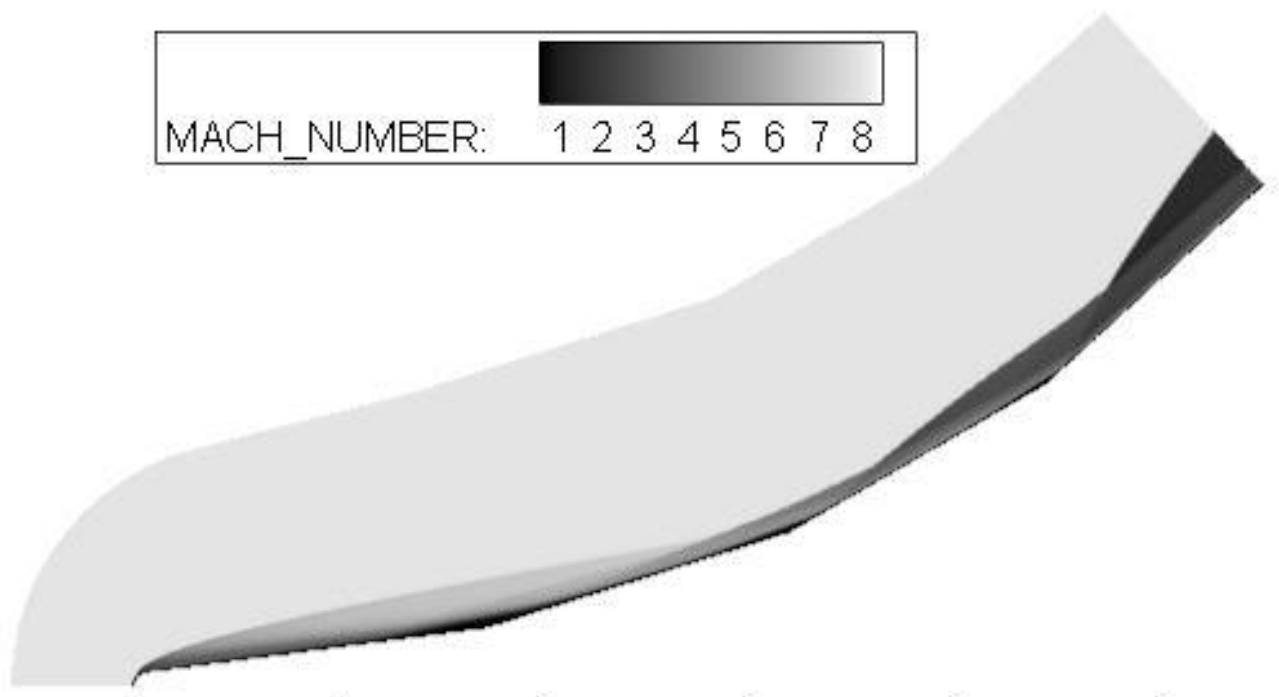
B-42.Triple Ramp 12.5, Quad Ramp 12.5 at Mach 8
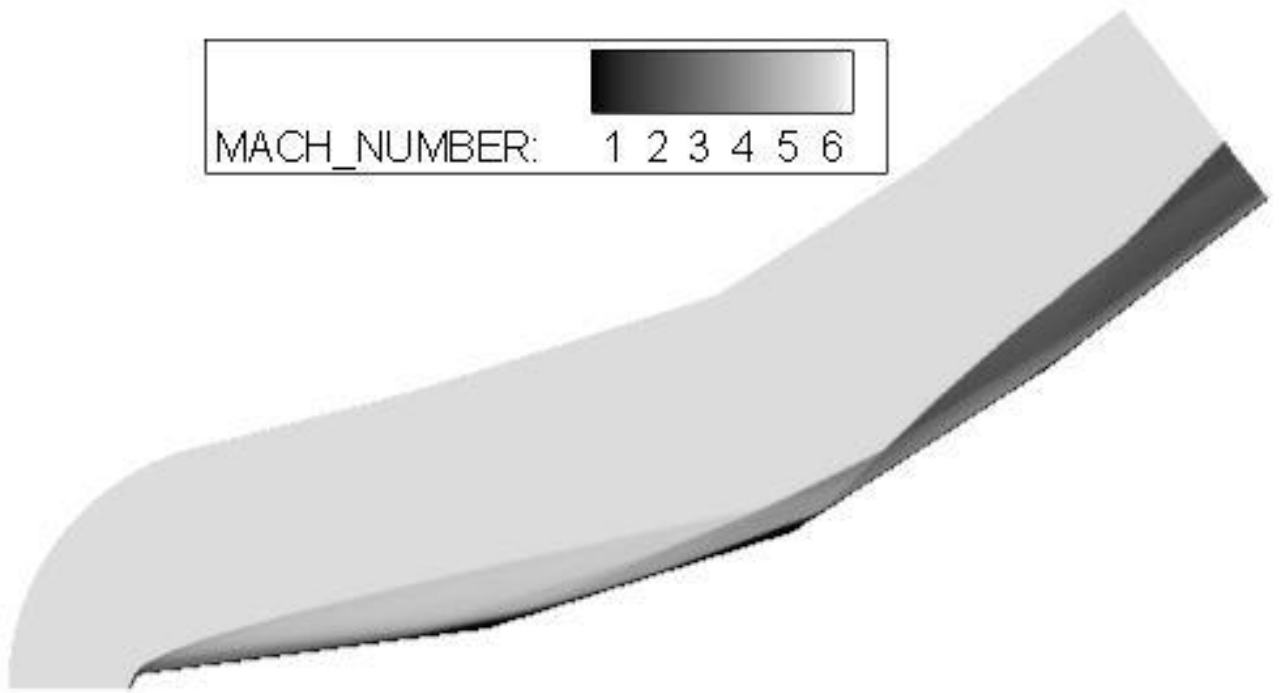
B-43.Triple Ramp 15, Quad Ramp 5 at Mach 6
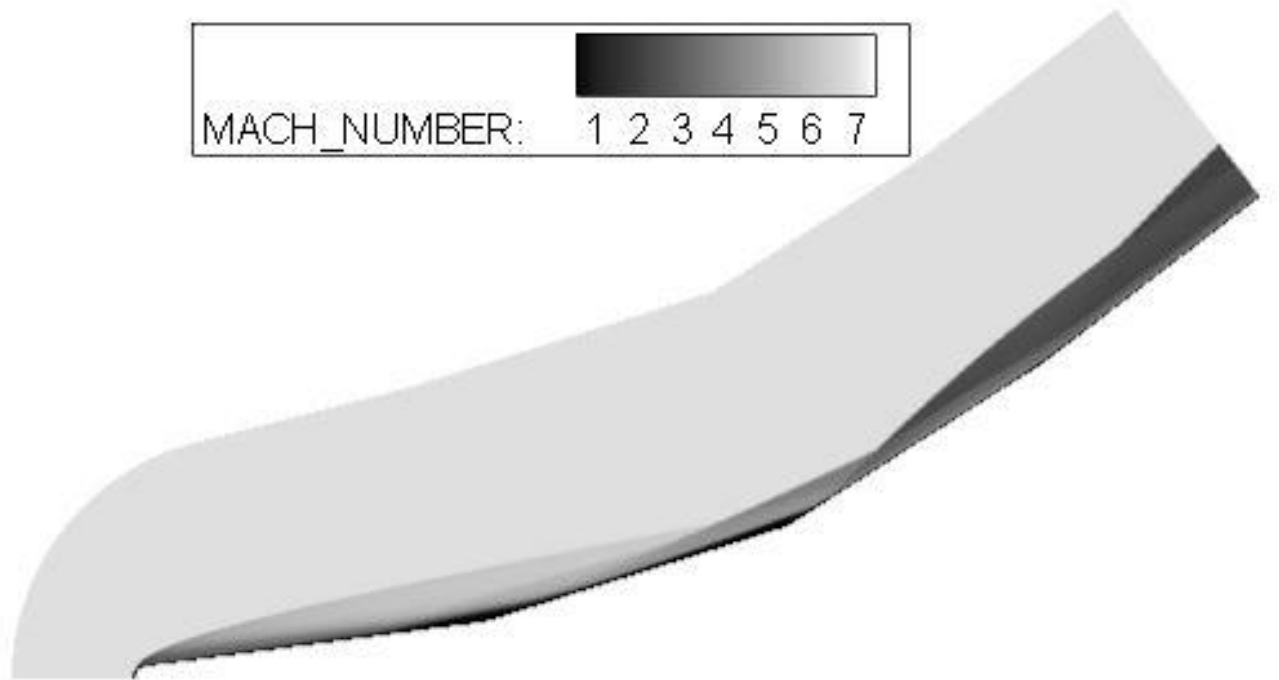
B-44.Triple Ramp 15, Quad Ramp 5 at Mach 7
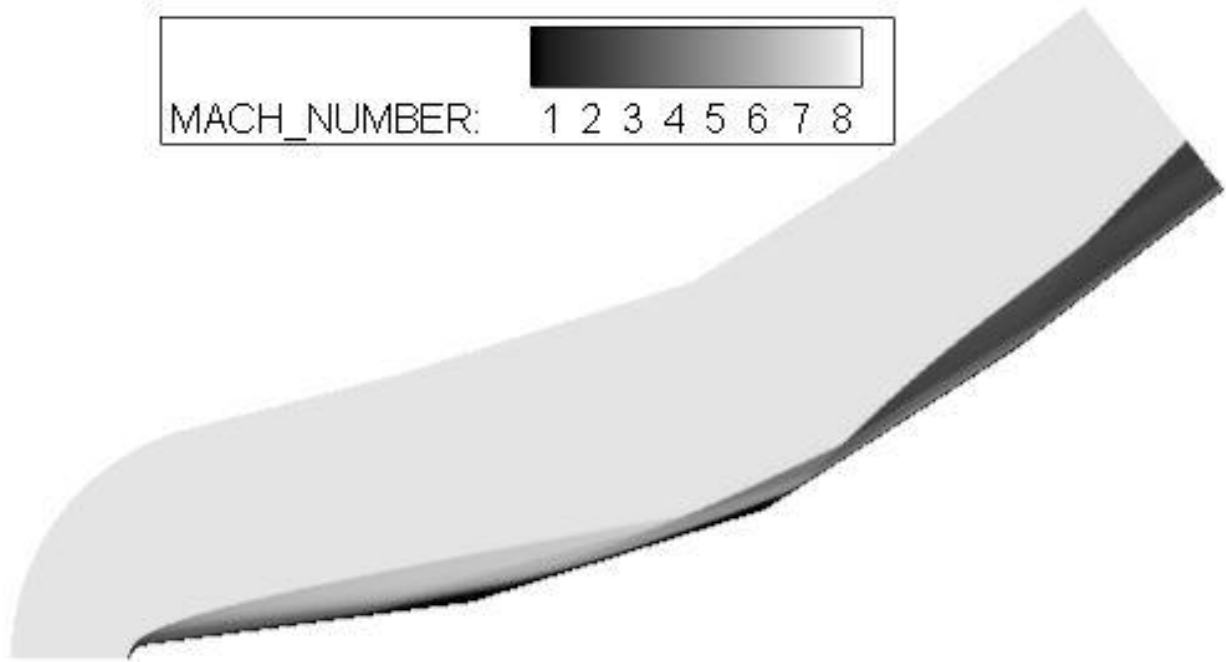
B-45.Triple Ramp 15, Quad Ramp 5 at Mach 8
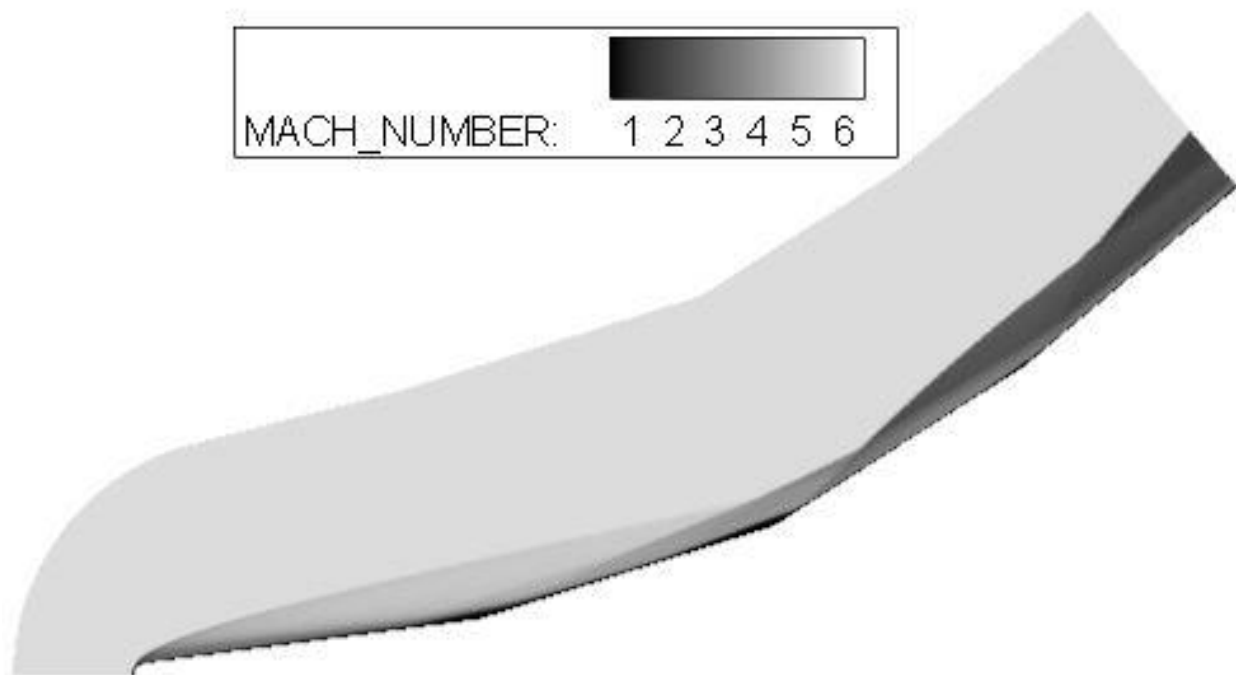
B-46.Triple Ramp 15, Quad Ramp 7.5 at Mach 6
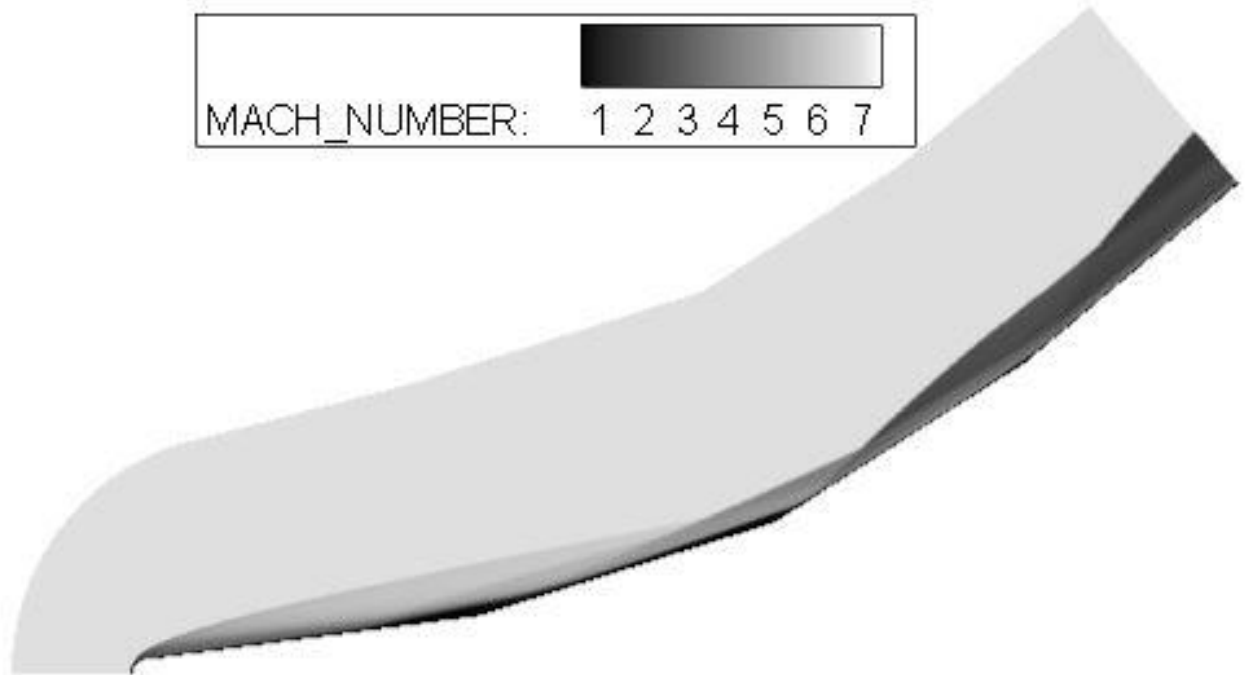
B-47.Triple Ramp 15, Quad Ramp 7.5 at Mach 7
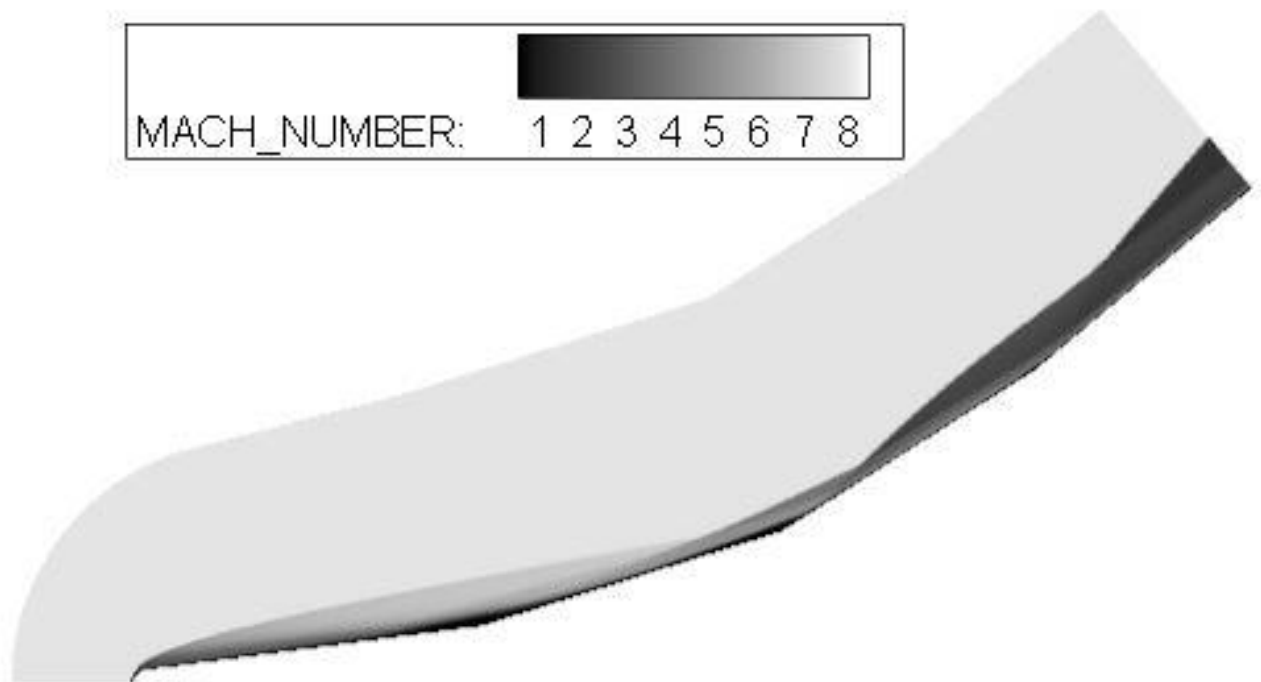
B-48.Triple Ramp 15, Quad Ramp 7.5 at Mach 8
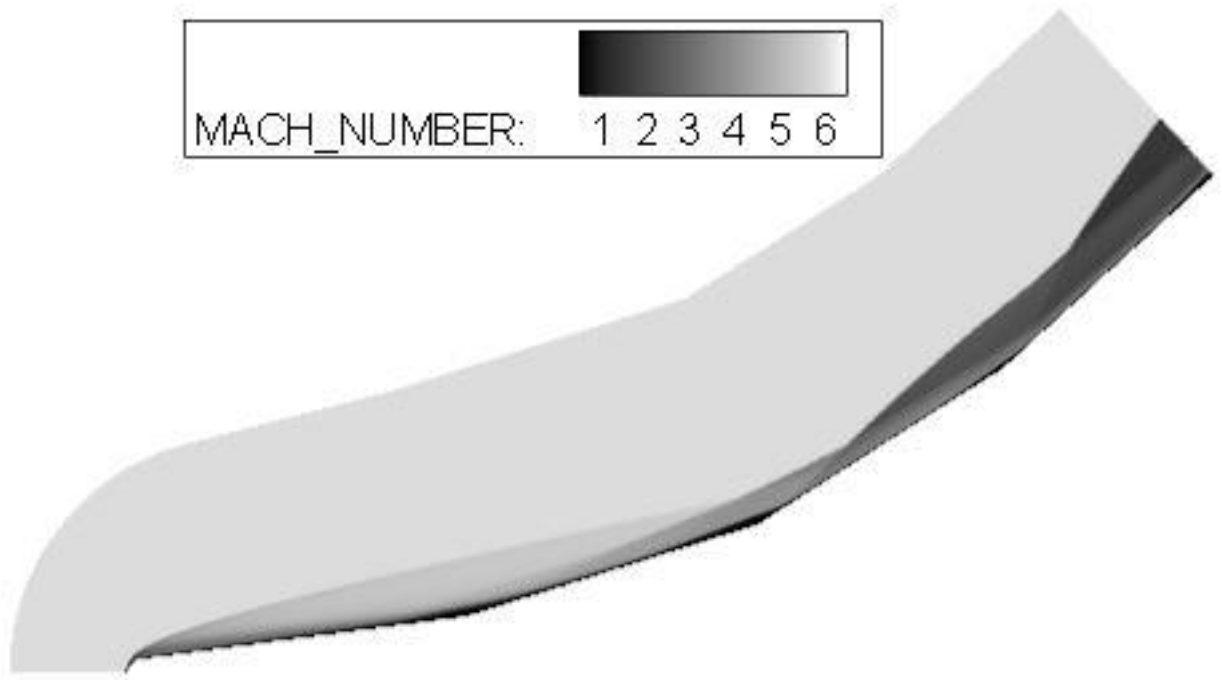
B-49.Triple Ramp 15, Quad Ramp 10 at Mach 6
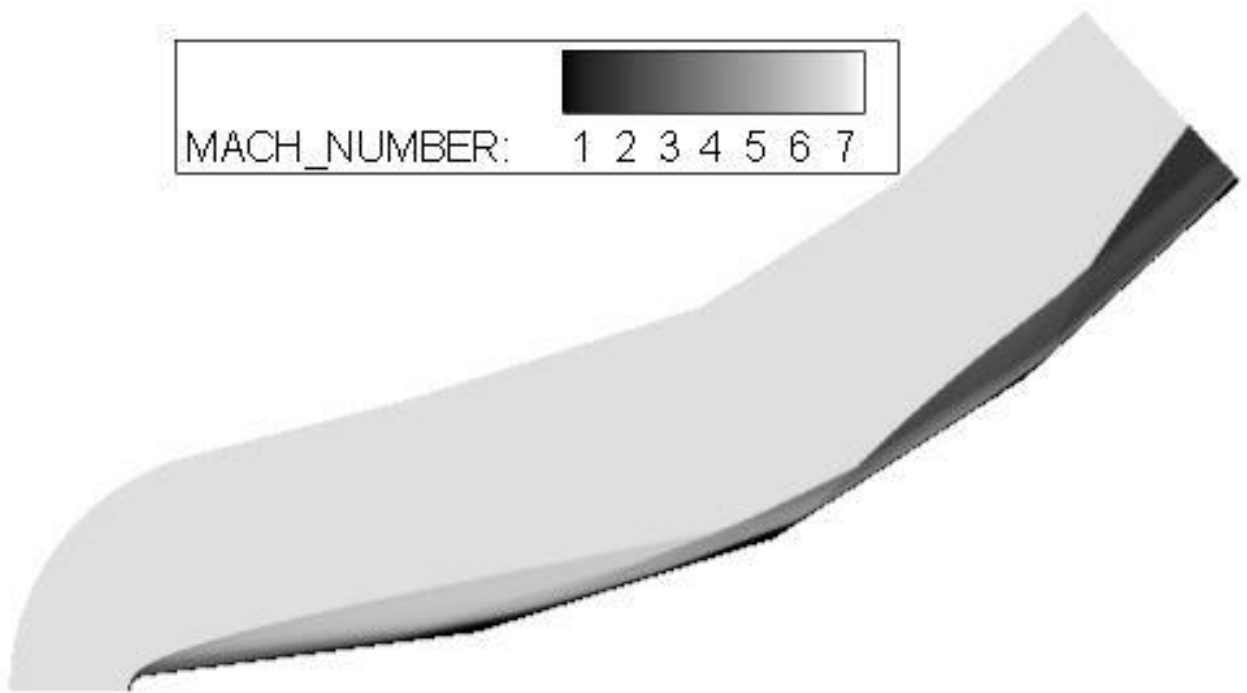
B-50.Triple Ramp 15, Quad Ramp 10 at Mach 7
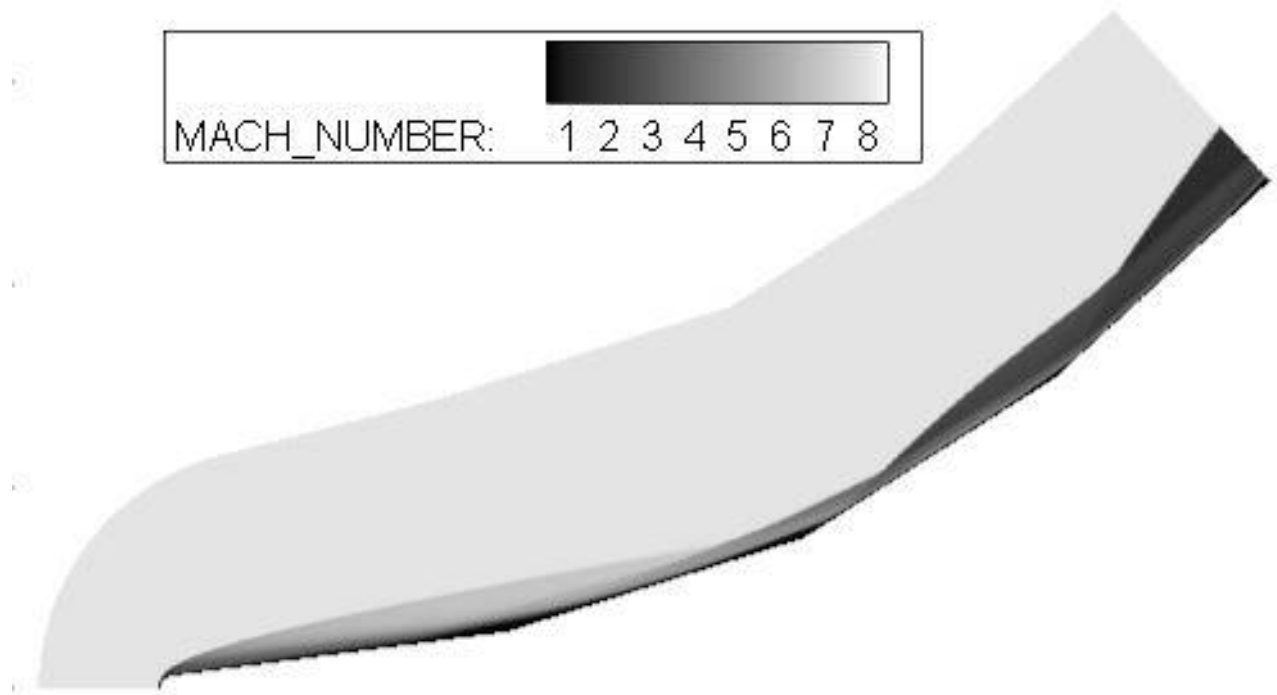
B-51.Triple Ramp 15, Quad Ramp 10 at Mach 8

B-52.Triple Ramp 15, Quad Ramp 12.5 at Mach 6

127

MACH_NUMBER: 1 2 3 4 5 6 7
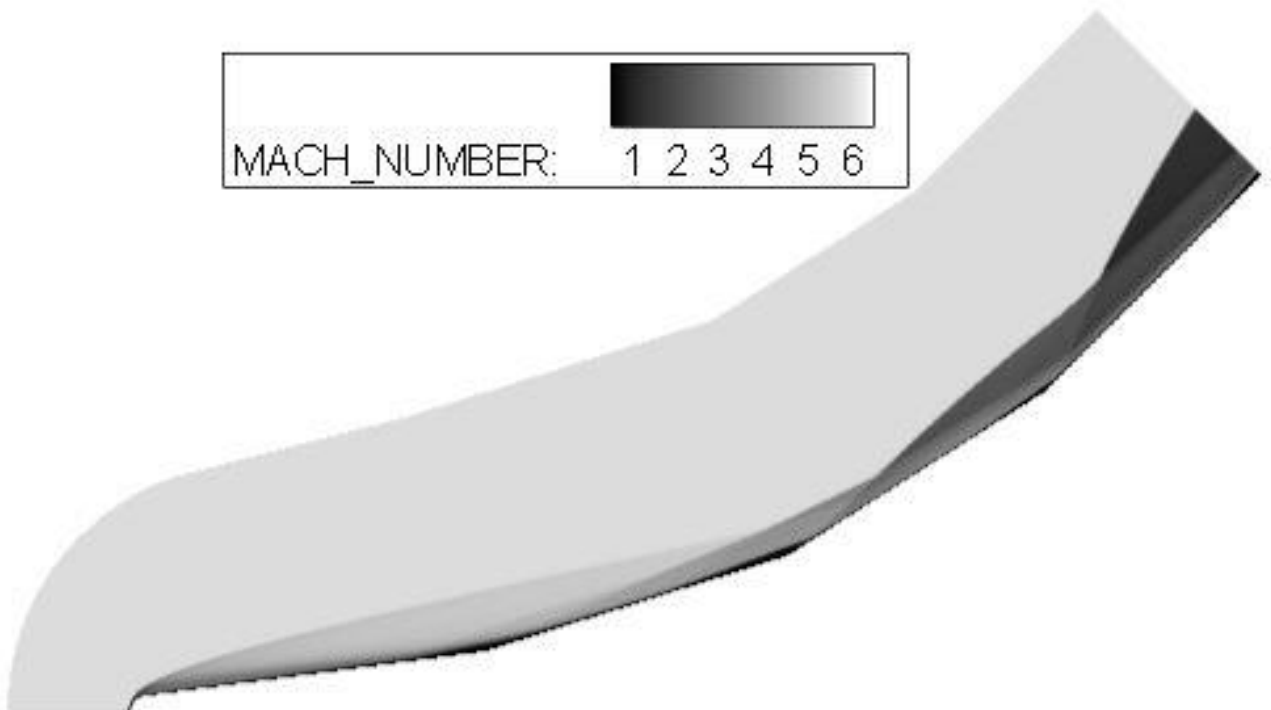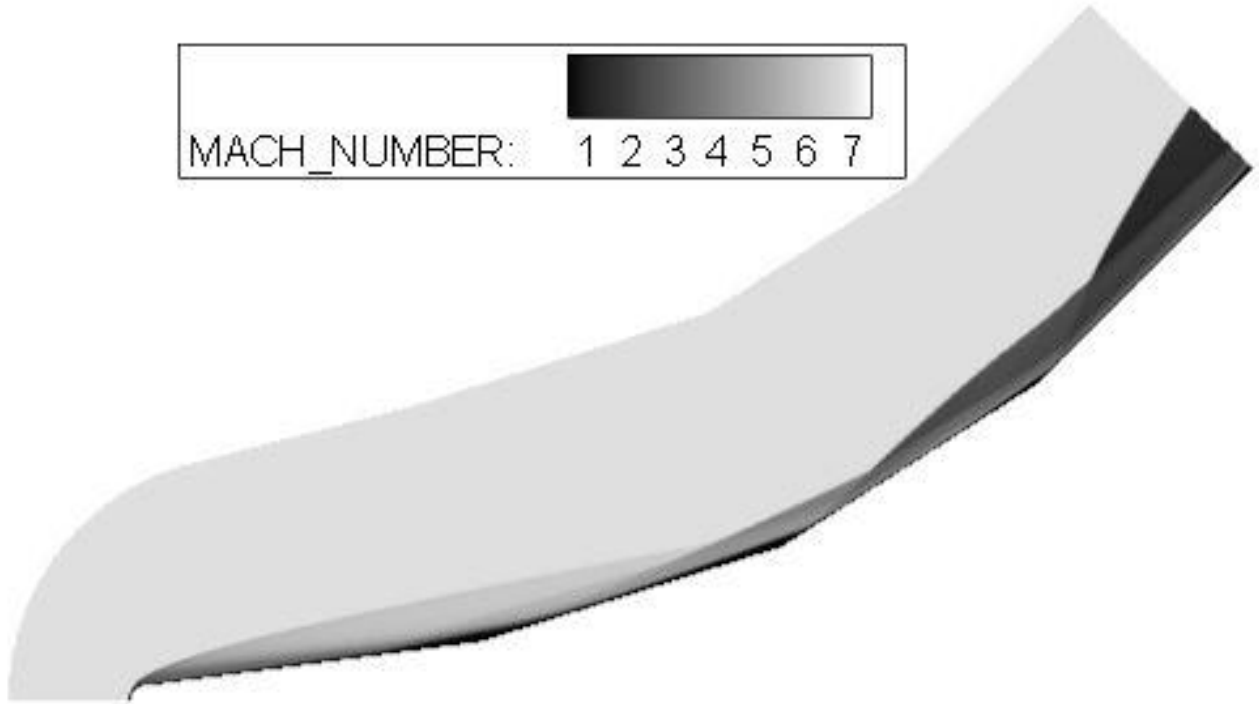
B-53.Triple Ramp 15, Quad Ramp 12.5 at Mach 7

MACH_NUMBER: 1 2 3 4 5 6 7 8
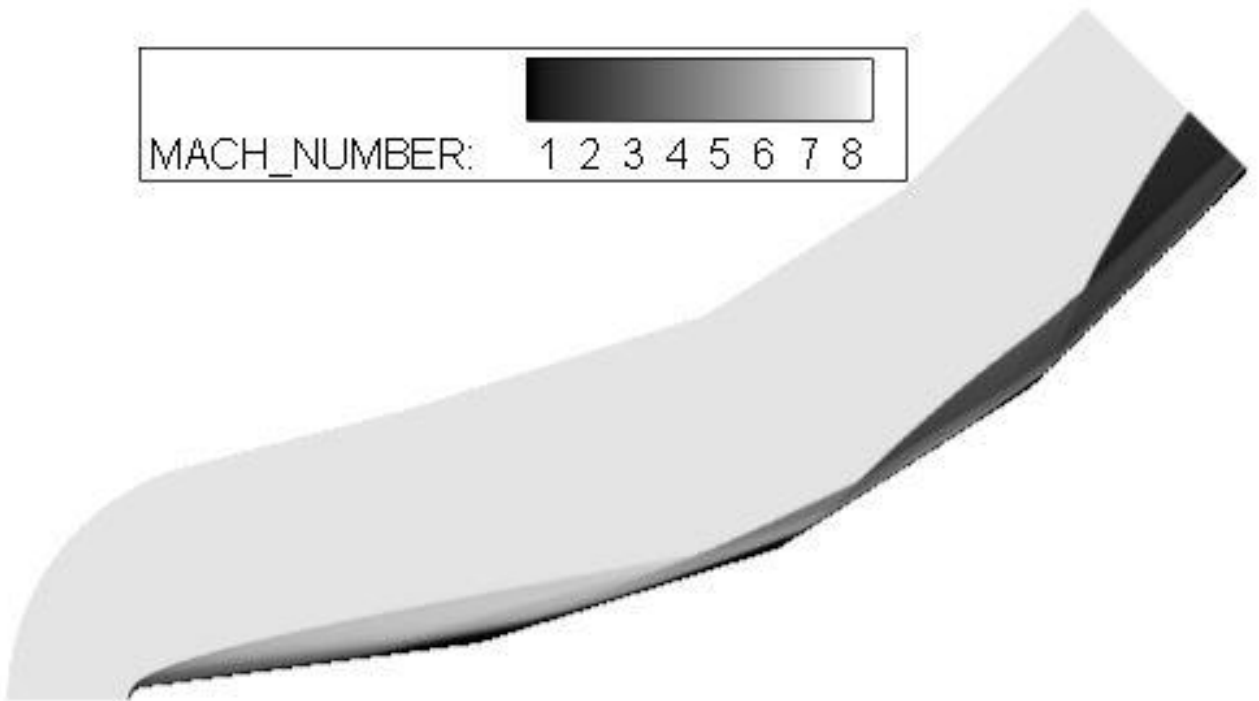
B-54.Triple Ramp 15, Quad Ramp 12.5 at Mach 8

B.3 VARYING LEADING EDGE BLUNTNESS
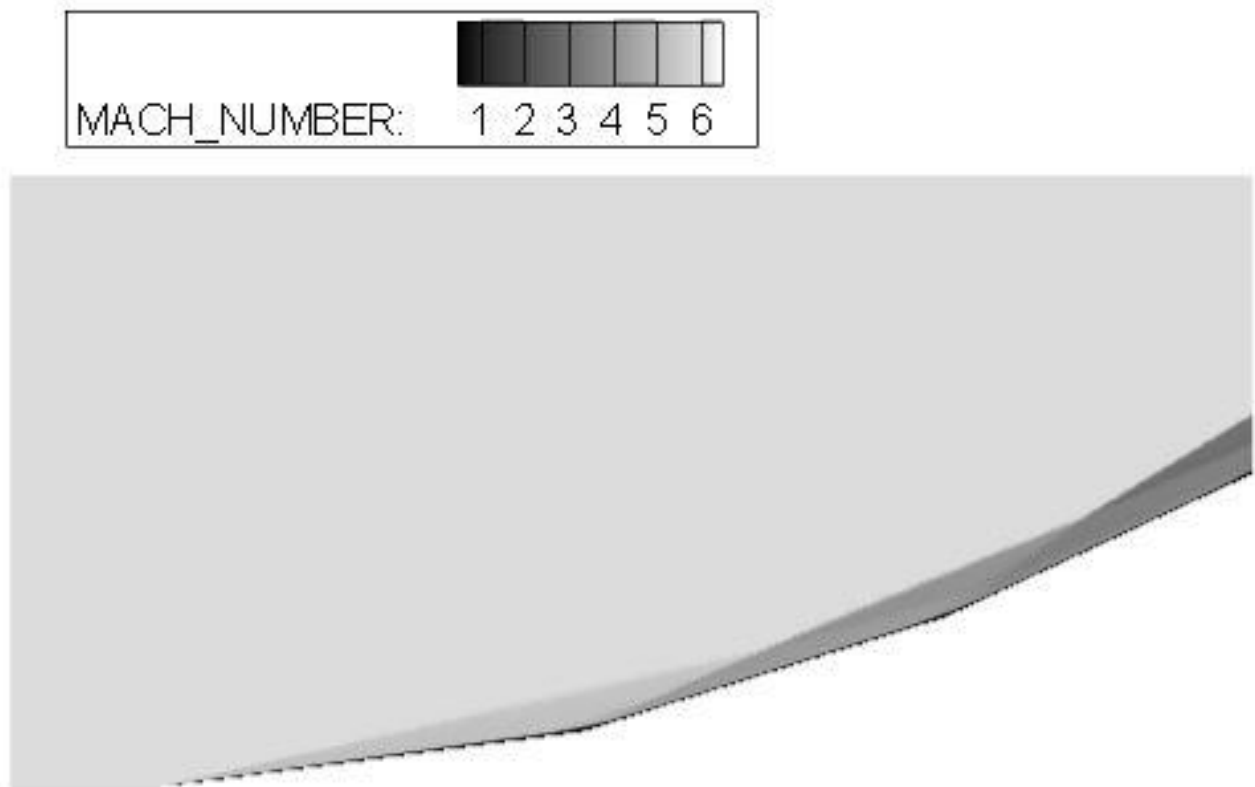
B-55.Triple Ramp 7.5 with Zero Bluntness
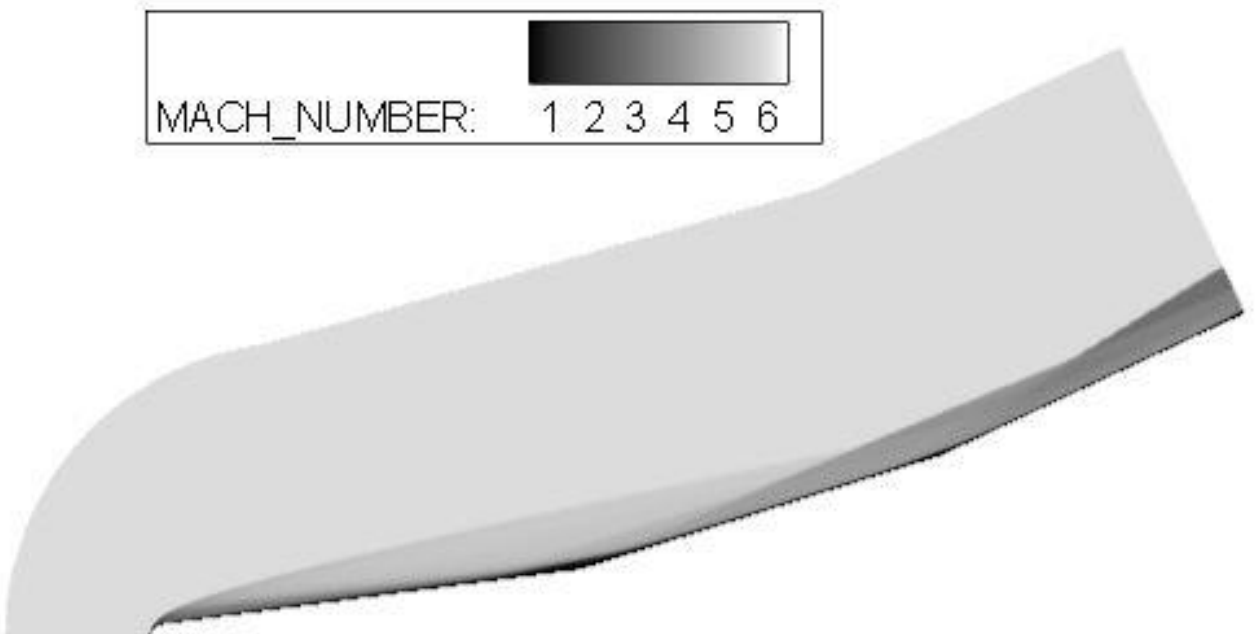
B-56.Triple Ramp 7.5 with 2.5mm Blunt radius
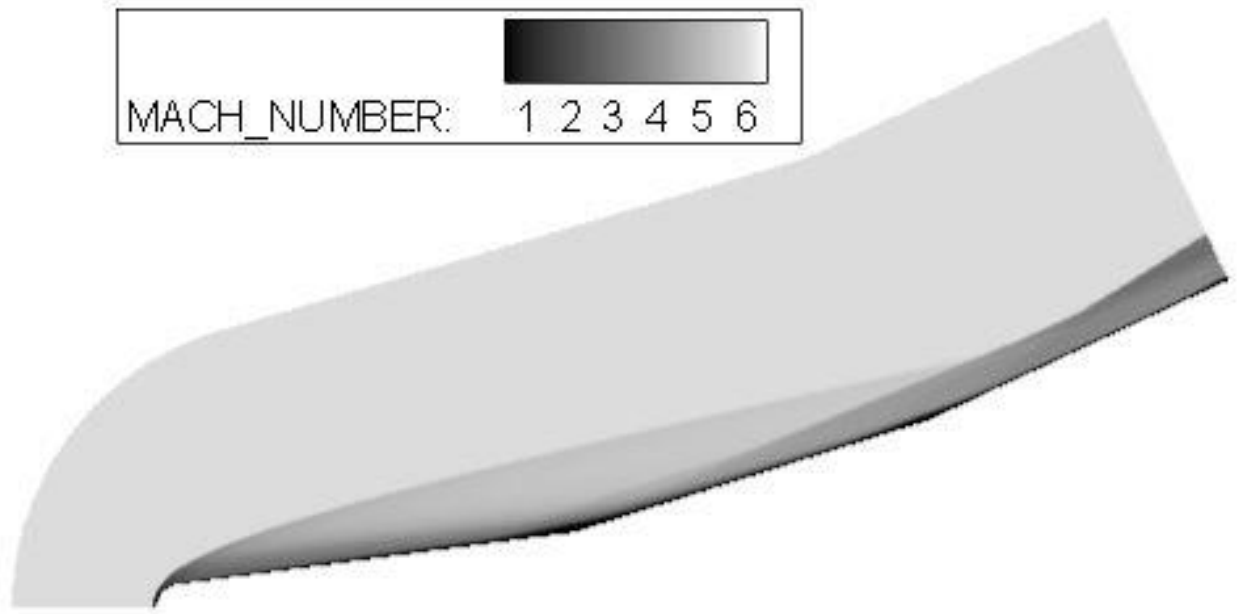
B-57.Triple Ramp 7.5 with 5mm Blunt radius
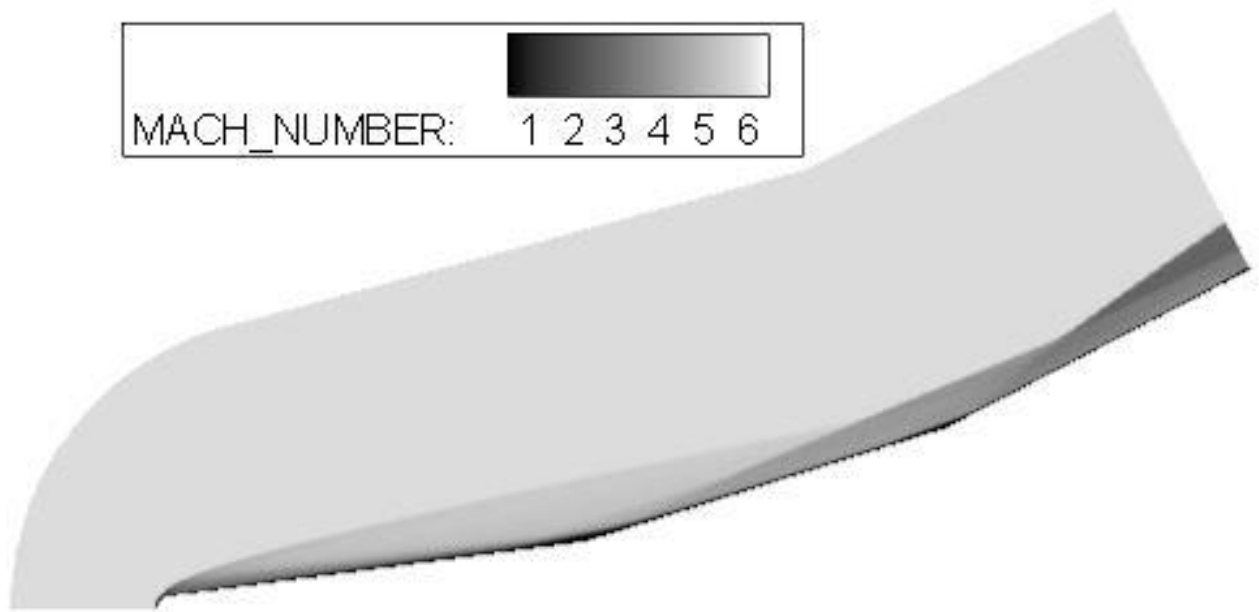
B-58.Triple Ramp 10 with 2.5mm Blunt radius
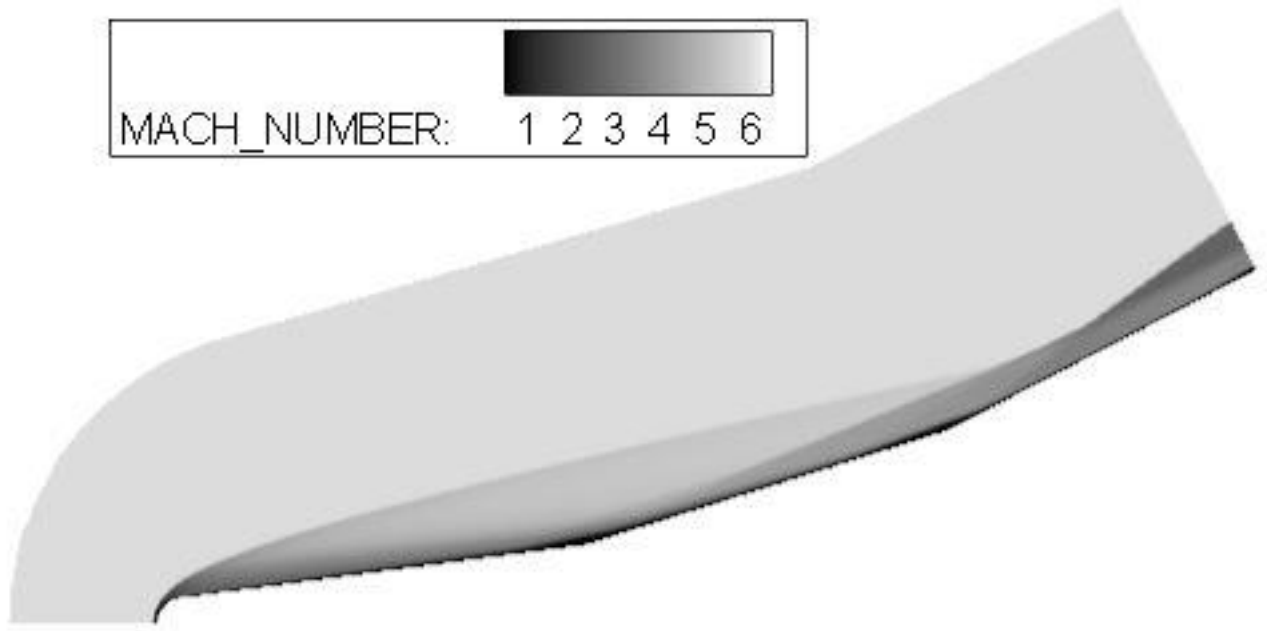
B-59.Triple Ramp 10 with 5mm Blunt radius
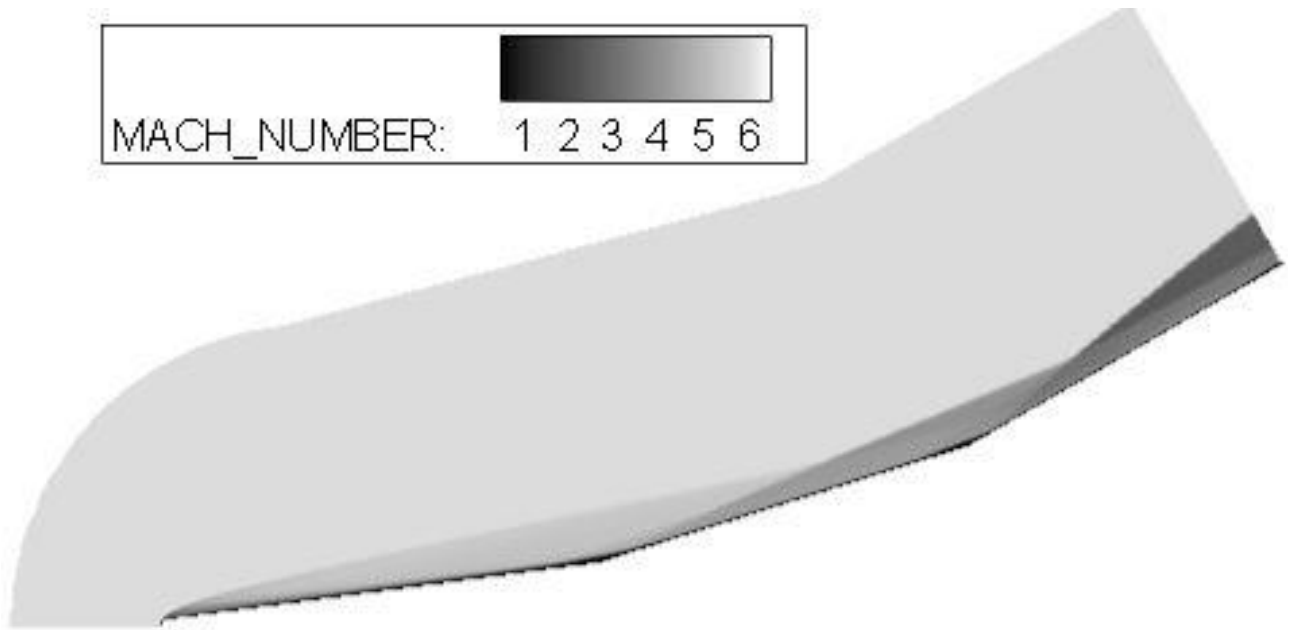
B-60.Triple Ramp 12.5 with 1.5mm Blunt radius
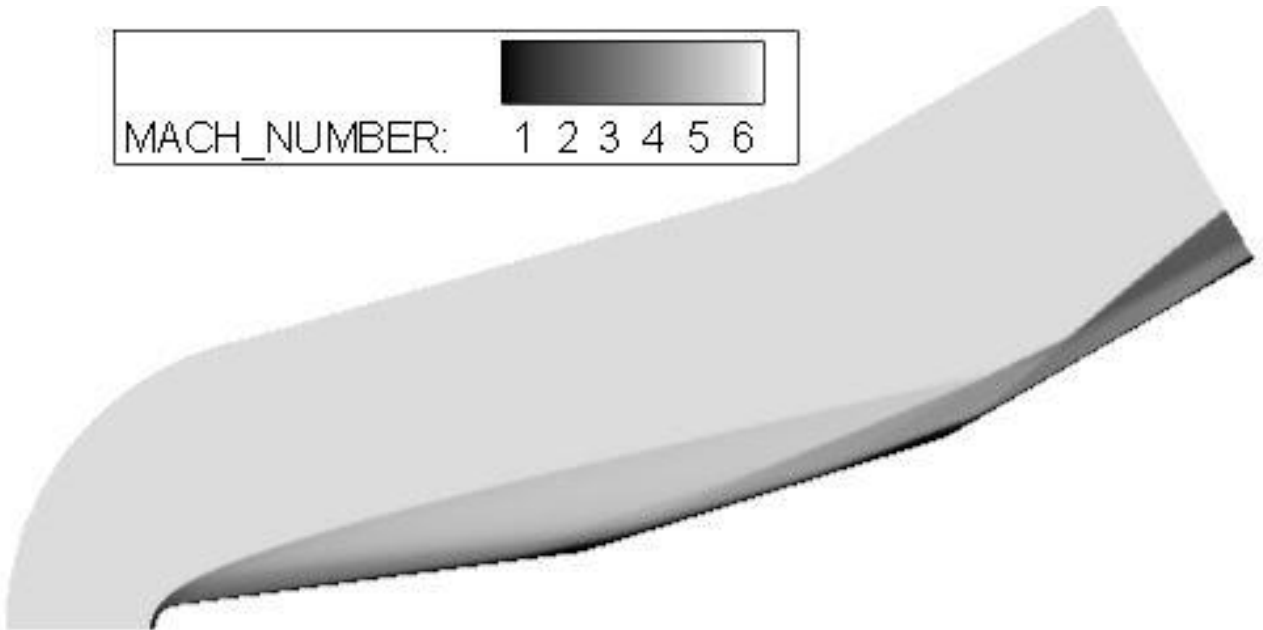
B-61.Triple Ramp 12.5 with 5mm Blunt radius
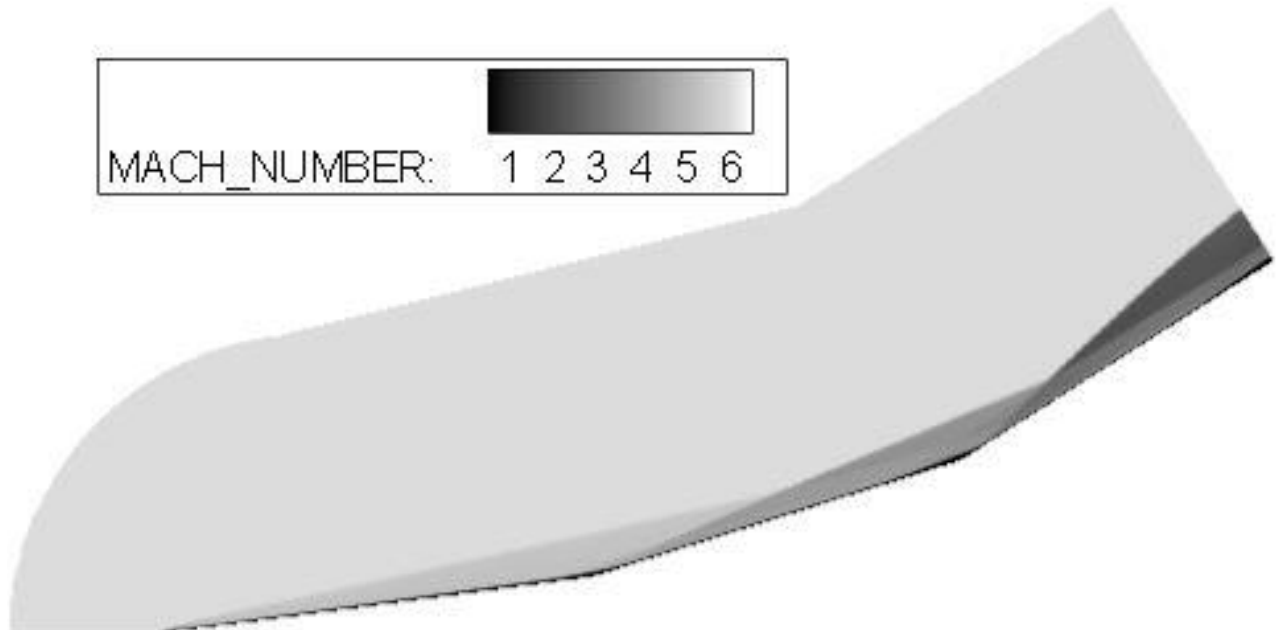
B-62.Triple Ramp 15 with 0.5mm Blunt radius
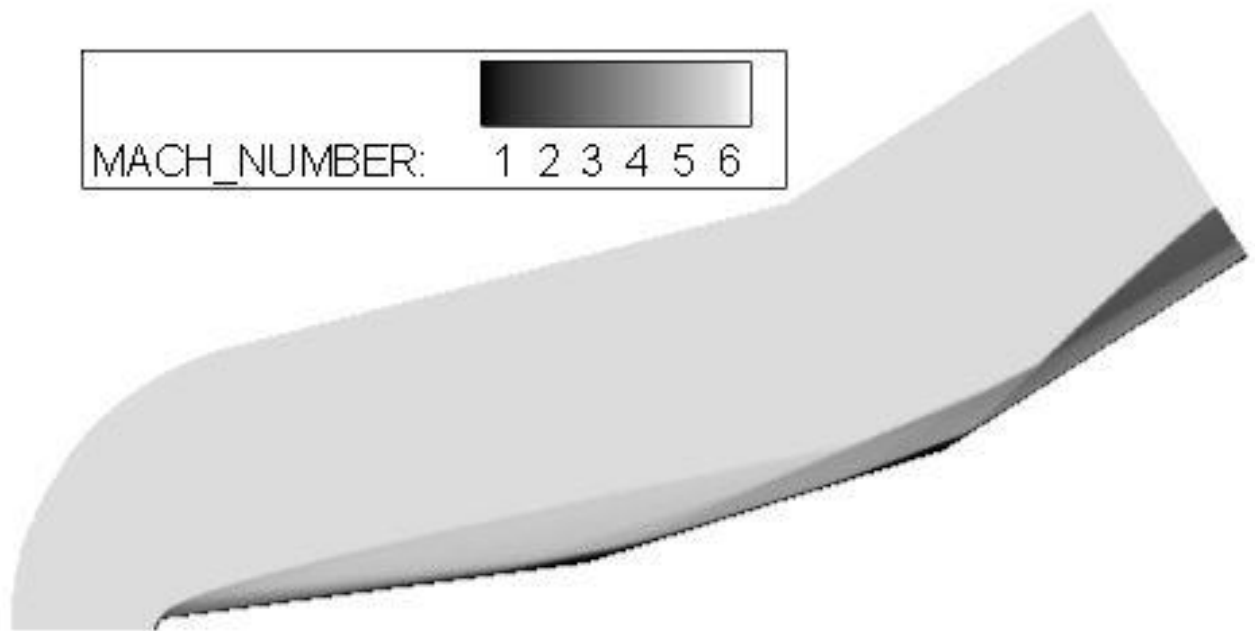
B-63.Triple Ramp 15 with 2.5mm Blunt radius

B.4 EXPERIMENTAL VALIDATION
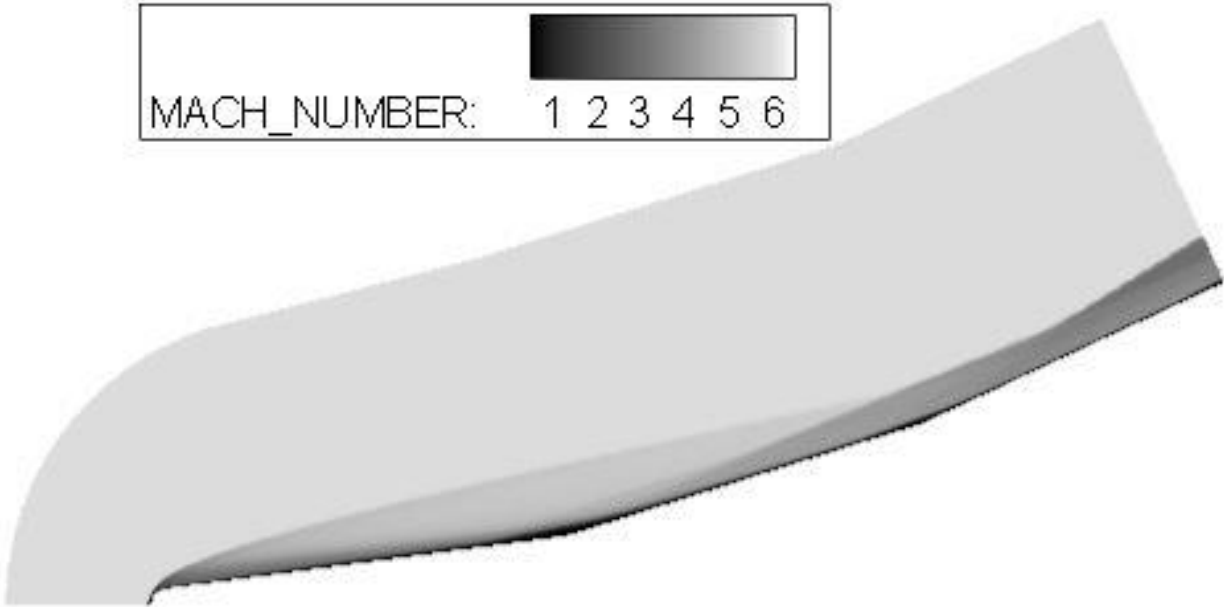
B-64.Triple Ramp 7.5
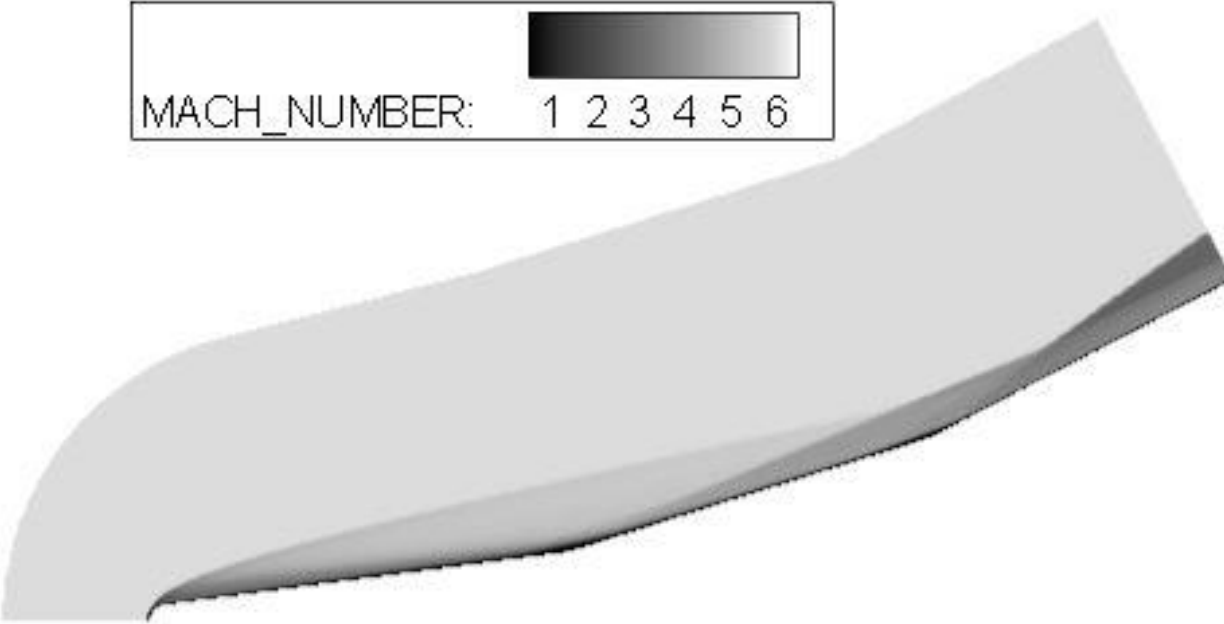
B-65.Triple Ramp 10
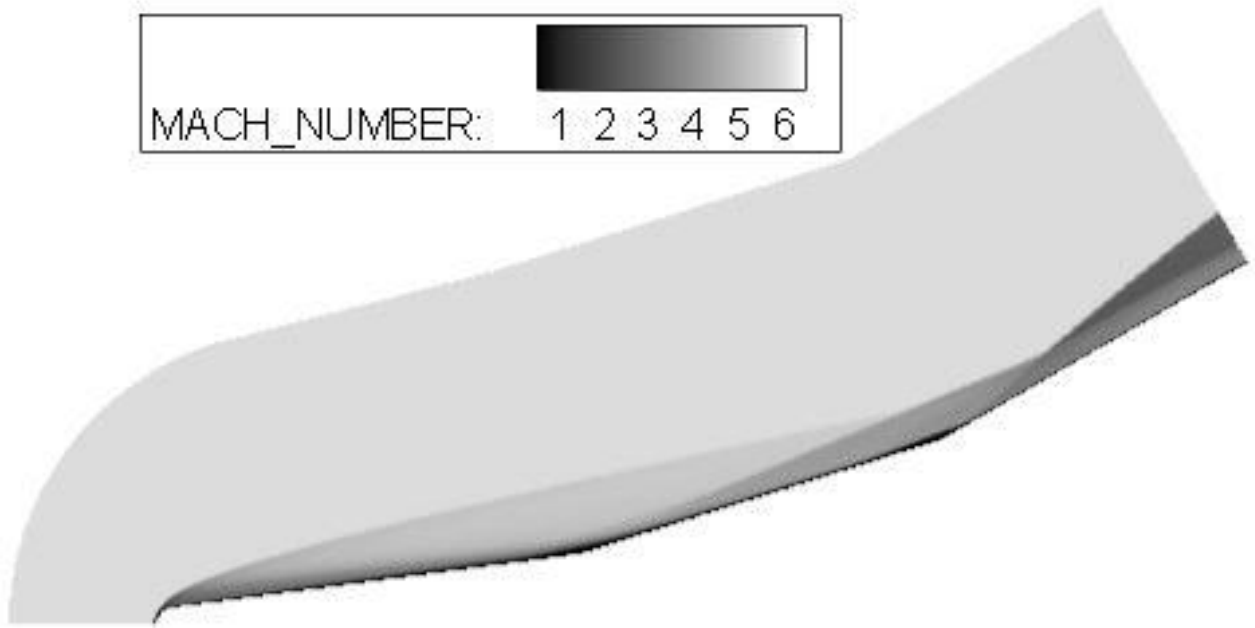
B-66.Triple Ramp 12.5
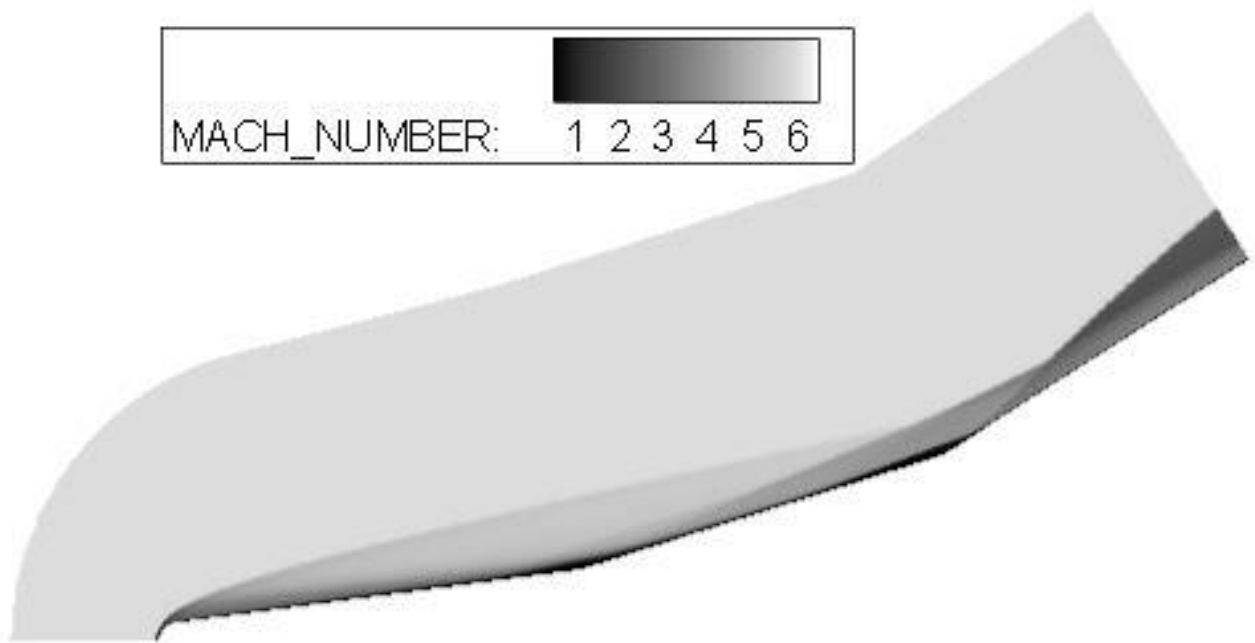
B-67.Triple Ramp 15
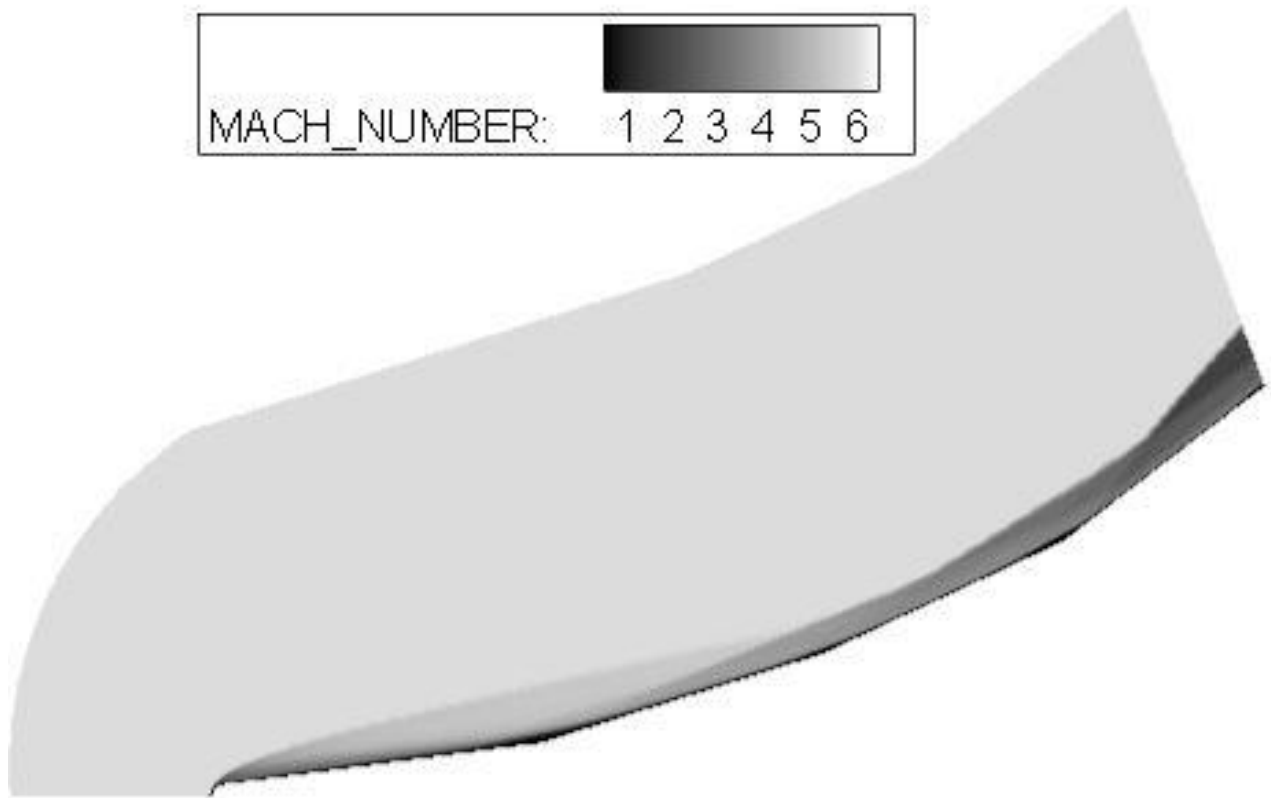
B-68.Triple Ramp 7.5, Quad Ramp 10

B.5APPENDIX C. PUBLICATIONS

(https://orcid.org)
Connecting Research and Researchers

👤 **Karthik Sundarraj** ⌄   English ⌄

Registry　　Search　　🔍

FOR RESEARCHERS(https://orcid.org/help)   **FOR ORGANIZATIONS(+)(https://orcid.org/organizations)**

✎ Karthik Sundarraj

ORCID iD

https://orcid.org/0000-0002-6743-209X

View public version (https://orcid.org/0000-0002-6743-209X)

📱 Display your iD on other sites ❓

🖨 Public record print view ❓

▦ Get a QR Code for your iD (https://orcid.org/qr-code) ❓

✎ **Also known as**

✎ **Country**
India

✎ **Keywords**
Computational Fluid Dynamics, Compressible Flows, High Speed Flows, Aerodynamics, Biomedical CFD, Electronics Thermal CFD

✎ **Websites & Social Links**
()

✎ **Other IDs**
Scopus Author ID: 55845684000 (http://www.scopus.com/inward/authorDetails.url?authorID=55845684000&partnerID=MN8TOARS)

✎ **Emails**
karthik_sundarraj@yahoo.com

Biography ❓   ✎

⌄ **Employment (4)** ❓

⇅ Sort

➕ Add employment

Hexagon MSC Software**:** Bengaluru, Karnataka, IN   ▾
2019-02-25 to present | Technical Manager (Technical and Business Development)
Employment

Source: Karthik Sundarraj   ★ Preferred source   ✎ 🗑

ARK Infosolutions Pvt. Ltd**:** Bengaluru, Karnataka, IN   ▾
2015-06-03 to 2019-02 | National Technical Manager (Technical)
Employment

Source: Karthik Sundarraj   ★ Preferred source   ✎ 🗑

Help

University of Petroleum and Energy Studies: Dehradun, Uttarakhand, IN
2012-06-25 to 2015-05 | Assistant Professor (Aerospace Engineering)
Employment

Source: Karthik Sundarraj   ★ Preferred source

Indian Institute of Science: Bangalore, Karnataka, IN
2011-12 to 2012-06 | Research Associate (Aerospace Engineering)
Employment

Source: Karthik Sundarraj   ★ Preferred source

❤ **Education and qualifications (2)** ❷

⇅ Sort

➕ Add education

➕ Add qualification

Brunel University London: Uxbridge, Middlesex, GB
2010-09 to 2011-11 | MSc (Aerospace Engineering)
Education

Source: Karthik Sundarraj   ★ Preferred source

JSS Academy of Technical Education Bangalore: Bangalore, Karnataka, IN
2006-09 to 2010-06 | B.E (Industrial Engineering and Management)
Education

Source: Karthik Sundarraj   ★ Preferred source

❤ **Invited positions and distinctions (0)** ❷

⇅ Sort

➕ Add distinction

➕ Add invited position

An invited position is an invited non-employment affiliation. A distinction is an honorary or other award, distinction, or prize. Add invited position or add distinction.

❤ **Membership and service (0)** ❷

⇅ Sort

➕ Add membership

➕ Add service

Membership is membership in any society or organization. Service is a dedication of time, money, or other resources. Add membership or add service.

❤ **Funding (0)** ❷

⇅ Sort

➕   ⬆

Funding captures grants and other awards you have received to support your research. Add funding.

❤ **Works (8 of 8)** ❷

⇅ Sort

➕   📄   ⬆   ⬇

☐   ⚡ COMBINE   🗑 DELETE

☐ Computational Study on the Effect of Aft-Body Attachments on Base
Drag Using Locked Vortex Flow Management Technique

Lecture Notes on Multidisciplinary Industrial Engineering

2019-10-04 | book-chapter

DOI: 10.1007/978-981-13-8468-4_9 (https://doi.org/10.1007/978-981-13-8468-4_9)

Part of ISBN: 9789811384677 (https://www.worldcat.org/isbn/9789811384677)

Part of ISBN: 9789811384684 (https://www.worldcat.org/isbn/9789811384684)

Part of ISSN: 2522-5022 (https://portal.issn.org/resource/ISSN/2522-5022)

Part of ISSN: 2522-5030 (https://portal.issn.org/resource/ISSN/2522-5030)

Source: Karthik Sundarraj   ★ Preferred source

☐ Effect of Varying Ramp Angle and Leading-Edge Bluntness on the
Behavior of Ramp Induced Shock Wave over Triple Ramped Cone Flare
Configuration at Hypersonic Speed

International Journal of Recent Technology and Engineering

2019-09-30 | journal-article

DOI: 10.35940/ijrte.c5844.098319 (https://doi.org/10.35940/ijrte.c5844.098319)

Part of ISSN: 2277-3878 (https://portal.issn.org/resource/ISSN/2277-3878)

Source: Karthik Sundarraj   ★ Preferred source (of 2)

☐ Hypersonic Flows Over Multi-Ramp Configurations

International Journal of Recent Technology and Engineering

2019-09-30 | journal-article

DOI: 10.35940/ijrte.c6406.098319 (https://doi.org/10.35940/ijrte.c6406.098319)

Part of ISSN: 2277-3878 (https://portal.issn.org/resource/ISSN/2277-3878)

Source: Karthik Sundarraj   ★ Preferred source (of 2)

☐ Numerical Study Of Base Drag Reduction Using Locked Vortex Flow
Management Technique For Lower Subsonic Regime

Zenodo

2018-03-01 | journal-article

DOI: 10.5281/ZENODO.1316596 (https://doi.org/10.5281/ZENODO.1316596)

Source: Karthik Sundarraj   ★ Preferred source

☐ Experimental wake and drag comparison between wavy tooth and
saw tooth trailing edge modification

International Journal of Applied Engineering Research

2015 | journal-article

EID: 2-s2.0-84955577679

Part of ISBN: 09739769 09734562

Source: Karthik Sundarraj *via* Scopus - Elsevier   ★ Preferred source

---

☐ Effect of eccentricity on the heat transfer rates of a re entry vehicle
with concave windward surface

Proceedings of the International Astronautical Congress, IAC

2012 | conference-paper

EID: 2-s2.0-84883515295

Part of ISBN: 00741795

Source: Karthik Sundarraj *via* Scopus - Elsevier   ★ Preferred source

Effect of nose cavity on heat transfer rates to the surface of an aeroshell descending through the Martian atmosphere

Proceedings of the International Astronautical Congress, IAC

2012 | conference-paper

EID: 2-s2.0-84883497713

Part of ISBN: 00741795

Source: Karthik Sundarraj *via* Scopus - Elsevier   ★ Preferred source

Effect of nose cavity on the heat fluxes to reentry vehicle in titan's atmosphere

Proceedings of the International Astronautical Congress, IAC

2012 | conference-paper

EID: 2-s2.0-84883515286

Part of ISBN: 00741795

Source: Karthik Sundarraj *via* Scopus - Elsevier   ★ Preferred source

Privacy Policy (https://orcid.org/footer/privacy-policy)

Terms of Use (https://orcid.org/content/orcid-terms-use)

Dispute procedures (https://orcid.org/orcid-dispute-procedures)

Contact us (https://support.orcid.org/hc/en-us/requests/new)

Trademark & iD display guidelines (https://orcid.org/trademark-and-id-display-guidelines)

Effect of varying ramp angle and leading-edge bluntness on the behavior of ramp induced shock wave over triple ramped cone flare configuration at hypersonic speed

Karthik Sundarraj, Ugur Guven, P S Kulkarni, Om Prakash, Ganesh Pawar R

Abstract: Numerical simulation results are presented to show the effect of ramp angle variations and leading-edge bluntness on the flow around triple ramped cone flare in hypersonic flow. This study investigates the changes associated with shock wave boundary layer interaction due to ramp induced flow breakdown and the fluctuation in flow in the presence of blunted leading edge. This type of ramp junctions typically features in re-entry vehicles, engine intakes, system and sub-system junctions, control surfaces, etc. Ramp junctions usually are associated with strong separation bubble that has significant upstream influence impacting the effectiveness of aerodynamic surfaces, engine performance, thermal behavior and stability. Computation studies are carried out using finite volume-based RANS solver, accuracy of second order and considering compressible laminar flow characteristics, with solver settings provided similar to experimental conditions as per literature. Comprehensive double ramp studies with suggestions on reducing the separation bubble size are invariantly considered in literature, however there has been no study in understanding the inclusion of additional ramps in such flow scenarios, hence efforts are taken to understand the benefits and implications of including a third ramp along with varying bluntness on the bubble size and its upstream intensity.

Keywords: Hypersonic, Leading edge bluntness, ramp angle, Shock wave and boundary layer interactions

I.   INTRODUCTION

The current technological advancements stand at a stage where the gap between space flight and atmospheric flight are closing in through human interventions and are now a dream that can be realized. The advent of hypersonic vehicle has created hope in this closure of gap and hence a lot of research is conducted in this area. Man's desire to explore deep space led to many space missions and through these the concept of reentry and reentry vehicles were understood. Apart from hypersonic reentry vehicles there are other hypersonic vehicles such as missiles and transport aircrafts in existence or at least in their nascent stages of development. Most of the reentry vehicles enter earth's atmosphere at very high velocities leading to excessive aerodynamic heating [21].

* Correspondence Author

Karthik Sundarraj*, CFD Software Soln., MSC Software Corporation, Bangalore, India. Email: karthik_sundarraj@yahoo.com

Ugur Guven, Department of Aerospace Engineering, UPES, Dehradun, India. Email: uguven@ddn.upes.ac.in

P S Kulkarni, Aerospace Engineering, Indian Institute of Science, Bangalore, India. Email: psk@iisc.ac.in

Om Prakash, Department of Aerospace Engineering, UPES, Dehradun, India. Email: omprakash@ddn.upes.ac.in

Ganesh Pawar R, Aerospace Engineering, Indian Institute of Science, Bangalore, India. Email: ganesh.pawar66@gmail.com

The temperature of the object becomes very high due to the transformation of kinetic energy of the falling object into heat energy. At such situations the design of the spacecraft is of prime importance. Various researchers [1-10] have investigated shock wave boundary layer and interaction physics through design modifications such as blunting, cavitation, ramping, flaring, external attachments such as aero disc or spike etc. to evaluate and understand the importance of these design features and also to measure the dependency on these features.

High speed aerodynamics mainly revolves around shocks and shock interactions that change the course of flow field and their behavior. The heat loads and forces are affected due to these alterations. The study along these lines is called shock wave and boundary layer interaction majorly dealing with the interactions between inviscid and viscous regions [3]. These interactions in the flow affect both internal and external flow aerodynamics. Generation of separation bubble, boundary layer separation, increased heating and even turbulent re-attachment could be caused through the presence of SWBLI. Careful attention must be given to the design of space vehicle subsystems such as wing body junction, engine inlet, nozzle etc., which experience such SWBLI [3]. As an outcome of design refinement several flow control techniques have been developed to suppress the effects of SWBLI [2]. Hypersonic flow field around blunted cone flare is a very good example that exhibits SWBLI. This example exhibits major feature of flows around a space vehicle such as detached bow shock ahead of the cone and oblique shock with boundary layer interaction at the cone flare junction [1]. The SWBLI can produce separated flow at the upstream forward-facing corner where the deflection in the form of a ramp/flare is present. The length of separation has implications for control, stability etc., of a hypersonic reentry vehicle [4]. A separation shock wave is generated due to an abrupt change in flow direction in the presence of ramp. The shock interacts with the boundary layer over the wall which experiences adverse pressure gradient. Flow separation in the presence of such gradients majorly depends on factors associated with flow conditions, geometrical conditions and boundary layer behaviour. The parameter at interest is the angle known as incipient separation angle given by Needham and Stollery [6].

$$M_\infty \theta_{is} = 80\sqrt{\overline{X_L}} \qquad (1)$$

Where $\overline{X}_L$ is the viscous interaction parameter at ramp junctions;

$$\bar{X}_L = M_\infty^3 \sqrt{C} / \sqrt{Re_L}$$

where $C = \dfrac{\mu_w}{\mu_\infty} \dfrac{T_\infty}{T_w}$ (2)

Boundary layer separation takes place if the incipient separation angle is lesser than deflection angle. Separation occurs at a point ahead of the compression corner, separation leads to compression waves forming a separation shock ahead of the separation region. Separation bubble can be identified by sudden increase in the pressure from nearly constant in the downstream region to a sudden increase in the compression region. The flow reattaches at a point on the ramp surface, the recirculation zone extends between the separation and reattachment point and the distance between these two points is called as length of separation bubble [2]. In case the ramp angle was smaller than the incipient separation angles the flow would have not undergone much deflection as in the previous case and would have followed a laminar boundary layer profile without separation at the ramp [3]. To enhance the performance of Ramp based SWBLI by reducing the intensity of this interaction through delayed separation several control mechanisms are reported to have been employed. A forward-facing blunted leading-edge is used widely as a control mechanism to control the shock interactions. Leading-edge bluntness completely changes the dynamics of the shock and the boundary layer interaction. The primary reason is the presence of a stronger detached bow shock in place of attached oblique shock. This replacement leads to the formation of strong entropy layer and it interacts with the boundary layer. Flow over the object also gets accelerated due to favorable pressure gradient [4]. Hence a high-speed shear flow approaches the ramp which influences the location of separation bubble, bubble size, incipient separation angle and the reattachment point. Based on research the addition of bluntness to the leading edge provides better suppression of shock interaction when compared to the sharp leading edge.

Several researchers have investigated shock wave boundary layer phenomenon through several design modifications as stated in earlier sections. R. Savino and D. Paterna [1] conducted validation studies of flow around blunted cone flare in hypersonic flows. Experimental studies were performed at the Von Karman Institute H3 Mach 6 wind tunnel in laminar flow conditions. This work gives a detailed insight on the importance of grid independent study and the influence of mesh size on wall pressure, heat flux and skin friction parameters. It has also been noted through this study that the accuracy of separation bubble size, its location, the flow separation and reattachment locations are all dependent on the resolution of mesh near the wall and at the ramp junction. Sensitivity of wall pressure and heat flux to small changes in surface temperature has also been studied in this work. It has been with increase in surface temperature, the separation bubble length increases. The authors have also considered thermal conductivity effects by considering different materials properties of the experimental model and validating the same through computational methods. Bibin John and Vinayak Kulkarni [2 – 4] have performed wide range of numerical investigations addressing the ramp induced shock wave boundary layer interactions. Extensive and in-depth details on the effect of various flow and geometric parameters and their correlation with the shock wave boundary layer interaction in hypersonic flows performed through finite volume based computational solver are presented. Importance of Qualitative approach over quantitative measurements to estimate the separation bubble length and upstream influence through skin friction and wall shear has been detailed out, which gives a clear insight on the method of approach to understand separation physics [3]. The study also clearly points out the fact that the incipient separation angle concept work well only for well separated flows. It is found from these investigations that the separation bubble length is clearly dependent on flow and design parameters. Strong correlation between leading edge bluntness on separation bubble length has been identified and presented. It is understood from this investigation the presence of two critical radius of leading-edge bluntness [4]. The initial trend of leading edge bluntness and separation bubble size indicates that the entropy layer is engulfed by the boundary layer attributing to the increase in bubble length, while further increase in leading edge bluntness leads to the inversion of boundary layer physics wherein the boundary layer gets engulfed by high enthalpy layers when the separation bubble lengths starts to decrease monotonically [3, 4].

From the literature studies it is evident that control of separation bubble is critical to minimize the effects of shock wave interactions with space vehicle systems and sub-systems. It can also be noticed that almost every literature investigation addresses only regions with single and double ramp junctions, but there is almost no research finding related to multi-ramp junctions which also gets featured in such hypersonic vehicle component and system designs. Multi-ramp junctions also pose severe design challenges and it is necessary to take conscious efforts while designing space vehicles. While these previous research works provide very good insights on the SWBLI by varying ramp angles, leading edge bluntness, freestream velocity etc., which becomes the core basis of the current work, while the present research work focuses on the study of shock wave and boundary layer interactions with triple ramp configuration, considering the basic understanding of flow physics around single and double ramp configurations. This way it also helps in understanding the effects of having a third ramp on the upstream separation bubble already present at the second ramp junction along with the understanding of how the presence of third ramp overall changes the shock structure and flow. Computational investigations are carried out to study and understand the behavior of ramp induced shock wave and boundary layer interactions for three ramp configurations, wherein the first two ramps are considered as specified by R. Savino and D. Paterna [1], while the third ramp angles are varied to study the effect of ramp angle variations on the separation bubble length both at the second and third ramp junctions. Since the studies presented by Bibin John and Vinayak Kulkarni [4] emphasize the strong correlation between leading edge bluntness and the separation bubble size, it becomes a key consideration to test the correlation on triple ramp configuration and to assess if the leading edge bluntness still continues to be an effective technique for separation control and hence the current research work considers leading-edge radius ranging between 0.5 mm to 5 mm along with a sharp

leading edge ramp configuration. Simulation tool validation is performed using the base geometry and boundary conditions as provided by R. Savino [1] in their computational and experimental validation studies. Post successful validation, efforts are taken to initially study the effect of adding a third ramp to the base geometry on the shock wave boundary layer interaction, followed by considering the leading-edge radius effects on these parameters in the presence of third ramp. Details on the solution methodology, model and discretization details are presented in the next section. Discussions on the findings of adding a third ramp with and without leading edge bluntness and its implications on the separation bubble is discussed in Section III, followed by conclusions and future works in Section IV.

II. COMPUTATION METHODOLOGY

The numerical investigations are carried out using High Resolution Flow Solver on Unstructured meshes (HiFUN), considering it to be compressible laminar flow solver. Following conservation equations for mass and momentum are considered in the solver algorithm,

$$\frac{\partial U}{\partial t} + \frac{\partial (f_i + f_v)}{\partial x} + \frac{\partial (g_i + g_v)}{\partial y} = 0 \tag{3}$$

Where,

$$U = \begin{bmatrix} \rho \\ \rho u \\ \rho v \\ \rho E \end{bmatrix} \quad f_i = \begin{bmatrix} \rho u \\ \rho u^2 + p \\ \rho uv \\ \rho uH \end{bmatrix} \quad g_i = \begin{bmatrix} \rho v \\ \rho uv \\ \rho v^2 + p \\ \rho vH \end{bmatrix}$$

And,

$$f_v = \begin{bmatrix} 0 \\ \tau_{xx} \\ \tau_{xy} \\ u\tau_{xx} + v\tau_{xy} - q_x \end{bmatrix} g_v = \begin{bmatrix} 0 \\ \tau_{xy} \\ \tau_{yy} \\ u\tau_{xy} + v\tau_{yy} - q_y \end{bmatrix} \tag{4}$$

Here, U is the vector of conserved variables, f_i and g_i are inviscid flux vectors along x and y directions respectively. Also f_v and g_v are viscous flux vectors along x and y respectively,
The expressions for the viscous stress and heat conduction terms are given below:

$$\tau_{xx} = \frac{\mu}{Re_\infty}\left(\frac{4}{3}\frac{\partial u}{\partial x} - \frac{2}{3}\frac{\partial v}{\partial y}\right), \quad \tau_{yy} = \frac{\mu}{Re_\infty}\left(\frac{4}{3}\frac{\partial v}{\partial y} - \frac{2}{3}\frac{\partial u}{\partial x}\right)$$

$$\tau_{xy} = \frac{\mu}{Re_\infty}\left(\frac{\partial u}{\partial y} + \frac{\partial v}{\partial x}\right)$$

$$q_x = \frac{\mu}{M_\infty^2 Pr_\infty Re_\infty (\gamma - 1)}\frac{\partial T}{\partial x}$$

$$q_y = \frac{\mu}{M_\infty^2 Pr_\infty Re_\infty (\gamma - 1)}\frac{\partial T}{\partial y}$$

For the present study, fluid is assumed to be as ideal gas. HLLC flux [11, 12] is adopted for inviscid flux scheme and Green Gauss [13] for viscous flux scheme with a special accuracy of 1. Implicit time integration approach is used for obtaining numerical approximation of the solution, with the relaxation faction of 0.4 and the permissible range of CFL (Courant-Friedrichs-Lewy) [19, 20] number is 0.09 – 1.

$$\frac{\mu}{\mu_{ref}} = \left(\frac{T}{T_{ref}}\right)^{\frac{3}{2}}\left(\frac{T_{ref} + S}{T + T_\infty}\right) \tag{5}$$

Laminar viscosity (μ) is computed by using Sutherland's law [18], where (μ_{ref}) is the reference viscosity ($17.16 \times 10^{-6}\ N\ s/m^2$) of air at a reference temperature (T_{ref}) of ($273.15\ K$), the Sutherland's constant (S) for air is considered as (110.56), while the Prandtl number (Pr) is assumed to be 0.74.

III. NUMERICAL INVESTIGATIONS

The model and boundary conditions considered by R. Savino [1] are initially considered to perform inter-code comparison, grid dependency study and theoretical validation stagnation pressure and post shock temperature. The base model considered for initial validation studies is henceforth referred as double ramp, which is 159.11 mm in total length, with first ramp angle 7.5^0, second ramp angle 10^0 and a leading-edge bluntness of radii 3.5 mm. A third ramp of length 63 mm is attached to the base double ramp model along with the consideration of various leading-edge bluntness, for the current investigation on ramp induced shock wave boundary layer interactions. Model details along with the computation domain and boundary conditions are shown in Fig. 1. The freestream conditions and the details about ramp angles and leading-edge bluntness are mentioned in Table-I. Multi-block structured meshing has been performed to discretise the computation domain. Four different mesh combinations with variations in mesh spacing both in normal and along the body are considered, the detailed of the same is shown in Table-II, a sample grid used throughout this investigation is shown in Fig. 2. Due to availability of multiple computation tools, inter-code comparison was necessary to ensure the chosen tool is the best to capture the flow physics that involves, laminar high-speed flows with high gradient flow separations along with the formation of shocks. The pressure distribution along the double ramp model [1] was taken as a standard to perform the inter-code comparison. Both the simulation tools were run with the same mesh count and boundary conditions, while different solver settings were tried to ensure the best solver setting specific to the tool has been explored. It is evident from Fig. 3, there is excellent agreement with the experimental pressure plot, the separation and reattachment points for simulations done with HiFUN, for this reason it has been used for all simulations in this investigation. Through grid independence study it was found that the mesh parameters used by R. Savino [1] was not suitable for HiFUN to match the experimental data. Grid spacing normal to the model was found as the major criterion to reach solver

(a) Double Ramp [1]

(b) Triple Ramp

(c) Computational Domain
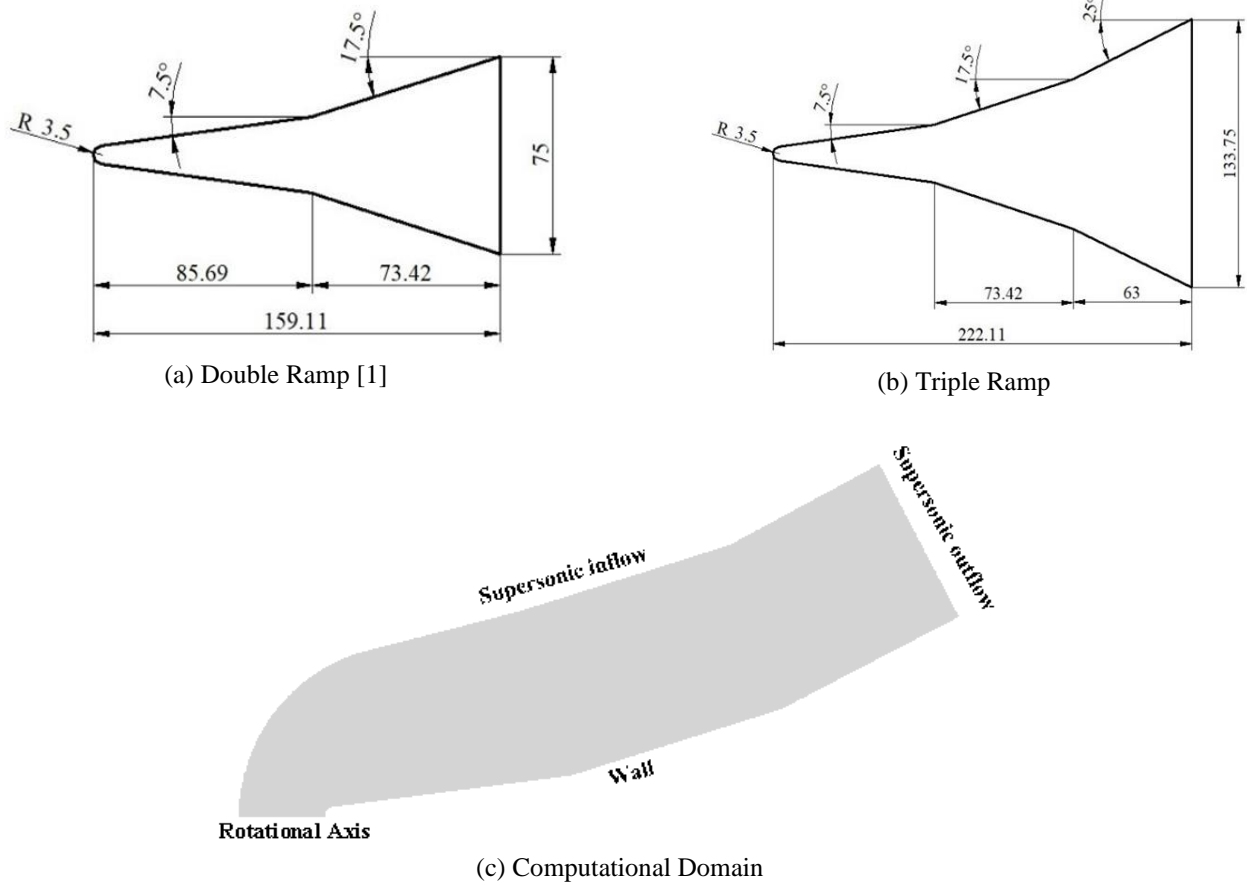
Fig. 1. Models and computation domain (model dimensions are in mm)

Table-1: Freestream and Geometry Conditions

M_∞	P_∞ (Pa)	T_∞ (K)	μ (Pa-s)	k (N/s-K)	Ramp Angle (α)	Nose Radius (mm)
6	673.67	67.07	$4.47e^{-6}$	0.00607	7.5, 10, 12.5, 15	0, 0.5, 1, 1.5, 2.5, 3.5, 5

Table-II: Details of grids used for grid independence study

Grid	Δn_0	Δn_h	Δs_0	Δs_h
240 x 40 [1]	0.003	0.05	0.0675	0.018
480 x 80 [1]	0.0015	0.005	0.0337	0.009
960 x 160 [1]	0.00075	0.0025	0.0168	0.0045
240 x 40	0.0015	0.0015	0.0675	0.018
480 x 80	0.0015	0.0015	0.0337	0.009
240 x 40			0.0675	0.018
480 x 80	0.015	0.015	0.0337	0.009
660 x 120			0.0337	0.009
960 x 160			0.0168	0.0045
240 x 40			0.0675	0.018
480 x 80	0.03	0.03	0.0337	0.009
660 x 120			0.0337	0.009
960 x 160			0.0168	0.0045
240 x 40			0.0675	0.018
480 x 80	0.045	0.045	0.0337	0.009
660 x 120			0.0337	0.009
960 x 160			0.0168	0.0045
240 x 40			0.0675	0.018
480 x 80	0.06	0.06	0.0337	0.009
960 x 160			0.0168	0.0045

Δn_0, Δn_h = normal spacing at stagnation and ramp; Δs_0, Δs_h = tangential spacing at stagnation and ramp

Fig. 2. Sample Grid used for triple ramp

accuracy, while maintaining the overall mesh count same as in literature. It was found from grid independence study that the mesh size of 960 x 160 and 480 x 80 with 30micron normal mesh spacing had excellent agreement with experimental surface pressure values as shown in Fig. 4a. The separation and reattachment points have very good match while there is slight but acceptable computational underprediction in the post attachment zone. It can be noticed that 480 x 80 captures the bubble region better, but the post reattachment region is extremely critical for multi-ramp studies which is captured better by 960 x 160 grid. The importance of qualitative approach to determine the separation bubble length as emphasised by Bibin Jon [3], the skin friction co-efficient parameters were also validated, shown in Fig. 4b. There is underprediction of the separation bubble length as compared to the CFD simulations results in the literature, this could be attributed to the difference in mesh count and the solver setting differences but it is evident that the HiFUN code is predicting the separation bubble length much accurately as indicated in the inter-code comparison. In addition, a theoretical comparison of stagnation pressure and post-shock temperature with simulation outcome using the HiFUN solver also proves the solution to be independent of the grid and the code. Fig. 5a & 5b shows the closer view of stagnation region, where the stagnation pressure value is about 31,683 Pa and the post-shock temperature is 549 K, which matches with values calculated using normal shock theory, where the stagnation pressure is calculated to be 31,538 Pa and temperature 533 K. Similar methodology was followed to perform grid independence study for triple ramp configuration. From the double ramp validation, it was found

that 960 x 160 was the most reliable mesh for all design variations and hence the same mesh sizing was continued for triple ramp by adding an equal mesh division on the third ramp making the total mesh size for triple ramp as 1320 x 160, a sample grid independence plot shown in Fig. 6. It is evident that lesser grid size is unable to capture the separation bubble accurately.
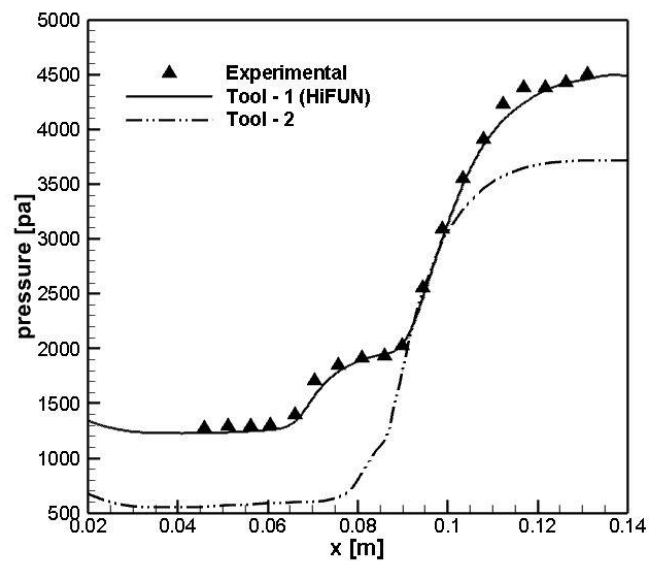
Fig. 3. Inter-code comparison of surface pressure
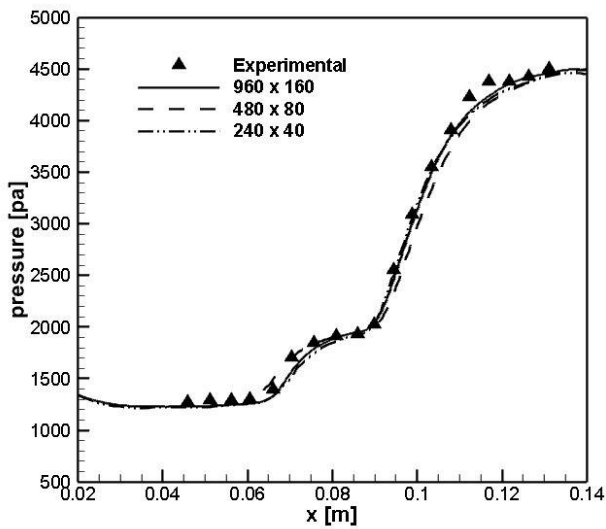
Fig. 4a. Grid independence study of surface pressure profile over double ramp
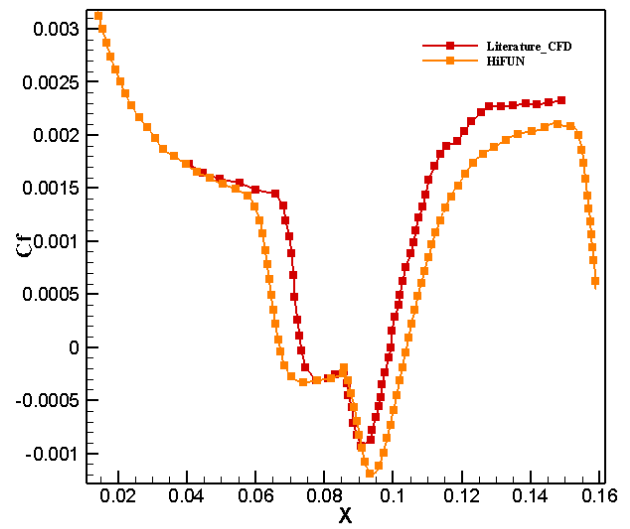
Fig. 4b. Grid independence study of skin friction coefficient
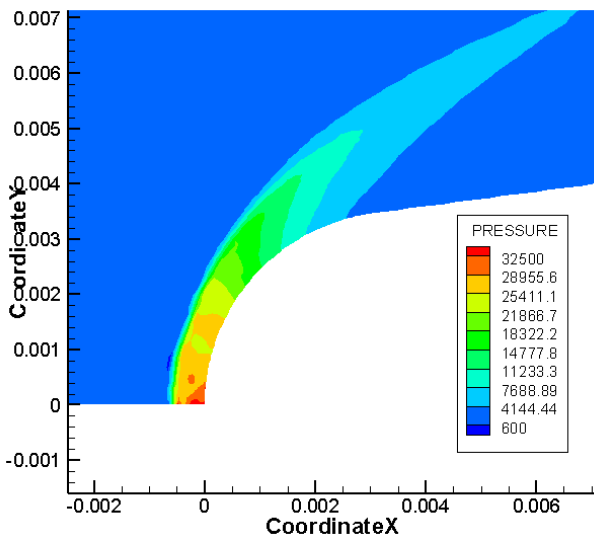
Fig. 5a. Stagnation pressure
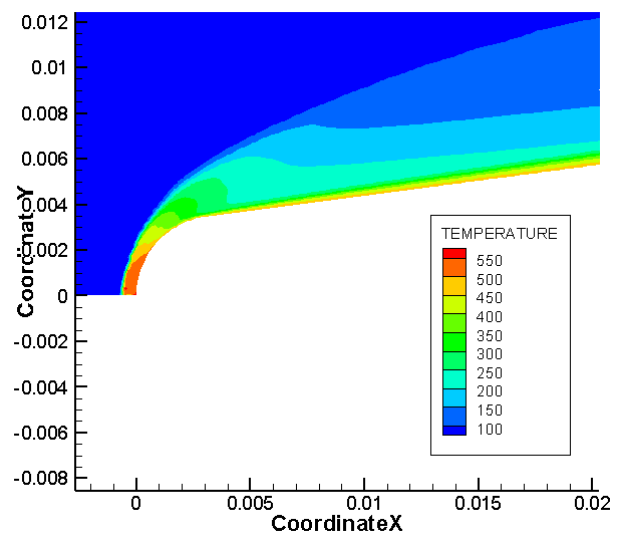
Fig 5b. Stagnation Temperature
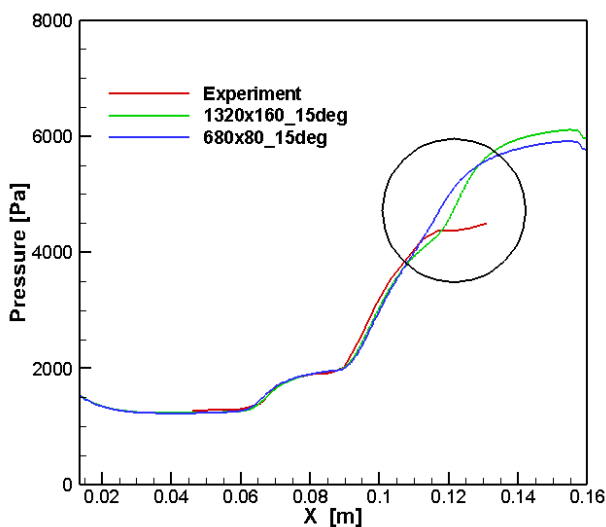
Fig. 6. Grid Independence study of surface pressure over triple ramp

A. Effect of varying ramp angle

The study on effect of adding a third ramp to the standard double ramp model used by R. Savino [1] and consequently varying the third ramp angle are carried out and the changes observed in shock wave boundary layer interactions, separation bubble lengths and surface pressure due to this addition are discussed in this section. This study also enumerates the observations done by Bibin John [3, 4] from the computational studies the importance of reducing the separation bubble length for better design performance and to verify the incipient separation condition through boundary layer separation. The triple ramp configuration (Fig. 1-b) with different third ramp angle $\theta = 7.5^0$, 10^0, 12.5^0 and 15^0 are considered to study the effects of such unique junction configurations. The freestream conditions are as mentioned in Table-1, which are same as per the experiments conducted by R. Savino et al [1]. As mentioned in earlier section the simulation tool has been validated and the grid fixed based on grid independence study done using the experimental data
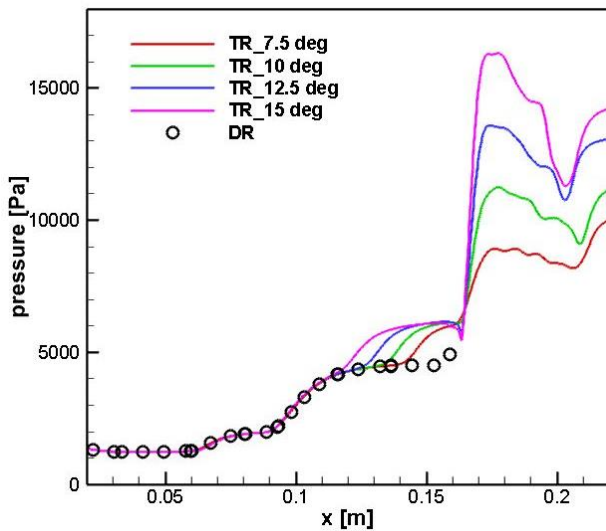
Fig. 7. Effect of third ramp angle variations on pressure distribution
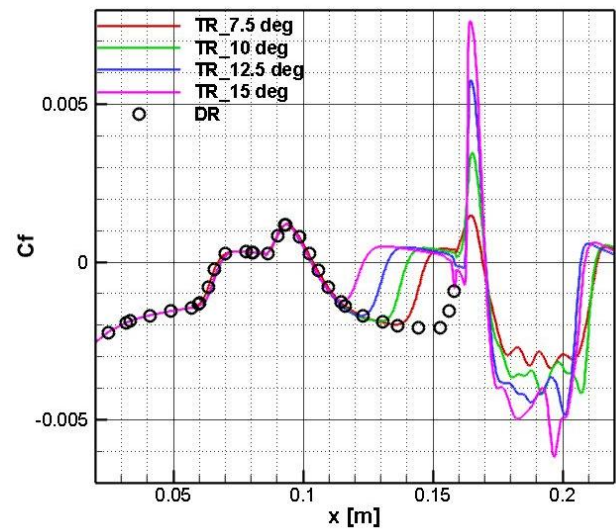
Fig. 8. Effect of third ramp angle on skin friction distribution and bubble length

Table-III: Summary on changes in separation bubble parameters

	Double Ramp	Triple Ramp 7.5^0		Triple Ramp 10^0		Triple Ramp 12.5^0		Triple Ramp 15^0	
	FB	FB	SB	FB	SB	FB	SB	FB	SB
L_b	0.0368	0.0366	0.0216	0.035	0.0299	0.0346	0.0378	0.0345	0.0469

L_b= bubble length (in meter), FB = Bubble at 1st ramp junction, SB = bubble at 2nd ramp junction
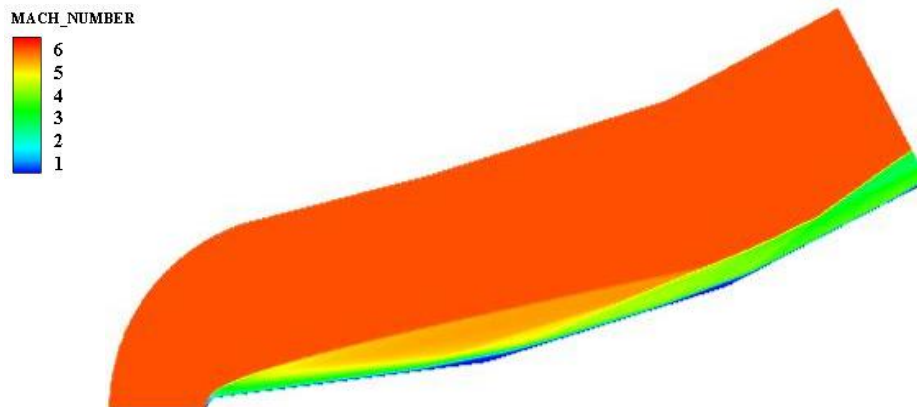
Fig. 9. Shock wave boundary layer interaction over triple ramp configuration (Mach contour)

obtained by R. Savino et al [1], the same grid parameters considered for this study. The variation of surface pressure distribution for different third ramp angles and its implications on the bubble is shown in Fig. 7. The pressure distribution on double ramp is also integrated in the plot to give a perspective on separation bubble of double ramp and the formation of secondary bubble region in case of third ramp. From the graph it can be deduced that the presence of third ramp does not majorly affect the flow over second ramp and follows almost the same pressure trends. As per the findings by Bibin John et al. [3] and Marini [16, 17], the size of separation bubble increases with increase in ramp angle, which continues to be true even with a third ramp as can be seen in the figure. As can be seen in Fig. 9, this configuration has highly complex flow structure, with a detached bow shock at the leading edge, the separation shock at the first

ramp along with the reattachment shock forming the first corner shock, which can also be seen in Fig. 7 as a spike in pressure, followed by second corner shock formed due to the second separation bubble, leading to a highly turbulent reattachment shock. From the pressure distribution plot there is no conclusive evidence on the effects of having a third ramp on the bubble size and based on studies done by Bibin John et al. [4], a quantitative approach is considered by measuring the separation bubble size through skin friction distribution as shown in Fig. 8. The separation and reattachment points are determined where the curves cross the zero line. Summary on the separation bubble details are given in Table-III, where it can be noticed the length of the bubble at the first ramp is decreasing in the presence of a third ramp when compared with the double ramp. These reductions may be small in magnitude but cannot be neglected as the

overall objective is to reduce the bubble size and can provide considerable insights for design consideration. Referring to Fig. 8, a clear separation bubble is indicated for ramp angles 7.5^0 and 10^0, while a complex bubble activity can be noticed for 12.5^0 and 15^0 ramp angles. This could be indicative of the presence of a strong and a weak circulation zone caused due to turbulent reattachment or even transitional in the presence of a strong shock which can be noticed in the form a high fluctuation, both in pressure and skin friction plots. It is evident from this simulation study that design considerations while encountering scenarios of ramp type junctions with more than the typical two ramps must be carefully assessed and fine-tuned to ensure reduced flow separations and shock interactions.

B. Effect of blunted leading edge

This study presents a detailed understanding on the effect of blunted leading edge over shock wave boundary layer interactions with triple ramp configuration. The boundary conditions are the same as mentioned in Table-I, with variations in the leading-edge bluntness and ramp angle. The first two ramps are retained as per the experimental model considered by R. Savino et al. [1], while the third ramp with varying angle is attached to this base model. Considering leading edge bluntness is primarily logical as it is nearly impossible to manufacture with a sharp leading edge. Apart from this very point, leading-edge bluntness has significant effect on shock wave and boundary layer, primarily because the bluntness causes a detached bow shock when compared to sharp leading edge with attached oblique shock [3]. Presence of a bow shock reduces the flow velocity approaching the ramp even while the freestream Mach number in both cases are same. Investigations by Bibin John et al. [3] also indicates with reduction in Mach number the shock wave boundary layer integration becomes prominent. Presence of leading-edge bluntness also helps in significantly reducing the surface heating rate and stabilizes the flow through strong circulations at the boundary layer. The computed surface pressure distributions over triple ramp models with varying ramp angles and leading-edge bluntness are shown in Fig. 10 – 13. Commonly noticeable trends in all these surface pressure distribution plots are the behavior of the separation bubble, the reattachment shock and the shear layer region. Interestingly, the length of separation bubble at the double ramp junction is more prominent at lower triple ramp angles (Fig. 10), while the separation bubble at triple ramp junction becomes more prominent at higher triple ramp angles (Fig. 12, 13). This is primarily because the reattachment shock at the double ramp junction tends to grow weaker with combined increment of nose bluntness and the third ramp angle, leading to an early upstream separation at the third ramp junction. What can also be noticed from the pressure distribution plots is that, the reattachment shocks after the double ramp junction is strong but not turbulent over the second ramp, causing a laminar shear region, whereas the reattachment shocks post the triple ramp junction is increasingly strong with increase in third ramp angle and highly turbulent causing a highly unstable shear region over the third ramp. It can be noticed in Fig. 13, there is almost no reattachment at the double ramp junction for both 3.5 and 5

mm blunt radius, there is a considerable downstream shift in the reattachment point at the double ramp junction and upstream shift in the separation point at the triple ramp junction leading to singularization of both the bubbles causing detached flow between both the junctions. The flow reattaches only after the third ramp junction characterized by highly turbulent strong post shock shear region.

The present study also considered the qualitative approach to measure the length of separation bubble though skin friction coefficient. As observed by Bibin John et al. [4] a strong correlation exists between the leading-edge bluntness and the separation bubble length. It is noticed from this study that even bluntness has significant effect on the flow field. Bibin John et al. [3] identified the presence of two critical nose radius, inversion and equivalent radius. The separation bubble size increases with increase in blunt radius (BR) until it reaches the inversion radius. This increase in separation bubble size is attributed to the dominance of boundary layer over the entropy layer. Post the inversion radius the bubble tends to decrease in size with increase in leading-edge bluntness due to the shift in dominance of entropy layer over boundary layer. Computational results of skin friction coefficient over triple ramp configuration with varying blunt radius is shown in Fig. 14 – 17. Similar to the pressure distribution plots it is noticed that the separation bubble size at the double ramp decreases in size with increase in third ramp angle and the reverse is noticed with respect to the bubble size at the third ramp junction. In case of 15^0 third ramp angle the separation behavior is reconfirmed through Fig. 17, where it can be noticed that the reattachment does not occur post the double ramp junction leading to detached flow between both the junctions. From the skin friction coefficient, the separation and reattachment points can be located as the ones where the distribution curve crosses the x-axis line. The changes in the locations of these two points for different third ramp angles along with different leading-edge radii are plotted in Fig. 18. Separation and reattachment points of both the separation bubbles, one over double ramp junction called as first bubble (FB) and the other over triple ramp junction called as second bubble (SB) are both considered for analogy in this plot. From this figure it is evident, with initial increase in leading edge blunt radius the separation point shifts upstream and the reattachment point shifts downstream, increasing the separation bubble length for initial radii indicating the dominance of boundary layer over entropy layer. The first critical radius or the inversion radius is noticed anywhere between 3.8^0 to 4.4^0 where the boundary layer and the entropy layer are assumed to be of same thickness. With further increase in leading-edge radius, the separation point seems to move downstream, and the reattachment point upstream decreasing the length of the separation bubble, indicating the fact the dominance of entropy layer over boundary layer. Yet again it can be noticed the reattachment point for 15^0 third ramp angle is increasing with increase in blunt radius and the separation point also indicating the same proving completely detached flow. It also confirms that the addition of third ramp does not alter the correlation between blunt radius and the separation bubble length as reported by Bibin John et al. [3, 4], while there are noticeable upstream effects on the separation, reattachment and the overall shock wave boundary layer interaction.
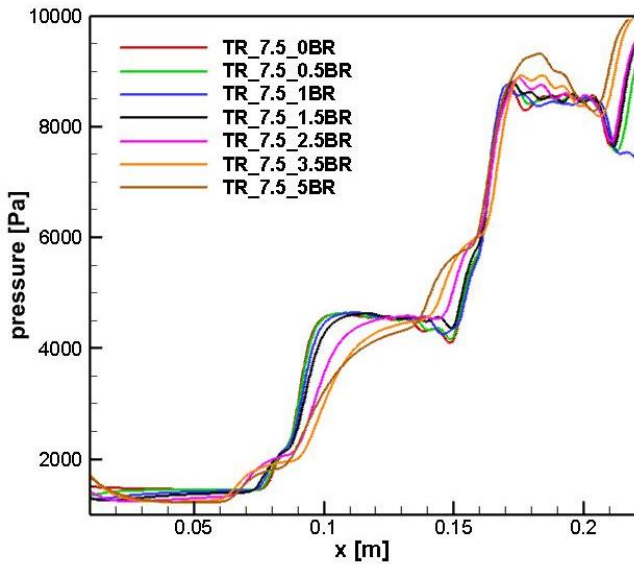
Fig. 10. Pressure distribution over 7.5^0 third ramp angle
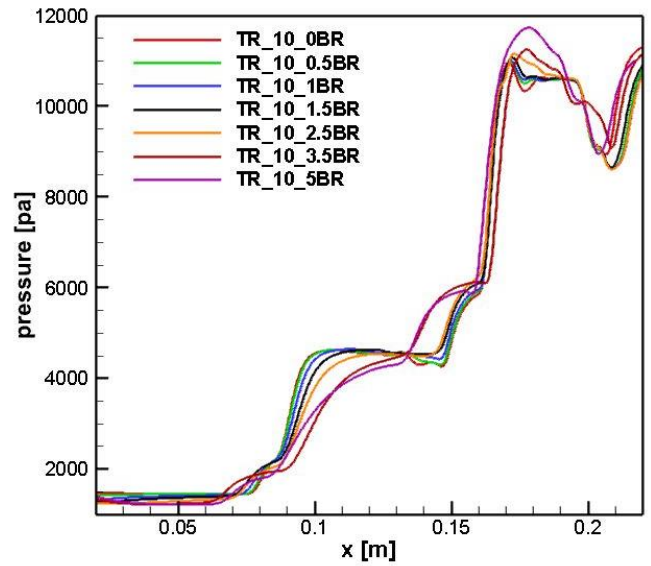
Fig. 11. Pressure distribution over 10^0 third ramp angle
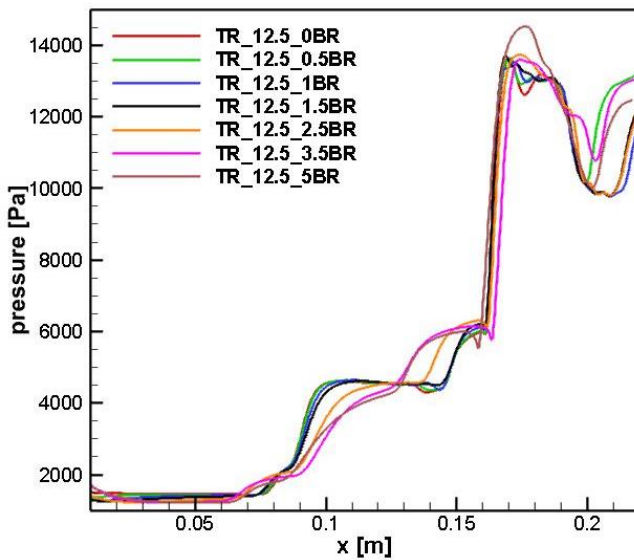
Fig. 12. Pressure distribution over 12.5^0 third ramp angle
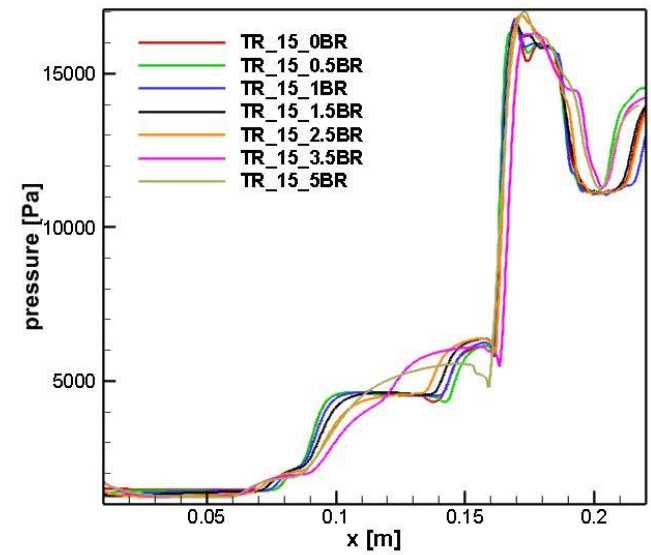
Fig. 13. Pressure distribution over 15^0 third ramp angle
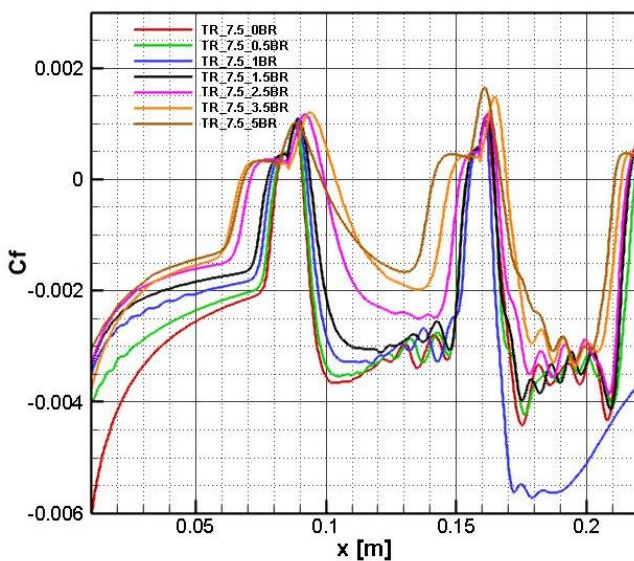
Fig. 14. Skin friction coefficient over 7.5^0 third ramp angle for different leading-edge radius
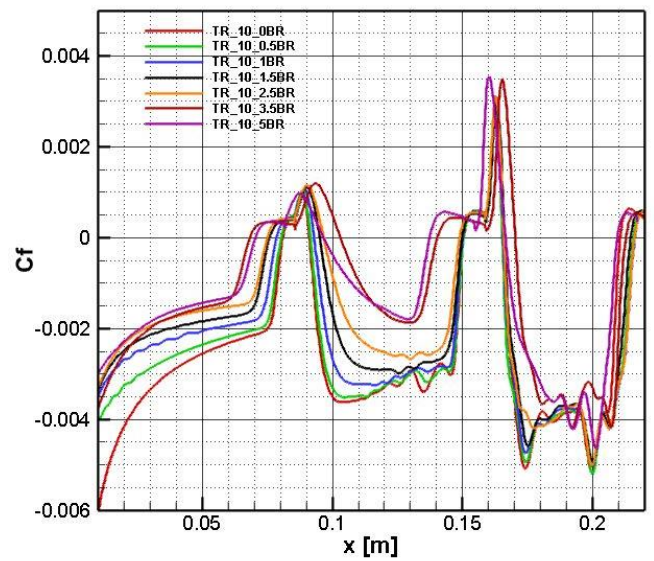
Fig. 15. Skin friction coefficient over 10^0 third ramp angle for different leading-edge radius
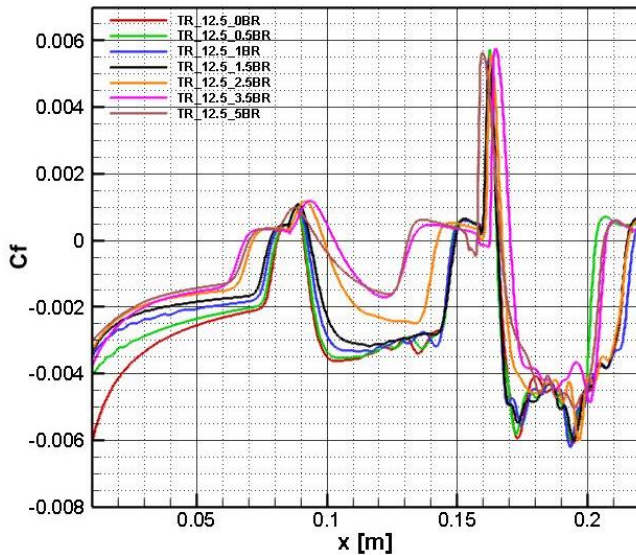
Fig. 16. Skin friction coefficient over 12.5^0 third ramp angle for different leading-edge radius
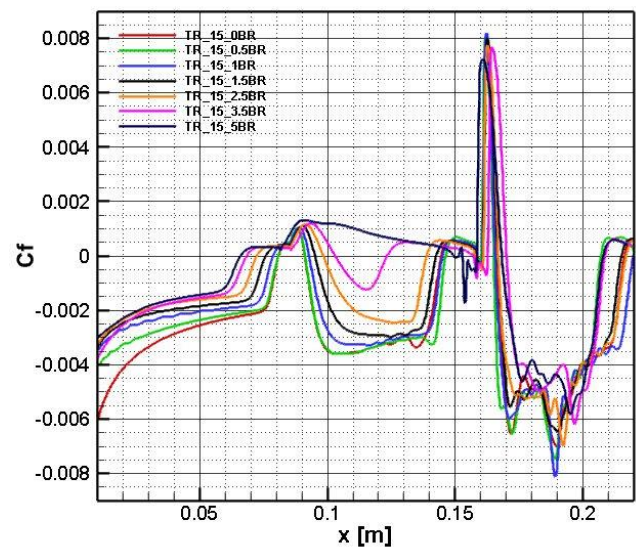
Fig. 17. Skin friction coefficient over 15^0 third ramp angle for different leading-edge radius
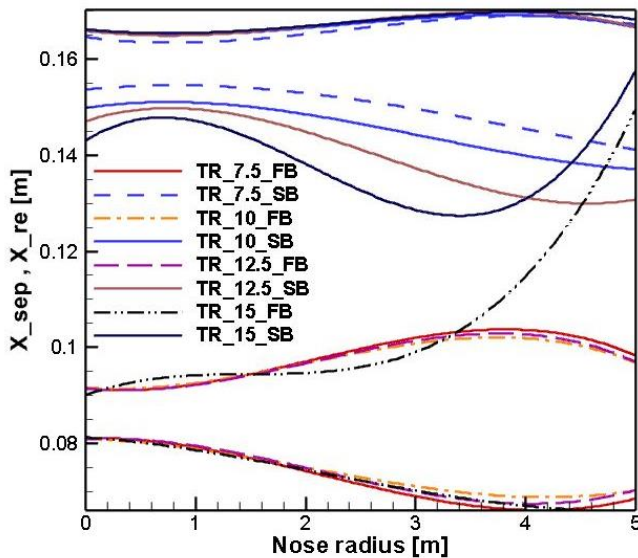
Fig. 18. Separation and reattachment points variation for different blunt radii and third ramp angle

IV. CONCLUSION

Numerical investigations were performed to investigate the effects of varying different geometrical parameters on the shock wave and boundary layer interaction physics in laminar hypersonic flow regime using high resolution flow solver HiFUN. Extensive validation activity was performed to ensure accuracy of flow solver through inter-code comparison and grid independence based on which a common solver and grid was chosen as the outcome of this validation. Efforts were taken to initially study the effect of adding a third ramp on the shock wave and boundary layer interaction, followed by considering the variations in leading-edge radii in combination with varying third ramp angle. This study focused on studying a niche area of multi-ramp configurations, in this case triple ramp configuration which does not feature much in any of the past literatures, but poses equal or even higher design challenges due to the complexity in flow patterns, separation and attachment physics and highly turbulent shear region. Both qualitative and

quantitative methods are employed to understand the overall effects of these design configurations on the shock wave boundary layer interaction. From computational studies it is noted that the triple ramp configuration has highly complex flow structure, with a detached bow shock at the leading edge, the separation shock at the first ramp along with the reattachment shock forming the first corner shock, followed by second corner shock formed due to the second separation bubble, leading to a highly turbulent reattachment shock. This proves that computation methods can no more assume laminarity and must consider turbulent flow modeling for upcoming research studies. Quantitative study by measuring the separation bubble size through skin friction distribution indicates the length of separation bubble at the first ramp decreases in the presence of a third ramp when compared with the double ramp. These decrements though small in magnitude cannot be neglected as the overall objective is to reduce the bubble size and can provide considerable insights for design consideration. The skin friction distribution also shows a clear separation bubble for smaller third ramp angles, while a complex bubble activity can be noticed for higher ramp angles. This could be indicative of the presence of a strong and a weak circulation zone caused due to turbulent reattachment or even transitional in the presence of a strong shock. Study on effect of varying the leading-edge bluntness offered some interesting outcomes wherein, the length of separation bubble at the double ramp junction is more prominent at lower triple ramp angles, while the separation bubble at triple ramp junction becomes more prominent at higher triple ramp angles. It has been identified that the reattachment shock at the double ramp junction tends to grow weaker with combined increment of nose bluntness and the third ramp angle, leading to an early upstream separation at the third ramp junction. What was also noticed from the pressure distribution plots is that, the reattachment shocks after the double ramp junction is strong but not turbulent over the second ramp, causing a laminar shear region, whereas the reattachment shocks post the triple ramp junction is increasingly strong with increase in third ramp angle and highly turbulent causing a highly unstable shear region over the third ramp. The first critical radius or the inversion radius

is noticed anywhere between 3.8^0 to 4.4^0, with further increase in radii leading to a reduction in separation bubble size. It is evident that design considerations while encountering scenarios of multi-ramp type junctions must be carefully assessed and fine-tuned to ensure reduced flow separations and improved shock interactions. Future study will explore effects of changes in freestream conditions such as Mach number and surface property changes such as temperature. Additional design changes shall also be considered by adding more ramps to the typical base configuration and ensuring the consideration of turbulence in the flow to better predict the separation bubble dynamics.

V.   ACKNOWLEDGEMENT

VI.   REFERENCES

[1] R. Savino and D. Peterna, "Blunted cone-flare in hypersonic flow," *Computers & Fluids,* pp. 859-875, 2005.

[2] B. John and V. Kulkarni, "Numerical assessment of correlations for shock wave boundary layer interaction," *Computers & Fluids,* vol. 90, pp. 42-50, 2014.

[3] B. John, V. Kulkarni and G. Natarajan, "Shock wave boundary layer interactions in hypersonic flows," *International Journal of Heat and Mass Transfer,* vol. 70, pp. 81-90, 2014.

[4] B. John and V. Kulkarni, "Effect of leading edge bluntness on the interaction of ramp induced shock wave with laminar boundary layer at hypersonic speed," *Computers & Fluids,* vol. 96, pp. 177-190, 2014.

[5] S. Reichel and R. Groll, "Numerical simulation and experimental validation of a hypersonic flow for numerical modulation of re-entry phenomena prediction using adaptive mesh refinement," *International Journal of Computational Methods and Experimental Measurements,* vol. 1, no. 4, pp. 381-394, 2013.

[6] D. A. Needham and J. L. Stollery, "Boundary layer separation in hypersonic flow," *University of London,* 1966.

[7] C. L. Runninga, T. J. Julianoa, J. S. Jewell, M. P. Borgb and R. L. Kimmel, "Hypersonic Shock-Wave/Boundary-Layer Interactions on a Cone/Flare," *Experimental Thermal and Fluid Science,* 2019.

[8] D. V. Gaitonde, "Progress in shock wave/boundary layer interactions," *Progress in Aerospace Sciences,* vol. 72, pp. 80-99, 2015.

[9] I. G. Brykina, B. V. Rogov, G. A. Tirskiy, V. A. Titarev and S. V. Utyuzhnikov, "A comparative analysis of approaches for investigating hypersonic flow over blunt bodies in a transitional regime," *Journal of Applied Mathematics and Mechanics,* vol. 77, pp. 9-16, 2013.

[10] H. S. Massimi, H. Shen, C. Y. Wen, Y. S. Chen and S. M. Lian, "Numerical analysis of hypersonic flows around blunt-nosed models and a space vehicle," *Aerospace Science and Technology,* vol. 43, pp. 360-371, 2015.

[11] Z. Shena, W. Yan and G. Yuan, "A robust HLLC-type Riemann solver for strong shock," *Journal of Computational Physics,* vol. 309, pp. 185-206, 2016.

[12] S. Simon and M. J. C, "A simple cure for numerical shock instability in the HLLC Riemann solver," *Journal of Computational Physics,* vol. 378, pp. 477-496, 2019.

[13] H. Nishikawa, "From hyperbolic diffusion scheme to gradient method: Implicit Green–Gauss gradients for unstructured grids," *Journal of Computational Physics,* vol. 372, pp. 126-160, 2018.

[14] D. Sun, F. Qu and C. Yan, "An effective flux scheme for hypersonic heating prediction of re-entry vehicles," *Computers and Fluids,* vol. 176, pp. 109-116, 2018.

[15] F. Qu, J. Chen, D. Sun, J. Bai and G. Zuo, "A grid strategy for predicting the space plane's hypersonic aerodynamic heating loads," *Aerospace Science and Technology,* vol. 86, pp. 659-670, 2019.

[16] F. Grasso and M. Marini, "Analysis of hypersonic shock-wave laminar boundary-layer interaction phenomena," *Computers & Fluids,* vol. 25, no. 6, pp. 561-581, 1996.

[17] M. Marini, "Analysis of hypersonic compression ramp laminar flows under sharp leading edge conditions," *Aerospace Science and Technology,* vol. 5, no. 4, pp. 257-271, 2001.

[18] W. Sutherland, "The viscosity of gases and molecular force," *Philosophical Magazine Series 5,* vol. 36, pp. 507-531, 1893.

[19] H. Mahgerefteh, Y. Rykov and G. Denton, "Courant, Friedrichs and Lewy (CFL) impact on numerical convergence of highly transient flows," *Chemical Engineering Science,* vol. 64, no. 23, pp. 4969-4975, 2009.

[20] J. H. Ferziger and M. Peric, Computational Methods for Fluid Dynamics, Delhi: Springer.

[21] J. D. Anderson Jr, Hypersonic and High Temperature Gas Dynamics, New Delhi: McGraw Hill, 2011.

AUTHORS PROFILE

Mr. Karthik Sundarraj is an Aerospace Engineer with a Master of science, specialized in CFD from Brunel University, London. He currently works as the Technical Manager handling CFD Solutions portfolio for Indo-Pacific region at MSC Software Corporation. He comes with a rich industrial experience handling multiple CFD and other technology teams. He also worked as a Professor at UPES, Dehradun where he coordinated M.Tech in CFD program. He possesses strong research exposure working majorly in the areas of High-speed flows, external and internal flows. His other areas of interest include CFD applications in Biomedical, automotive and sports sectors. He has been associated with IISc since 2009, started as Project assistant and then moved on to be a research associate and later continued the association through collaborated projects and research initiatives.

Prof. Dr. Ugur Guven is an Aerospace Engineer (PhD, BSc) and a Nuclear Engineer (MSc). He is of now currently working as the Senior Professor of Aerospace Engineering at UPES and conducting research related to Interstellar Travel and Utilization of Nuclear Energy for Space Missions and Space Habitats. On the international front he is serving as the Advisory Council Member to United Nations Center for Space Science and Space Technology Education in Asia-Pacific Region (UN CSSTEAP) and he is also the Member of the Academic Council on United Nations Systems and Member of the European Association for International Education (EAIE). He is also currently the member of NAFSA as an educator. Dr Ugur GUVEN has 25+ years of work experience and over 150+ academic publications comprising of journal papers, conference proceedings, project reports, and books.

Dr. Prakash S Kulkarni is an Aerospace Engineer with M.Tech and PhD from Indian Institute of Science. He currently works as Chief Research Scientist and Professor at Department of Aerospace Engineering, Indian Institute of Science, Bengaluru. He was involved in the development of various robust kinetic theory-based algorithms to include higher accuracy and high-fidelity physics to simulate complex flows and algorithms based on moving mesh for unsteady aerodynamics. Currently he works in applying these algorithms to the practical configurations for aerodynamic analysis, verification and validation. His other areas of interests include CFD for biofluids, flow control devices and parallel computing

Dr. Om Prakash is an Aerospace Engineer (PhD, B. E) and an expert in flight mechanics (M.Tech). He currently is working as Professor of Aerospace Engineering at UPES and conducting research in the areas of flight mechanics, modeling and simulation, parachute and parafoil systems. Dr. Om Prakash serves as Faculty and Head of Aerospace Engineering at UPES and he also held the position of Head of Department of Aerospace Engineering at BBD University, Lucknow.

Mr. Ganesh Pawar R is a Research Intern in Computational Mechanics Lab (CML), Dept., of Aerospace Engineering, IISc, Bengaluru. He has pursued his Master of Technology in Thermal Engineering and bachelor's degree in Mechanical Engineering from Visvesvaraya Technological University (VTU), Belagavi. His area of interest involves CFD algorithm development, Assessment of generalized finite difference method (Meshless method), and high speed internal and external flows. He holds, three research publications together in journal and national conference.

Hypersonic flows over multi-ramp configurations

Karthik Sundarraj, Ugur Guven, P S Kulkarni, Om Prakash, Ganesh Pawar R

Abstract: The effects of attaching multiple ramps to the standard double ramp configuration along with variations in ramp angle, free-stream Mach number and surface temperature are discussed in this investigation. This study investigates the changes associated with shock wave boundary layer interaction (SWBLI) due to ramp induced flow breakdown and the flow field fluctuation with changes in flow characteristics and design. This type of ramp junctions typically features in re-entry vehicles, engine intakes, system and sub-system junctions, control surfaces, etc. Ramp junctions usually are associated with strong separation bubble that has significant upstream influence impacting the effectiveness of aerodynamic surfaces, engine performance, thermal behavior and stability. Computation studies are carried out using Second order accurate, finite volume RANS solver considering compressible laminar flow characteristics, with solver settings provided like experimental conditions as per literature. Comprehensive double ramp studies with suggestions on reducing the separation bubble size are invariantly considered in literature, however there has been no study in understanding the inclusion of additional ramps in such flow scenarios. At the end of this study it was evident that such complex junction needs detailed understanding on how they benefit or impact the overall design of the system. It also gave a very good insight on the nature of flow around such complex junctions and instills motivation for detailed experimental understanding.

Keywords: Multi-ramp, heat flux, hypersonic flows

I. INTRODUCTION

High speed aerodynamics mainly revolves around shocks and shock interactions that change the course of flow field and their behavior. The heat loads and forces are affected due to these alterations. The current technological advancements stand at a stage where the gap between space flight and atmospheric flight are closing in through human interventions and are now a dream that can be realized. The advent of hypersonic vehicle has created hope in this closure of gap and hence a lot of research is conducted in this area. Various researchers [1-10] have investigated shock wave boundary layer and interaction physics through design modifications such as blunting, cavitation, ramping, flaring, external attachments such as aero disc or spike etc. to evaluate and understand the importance of these design features and also to measure the dependency on these features. The study of interactions between inviscid and viscous regions is called as

shock wave and boundary layer interaction and the presence of these interactions in the flow affect both internal and external flow aerodynamics [3]. Generation of separation bubble, boundary layer separation, increased heating and even turbulent re-attachment could be caused through the presence of SWBLI. Careful attention must be given to the design of space vehicle systems and subsystems which experience such SWBLI [3]. As an outcome of design refinement several flow control techniques have been developed to suppress the effects of SWBLI [2]. Hypersonic flow field around blunted cone flare is a very good example that exhibits SWBLI. This example exhibits major features of flow around a space vehicle such as detached bow shock ahead of the cone and oblique shock with boundary layer interaction at the cone flare junction [1]. The SWBLI can produce separated flow at the upstream forward-facing corner where the deflection in the form of a ramp/flare is present. The length of separation has implications for control, stability etc., of a hypersonic reentry vehicle [4]. A separation shock wave is generated due to an abrupt change in flow direction in the presence of ramp. The shock interacts with the boundary layer over the wall which experiences adverse pressure gradient. Flow separation in the presence of such gradients majorly depends on factors associated with flow conditions, geometrical conditions and boundary layer behavior. The parameter at interest is the angle known as incipient separation angle given by Needham and Stollery [6].

$$M_\infty \theta_{is} = 80\sqrt{\overline{X_L}} \qquad (1)$$

Where $\overline{X_L}$ is the viscous interaction parameter at ramp junctions;

$$\overline{X_L} = M_\infty^3 \sqrt{C} / \sqrt{Re_L}$$
$$\text{where } C = \frac{\mu_w}{\mu_\infty} \frac{T_\infty}{T_w} \qquad (2)$$

Boundary layer separation takes place if the incipient separation angle is lesser than deflection angle. Separation occurs at a point ahead of the compression corner, separation leads to compression waves forming a separation shock ahead of the separation region. Separation bubble can be identified by sudden increase in the pressure from nearly constant in the downstream region to a sudden increase in the compression region. The flow reattaches at a point on the ramp surface, the recirculation zone extends between the separation and reattachment point and the distance between these two points is called as length of separation bubble [2]. In case the ramp angle was smaller than the incipient separation angles the flow would have not undergone much deflection as in the previous case and would have followed a laminar boundary layer profile without separation at the ramp [3]. Such flow

alterations occur mainly due to the influence of the ramp on the upstream flow physics. The area of interest shall be the distance between the ramp junction and the upstream point of influence. To enhance the performance of Ramp based SWBLI by reducing the intensity of this interaction through delayed separation several control mechanisms are reported to have been employed, reference to such control mechanisms can be seen is many past investigations. The current research work also pursues the idea of enhancing the performance of any system or subsystem functioning at hypersonic flow regime by altering flow paths through design modifications or study the nature of flow behavior in an unforeseen and unexplored design conditions such as multi-ramps.

Several researchers have investigated shock wave boundary layer phenomenon through several design modifications as stated in earlier sections. R. Savino and D. Paterna [1] conducted validation studies of flow around blunted cone flare in hypersonic flows. Experimental studies were performed in H3 Mach 6 wind tunnel at Von Karman Institute under laminar flow conditions. This work gives a detailed insight on the importance of grid independent study and the influence of mesh size on wall pressure, heat flux and skin friction parameters. It has also been noted through this study that the accuracy of separation bubble size, its location, the flow separation and reattachment locations are all dependent on the resolution of mesh near the wall and at the ramp junction. Sensitivity of wall pressure and heat flux to small changes in surface temperature has also been studied. It has been noticed with increase in surface temperature, the separation bubble length increases. The authors have also considered thermal conductivity effects by considering different materials properties of the experimental model and validating the same through computational methods. Bibin John and Vinayak Kulkarni [2 – 4] have performed wide range of numerical investigations addressing the ramp induced shock wave boundary layer interactions. Extensive and in-depth details on the effect of various flow and geometric parameters and their correlation with the shock wave boundary layer interaction in hypersonic flows performed through finite volume based computational solver are presented. Importance of Quantitative approach over qualitative measurements to estimate the separation bubble length and upstream influence through skin friction and wall shear has been detailed out, which gives a clear insight on the method of approach to understand separation physics [3]. The study also clearly points out the fact that the incipient separation angle concept work well only for well separated flows. It is found from these investigations that the separation bubble length is clearly dependent on flow and design parameters, where with increase in wall temperature the bubble length seems to increase in size and with increase in Mach number the bubble length seems to decrease in size. Strong correlation between leading edge bluntness on separation bubble length has been identified and presented. It is understood from this investigation the presence of two critical radius of leading-edge bluntness [4].

It is evident from the many literature studies that control of separation bubble is critical to minimize the effects of shock wave interactions in space vehicle systems and sub-systems. It can also be noticed that almost every literature investigation addresses only regions with single and double ramp junctions,

but there are almost nil investigations related to multi-ramp junctions which also gets featured in such hypersonic vehicle component and system designs. Multi-ramp junctions also pose severe design challenges and it is necessary to take conscious efforts while designing space vehicles. While these previous research works provide very good insights on the SWBLI by varying ramp angles, leading edge bluntness, freestream velocity etc., which becomes the core basis of the current work, the present research work focuses on the study of shock wave and boundary layer interactions with triple ramp and quad ramp configurations, considering the basic understanding of flow physics around single and double ramp configurations. This way it also helps in understanding the effects of having a multiple ramp on the upstream separation bubble already present at the second ramp junction along with the understanding of how the presence of additional downstream ramps overall changes the shock structure and flow. Computational investigations are carried out to study and understand the behavior of ramp induced shock wave and boundary layer interactions for three and four ramp configurations, wherein the first two ramps are considered as specified by R. Savino and D. Paterna [1], while the third and fourth ramp angles are varied in combination along with variations in freestream and surface temperature, to study the effects on the separation bubble length at all three ramp junctions. Since the studies presented by Bibin John and Vinayak Kulkarni [3] address in detail the relation between flow conditions and design variations on separation bubble size, it becomes a key consideration to test these correlations on multi-ramp configurations and to assess if these variations still continues to be an effective technique to understand and predict separation and hence the current research work considers triple ramp angles of 7.5^0, 10^0, 12.5^0 and 15^0, with same angles considered for fourth ramp along with a blunt radius of 3.5mm. All combinations of ramp angle variations between third and fourth ramps are considered for this simulation study. The freestream Mach number is varied between 6 to 8 and the surface temperatures as 270K, 300K and 330K. Simulation tool validation is performed using the base geometry and boundary conditions as provided by R. Savino [1] in their computational and experimental validation studies. Post successful validation, efforts are taken to initially study the effect of adding multiple ramp junctions to the base geometry on the shock wave boundary layer interaction, followed by considering variations in freestream Mach number and surface temperatures in the presence of third and fourth ramp. Details on the solution methodology, model and discretization details are presented in the next section. Discussions on the findings of adding multiple ramp junctions in association with freestream variations, thermal variation and its implications on the separation bubble is discussed in Section III, followed by conclusions and future works in Section IV.

II. COMPUTATION METHODLOGY

The numerical investigations are carried out using High Resolution Flow Solver on Unstructured meshes (HiFUN), considering it to be compressible laminar flow solver. Following conservation equations for mass and momentum are considered in the solver algorithm,

$$\frac{\partial \mathbf{U}}{\partial t} + \frac{\partial (f_i + f_v)}{\partial x} + \frac{\partial (g_i + g_v)}{\partial y} = 0 \qquad (3)$$

Where,

$$\mathbf{U} = \begin{bmatrix} \rho \\ \rho u \\ \rho v \\ \rho E \end{bmatrix} \quad f_i = \begin{bmatrix} \rho u \\ \rho u^2 + p \\ \rho u v \\ \rho u H \end{bmatrix} \quad g_i = \begin{bmatrix} \rho v \\ \rho u v \\ \rho v^2 + p \\ \rho v H \end{bmatrix}$$

And,

$$f_v = \begin{bmatrix} 0 \\ \tau_{xx} \\ \tau_{xy} \\ u\tau_{xx} + v\tau_{xy} - q_x \end{bmatrix} \quad g_v = \begin{bmatrix} 0 \\ \tau_{xy} \\ \tau_{yy} \\ u\tau_{xy} + v\tau_{yy} - q_y \end{bmatrix} \qquad (4)$$

Here, U is the vector of conserved variables, f_i and g_i are inviscid flux vectors along x and y directions respectively. Also f_v and g_v are viscous flux vectors along x and y respectively,
The expressions for the viscous stress and heat conduction terms are given below:

$$\tau_{xx} = \frac{\mu}{Re_\infty}\left(\frac{4}{3}\frac{\partial u}{\partial x} - \frac{2}{3}\frac{\partial v}{\partial y}\right), \quad \tau_{yy} = \frac{\mu}{Re_\infty}\left(\frac{4}{3}\frac{\partial v}{\partial y} - \frac{2}{3}\frac{\partial u}{\partial x}\right)$$

$$\tau_{xy} = \frac{\mu}{Re_\infty}\left(\frac{\partial u}{\partial y} + \frac{\partial v}{\partial x}\right)$$

$$q_x = \frac{\mu}{M_\infty^2 Pr_\infty Re_\infty (\gamma - 1)}\frac{\partial T}{\partial x}$$

$$q_y = \frac{\mu}{M_\infty^2 Pr_\infty Re_\infty (\gamma - 1)}\frac{\partial T}{\partial y}$$

For the present study, fluid is assumed to be as ideal gas. HLLC flux [11, 12] is adopted for inviscid flux scheme and Green Gauss [13] for viscous flux scheme with a special accuracy of 1. Implicit time integration approach is used for obtaining numerical approximation of the solution, with the relaxation faction of 0.4 and the permissible range of CFL (Courant-Friedrichs-Lewy) [19, 20] number is 0.09 – 1.

$$\frac{\mu}{\mu_{ref}} = \left(\frac{T}{T_{ref}}\right)^{\frac{3}{2}}\left(\frac{T_{ref} + S}{T + T_\infty}\right) \qquad (5)$$

Laminar viscosity (μ) is computed by using Sutherland's law [18], where he Sutherland's constant (S) for air is considered as (110.56), the reference viscosity (μ_{ref}) is ($17.16 \times 10^{-6} \, N \, s/m^2$) of air at a reference temperature (T_{ref}) of (273.15 K), t, while the Prandtl number (Pr) is assumed to be 0.74.

III. NUMERICAL INVESTIGATIONS

Inter-code comparison, grid dependency study and theoretical validation stagnation pressure and post shock temperature are performed on the model and boundary conditions as considered by R. Savino [1]. The base model considered for initial validation studies is henceforth referred as double ramp, which is 159.11 mm in total length, with first ramp angle 7.5^0, second ramp angle 10^0 and a leading-edge bluntness of radii 3.5 mm. A third and fourth ramps of length 62.5 mm and 53.5 mm are attached to the base double ramp model, for the current investigation on ramp induced shock wave boundary layer interactions. Model details along with the computation domain and boundary conditions are shown in Fig. 1 & 2. The freestream conditions and the details about both the ramp angles are mentioned in Table-I. Multi-block structured meshing has been performed to discretise the computation domain. Different mesh combinations with variations in mesh spacing both in normal and along the body are considered, the detailed of the same is shown in Table-II, a sample grid used throughout this investigation is shown in Fig. 3. Due to availability of multiple computation tools, inter-code comparison was necessary to ensure the chosen tool is the best to capture the flow physics that involves, laminar high-speed flows with high gradient flow separations along with the formation of shocks. The pressure distribution along the double ramp model [1] was taken as a standard to perform the inter-code comparison. HiFUN proved to predict the experimental results very accurately and for this reason it has been chosen for all simulations in this investigation. Through grid independence study it was found that the mesh parameters used by R. Savino [1] was not suitable for HiFUN to match the experimental data. Grid spacing normal to the model was found as the major criterion to reach solver accuracy, while maintaining the overall mesh count same as in literature. It was found from grid independence study that the mesh size of 960 x 160 and 480 x 80 with 30micron normal mesh spacing had excellent agreement with experimental surface pressure values as shown in Fig. 3a. The separation and reattachment points have very good match while there is slight but acceptable computational underprediction in the post attachment zone. It can be noticed that 480 x 80 captures the bubble region better, but the post reattachment region is extremely critical for multi-ramp studies as it involves reattachment shocks and shear region which is captured better by 960 x 160 grid. Quantitative parameters such as surface heat flux was also validated, represented in Fig. 3b. As can be seen, there is underprediction of the separation point and a higher heat flux prediction post reattachment when compared to the experimental data. As indicated in the findings by R. Savino et. al [1], there are noticeable changes in bubble length and heat flux with time during an experimental study. The surface temperature increases with time while conducting a high-speed flow experimentation study. There is delay associated with data acquisition during which time the surface temperature increases by almost 10%. Increase in surface temperature over time has proven to increase the size of the separation bubble and reduce the heat flux prediction. This phenomenon can exactly be noticed in Fig. 3b, where the simulation cases are run for steady state conditions at t = 0,

Ramp 1
(Constant angle)

Ramp 2
(Constant angle)

Ramp 3
(Variable angle)

Ramp 4
(Variable angle)

Fig. 1. Multi-ramp model details

Fig. 2. Computational Domain

Table-1: Freestream and Geometry Conditions

M_∞	P_∞ (Pa)	T_∞ (K)	μ (Pa-s)	k (N/s-K)	Ramp 1 (α)	Ramp 2 (α)	Ramp 3 (α)	Ramp 4 (α)
6	673.67	67.07	$4.47e^{-6}$	0.00607	7.5	10	7.5, 10, 12.5, 15	5, 7.5, 10, 12.5

Table-II: Details of grids used for grid independence study

Model	Grid	Δn_0	Δn_h	Δs_0	Δs_h
Double Ramp	240 x 40	0.0015, 0.015, 0.03, 0.045, 0.06	0.0015, 0.015, 0.03, 0.045, 0.06	0.0675	0.018
	480 x 80			0.0337	0.009
	960 x 160			0.0168	0.0045
Triple Ramp	680 x 80	0.03	0.03	0.0168	0.0045
	1320 x 160				
Quad Ramp	1720 x 160	0.03	0.03	0.0168	0.0045

Δn_0, Δn_h = normal spacing at stagnation and ramp; Δs_0, Δs_h = tangential spacing at stagnation and ramp

Fig. 3. Sample grid used for quad ramp configuration

Fig. 3a. Grid independence study of surface pressure profile over double ramp

Fig. 3b. Grid independence study of surface heat flux profile over double ramp

which underpredicts the separation point and the surface heat flux is higher that the experimental value. The experimental values show the exact trend of predicting a bigger separation bubble and a reduced surface heat flux, indicating a possible delay in data acquisition. There are also chances of non-uniform flows in the test section resulting in boundary layer excitation causing early separation and lower heat flux due to turbulent convection. From the double ramp validation, it was found that 960 x 160 was the most reliable mesh for all design variations and hence the same mesh sizing was continued for the multi-ramp configurations having third and fourth ramps

by adding equal mesh divisions of 400 elements on each ramp making it 1320 x 160 on triple ramp configuration and 1720 x 160 on quad ramp configuration, any lesser mesh count was unable to capture separation and reattachment points accurately on downstream ramp junctions. The following sub-sections shall discuss on the effect of varying free-stream Mach number on triple and quad ramp configurations, the effect of changing surface temperatures on the separation bubble length and surface heat flux and the study on combined ramp angle variations between third and fourth ramps on shock wave boundary layer interaction.

IV. TRIPLE RAMP CONFIGURATION

A. Combined effects of varying free-stream Mach number and ramp angle

From the investigations done by Bibin John et. al. [3], it is evident that variation in ramp angle has a direct connect with freestream Mach number, the incipient separation angle decreases with an increase in freestream flow velocity (Mach). The study also reveals the fact that increasing ramp angle increases the bubble length and increasing the freestream Mach number reduced the length of bubble. The current study details out the combined effects of varying the free-stream Mach number and ramp angles to understand the changes in flow field and the shock wave boundary layer interactions. The base model or a double ramp configuration with first ramp angle of 7.5^0 and second ramp angle of 10^0 [1] is considered. To this base model a third ramp with varying angles as mentioned in Table-I is attached. Freestream Mach number is varied over all third ramp conditions to understand the changes in surface pressure distribution, skin friction coefficient and the separation bubble length. The surface pressure distributions are presented from Fig. 4 (a-d) and the skin friction coefficients are presented from Fig. 5 (a-d). From the plots it is evident that the flows are fully separated at both the ramp junctions and hence the deflection angles are above the incipient separation angle as described in the literature. Interestingly it is noticed that the correlation between Mach number and bubble size seems to not follow the trend as mentioned in earlier studies. Ideally the separation bubble length must be smaller for higher Mach numbers as per earlier findings, but from the pressure distribution plots, Fig. 4a to 4d, it is evident that this correlation no more is valid for configurations above double ramps. The correlation has been reversed in the case of triple ramp configurations wherein the separation point and reattachment points have been pushed upstream and downstream respectively in case of higher Mach number, while the separation point has moved downstream, and reattachment point upstream in case of lower Mach number. This trend remains same for all third ramp angles with increase in freestream Mach conditions, this could be attributed to the upstream influence of the presence of a third ramp junction. Quantitative understanding through skin friction coefficient gives even better insights on separation and reattachment behavior in the presence of a third ramp. From Fig. 5 (a-d) it is interesting to notice that the size of the separation bubble is bigger for higher Mach numbers at the first junction while the separation bubble size is smaller for higher Mach numbers at the second junction. This is unique as two different correlations between Mach number and bubble size can be noticed at the same time, wherein the correlation is following inverse trends at the first junction while it follows the typical trend at the second junction as compared to the study by Bibin John et. al [3]. This is indicative of a significant downstream effect of having a third ramp on the flow physics. The separation point at the first junction moves downstream with increase in third ramp angles. The downstream effects are primarily due to changes in boundary layer caused by the compression corner at the second junction. What can also be noticed is that the reattachment shocks are becoming weaker at the first junction with increase in third ramp angle which are resulting in upstream shift in separation points at the second junction leading to increase in bubble size for lower Mach and reduction in bubble size for higher Mach. This is attributed to the reduction in inertia of the flow, where the lower Mach flows tends to become slower at the second junction resulting in early separation, while the higher Mach flows are still faster at the second junction resulting in later separation and so reduced bubble length. The skin friction peaks that can be noticed in the plots are indicative of a turbulent reattachment shock that also leads to a highly turbulent post shock shear region which are indicated as fluctuations post the reattachment point at the second junction. Table-III reassures that the presence of third ramp has effects on the length of the separation bubble located at the first junction. The table compares size of separation bubble between double ramp and triple ramp configurations. As can be seen the biggest bubble corresponds to the double ramp measuring 36.8 mm while all other bubble sizes corresponding to triple ramp are smaller indicating an upstream influence. The upstream influence could be because of the thickening of the boundary layer due to the compression corner at second junction. The entropy layer might be engulfed inside the boundary layer leading to the increase of separation bubble size at the first junction. Completely engulfed entropy layer alters the flow properties which is assumed to affect the separation and reattachment points at the first junction. It is critical to understand this flow physics in detail which is identified to occur in situations where there could be a complex junction in a system or a subsystem of high speed vehicles and so experimentation must be considered as the next step for better understanding of such complex flow physics and also to add basis for all the computational investigations.

B. Wall temperature effects at different Mach numbers

It is evident from the investigations done by R. Savino [1] and Bibin John [3] that variations in surface temperature has significant effect on the shock wave boundary layer interaction, hence it is important to study this parametric change on triple ramp configuration as well, to understand whether the correlation still follows the same trend for multi-ramp junctions. For this study triple ramp configuration with 7.5^0 third ramp angle is considered as it exhibits fully separated flow at both ramps with lowest pressure peaks at second junction. Freestream Mach number chosen as between 6 to 8 and surface temperatures considered are 270 K, 300 K and 330 K. Surface heat flux for different Freestream Mach numbers are shown in Fig. 6-8 and the surface pressure distribution for Mach 6 is shown in Fig. 9. Simulation with adiabatic wall condition is also considered and plotted along with the isothermal wall boundary, to understand the upstream influence on the flow physics with these different wall thermal treatments. Table-IV gives a detailed perspective on the effects of bubble sizes due to the variations in freestream Mach number in combination with varying surface temperature. It can be understood from this study that there is a definite upstream influence with increase in wall temperature. This influence is seen throughout the configuration at all locations and the presence of third ramp

(a) 7.5⁰ third ramp angle

(b) 10⁰ third ramp angle

(c) 12.5⁰ third ramp angle

(d) 15⁰ third ramp angle

Fig. 4. Surface pressure distributions of triple ramp configurations at different Mach numbers

(a) 7.5⁰ third ramp angle

Triple ramp model

(b) 10⁰ third ramp angle

(c) 12.5⁰ third ramp angle

(d) 15⁰ third ramp angle
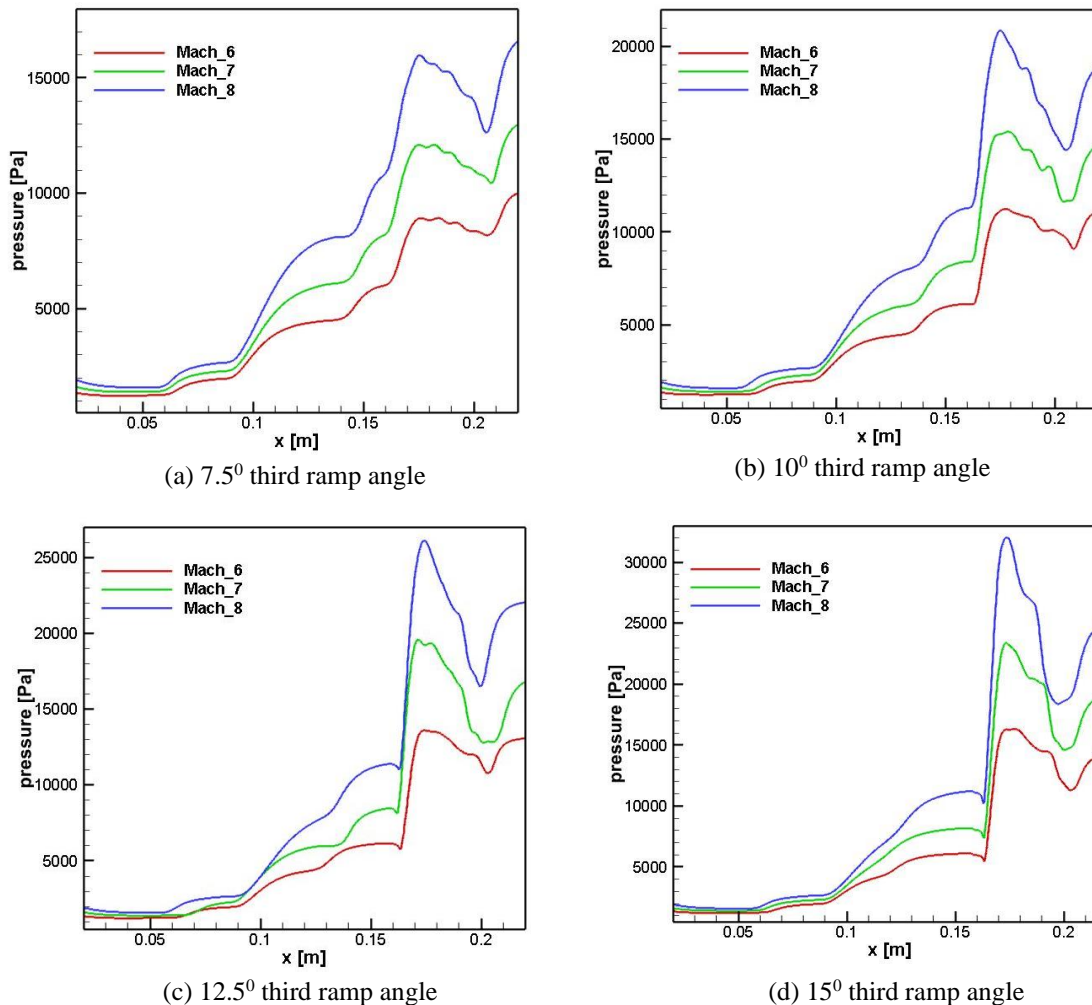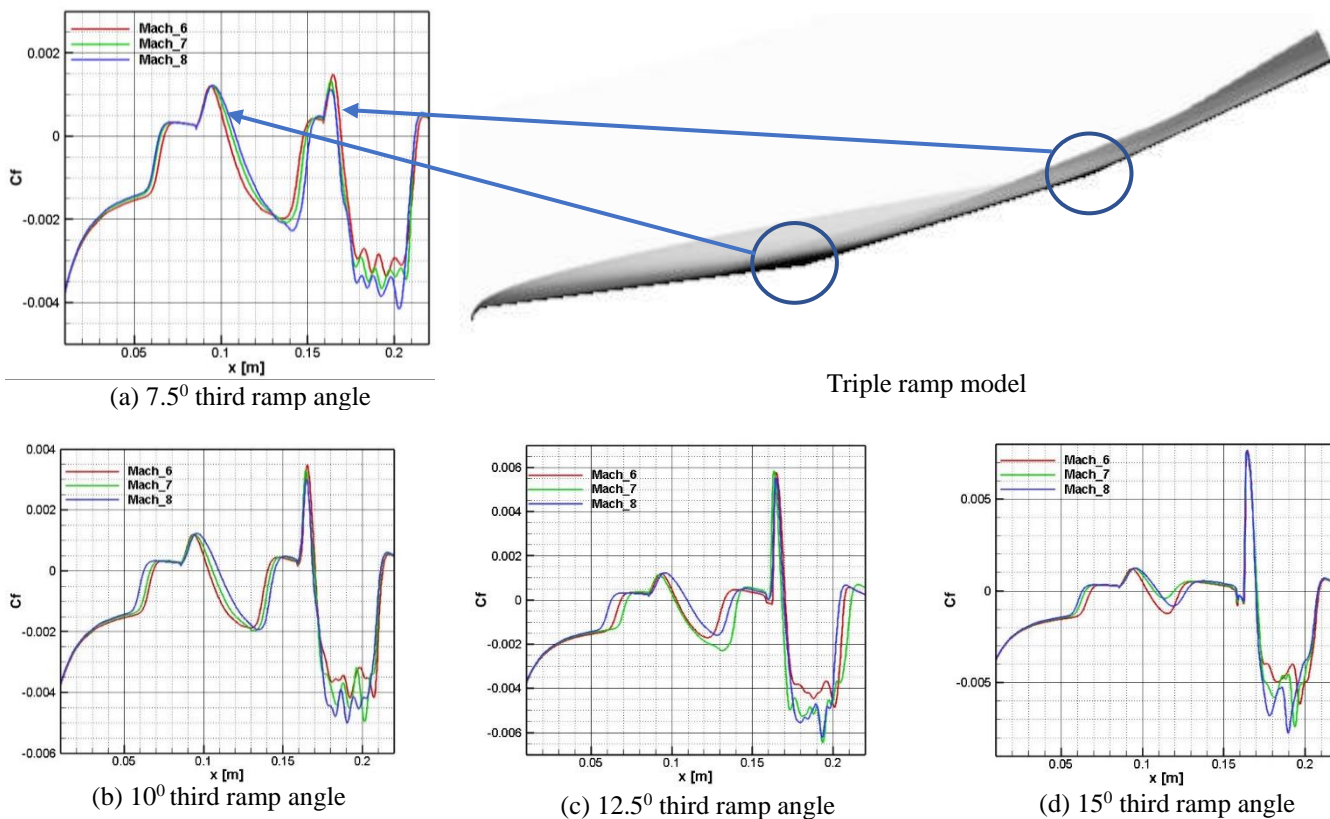
Fig. 5. Skin friction coefficients of triple ramp configurations at different Mach numbers

Table-III: Summary of separation bubble sizes for varying freestream Mach numbers and ramp angles

M_∞	Configuration	α	Bubble	L_b
6	DR		FB	36.8
	TR	7.5	FB	36.47
			SB	21.6
	TR	10	FB	34.87
			SB	29.94
	TR	12.5	FB	34.47
			SB	7.88
	TR	15	FB	34.6
			SB	12.95
8	DR		FB	31.72
	TR	7.5	FB	44.31
			SB	15.92
	TR	10	FB	47.2
			SB	24.06
	TR	12.5	FB	46.8
			SB	31.95
	TR	15	FB	46.3
			SB	11.83

DR = double ramp, TR = triple ramp, α = third ramp angle, FB = first bubble, SB = second bubble, L_b = bubble length

Fig. 6. Wall temperature effects on surface heat flux distribution at Mach 6
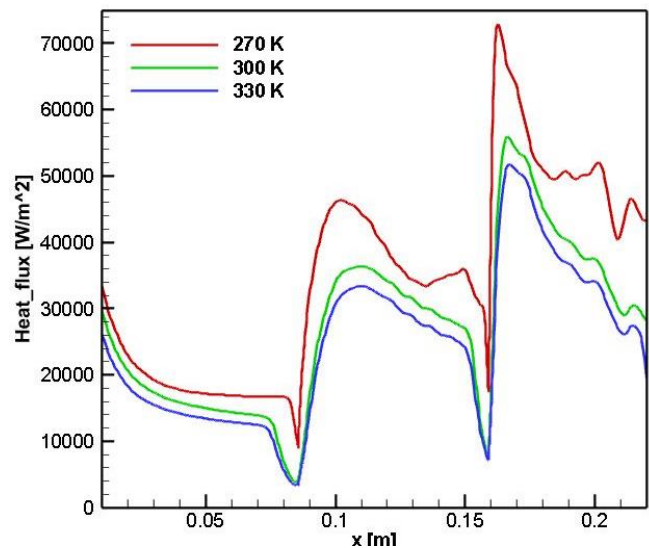
Fig. 7. Wall temperature effects on surface heat flux distribution at Mach 7

does not alter the correlation between surface heat flux and SWBLI. It is interesting to observe from the heat flux plots that the combined study of freestream Mach number, surface temperature and the third ramp has major upstream influences and has noticeable increase in peak pressure values post reattachment at both the junctions. The increase in peak pressure values are mainly attributed to smaller but stronger separation bubbles at higher freestream Mach which causes stronger compression corner shocks and a much stronger reattachment shock followed by highly turbulent shear zone. Increase in surface temperature causes rise in viscosity properties of the flow which causes an increase in the boundary layer thickness. Thicker boundary layer reduces heat flux while also causes early separation as can be seen in Table-IV. It is also noticed that the separation point is moved downstream with increase in freestream Mach number at both ramp junction while still early separation is noticed with increased wall temperature. It can be deduced that increase in

Mach number does reduce the bubble length at both junctions while bubble length remains to be bigger for higher wall temperatures. Biggest separation bubble of size 36.47 mm and 21.6 mm at the first and second junctions respectively can be seen for Adiabatic wall condition at Mach 6 indicating the effects of surface temperature on boundary layer thickness. The bubble size continues to increase at the first junction in case of adiabatic conditions with bubble size reaching a maximum of 44.31 mm at first junction for Mach 8 while the maximum bubble size in case of isothermal surface temperature of 330 K at Mach 8 freestream condition in just 14.31 mm. This is a considerable reduction in bubble size noticed due to surface temperature changes. Hence it is evident that increase in freestream velocity with increase in wall temperature reduces the bubble size considerably while also reducing the heat flux, on the contrary considering adiabatic wall conditions with increase in freestream Mach number has adverse bubble growth at the first junction.

Fig. 8. Wall temperature effects on surface heat flux distribution at Mach 8
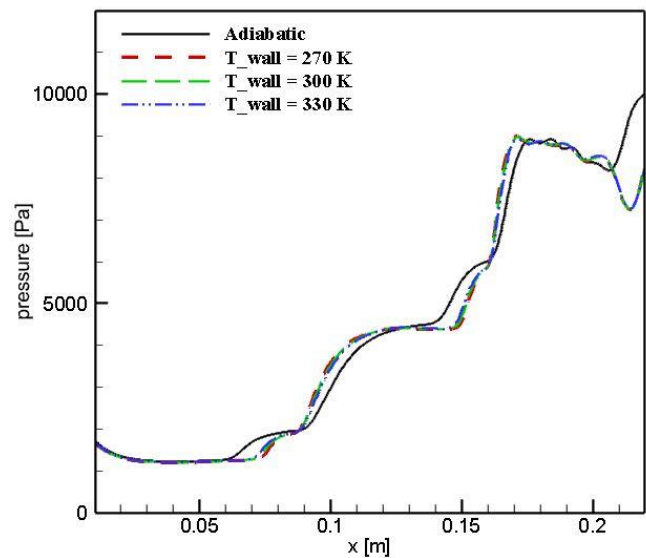
Fig. 9. Wall temperature effects on pressure distribution at Mach 6

Table-IV: Summary on effects of bubble sizes due to the variations in freestream Mach number and surface temperature

M_∞	T_W (K)	FB			SB		
		X_{sep} (mm)	X_{re} (mm)	L_b(mm)	X_{sep} (mm)	X_{re} (mm)	L_b(mm)
6	Adiabatic	67.31	103.78	36.47	147.6	169.2	21.6
7	Adiabatic	65.01	106.58	41.57	149.2	167.5	18.3
8	Adiabatic	64.27	108.59	44.31	151.38	167.3	15.92
6	270	77.15	94.7	17.54	153.4	163.98	10.58
7	270	84.07	88.01	3.93	158.4	159.9	1.5
6	300	75.94	95.79	19.84	152.8	164.5	11.7
7	300	78.31	94.3	15.99	154.92	162.5	7.58
6	330	74.76	96.96	22.20	152.1	165.28	13.18
7	330	77.27	95.4	18.12	154.55	162.8	8.25
8	330	79.45	93.76	14.31	156.4	162.3	5.9

M_∞= freestream Mach, X_{sep}= separation point, X_{re}= reattachment point, L_b= bubble length, T_W= wall temperature

V. QUAD-RAMP CONFIGURATION

A. *Effects of varying freestream Mach number and ramp angle*

From earlier investigations, it is evident that multi-ramp design configurations have significant effects in the flow physics leading to changes in correlations between freestream and design modifications. It is also certain that the flow around such complex multi-junction configurations have some of the most complex flow structure and shock interactions and must not be studied in detail. These multi-ramp junctions also change the understandings derived from earlier research findings of Bibin John et. al [3] where the correlation between freestream Mach number and bubble length vary with increase in ramp junction as noticed in the earlier section. Numerical simulations are carried out to study the effects of adding a fourth ramp to the earlier considered three ramp configurations on the flow physics associated with shock wave boundary layer interaction. The first and second ramp are the same as base model, the third ramp is fixed at 7.5^0 ramp angle. To this triple ramp configuration, a fourth ramp is attached making it a Quad-ramp configuration. Fourth ramp angles are varied between 5^0 to 12.5^0 with a varying freestream Mach number between 6 to 8 and the

associated effects on skin friction coefficient and surface pressure distributions are shown in Fig. 10 (a-d) and Fig. 11. (a-d) respectively. A minimum ramp angle of 5^0 is considered for the fourth ramp as it is critical to test the validity of incipient separation angle. It is evident from the pressure distribution plots that the incipient separation theory by Bibin John et. al [3] still holds, where the separation bubble for 5^0 ramp angles is almost negligible in size indicating that it is not a fully separated flow whereas, the bubble sizes increase with higher ramp angles beyond 7.5^0 as per earlier studies. From the skin friction coefficient plots, the trends upto the second junction is exactly as depicted in triple ramp configuration, where the bubble size is larger for higher freestream Mach at first junction and the bubble size is least for lower freestream Mach. At the third junction the separation and reattachment points do not show noticeable variations with increase in freestream Mach number, indicating that the separation bubble size at the third junction is no more dependent on the freestream velocity conditions. This could attribute to low inertia by the time the flow reaches the third junction across all Mach conditions. It is also noticed across all ramp variations that the region after the reattachment at the second junction is highly turbulent due to a turbulent reattachment causing a highly turbulent shear region, the effects of the turbulent shear and the shock follows

(a) 5^0 quad-ramp angle

(b) 7.5^0 quad-ramp angle   (c) 10^0 quad-ramp angle   (d) 12.5^0 quad-ramp angle

Fig. 10. Skin friction coefficients of quad-ramp configurations at different Mach numbers
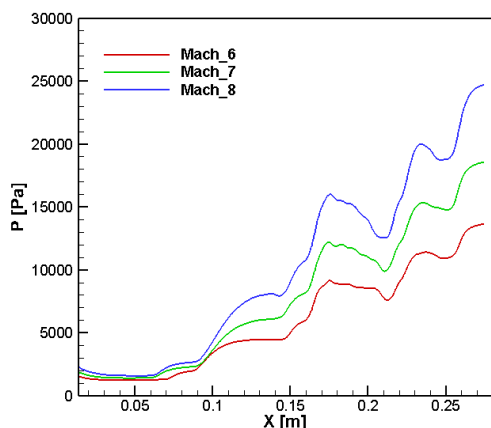
(a) 5^0 quad-ramp angle
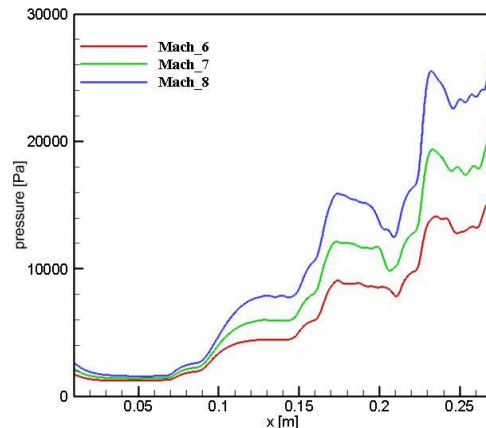
(b) 7.5^0 quad-ramp angle
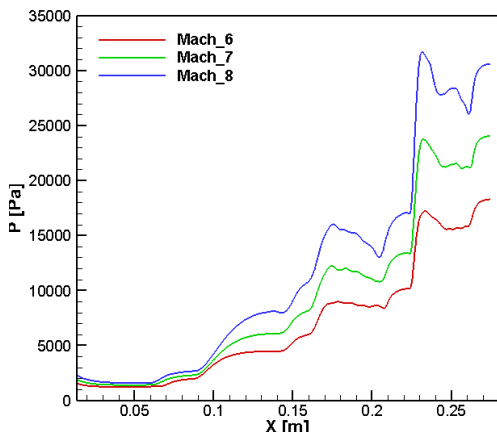
(c) 10^0 quad-ramp angle
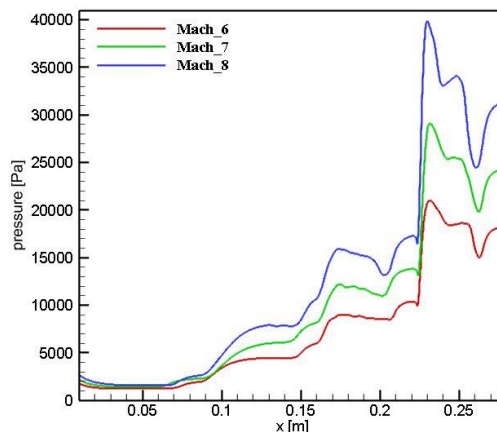
(d) 12.5^0 quad-ramp angle

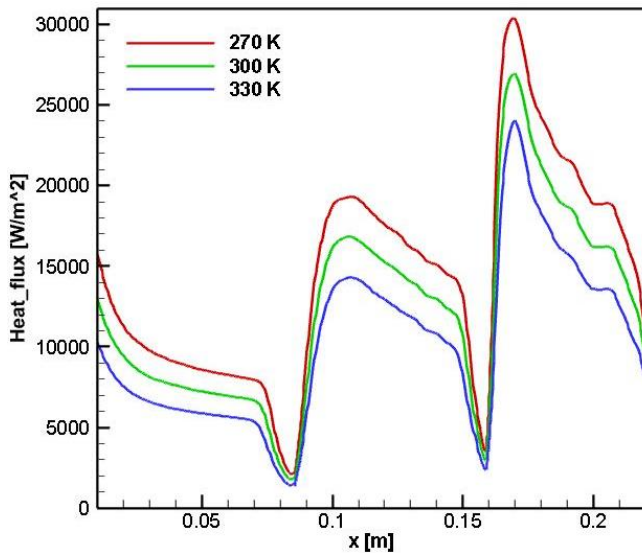Fig. 11. Surface pressure distributions of quad-ramp configurations at different Mach numbers

downstream towards the third junction increasing the intensity of reattachment shock at the third junction. This could be attributed to turbulence dissipation downstream through shear layers causing a stronger corner shock at the third junction. These studies indicate that such complex junctions have very unpredictable flow natures and may not follow every correlation that proves well for a simple double ramp configuration, encouraging the need for detailed and in-depth experimental studies to clearly understand flow physics when design scenarios lead to such complex multi-ramp junctions.
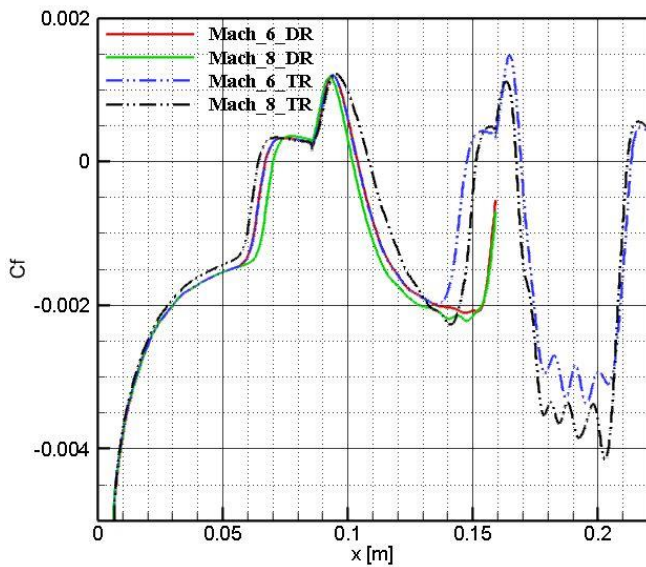
Fig. 12. Separation bubble comparison between double and triple ramp configurations

VI. CONCLUSION

Complex multi-ramp junctions were investigated to study the effects of these design modifications on flow physics followed by a detailed study on how changes in flow conditions and surface properties in combination with design changes the different characteristics of shock wave and boundary layer interactions which includes understanding of separation and reattachment behaviors, shock interactions, shear regions and boundary layer physics. Extensive validation activity was performed to ensure accuracy of flow solver through inter-code comparison and grid independence based on which a common solver and grid was chosen as the outcome of this validation. Two different ramp configurations with complex multi-ramp junctions are considered for flow computation studies, one the triple ramp configuration with two distinct ramp junctions with three ramps and the other a quad-ramp with three ramp junctions with four ramps. These complex design configurations do not feature much in any of the past literatures but poses equal or even higher design challenges due to the complexity in flow patterns. Both qualitative and quantitative methods are employed to understand the overall effects of these design configurations on the shock wave boundary layer interaction. Current study investigates the combined effects of varying the free-stream Mach number and ramp angles to understand the changes in flow field for both the configurations. The most crucial finding is that such complex junctions have very

unpredictable flow natures and may not follow every correlation that proves well for a simple ramp junction. One such correlation that seems to fail is the behavior of bubble length with increasing freestream Mach number. It has been found that with increase in ramp junctions, the bubble at the first junction increases with increase in freestream Mach number which is an inverse correlation when compared to literature studies, while the bubble length decreases in size with higher freestream Mach numbers at the second junction. The bubble length at third junction seems to no more change its characteristics with increase in freestream Mach number with almost same separation and reattachment points. The effect on the first junction is mainly attributed to the upstream influence of the presence of multiple ramps, causing the boundary layer to thicken. The entropy layer might be engulfed inside the boundary layer leading to the increase of separation bubble size at the first junction. Loss of inertia causes the bubble size to increase at higher ramp junctions for lower Mach numbers eventually becoming almost constant size for all Mach numbers at third junction. The bubble behavior on a double ramp junction follows the correlation of smaller bubble length at higher Mach number whereas the reverse is seen when there are additional ramps, this is evident and seen in 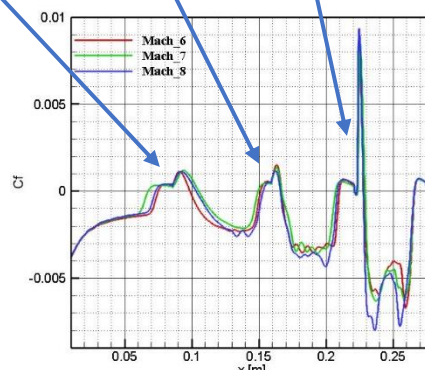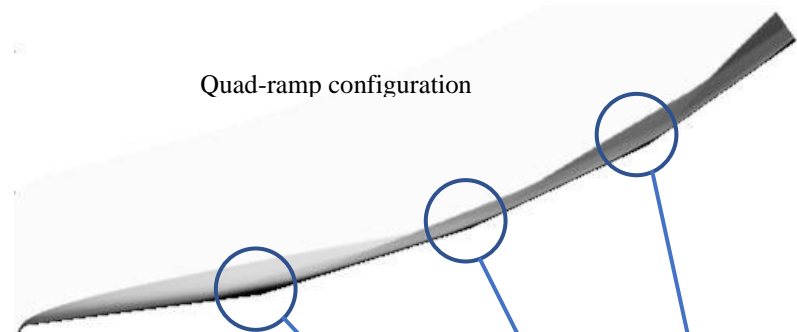the Fig. 12. The bubble lengths can also be referred to in Table-III, where same trends are noticed. These multi-ramp configurations also exhibit highly turbulent reattachment shocks and turbulent shear regions making it evident that laminar considerations will not be the right method, while reliable understanding on physics can be achieved and yet will require turbulent computational studies to derive at more accurate inference. Wall temperature variation and its effects on shock wave boundary layer interactions are also studied in this investigation. Simulation with adiabatic wall condition is also considered and plotted along with the isothermal wall boundary, to understand the upstream influence on the flow physics with these different wall thermal treatments. It can be understood from this study that there is a definite upstream influence with increase in wall temperature. From the investigation in can be deduced that increase in Mach number does reduce the bubble length at both junctions while bubble length remains to be bigger for higher wall temperatures. Adiabatic wall condition is found to have the biggest bubble size, this mainly is found to happen because increase in temperature increases the boundary layer thickness and hence early separation. These studies indicate that such complex junctions have very unpredictable flow natures and may not follow every correlation that proves well for a simple double ramp configuration, encouraging the need for detailed and in-depth experimental studies to clearly understand flow physics when design scenarios lead to such complex multi-ramp junctions. Future studies will investigate such multi-ramp configurations in detail through experimental methods where detailed insights can be arrived at with respect to multi-ramp configurations and their effects on shock wave boundary layer interactions.

VII.   ACKNOWLEDGEMENT

VIII.   REFERENCES

[1] R. Savino and D. Peterna, "Blunted cone-flare in hypersonic flow," *Computers & Fluids,* pp. 859-875, 2005.

[2] B. John and V. Kulkarni, "Numerical assessment of correlations for shock wave boundary layer interaction," *Computers & Fluids,* vol. 90, pp. 42-50, 2014.

[3] B. John, V. Kulkarni and G. Natarajan, "Shock wave boundary layer interactions in hypersonic flows," *International Journal of Heat and Mass Transfer,* vol. 70, pp. 81-90, 2014.

[4] B. John and V. Kulkarni, "Effect of leading edge bluntness on the interaction of ramp induced shock wave with laminar boundary layer at hypersonic speed," *Computers & Fluids,* vol. 96, pp. 177-190, 2014.

[5] S. Reichel and R. Groll, "Numerical simulation and experimental validation of a hypersonic flow for numerical modulation of re-entry phenomena prediction using adaptive mesh refinement," *International Journal of Computational Methods and Experimental Measurements,* vol. 1, no. 4, pp. 381-394, 2013.

[6] D. A. Needham and J. L. Stollery, "Boundary layer separation in hypersonic flow," *University of London,* 1966.

[7] C. L. Runninga, T. J. Julianoa, J. S. Jewell, M. P. Borgb and R. L. Kimmel, "Hypersonic Shock-Wave/Boundary-Layer Interactions on a Cone/Flare," *Experimental Thermal and Fluid Science,* 2019.

[8] D. V. Gaitonde, "Progress in shock wave/boundary layer interactions," *Progress in Aerospace Sciences,* vol. 72, pp. 80-99, 2015.

[9] I. G. Brykina, B. V. Rogov, G. A. Tirskiy, V. A. Titarev and S. V. Utyuzhnikov, "A comparative analysis of approaches for investigating hypersonic flow over blunt bodies in a transitional regime," *Journal of Applied Mathematics and Mechanics,* vol. 77, pp. 9-16, 2013.

[10] H. S. Massimi, H. Shen, C. Y. Wen, Y. S. Chen and S. M. Lian, "Numerical analysis of hypersonic flows around blunt-nosed models and a space vehicle," *Aerospace Science and Technology,* vol. 43, pp. 360-371, 2015.

[11] Z. Shena, W. Yan and G. Yuan, "A robust HLLC-type Riemann solver for strong shock," *Journal of Computational Physics,* vol. 309, pp. 185-206, 2016.

[12] S. Simon and J C. Mandal, "A simple cure for numerical shock instability in the HLLC Riemann solver," *Journal of Computational Physics,* vol. 378, pp. 477-496, 2019.

[13] H. Nishikawa, "From hyperbolic diffusion scheme to gradient method: Implicit Green–Gauss gradients for unstructured grids," *Journal of Computational Physics,* vol. 372, pp. 126-160, 2018.

[14] D. Sun, F. Qu and C. Yan, "An effective flux scheme for hypersonic heating prediction of re-entry vehicles," *Computers and Fluids,* vol. 176, pp. 109-116, 2018.

[15] F. Qu, J. Chen, D. Sun, J. Bai and G. Zuo, "A grid strategy for predicting the space plane's hypersonic aerodynamic heating loads," *Aerospace Science and Technology,* vol. 86, pp. 659-670, 2019.

[16] F. Grasso and M. Marini, "Analysis of hypersonic shock-wave laminar boundary-layer interaction phenomena," *Computers & Fluids,* vol. 25, no. 6, pp. 561-581, 1996.

[17] M. Marini, "Analysis of hypersonic compression ramp laminar flows under sharp leading edge conditions," *Aerospace Science and Technology,* vol. 5, no. 4, pp. 257-271, 2001.

[18] W. Sutherland, "The viscosity of gases and molecular force," *Philosophical Magazine Series 5,* vol. 36, pp. 507-531, 1893.

[19] H. Mahgerefteh, Y. Rykov and G. Denton, "Courant, Friedrichs and Lewy (CFL) impact on numerical convergence of highly transient flows," *Chemical Engineering Science,* vol. 64, no. 23, pp. 4969-4975, 2009.

[20] J. H. Ferziger and M. Peric, Computational Methods for Fluid Dynamics, Delhi: Springer.

[21] J. D. Anderson Jr, Hypersonic and High Temperature Gas Dynamics, New Delhi: McGraw Hill, 2011.

AUTHORS PROFILE

Mr. Karthik Sundarraj is an Aerospace Engineer with a Master of science, specialized in CFD from Brunel University, London. He currently works as the Technical Manager handling CFD Solutions portfolio for Indo-Pacific region at MSC Software Corporation. He comes with a rich industrial experience handling multiple CFD and other technology teams. He also worked as a Professor at UPES, Dehradun where he coordinated M.Tech CFD program. He possesses strong research exposure working majorly in the areas of High-speed flows, external and internal flows. His other areas of interest include CFD applications in Biomedical, automotive and sports sectors. He has been associated with IISc since 2009, started as Project assistant and then moved on to be a research associate and later continued the association through collaborated projects and research initiatives.

Prof. Dr. Ugur Guven is an Aerospace Engineer (PhD, BSc) and a Nuclear Engineer (MSc). He is of now currently working as the Senior Professor of Aerospace Engineering at UPES and conducting research related to Interstellar Travel and Utilization of Nuclear Energy for Space Missions and Space Habitats. On the international front he is serving as the Advisory Council Member to United Nations Center for Space Science and Space Technology Education in Asia-Pacific Region (UN CSSTEAP) and he is also the Member of the Academic Council on United Nations Systems and Member of the European Association for International Education (EAIE). He is also currently the member of NAFSA as an educator. Dr Ugur GUVEN has 25+ years of work experience and over 150+ academic publications comprising of journal papers, conference proceedings, project reports, and books.

Dr. Prakash S Kulkarni is an Aerospace Engineer with M.S and PhD from Indian Institute of Science. He currently works as Chief Research Scientist and Professor at Department of Aerospace Engineering, Indian Institute of Science, Bengaluru. He was involved in the development of various robust kinetic theory-based algorithms to include higher accuracy and high-fidelity physics to simulate complex flows and algorithms based on moving mesh for unsteady aerodynamics. Currently he works in applying these algorithms to the practical configurations for aerodynamic analysis, verification and validation. His other areas of interests include CFD for biofluids, flow control devices and parallel computing

Dr. Om Prakash is an Aerospace Engineer (PhD, B. E) and an expert in flight mechanics (M.Tech). He currently is working as Professor of Aerospace Engineering at UPES and conducting research in the areas of flight mechanics, modeling and simulation, parachute and parafoil systems. Dr. Om Prakash serves as Faculty and Head of Aerospace Engineering at UPES and he also held the position of Head of Department of Aerospace Engineering at BBD University, Lucknow.

Mr. Ganesh Pawar R is a Research Intern in Computational Mechanics Lab (CML), Dept., of Aerospace Engineering, IISc, Bengaluru. He has pursued his Master of Technology in Thermal Engineering and bachelor's degree in Mechanical Engineering from Visvesvaraya Technological University (VTU), Belagavi. His area of interest involves CFD algorithm development, Assessment of generalized finite difference method (Meshless method), and high speed internal and external flows. He holds, three research publications together in journal and national conference.

EFFECT OF VARYING MACH NUMBER & WALL TEMPERATURE ON SURFACE HEAT FLUX OF MULTI-RAMP BODY

Karthik Sundarraj [1*], Niranjan Gandigudi[2], Ganesh Pawar[3], Prakash S Kulkarni [4], Ugur Guven[5]
Sudhir Joshi[6], Rajesh Yadav[7]

[1] Technical Head, ARK Infosolutions Pvt. Ltd, Bangalore (karthik_sundarraj@yahoo.com)
[2] M.Tech Student, UPES, Dehradun, INDIA
[3] M.Tech Student, JSS Academy of Technical Education, Bangalore
[4] Professor, JATP, Computational Mechanics Lab (CML), Dept. of Aerospace Engineering, IISc, Bangalore, INDIA
[5] Senior Professor, Dept. of Aerospace Engineering, UPES, Dehradun, INDIA
[6] HOD, Dept. of Aerospace Engineering, UPES, Dehradun, INDIA
[7] Asst. Professor, Dept. of Aerospace Engineering, UPES, Dehradun, INDIA

ABSTRACT

Shock-wave boundary layer interaction (SWBLI) and changes associated with heat flux for a multi ramp body is considered in the present studies. we are focusing on laminar boundary separation in in hypersonic condition for a triple ramp geometry. Effect of freestream Mach number and wall temperature and surface heat flux is considered for present study. The surface heat flux of the re-entry vehicles at supersonic and hypersonic conditions is one of the major problem, to get a better idea how the heat flux varies the analysis is carried out with three different Mach number 6, 7, 8 and different wall temperatures 270K, 300K, 330K. For verification and validation, we have considered a literature paper in which a study was carried out on a double ramp. A grid independence test is carried out for double ramp and the mesh with close to the experimental value is selected for the study of triple ramp. For all the simulation carried out in this paper the meshing part is done in ICEM CFD and the solving part is done by using HiFUN software.

Keywords: SWBLI, Surface heat flux, hypersonic flow, triple ramp, ICEM CFD, Hi-fun

NOMENCLATURE

P_∞	Free stream Pressure
T_∞	Free stream Temperature
M_∞	Free stream Mach Number
μ_∞	Free stream Dynamic viscosity
L_{sep}	Separation length
T_w	Wall Temperature
X	Distance along x direction
Δn	Spacing distribution along the stagnation line or in normal direction
Δs	Tangential spacing along the body
λ	Thermal Conductivity

INTRODUCTION:

Aerodynamic heating and the surface heat flux are the major problems in re-entry vehicle at supersonic or hypersonic conditions and a lot of research work is going on it. When a blunted cone-flare body is moving at supersonic or hypersonic condition it produces a detached bow shock at the blunt portion and the shear boundary layer is formed near the wall region, but near the cone-flare junction the flow detaches and then it reattaches to the oblique shock formed after the junction due to which the bubble is formed at the region of the cone-flare junction. This is called the oblique shock wave/boundary layer interaction. The distance from the detachment to reattachment is known

as separation length. The shock separation and reattachment cause to change in the surface heat flux. Which in turn effect the other parameters. The separation of laminar boundary layer depends on various factors i.e., Mach number, Reynolds number, flare deflection. The prediction of the separation length is the challenging task in fluid dynamics.

R. Savino, D. Paterna investigated the hypersonic flow over a blunted cone flare body, they carried out the experimental and computational work on the blunted cone-flare body and have also studied the effect of wall temperature on such bodies so for our case we are considering the same parameters and the geometry for validation.

2. COMPUTATIONAL METHOD

2.1 Geometry

In this paper we are considering a double ramp geometry for grid independence test and for further simulation we are using a triple ramp body. The double ramp is having a spherical nose of radius 3.5mm followed by a conical part with an angle of 7.5º with respect to the axis of the cone and then followed by flare portion of conical shape with an angle of 17.5º with respect to the axis of the cone. The other end of the conical geometry is having a diameter of 75mm, the cone-flare junction is at 85.68mm form the spherical nose end. the details of the geometry are as shown in the figure-1. For triple ramp an additional conical shape is added to the end of the double ramp with an angle of 25º with respect to the axis of the cone body. Due to which the diameter of the conical end increases the details of the geometry is as shown in the figure 2.
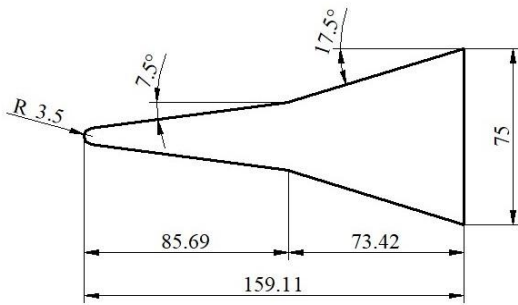
Figure 1- Geometry of Double ramp (dimensions are in mm)
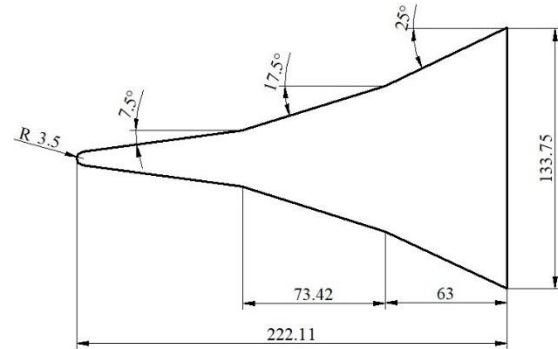
Figure 2- Geometry of Triple ramp (dimensions are in mm)

2.1 Meshing and solver setup

The Meshing is carried out in ICEM CFD software. A meshing size of 680x80 is considered for triple ramp, this is chosen based on grid independence test, the model consists of a total 54400 elements. The computational grid generated for triple ramp is as shown in the figure – 3
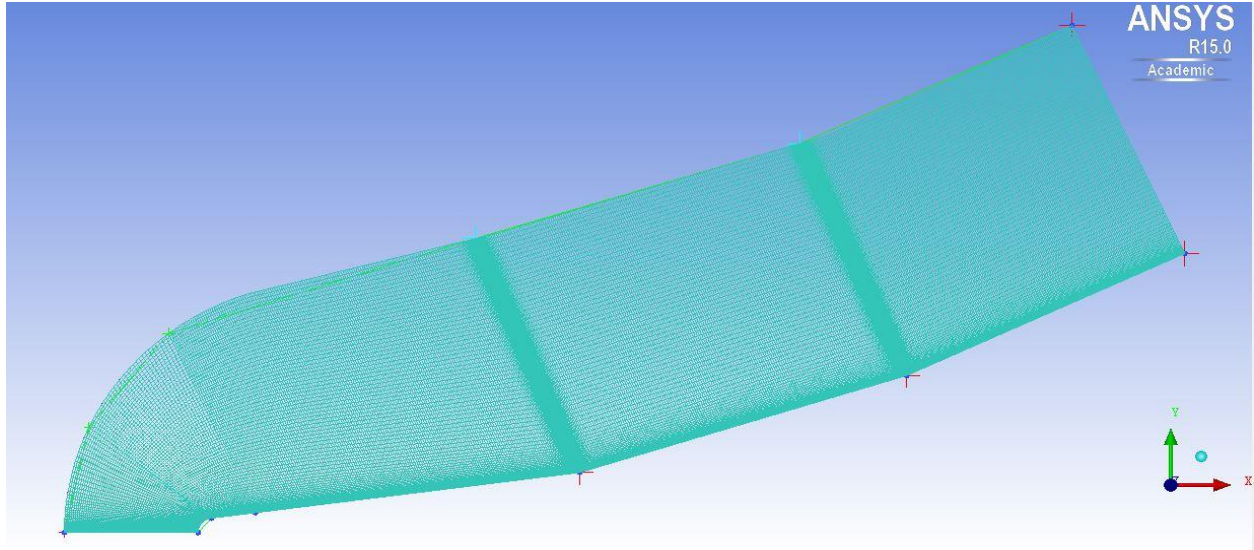
Figure 3- Triple ramp mesh of size 680x80

The grid spacing values of the mesh are as follows. $\Delta n_0 = 60 \times 10^{-6}$ m, $\Delta n_h = 60 \times 10^{-6}$ m, $\Delta s_0 = 33.7 \times 10^{-6}$m and $\Delta s_h = 9 \times 10^{-6}$m. Where 0 represent at stagnation region and h represent cone-flare junction. Δn spacing distribution normal to the ramp body, Δs is tangential spacing along the ramp body.

The solver part is carried out in HIFUN software the .msh file is imported in the software and a rotational or axisymmetirc case is selected. The boundary conditions are as follows, supersonic inflow for farfield, supersonic outflow for back, roational axis for axis, wall for the geometry. The spatial accuracy is of second order. Time integration is implicit, and the number of sweeps is 14. The free stream values are $P_\infty = 673.67$ Pa, $T_\infty = 67.07$ K, $\mu_\infty = 4.47 \times 10^{-6}$ Pa-s and $\lambda = 0.00607$ N/s-K. Here we are considering three mach number is 6, 7, 8 and for each Mach three different wall temperature are used i.e., 270K, 300K, 330K.

3. RESULTS AND DISCUSSION

3.1 Grid independence test

The double ramp from the literature is considered and different size mesh is used for the simulation and the results are compared with the literature. Here we are considering 5 different size of meshes the details of the mesh is given in the table 1. All the simulation in the grid independence test are calculated at Mach 6 and wall temperature of 300 K.

Case	Grid Size	Δn_0 in m	Δn_h in m	Δs_0 in m	Δs_h in m
1	240x40	60×10^{-6}	60×10^{-6}	33.7×10^{-6}	9×10^{-6}
2	480x80	30×10^{-6}	30×10^{-6}	33.7×10^{-6}	9×10^{-6}
3	480x80	60×10^{-6}	60×10^{-6}	33.7×10^{-6}	9×10^{-6}
4	660x120	15×10^{-6}	15×10^{-6}	33.7×10^{-6}	9×10^{-6}
5	960x160	30×10^{-6}	30×10^{-6}	33.7×10^{-6}	9×10^{-6}

Δn = is spacing distribution normal to the ramp body, Δs = Tangential spacing along the ramp body
0 = At the spherical nose, h = cone-flare junction

The heat fulx is plotted with respect to the horizontal direction x and the results are compared with the literature values the graph of comparison is as shown in the figure 4. As we can observe from the graph that the case 3 values are near to values from the literature so for our triple ramp case we are using the case 3 mesh.
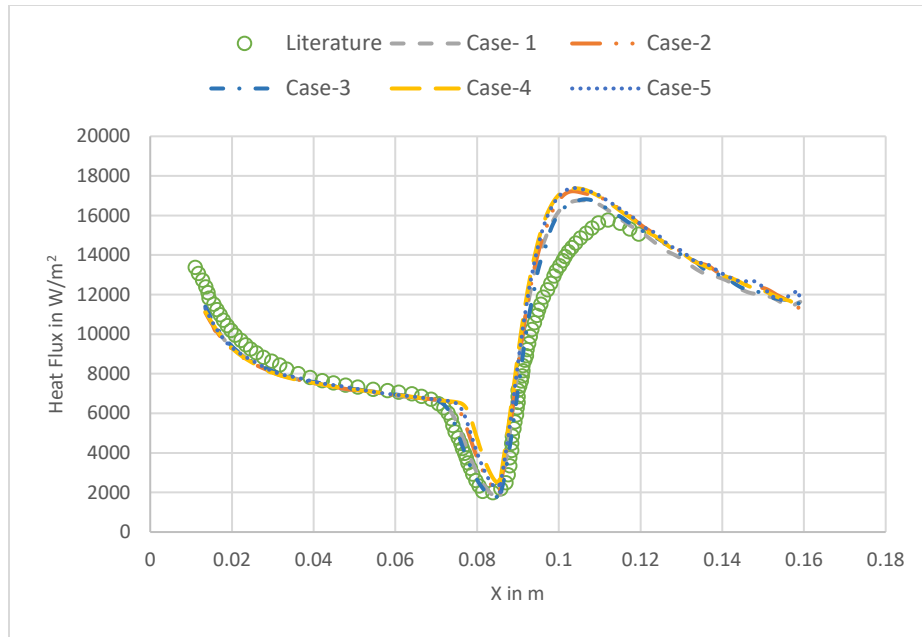
Figure 4 – comparision of double ramp mesh cases with literature

3.2 Results of triple ramp

Figure -5, 6, 7 shows the variation of heat flux with different wall temperature as we can see for all Mach, as the wall temperature is increasing the heat flux value after reattachment point is decreasing, this is due to the fact that increase in wall temperature leads to increase in the viscosity which in turn increases the thickness of the thermal boundary layer and this reduces the heat flux values at wall and this reduction in the heat flux is non negligible. The separation length is increasing with increase in the temperature this can be observed in the graph, this in turn increases the bubble size which is formed at the cone flare junction.

Figure -8 shows the variation of heat flux at different mach numbers at temp 300K. as we can see that at higher mach number the heat flux is high but at the cone-flare junction or after the flow deattaches the increment in the heat flux is less as compared to the other points of the geometry. And we can also observe that as the mach number increases the seperation length is decreasing, The bubble size reduces as the mach increases.

Table - 2 for variation of seperation length (approximate value) with different cases

M_∞	T_∞ in K	T_w in K	L_{sep} in mm at 1nd cone flare junction (app.)	L_{sep} in mm at 2nd cone flare junction (app.)	comment
6	67.07	270	16	15	$T_w\uparrow L_{sep}\uparrow$ at both cone flare junction for all mach number $M_\infty\uparrow L_{sep}\downarrow$ for all the wall temperature value
6	67.07	300	17	15.5	
6	67.07	330	18	16	
7	67.07	270	10	9	
7	67.07	300	14	12	
7	67.07	330	15	13	
8	67.07	270	14.5	6	
8	67.07	300	14.75	6.5	
8	67.07	330	15	7	
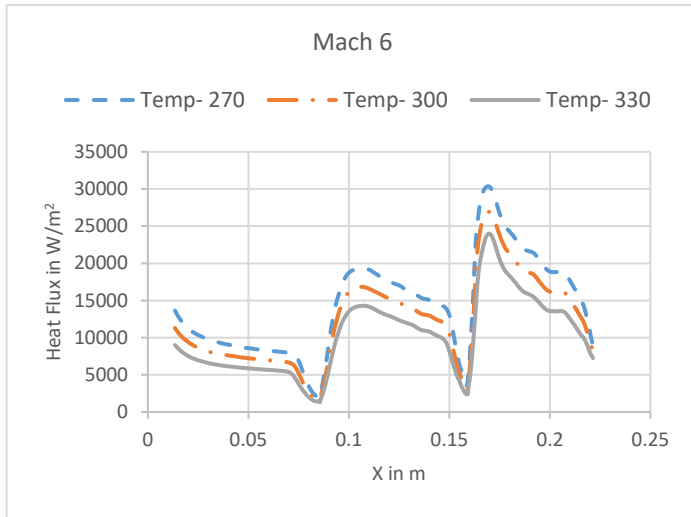
Figure-5 Variation of heat flux for different wall temperature at mach -6
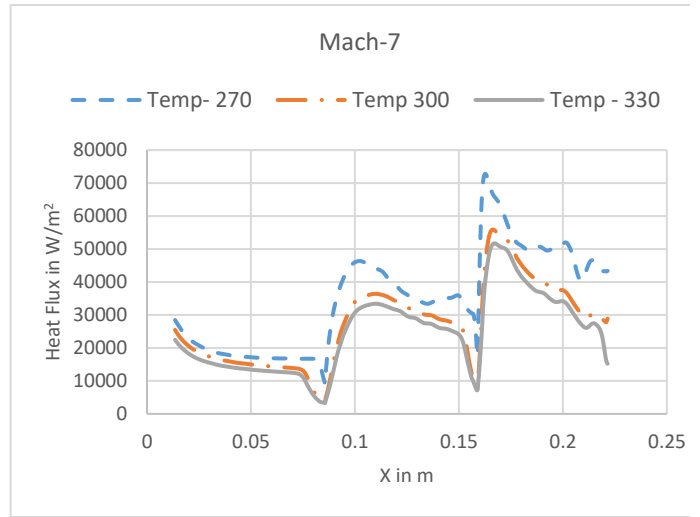
Figure-6 Variation of heat flux for different wall temperature at mach -7
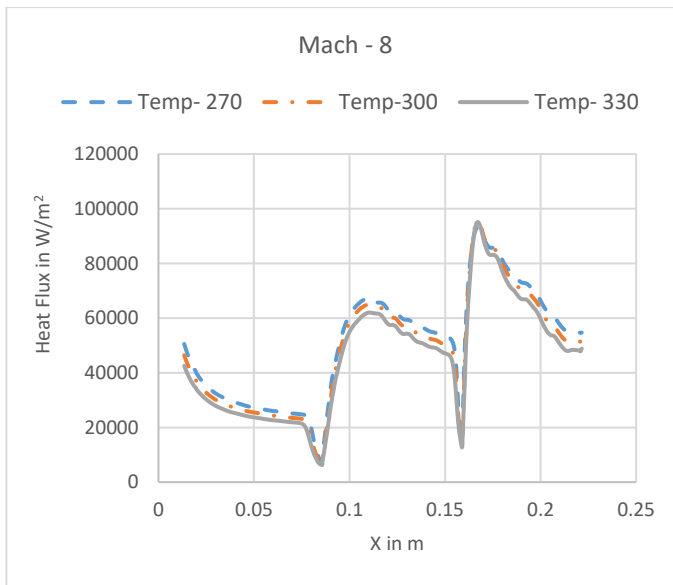
Figure-7 Variation of heat flux for different wall temperature at mach -8
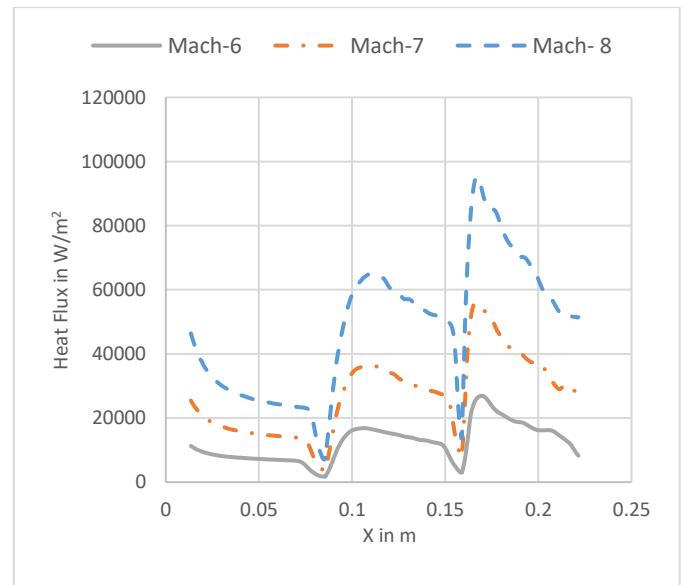
Figure-8 Variation of heat flux for different mach at wall temp-300K

4. CONCLUSION

As we aim to study of the effect of the wall temperatue on the multiramp body we can say that as the wall temperature increases the heat flux tend to decrease this is true for all the three mach numbers. And when we compared in variation of mach numbers the heat flux tend to increase with increase in mach number This helps to understand the behaviour of heat flux with the wall temperature. The study also shows that the bubble size decreases with increase in mach number and the bubble size increases with increase in wall temperature value on both the cone-fare junctions.

As from the table we can tell that the bubble formed at the second cone flare junction is smaller than the bubble formed at the first junction.

Work in progress: Currently simulations are running for Mach 9 condition and further comparison shall be included for the full-length paper.

REFERENCES

[1] R. Savino, D. Paterna , *Blunted cone flare in hypersonic flow*, Computers & Fluids 34 (2005) 859–875.

[2]Bibin John, Vinayak N. Kulkarni, Ganesh Natarajan*, Shock wave boundary layer interactions in hypersonic flows,* International Journal of Heat and Mass Transfer 70 (2014) 81–90.

[3] Bibin John, Vinayak Kulkarni. (2013). Numerical assessment of correlations for shock wave boundary layer interaction. Computers & Fluids. 90, 42 - 50.

FLOW OVER BLUNTED CONE FLARE HAVING TRIPLE RAMP

Karthik Sundararaj[1], Prakash S Kulkarni[2], Ugur Guven[3], Ganesh Pawar[4], B. Mohan Venkata Krishna Reddy[5], G. Praneeth[5], K. Chandra Sai Manoj[5], K. Siva Srinivas[5], B. Eswara Kumar[6]

[1]Technical Head, ARK Infosolutions Pvt Ltd, Bangalore (karthik_sundarraj@yahoo.com)
[2] Professor, Aerospace Engineering, IISc Bangalore
[3] Senior Professor, Dept. of Aerospace Engineering, UPES, Dehradun
[4] M.Tech Student, JSSATE, Bangalore
[5]Students, LBRCE, Mylavaram
[6]Professor, Aerospace Engineering, LBRCE, Mylavaram

ABSTRACT

This research study discussed about the flow field around a blunted triple ramp cone flare at high speed flow conditions. Multi-cone geometries shall prove to be useful for planetary entry vehicles at leading tip or they shall be useful for high speed intake ducts. There are numerous studies done on double cone flare geometries to understand the shock wave boundary layer interactions, but there is no study done on multi-cone geometries. Through this study, a clear understanding of flow over triple ramp cone flare can be achieved along with the understanding of attachment and detachment of shocks for higher ramp scenarios and how the separation bubble behaves for such multi-ramp geometries. Effects of varying the ramp angle at the third flare on the shock wave boundary layer interaction and the bubble size are also studied. Efforts are taken to develop a C-program code for finding the incipient angle for different ramp angles and Mach numbers. Grid sensitivity analysis has been performed until grid-solution independence is achieved. 2D Finite Volume solver is used to study the shock wave boundary layer interactions phenomenon with considering perfect gas assumption. Geometry and meshing is done using ICEM CFD and simulation is done in HiFUN.

Keywords: Re-entry vehicle, triple ramp, HiFUN, ICEM CFD.

NOMENCLATURE:

M_∞ = Free stream Mach number

$\theta_{i,s}$ = Incipient angle

$\overline{x_L}$ = Viscous interaction parameter.

μ_w = Coefficient of wall dynamic viscosity

μ_∞ = Coefficient of free stream dynamic viscosity

T_∞ = Free stream temperature

T_w = Wall temperature

1. INTRODUCTION:

The planetary re-entry vehicles carry human into space and bring back safely to earth and the problems associated with it are aerodynamic heating, surface heat flux and location of landing. Research works are going on these problems. The hypersonic flow field around a blunted cone–flare exhibits some of the major features of the flows around space vehicles, e.g. a detached bow shock in the stagnation region and the oblique shock wave/boundary layer interaction at the cone–flare junction [1]. The shock wave boundary layer interactions are generally formed when vehicles moving at supersonic and hypersonic speeds. It essentially deals with the inviscid - viscous interaction, boundary layer separation, enhanced heating loads or even turbulent re-attachments [2-3]. The separation of laminar boundary layer depends upon several factors i.e. Mach number, Reynolds number, flare deflection, wall temperature and boundary layer stability and ratio of specific heats [2]. The incipient separation angle of any case can be done from the relation given by Needham and Stollery [6].

$$M_\infty \theta_{i,s} = 80\sqrt{\overline{x_L}}$$

where $\overline{x_L}$ is the viscous interaction parameter, and is given by;

$$\bar{x}_L = M_\infty^3 \sqrt{C}/\sqrt{Re_L}$$

Where $C = \dfrac{\mu_w}{\mu_\infty}\dfrac{T_\infty}{T_w}$

The coefficient of dynamic viscosity is calculated by Sutherland's law in which air treated as perfect gas.

$$\mu = 1.716 \times 10^{-5} \left(\frac{T}{273}\right)^{\frac{3}{2}} \frac{384}{T+111} \text{ Kg/(ms)}$$

2. COMPUTATIONAL STUDY:

2.1. GEOMETRY:

The spherical nose of the probe has a radius of 3.5mm; the conical part has an angle of $7.5°$ with respect to the model axis, while the flare forms an angle of $10°$ with respect to the cone. The length of the double ramp model is 159.11mm and the cone–flare junction is located at 85.69mm from the nose. The diameter of double ramp is 75mm for double ramp [1].

The angles for the third ramp are 7.5°, 10°, 12.5° and 15° with respect to second ramp respectively. The angles are chosen such a way that they are greater than the incipient angle. For the triple ramp the length of the model is 221.11mm, and the second cone-flare junction is located at 159.11mm from the nose. The diameter for triple ramp is 133.75 for triple ramp angle 7.5° with respect to the second ramp as shown in Fig 1.

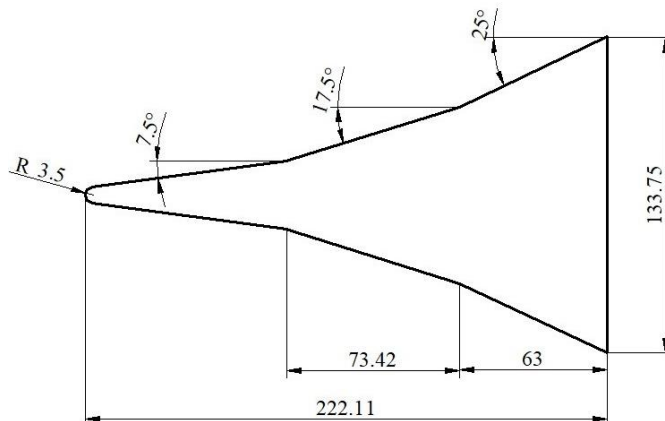Fig 1. Geometry of the cone–flare model with triple ramp (linear dimensions in mm)

2.2. MESH AND GRID INDEPENDENCE STUDY:

Meshing is carried out using ICEM CFD. The Coputational grid is shown in Fig 2 is for triple ramp, mesh size is 1320×160. It is composed of 211,200 quadrilateral cells, with 1320 cells in the direction tangential to the body and 160 cells in the normal direction.
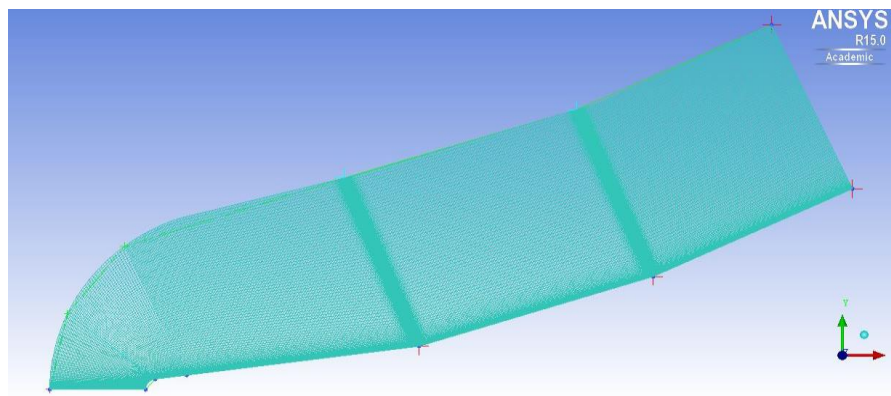

Fig 2. Triple ramp of mesh size:1320×160

2.2.1. Validation of Double Ramp Case

For the validation of double ramp case, following meshes were considered, 240x40 (Coarse mesh) with first spacing as given in literature and 30 microns, 480x80 (Medium Mesh) with first spacing as given in literature and 30 microns, 960x160 (Super Fine Mesh) with first spacing as given in literature and 30 microns and an additional Fine mesh which is not specified in literature but has been considered for this study considering the stiffness of the solver. The Fine mesh case is 660x120 with first spacing of 15 and 30 Microns respectively.

Case	Grid Size	Δn_0 in m	Δn_h in m	Δs_0 in m	Δs_h in m
1	240×40	30×10^{-6}	30×10^{-6}	33.7×10^{-6}	9×10^{-6}
2	480×80	30×10^{-6}	30×10^{-6}	33.7×10^{-6}	9×10^{-6}
3	660×120	15×10^{-6}	30×10^{-6}	33.7×10^{-6}	9×10^{-6}
4	960×160	30×10^{-6}	30×10^{-6}	33.7×10^{-6}	9×10^{-6}
5	240×40	3×10^{-6}	1×10^{-5}	6.75×10^{-5}	1.8×10^{-5}
6	480×80	1.5×10^{-6}	5×10^{-6}	3.37×10^{-5}	9×10^{-6}
7	960×160	0.75×10^{-6}	2.5×10^{-6}	1.68×10^{-5}	4.5×10^{-6}

Table1.Grid spacing details

$\Delta n =$ Spacing distribution along the stagnation line
$\Delta s =$ Tangential spacing along body
$0 =$ stagnation point; $h =$ cone–flare junction.
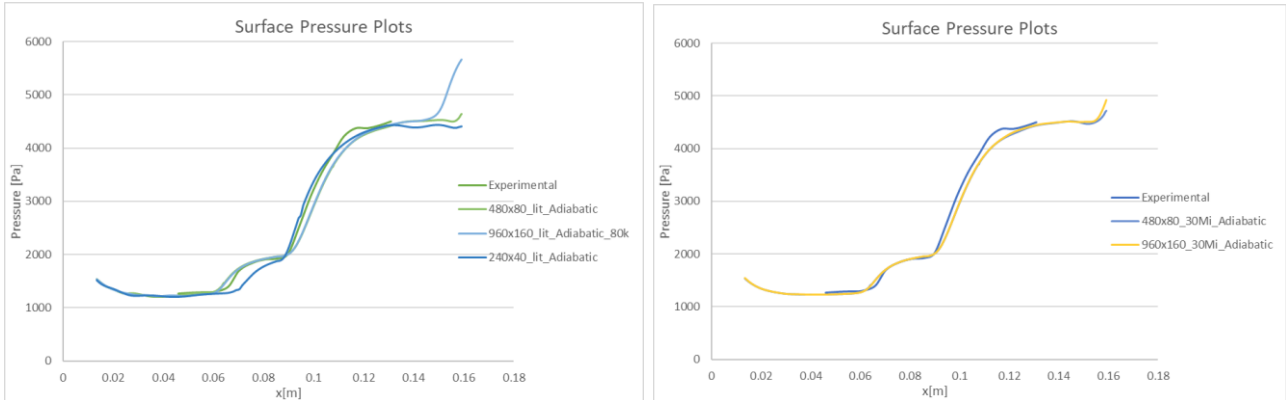
Fig 3: Validation between Experimental & Simulations with different mesh cases

From the above plots it can be noted that the literature mesh cases were less accurate when compared to the meshes with 30 Micron spacing. 960x160 & 480x80 with 30 microns spacing predicted closest to the Experimental data as seen in Fig 2. The separation and reattachment points have very good match while there is slight but acceptable computational underprediction in the post attachment zone. These two meshes shall be further considered for triple ramp cases.

2.2.2. Grid Independence of Triple Ramp Case

From the validation study of Double Ramp Case it was found that the meshes with size 960x160 and 480x80 with 30 Micron spacing in the normal direction predicted close results to the experimental results as given in the paper by *R.Savino & D Paterna*[1]. The same two meshes with additional ramp and equal mesh addition was considered for the triple ramp cases, and hence the meshes considered were 1320x160 and 680x80. Simulations were run with these two-mesh considerations with Third ramp angle of 7.5, 10, 12.5 and 15 degrees. The outcomes are as below:

(a)

(b)

(c)

(d)
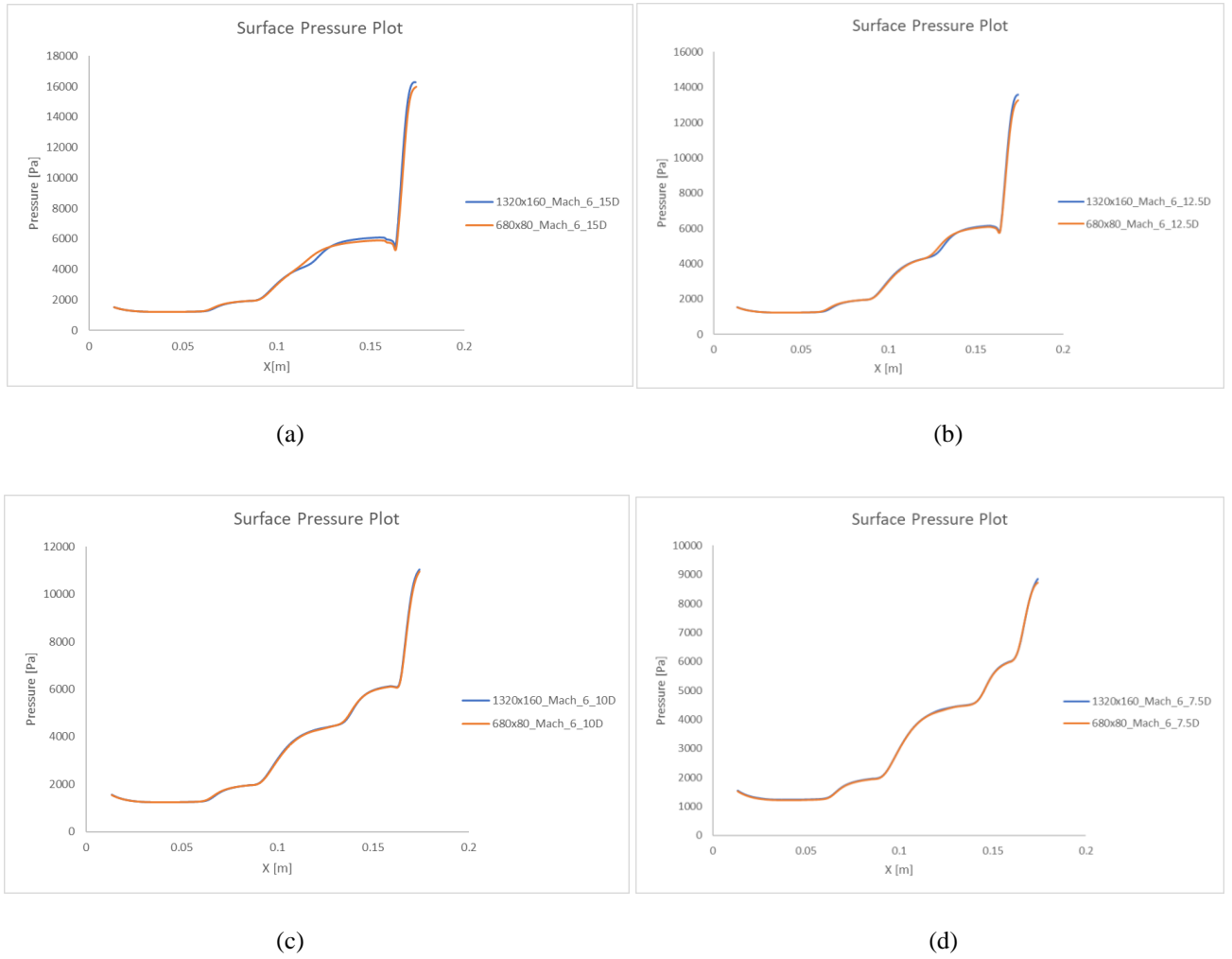
Fig 4. Surface Pressure comparison between two mesh types for different third ramp angles

In Fig 3(a), the second ramp separation is missed by the 680x80 mesh whereas the 1320x160 mesh captures the separation at the second ramp. Thus, making it clear that to capture the shock wave boundary layer interaction at the second ramp, higher mesh concentration is needed. Referring to Fig 3(b), it can be inferred that the 680x80 Mesh is slightly underpredicting the separation point at second ramp when compared to the case with higher mesh count. From the above studies it can be inferred that both the meshes predict same for lower third ramp angles, but under predicts the shock separation for higher third ramp angles. Hence for all further studies of third ramp cases, the 1320x160 Mesh shall be considered for simulation.

3. SOLVER SETUP:

HiFUN Solver is used for all simulations, boundaries used are Supersonic inlet for far field, supersonic outlet for rear surface, wall for geometry, rotational axis for axis. The spatial accuracy is of second order. Time integration is implicit, and the number of sweeps is 14. The simulations are done at free stream conditions of Mach number 6, pressure is 673.67 Pa, Temperature is 67.07K, Dynamic viscosity is 4.47e-6 Pa-s, thermal conductivity is 0.00607 W/m-K, the wall temperature is 300K. The maximum residual is of 1e-10 and time step is Local.

4. RESULTS AND DISCUSSIONS:

Computational studies are carried out to understand the effect of ramp angle on the shock induced boundary layer separation and evaluate the behaviour of separation bubble at third ramp. In addition, the simulations are also giving insights on the effects of incipient separation angle for three ramp conditions. Four angles are considered for the third ramp i.e., 7.5, 10, 12.5 and 15^0 respectively. The presence of a separation bubble is identified in every case with sudden pressure bump that can be noticed in Fig. 5. A well-defined pressure bump can be seen in the case of lower ramp angles indicating the presence of a well-separated scenario

whereas a diffused pressure bump is seen for higher ramp angles indicating the presence of a weak separation condition, in-fact for 15^0 third ramp angle the flow almost misses to separate indicating a fully attached flow and may not detach for any more higher angles. Also, an increase in upstream influence can be noticed, from early raise in pressure with an increase I ramp angle can be noticed from the graph shown in Fig.5, the bubble length at the third ramp is also found to be reduced when compared with the bubble at the second ramp. Table. 2 indicates approximate bubble length variations at second and third ramps. From Table.2 it can be understood that the presence of third ramp is not majorly influencing the boundary layer separation and bubble behaviour at the second ramp junction. From the pressure loading perspective, the case with 10^0 third ramp angle seems to be the most ideal, but depending on the trajectory path, the angles can be chosen accordingly, for steeper trajectory lower third ramp angle with higher pressure load can be used, while for less steep trajectory a higher ramp angle can be used which reduced the pressure load at third ramp, while also keeping in mind that separation needs to be suppressed.
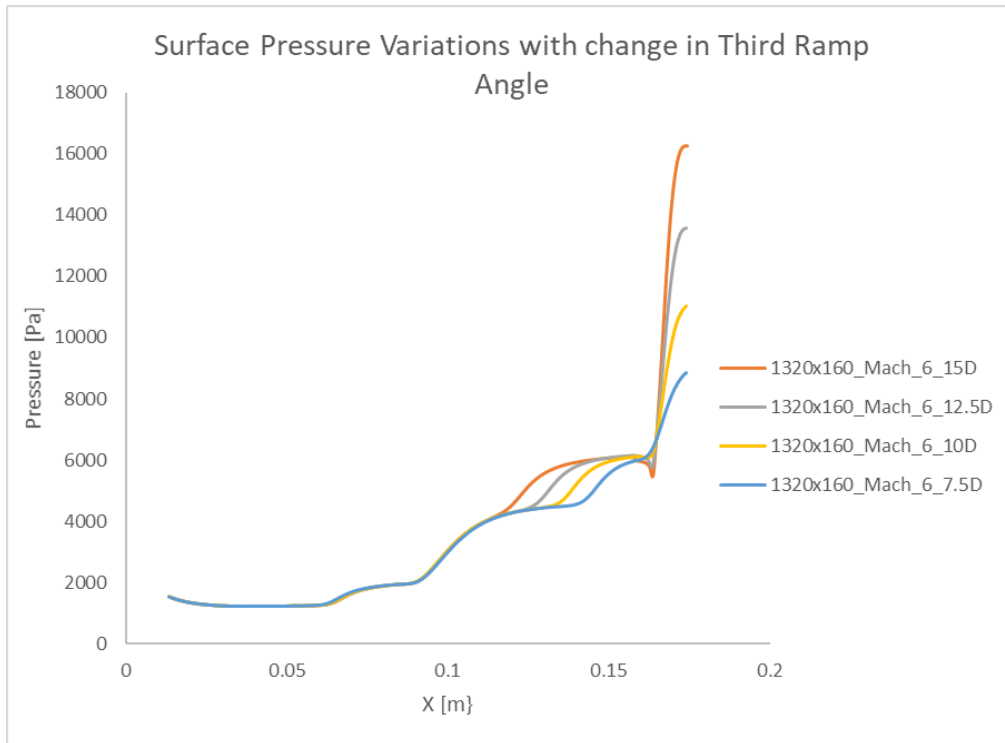
Fig 5. Surface Pressure Variations with change in Third Ramp Angle

θ^0	M_∞	T_∞ (K)	L_{sep} in mm at 1nd cone flare	L_{sep} in mm at 2nd cone flare	Comment
7.5	6	67.07	24	20	$\theta\uparrow$ $L_{sep}\uparrow$ at both cone flare junction
10	6	67.07	24	24	
12.5	6	67.07	24	33	
15	6	67.07	24	42	

Table 2. Variation of Separation bubble length with increase in ramp angle

5. CONCLUSIONS:

The aim of this study is to understand the effect of ramp angle on the shock wave boundary layer interactions at different cone flare junctions in laminar hypersonic flow conditions using High resolution flow solver HiFUN. Grid independence study is carried out for multiple meshes, the Medium and Superfine mesh negligible difference between the experimental data as provided in literature and the simulation study. Through Pressure distribution studies, a qualitative understanding of the flow separation, reattachment, bubble length and upstream influence is addressed. The incipient separation angle proves to have good correlation between the

flow separation and ramp angle. The length of separation bubble is found to increase with increase in ramp angle at the third cone flare junction. A significant upstream influence is identified on flows with higher ramp angles, while it is also understood from the study that the presence of third ramp does not influence flow at the second ramp. The study also gives an overall perspective on the pressure loading on multi-ramp geometries and its utilisation for stable trajectories and along a defined path. Further works shall be carried on multi-ramp cone flares at higher Mach numbers

6. ACKNOWLEDGEMENTS:

REFERENCES:

[1]. R. Savino, D. Paterna , *Blunted cone flare in hypersonic flow*, Computers & Fluids 34 (2005) 859–875.

[2]. Bibin John, Vinayak N. Kulkarni, Ganesh Natarajan*, Shock wave boundary layer interactions in hypersonic flows,*International Journal of Heat and Mass Transfer 70 (2014) 81–90.

[3]. Bibin John, Vinayak Kulkarni. (2014). Effect of leading edge bluntness on the interaction of ramp induced shock wave with laminar boundary layer at hypersonic speed. Computers & Fluids. 96, 177 - 190.

[4]. Reichel. S & Groll. R. (2013). Numerical simulation and experimental validation of a hypersonic flow for numerical modulation of re-entry phenomena prediction using adaptive mesh refinement. International Journal of Computational Methods and Experimental Measurements. 1 (4), 381 - 394.

[5]. Bibin John, Vinayak Kulkarni. (2013). Numerical assessment of correlations for shock wave boundary layer interaction. Computers & Fluids. 90, 42 - 50.

[6]. D.A. Needham, J.L. Stollery, Boundary-layer separation in hypersonic flow, in: AIAA paper 66-455, 1996.

Thesis V2

Internet Source

<1%

7   drguven.com
    Internet Source

<1%

8   link.springer.com
    Internet Source

<1%

9   "Fluid Mechanics and Fluid Power –
    Contemporary Research", Springer Science and
    Business Media LLC, 2017
    Publication

<1%

10 "30th International Symposium on Shock Waves
    2", Springer Nature, 2017
    Publication

<1%

11 Bibin John, Vinayak Kulkarni. "Numerical
    assessment of correlations for shock wave
    boundary layer interaction", Computers & Fluids,
    2014
    Publication

<1%

12 Meinhard T. Schobeiri. "Turbomachinery Flow
    Physics and Dynamic Performance", Springer
    Nature, 2012
    Publication

<1%

13 "New Results in Numerical and Experimental
    Fluid Mechanics III", Springer Nature, 2002
    Publication

<1%

14 Submitted to University of Hong Kong
    Student Paper   <1%

15 Bibin John, Vinayak Kulkarni. "Alterations in
    Critical Radii of Bluntness of Shock Wave
    Boundary Layer Interaction", Journal of   <1%
    Aerospace Engineering, 2017
    Publication

16 R. Prakash, L. M. Le Page, L. P. McQuellin, S.
    L. Gai, S. O'Byrne. "Direct simulation Monte
    Carlo computations and experiments on   <1%
    leading-edge separation in rarefied hypersonic
    flow", Journal of Fluid Mechanics, 2019
    Publication

17 Submitted to BITS, Pilani-Dubai
    Student Paper   <1%

18 John, Bibin, Srikanth Surendranath, Ganesh
    Natarajan, and Vinayak Kulkarni. "Analysis of
    dimensionality effect on shock wave boundary   <1%
    layer interaction in laminar hypersonic flows",
    International Journal of Heat and Fluid Flow,
    2016.
    Publication

19 Shock Waves, 2009.
    Publication   <1%

20 D.L. Carraway. "A transition detection study at
    Mach 1.5, 2.0 and 2.5 using a micro-thin hot-film   <1%

system", International Congress on Instrumentation in Aerospace Simulation Facilitie, 1989
Publication

21 Navaneetha Krishnan, R.. "Performance of numerical schemes in the simulation of two-phase free flows and wall bounded mini channel flows", Chemical Engineering Science, 20100915
Publication

<1%

22 Submitted to Emirates Aviation College, Aerospace & Academic Studies
Student Paper

<1%

23 "Chapter 600 IARC Fellowships for Cancer Research", Springer Nature America, Inc, 2019
Publication

<1%

24 R. Sriram, L. Srinath, Manoj Kumar K. Devaraj, G. Jagadeesh. "On the length scales of hypersonic shock-induced large separation bubbles near leading edges", Journal of Fluid Mechanics, 2016
Publication

<1%

25 Submitted to Queen Mary and Westfield College
Student Paper

<1%

26 Submitted to University of Hertfordshire
Student Paper

<1%

27 "30th International Symposium on Shock Waves 1", Springer Nature, 2017
Publication
<1%

28 Submitted to Cranfield University
Student Paper
<1%

29 core.ac.uk
Internet Source
<1%

30 Siddesh Desai, Shuvayan Brahmachary, Hrishikesh Gadgil, Vinayak Kulkarni. "Probing Real Gas and Leading-Edge Bluntness Effects on Shock Wave Boundary-Layer Interaction at Hypersonic Speeds", Journal of Aerospace Engineering, 2019
Publication
<1%

31 Siddesh Desai, Vinayak Kulkarni, Hrishikesh Gadgil. "Separation mitigation using pressure feedback technique for hypersonic shock wave boundary layer interaction", Proceedings of the Institution of Mechanical Engineers, Part G: Journal of Aerospace Engineering, 2018
Publication
<1%

32 mafiadoc.com
Internet Source
<1%

33 Juhong Jia, Debin Fu, Zepeng He, Junfan Yang, Lijie Hu. "Hypersonic aerodynamic interference investigation for a two-stage-to-orbit model",
<1%

Acta Astronautica, 2020
Publication

34   ediss.uni-goettingen.de
      Internet Source   <1%

35   Springer Aerospace Technology, 2015.
      Publication   <1%

36   Kim, H.D.. "A time-accurate high-resolution TVD
      scheme for solving the Navier-Stokes
      equations", Computers and Fluids, 199307/09   <1%
      Publication

37   Submitted to Higher Education Commission
      Pakistan   <1%
      Student Paper

38   eprints.kfupm.edu.sa
      Internet Source   <1%

39   Reinartz, Birgit, Josef Ballmann, and Russell
      Boyce. "Numerical Investigation of Wall
      Temperature and Entropy Layer Effects on
      Double Wedge Shock / Boundary Layer   <1%
      Interactions", 14th AIAA/AHI Space Planes and
      Hypersonic Systems and Technologies
      Conference, 2006.
      Publication

40   raiith.iith.ac.in
      Internet Source   <1%

d-nb.info

41   Internet Source

<1%

42   Submitted to The Scientific & Technological Research Council of Turkey (TUBITAK)
Student Paper

<1%

43   Adnan Qamar, Sanjeev Sanghi. "Aerodynamics Characteristic of Axisymmetric Surface Protuberance in Supersonic Regime", Engineering Applications of Computational Fluid Mechanics, 2014
Publication

<1%

44   Zhichao Yuan, Shizhang Huang, Xiaowei Gao, Jian Liu. "Effects of Surface-Catalysis Efficiency on Aeroheating Characteristics in Hypersonic Flow", Journal of Aerospace Engineering, 2017
Publication

<1%

45   MS Goyat, Vikram Jaglan, Vikram Tomar, Guillaume Louchaert et al. "Superior thermomechanical and wetting properties of ultrasonic dual mode mixing assisted epoxy-CNT nanocomposites", High Performance Polymers, 2017
Publication

<1%

46   "Basic Research and Technologies for Two-Stage-to-Orbit Vehicles", Wiley, 2005
Publication

<1%

47   Bibin John, Srikanth Surendranath, Ganesh Natarajan, Vinayak Kulkarni. "Analysis of dimensionality effect on shock wave boundary layer interaction in laminar hypersonic flows", International Journal of Heat and Fluid Flow, 2016
Publication

<1%

48   Rakeshkumar K. Patel, K. Venkatasubbaiah. "Numerical Simulation of the Orion CEV Reentry Vehicle", Journal of Aerospace Engineering, 2015
Publication

<1%

49   Submitted to University of Liverpool
Student Paper

<1%

50   H. S. Lee, J. H. Lee, G. Park, S. H. Park, Y. H. Byun. "Three-dimensional supersonic flow around double compression ramp with finite span", Shock Waves, 2016
Publication

<1%

51   export.arxiv.org
Internet Source

<1%

52   Navarro-Martinez, S.. "Numerical simulation of Gortler vortices in hypersonic compression ramps", Computers and Fluids, 200502
Publication

<1%

53   www.iccms2016.org

Internet Source

<1%

54   Mahsa Mortazavi, Doyle D. Knight. "Shock
       Wave Laminar Boundary Layer Interaction at a
       Hypersonic Flow Over a Blunt Fin-Plate
       Junction", 55th AIAA Aerospace Sciences
       Meeting, 2017
       Publication

<1%

55   Submitted to Heriot-Watt University
       Student Paper

<1%

56   Amna Khraibut, S. L. Gai, A. J. Neely.
       "Numerical study of bluntness effects on laminar
       leading edge separation in hypersonic flow",
       Journal of Fluid Mechanics, 2019
       Publication

<1%

57   Submitted to University of Sydney
       Student Paper

<1%

58   Ma, Xinzhou. "Electrochemical Machining of
       Gold Nanostructures and Optical
       Characterization with Cathodoluminescence",
       Universität Karlsruhe, 2011.
       Publication

<1%

59   Francis Jayakanth, Filbert Minj, Usha Silva,
       Sandhya Jagirdar. "ePrints@IISc: India's first
       and fastest growing institutional repository",
       OCLC Systems & Services: International digital

<1%

library perspectives, 2008
Publication

60 Submitted to Technische Universiteit Delft
Student Paper
<1%

61 Minoru Watari, Noriaki Hirabayashi, Tadao Koyama, Shinji Nagai et al. "Flow Qualities of JAXA Hypersonic Wind Tunnel Facilities", 14th AIAA/AHI Space Planes and Hypersonic Systems and Technologies Conference, 2006
Publication
<1%

62 "Shock Wave Interactions", Springer Nature, 2018
Publication
<1%

63 Neuenhahn, Thomas, and Herbert Olivier. "Influence of the Wall Temperature and the Entropy Layer Effects on Double Wedge Shock Boundary Layer Interactions", 14th AIAA/AHI Space Planes and Hypersonic Systems and Technologies Conference, 2006.
Publication
<1%

64 GROSS, L.. "The prediction of two-dimensional airfoil stall progression", 16th Aerospace Sciences Meeting, 1978.
Publication
<1%

65 Submitted to Coventry University
Student Paper
<1%

66 Submitted to Jawaharlal Nehru Technological University
Student Paper
<1%

67 F. Grasso, M. Marini. "Analysis of hypersonic shock-wave laminar boundary-layer interaction phenomena", Computers & Fluids, 1996
Publication
<1%

68 R. C. Mehta. "Peak heating for reattachment of separated flow on a spiked blunt-body", Heat and Mass Transfer, 2000
Publication
<1%

69 S. Barboy, A. Rashkovan, G. Ziskind. "Determination of hot spots on a heated wavy wall in channel flow", International Journal of Heat and Mass Transfer, 2012
Publication
<1%

70 R. Yadav, A. Bodavula, S. Joshi. "Numerical investigation of the effect of disk position on the aerodynamic heating and drag of a spiked blunt body in hypersonic flow", The Aeronautical Journal, 2018
Publication
<1%

71 M. Mahmood. "Hydromagnetic flow of viscous incompressible fluid past a wedge with permeable surface", ZAMM, 03/23/2009
Publication
<1%

72 Ola Lögdberg. "On the scaling of turbulent separating boundary layers", Physics of Fluids, 2008
Publication
<1%

73 S. A. Skillings. "Condensation phenomena in a turbine blade passage", Journal of Fluid Mechanics, 2006
Publication
<1%

74 Submitted to The Hong Kong Polytechnic University
Student Paper
<1%

75 Submitted to University of Aberdeen
Student Paper
<1%

76 YINDA, H.. "Experimental research on separation, heat transfer and ablation of the model of flat plate in supersonic turbulent flow", 4th Thermophysics and Heat Transfer Conference, 1986.
Publication
<1%

77 Kexin Wu, Senthil Kumar Raman, Vignesh Ram Petha Sethuraman, Guang Zhang, Heuy Dong Kim. "Effect of the wall temperature on Mach stem transformation in pseudo-steady shock wave reflections", International Journal of Heat and Mass Transfer, 2020
Publication
<1%